eman ta zabal zazu

Universidad
del País Vasco

Euskal Herriko
Unibertsitatea

Equilibrium and transport properties of hybrid junctions between superconductors and spin active materials

by

Bogusz Bujnowski

Supervisors:
Dr. Dario Bercioux
Dr. Jérôme Cayssol

A thesis submitted in the
Faculty of Physics, Chemistry and Materials Science
Department of Materials Physics

October 2019

List of Publications

- **published during the PhD:**
  - **Andreev spectrum of a Josephson junction with spin-splitt superconductors**
    B. Bujnowski, D. Bercioux, F. Konschelle, J. Cayssol and F.S. Bergeret, Europhysics Letters **115**, 67001 (2016).
  - **Quantum transport properties of an Exciton insulator/superconductor hybrid junction**
    D. Bercioux, B. Bujnowski and F.S. Bergeret, Advanced Quantum Technologies **2**, 1800049 (2019).
- **submitted:**
  - **Correspondence between bulk equilibrium spin-currents and edge spin accumulation in wires with spin-orbit coupling**
    I.V. Tokatly, B. Bujnowski and F.S. Bergeret, (2019), submitted to Physical Review B.
  - **Switchable Josephson current in junctions with spin-orbit coupling**
    B. Bujnowski, R. Biele and F.S. Bergeret, (2019), submitted to Physical Review B.
- **to be submitted soon:**
  - **Weyl semimetal interfaces as chiral valves**
    B. Bujnowski, A. Grushin and J. Cayssol.

Abbreviations

BCS	Bardeen Cooper Schrieffer
BdG	Bogoliubov de Gennes
DOS	Density Of States
LDOS	Local Density Of States
ABS	Andreev Bound States
S	Superconductor
N	Normal metal
F	Ferromagnet
DW	Domain Wall
SS	Spin-split Superconductor
SOC	Spin Orbit Coupling
LRTC	Long Range Triplet Component
DP	Dyakonov-Perell
ESC	Equilibrium Spin Currents
WSM	Weyl SemiMetal

Contents

Resumen

La superconductividad es un fenómeno cuántico a nivel macroscópico que se caracteriza por la ausencia de resistividad y la expulsión de campos magnéticos externos por debajo de una temperatura crítica. Inicialmente, los superconductores (S) eran considerados como elementos de resistencia cero en un circuito. Sin embargo, la naturaleza cuántica de este fenómeno permite un número aplicaciones potencialmente mucho más interesantes, número que sigue aumentando hoy en día. El avance en los métodos de fabricación y miniaturización de heteroestructuras formadas por superconductores de alta calidad (S), metales normales (N), partes ferromagnéticas (F), semiconductores, materiales con fuerte interacción espín-órbita (SOC por sus siglas en inglés) o gases de electrones 2D ha abierto el camino a estudiar una gran cantidad de efectos debidos a la coherencia de fase y ha hecho de los superconductores la base para futuras tecnologías emergentes, como la simulación cuántica, la detección cuántica y la computación cuántica.

El fundamento teórico para la explicación de la superconductividad se basa en la inestabilidad de un gas de Fermi a que los electrones con energías cercanas a la energía de Fermi se atraigan mediante una interacción arbitrariamente débil (teoría BCS). En los llamados superconductores convencionales, la interacción electrón-fonón es la causante de la atracción que une los electrones por parejas, conocidas como pares de Cooper. En estos superconductores, es energéticamente favorable unir electrones con momento y espín opuesto. Por ello, los pares de Cooper tienen un espín entero y se comportan como bosones, pudiendo poblar así el mismo estado cuántico macroscópicamente. La condensación de los electrones en pares de Cooper desemboca en la aparición de una banda de energías prohibidas en el espectro de excitaciones del superconductor alrededor de la energía de Fermi. La formación de pares de Cooper es un concepto general, por lo que existen diversos mecanismos de enlace entre electrones que se traduzca en la aparición de la superconductividad en gran variedad de materiales. Aún no se han entendido teóricamente todos estos mecanismos, por lo que, hoy en día, la búsqueda de nuevos tipos de superconductores sigue en marcha.

En esta tesis investigamos la evolución del estado singlete de un material superconductor convencional debido a campos dependientes del espín a su alrededor. Las correlaciones superconductoras no están únicamente ligadas al superconductor, sino que pueden penetran en materiales metálicos adyacentes una profundidad del orden del tamaño típico de los pares de Cooper (conocida como la longitud de coherencia superconductora), que a su vez depende fuertemente del propio material conductor. En general, el material no superconductor en contacto con el superconductor adquiere propiedades de este último. Este efecto se conoce como efecto de proximidad y da lugar a fenómenos de coherencia de fase muy interesantes.

Una de las manifestaciones destacadas de los efectos de proximidad es el efecto Josephson. El estado base de un superconductor se describe mediante una función de onda macroscópica, caracterizada por una fase. El efecto Josephson es la transmisión coherente de pares de Cooper entre dos superconductores, separados por una barrera aislante estrecha o una región conductora, que difieren en la fase de su propia función de onda macroscópica. Esta diferencia de fase genera una corriente no disipativa sin la necesidad de aplicar una diferencia de potencial (efecto Josephson de corriente continua).

La primera parte de la tesis introduce los efectos de proximidad en heteroestructuras superconductor – metal normal de manera didáctica. Repasamos brevemente distintos aspectos de la teoría BCS e introducimos dos formalismos distintos para describir propiedades de equilibrio y de transporte en sistemas superconductores no homogéneos, a saber, las ecuaciones Bogoliubov-de Gennes y las funciones de Green cuasiclásicas. Ambos formalismos van a ser usados a lo largo de la tesis. Dentro del formalismo de Bogoliubov-de Gennes, explicamos los procesos microscópicos que gobiernan el transporte en heteroestructuras N/S, es decir, las reflexiones de Andreev que ocurren en las interficies S/N y los estados localizados de Andreev que se forman en uniones S/N/S. Asimismo, poniendo como ejemplo los casos de una interficie S/F y una unión S/F/S, demostramos que un campo dependiente del espín puede alterar el efecto de proximidad y las propiedades de transporte de este tipo de sistemas, introduciendo así distintas maneras de controlar el transporte. El campo de canje en un material ferromagnético separa las bandas de energía anteriormente degeneradas en espín y, por consiguiente, el alineamiento de los espines de manera paralela se vuelve energéticamente favorable. Este efecto compite con el mecanismo convencional de emparejamiento entre los electrones que prefiere que los espines se encuentren colocados de manera antiparalela. En heteroestructuras S/F, la competición entre el ferromagnetismo y la superconductividad conduce a un efecto de proximidad de corto alcance y en uniones S/F/S, en función de la longitud de la unión y de la fuerza del campo de canje, a la inversión de la corriente Josephson continua máxima,, conocido como transición 0-π.

A la parte introductoria le siguen los resultados originales surgidos de la investigación. El segundo capítulo de la tesis se centra en la aparición de estados localizados de Andreev y en el efecto Josephson en uniones balísticas con superconductores con bandas de espín separadas (SS). Para obtener la separación de bandas de espín en películas superconductoras se puede, bien aplicar un campo magnético externo, bien poner en contacto capas de aislantes ferromagnéticos. En este último caso, la interacción de canje entre los electrones de conducción en el superconductor y los momentos magnéticos localizados en el aislante ferromagnético separa las bandas de espín en la densidad de estados del superconductor. Utilizar aislantes ferromagnéticos para lograr grandes separaciones evita tener que aplicar campos magnéticos fuertes, lo cual conlleva una gran ventaja. En uniones SS/N/SS, se puede controlar la orientación de los campos de canje en cada uno de los superconductores. Tal y como ha sido demostrado, es posible incrementar la corriente crítica en este tipo de uniones aumentando la magnitud de los campos de canje, cuando dichos campos están alineados de manera antiparalela. Considerando que la separación de las bandas de espín típicamente se traduce en la destrucción de pares de Cooper, este es un resultado ciertamente contraintuitivo. La dependencia de los estados de Andreev localizados en función de la diferencia de fase entre los lados superconductores no había sido estudiada hasta el momento. Por lo tanto, con el fin de incrementar el conocimiento alrededor de los procesos microscópicos subyacentes, hemos analizado las propiedades espectrales de este tipo de uniones dentro del formalismo Bogoliubov-de Gennes.

En una unión balística corta S/N/S con parámetros de orden iguales, el tuneleo a través de los estados de Andreev localizados es la contribución dominante a la corriente Josephson a baja temperatura. En las uniones equivalentes SS/N/SS, demostramos que cualquier desviación de la situación con campos de canje iguales en ambos superconductores, se traduce en la desaparición de los estados de Andreev localizados para un rango finito de diferencias de fase φ definido mediante una fase crítica, φ_c, de modo que $|\varphi| < \varphi_c$. Este es un fenómeno originado por la asimetría en la estructura de espín de las bandas prohibidas en los electrodos SS a la izquierda y a la derecha de la unión. Como consecuencia, la corriente Josephson en el intervalo de diferencias de fase superconductora anteriormente descrito se lleva a cabo exclusivamente por estados en la parte continua del espectro. El valor de φ_c no depende de la transmisión de la unión, por lo que es robusto ante imperfecciones. Cuando $|\varphi| < \varphi_c$, la corriente Josephson se compone por la suma de las contribuciones de los estados de Andreev localizados y aquellos en la parte continua del espectro. En uniones con perfecta transmisión, el tuneleo a través de los estados de Andreev domina en la corriente, mientras que en uniones con mala transmisión la corriente se describe únicamente mediante las excitaciones en la parte continua del espectro. Incluso cuando la banda de estados de Andreev de mayor energía se incorpora a la parte continua del espectro, hay otros estados de Andreev localizados de menor energía que están definidos para todos los valores de φ. Por lo tanto, el valor de φ_c decrece cuando la longitud de la unión crece.

Después de cubrir el efecto de proximidad en sistemas balísticos con materiales ferromagnéticos en detalle, cambiamos el tema para centrarnos en sistemas difusivos. Discutimos la aparición de las llamadas correlaciones triplete de largo alcance (LRTC por sus siglas en inglés) en materiales con fuerte ferromagnetismo y cómo estas afectan al efecto Josephson.

La coexistencia de superconductividad y ferromagnetismo deriva en correlaciones superconductoras del tipo triplete. En una heteroestructura S/F con un campo de canje homogéneo, los pares de Cooper en estado singlete que penetran el material ferromagnético se convierten parcialmente en pares del tipo triplete, cuya proyección de espín total con respecto al campo de canje es igual a cero. En un monodominio magnético difusivo, las correlaciones singlete y triplete del condensado decaen a lo largo de la longitud magnética característica, ξ_h, la cual depende de la magnitud del campo de canje. En superconductores convencionales y para magnitudes de campos de canje típicas, ξ_h es mucho menor que la longitud térmica característica de decaimiento, ξ_ω, de los sistemas sin magnetismo. A su vez, las componentes del estado triplete con proyecciones de espín finitas, esto es, perpendiculares al campo de canje, no son afectadas por el efecto de ruptura de pares y su longitud de decaimiento característica es comparable a ξ_ω. Este tipo de LRTC pueden generarse por la falta de homogeneidad del campo de canje o debido a la presencia de SOC junto a un campo de canje homogéneo. La predicción de LRTC en estructuras híbridas S/F ha ha sido corroborada por medio de diversos trabajos experimentales.

Por el contrario, la generación de LRTC en sistemas con SOC y campos de canje homogéneos aún no se ha observado. Recientemente, se han explorado experimentalmente uniones Josephson transversales con campos magnéticos dentro del plano y materiales con SOC, pero no se ha encontrado ninguna evidencia de LRTC en la corriente Josephson. En este tipo de uniones S/F/S multicapa la condición para que aparezcan LRTC es bastante restrictiva. Por ejemplo, para que un acoplamiento espín-órbita del tipo Rashba genere LRTC, la magnetización tiene que tener una componente fuera del plano. Este es un escenario bastante desfavorable, ya que campos de canje de este tipo pueden crear vórtices en el superconductor que compliquen la interpretación de los resultados experimentales.

Las estructuras laterales son mucho más adecuadas para la observación de LRTC inducidas por SOC, ya que las corrientes también tienen una componente a lo largo de la interfaz híbrida. En el capítulo 3 repasamos brevemente el efecto de proximidad bajo la influencia de de campos dependientes del espín en heteroestructuras difusivas y demostramos que las uniones laterales son la configuración idónea para el estudio de corrientes Josephson de largo alcance. Seguidamente, proponemos dos tipos de uniones realistas, las cuales representan las configuraciones más favorables para observar la generación de LRTC. Calculamos la corriente Josephson en presencia de SOC del tipo Rashba y Dresselhauss, lo cual resulta en efectos anisotrópicos de relajación y precesión del espín. La contribución de estos dos efectos a la corriente Josephson depende fuertemente en la orientación de los campos de canje y su coexistencia conlleva a una variedad de escenarios donde la corriente se invierte.

Consideramos dos geometrías posibles de uniones laterales. La primera de ellas consiste en un puente ferromagnético que une los electrodos superconductores, mientras que los campos de SOC se originan mediante capas de metales pesados intercaladas entre los finales S y el puente. En el segundo tipo de unión, el campo de canje y el SOC son finitos a lo largo de todo el puente. En una configuración realista, el segundo escenario puede realizarse por medio de un puente 2D semiconductor en un campo magnético externo. Presentamos resultados analíticos de la ecuación de Usadel linealizada para la corriente Josephson en el primer tipo de uniones. Estos resultados analíticos son complementados por cálculos numéricos en ambos tipos de uniones. Tanto los resultados analíticos como los numéricos muestran que se puede controlar la magnitud y signo de la corriente Josephson mediante la variación de la dirección del campo de canje y la magnitud del SOC. Además su posible aplicación como válvula de supercorrientes, estos resultados demuestran que este tipo de uniones laterales pueden ser usadas como detectores del efecto de proximidad de largo alcance inducido por SOC y campos de canje homogéneos.

Siguiendo estos estudios centrados en el efecto Josephson, nos centramos ahora en otro fenómeno de equilibrio, a saber, las corrientes de equilibrio de espín (ESC por sus siglas en inglés). Al contrario que la corriente Josephson, las ESCs no son corrientes de transporte, por lo que no pueden desembocar en acumulación de espín en presencia de simetría de inversión temporal. En el capítulo 4 mostramos que un nanohilo con SOC y simetría de inversión temporal rota por un campo de Zeeman presenta una ESC, la cual se manifiesta como una polarización de espín no despreciable perpendicular al campo Zeeman.

Desde el principio, el mismo Rashba demostró que cualquier sistema descrito por el hamiltoniano Rashba estándar de dos dimensiones permite corrientes de espín incluso en equilibrio termodinámico. Estas corrientes de espín en equilibrio en materiales con acoplamiento espín-órbita (SOC por sus siglas en inglés) han atraído gran atención. Las corrientes de espín normalmente son detectadas de forma indirecta, por ejemplo, midiendo el voltaje de la corriente de espín inducida por la acumulación de espín fuera del equilibrio con un sensor ferromagnético, o resistencia magnética “spin-Hall”. No obstante, las ESC no conducen a esa acumulación de espín y por tanto no pueden ser detectadas por los métodos dichos anteriormente. De hecho, las ESC, parecen ser conceptualmente no observables al ser corrientes de fondo que no se transportan, aunque se han presentado propuestas que las relacionan con el esfuerzo de torsión mecánico, el cual sí es detectable. Por estas razones, la interpretación de las ECS es aún objeto de debate. Además, en presencia de SOC, el espín no se conserva de la forma que estamos acostumbrados. Teóricamente, esta controversia se puede eliminar tratando el SOC como un campo externo modificado de tipo SU(2), aunque desde el punto de vista experimental las ESC siguen siendo huidizas.

En el capítulo 4 demostramos una correspondencia entre las ESC en hilos nanométricos con SOC y una polarización transversal del espín inducida en el filo del hilo nanométrico. Al contrario que las ESC, la polarización del espín puede ser detectada experimentalmente. La correspondencia puede considerarse universal puesto que se cumple para cualquier sistema unidimensional (o quasi-unidimensional) de varios cuerpos, siempre y cuando la interacción partícula-partícula sea independiente del espín. Las ESC aparecen específicamente cuando se aplica un campo magnético B con un componente perpendicular al SOC, induciendo una división Zeeman del campo, $h = g\mu_B B$. Mostramos que estas ESC internas siempre van acompañadas con una acumulación de espín en el filo que es transversal tanto al campo Zeeman como al SOC. Esta acumulación transversal de espín en equilibrio también puede entenderse como una redistribución de la densidad de espín en el sistema como una respuesta a una corriente electromagnética directa. Por tanto, la medida de la densidad de espín transversal debería ser una evidencia de las ESC en hilos nanométricos. Esta acumulación transversal de espín no se muestra solo en el estado normal, si no que también cuando el nanohilo tiene una diferencia Δ de superconductividad en la densidad de los estados inducidos, por ejemplo, por proximidad a un superconductor. Es decir, encontramos una conexión entre la existencia de ESC y una respuesta paramagnética anómala del superconductor que generaliza la teoría, ya establecida, de "Knight-shift" en superconductores.

Recientemente los nanohilos semiconductores con acoplamiento espín-órbita, como InAs y InSb, conectados con superconductores tradicionales han sido explorados de manera intensiva debido mayormente a la posibilidad de crear modos cero de Majorana y superconductividad topológica en estos sistemas. Tanto las ESC como los modos cero de Majorana, necesitan un componente de campo de Zeeman perpendicular al SOC. En el contexto de los fermiones de Majorana, muchos estudios teóricos han hecho la conexión entre la polarización del espín inducida en el filo del hilo y la transición topológica cuando $h = \sqrt{\mu^2 + \Delta^2}$, siendo μ el potencial químico. En este capítulo demostramos que la polarización transversal del espín en el filo es una propiedad universal de los nanohilos que permiten las ESC y existe para todos los valores de h, incluidos aquellos muy por debajo de la transición topologica. Por lo tanto, su detección no puede ser asociada directamente a los modos cero de Majorana, si no a la existencia de ESC. Específicamente, en función del campo Zeeman h, la acumulación total del espín muestra en general una cúspide en $h = \sqrt{\mu^2 + \Delta^2}$. Cabe destacar que cuando $\Delta \ll \mu$, la acumulación transversal de espín muestra además un máximo pronunciado en $h \approx \Delta$ y puede ser mucho mayor que la magnitud de la cúspide cuando $h = \mu$. Analizamos en detalle este máximo de la acumulación de espín y muestra robustez ante el desorden. Finalmente, presentamos resultados analíticos para la distribución espacial del momento magnético inducido como respuesta al campo de Zeeman. Encontramos que la susceptibilidad transversal cerca al filo del hilo puede ser mucho mayor que la longitudinal para valores pequeños de SOC.

Los capítulos previos han estado centrados en heteroestructuras superconductoras, donde el estado normal de dispersión es cuadrático en momento. Para la parte final de la tesis, nuestro propósito fue estudiar el efecto de proximidad en heteroestructuras entre superconductores y los recientemente descubiertos, semimetales Weyl (WSM por sus siglas en inglés). Siendo un tipo de material novedoso y emocionante que muestra una dispersión pseudo-relativista alrededor de los llamados puntos Weyl en la zona de Brillouin, y estados de superficia inusuales llamados arcos de Fermi, que son una consecuencia de la estructura topológica de la dispersión del interior, del "bulk". Este estudio inicial de las propiedades de transporte en la interfaz de WSMs en el estado normal, como una introducción básica al tema, condujo al descubrimiento de un interesante efecto de filtrado, el cual es el protagonista del último capítulo de esta tesis.

La posibilidad de filtrar grados de libertad de mecánica cuántica es la esencia de la computación. Por ejemplo, los transistores electronicos están basados en la filtración de carga eléctrica para controlar el flujo de corriente, mientras que en espintrónica se basa en filtrar la proyección del espín hacia arriba y del espín hacia abajo para codificar información. En metales donde las quasi-partículas de baja energía se comportan como partículas pseudo-relativistas, como el caso de grafeno bidimensional o WSMs tridimensionales, existe un grado de libertad adicional que puede servir como alternativas para la computación. En dos dimensiones, las quasi-partículas de Dirac son excitaciones en torno a un específico momento conocido como valles, con relaciones de dispersión lineal. Mediante la población selectiva de uno de los valles, este grado de libertad puede ser usado para codificar información, pudiendo ser llamado valletrónica. En tres dimensiones, las quasi-partículas Weyl son excitaciones en pareja dando lugar a nodos Weyl en posiciones arbitrarias del espacio momento con quiralidad opuesta. La quiralidad es un grado de libertad mecanico-cuántico que se refiere a si el momento de la quasi-partícula esta apuntando en paralelo o anti-paralelo con respecto a su espín. De forma similar al filtro del valle, un filtro de quiralidad puede ser usado para codificar información. En el último capítulo repasamos brevemente la ecuación de Dirac y la ecuación de Weyl que describen masas relativistas y fermiones de espín $1/2$ sin masa, respectivamente. Presentamos, además, la conexión con realizaciones en materia condensada mediante la inserción de un código mínimo que describe estos dos tipos de quasi-partículas fermionicas. Proponemos una simple realización de un filtro de quiralidad tridimensional. El filtro está basado en la interfaz de dos WSMs de diferente quiralidad, WSM$_1$ y WSM$_2$, donde los nodos de Weyl de quiralidad opuesta están separados en energía y momento en cada lado de la interfaz. La condición general para la transmisión/bloqueo en los nodos con la misma quiralidad es, que las proyecciones de superficies de Fermi alrededor de nodos en WSM$_1$ y WSM$_2$ en el plano de la interfaz tenga una superposición o no estén unidos. Los efecto de filtrado propuesto no requiere diferencias en dopado, barreras de potencial o campos externos. Calculamos la conductancia diferencial a través de la interfaz por la cual puede ser medido en los experimentos e identificamos el régimen en el cual es posible conseguir la transición de una, ninguna o ambas quiralidades. También, un nodo intermedio moderador y el caso de una barrera geométrica WSM$_1$/WSM$_2$/WSM$_1$ han sido investigados, donde mostramos que ambos casos restringen el régimen del parámetro donde aparecen efectos de filtrado.

Résumé

La supraconductivité est un phénomène quantique macroscopique caractérisé par l'annulation de la résistivité électrique et l'expulsion du champ magnétique en dessous d'une température critique. Initialement, les supraconducteurs (S) furent considérés comme des éléments de circuits électriques à résistance nulle. Cependant, la nature quantique de ce phénomène a conduit à des applications radicalement nouvelles et excitantes. Les progrès constants dans la fabrication et la miniaturisation d'hétérostructures supraconductrices comprenant des éléments métalliques dans l'état normal (N), des ferromagnétiques (F), des semi-conducteurs, des matériaux à fort spin orbite, ou encore des gaz d'électrons 2D, ont ouvert la voie à l'étude de nombreux effects cohérents de phase et ont placé les supraconducteurs à la base des technologies émergentes pour le futur comme la détection quantique, la simulation et le calcul quantiques.

L'origine physique de la supraconductivité réside dans une instabilité du liquide de Fermi électronique vis à vis d'une attraction même infinitésimale entre les électrons au voisinage de la surface de Fermi (théorie BCS). Dans les supraconducteurs dits conventionnels, l'attraction entre les électrons est véhiculée par échange de phonons, et force les électrons à se combiner en paires de Cooper. Ces paires de Cooper combinant des électrons de moment et de spin opposés, forment des quasi-bosons composites de spin nul et d'impulsion totale nulle, pouvant se condenser dans un état quantique macroscopique unique. Cette condensation conduit à la formation d'un gap supraconducteur dans le spectre d'excitation du supraconducteur. Ce concept de formation de paires de Cooper peut être généralisé à d'autres types de mécanismes de pairing. Actuellement, certains de ces mécanismes ne sont pas complètement compris et la recherche de nouveaux types de pairing reste active.

Dans cette thèse, nous étudions la compétition entre la supraconductivité de type singulet de spin et s-wave avec les champs d'échange et spin-orbite susceptibles d'influencer différemment les spins opposés des paires de Cooper. Les corrélations supraconductrices ne sont pas confinées aux seuls matériaux supraconducteurs, et peuvent pénétrer un conducteur normal sur une échelle spatiale de l'ordre de la longueur de cohérence. Cette longueur dépend des caractéristiques du matériau normal. D'une manière générale, des conducteurs normaux peuvent ainsi acquérir certaines propriétés supraconductrices par effet de proximité, donnant lieu à des phénomènes cohérents de phase intéressants.

L'effet Josephson est l'une des manifestations les plus importantes de l'effet de proximité. L'état fondamental d'un supraconducteur est décrit par une fonction d'onde macroscopique caractérisée par une phase. L'effet Josephson consiste en un supercourant de paires de Cooper s'établissant entre deux supraconducteurs dotés de phase distinctes et séparés par une barrière isolante, ou un métal normal. Ce courant non-dissipatif s'écoule à voltage nul et dépend de la différence de phase entre les deux électrodes supraconductrices (effet Josephson DC).

La première partie de ce manuscrit de thèse est une introduction à l'effet de proximité dans des hétérostructures entre supraconducteurs et métaux normaux. Après avoir rappelé brièvement quelques éléments de la théorie BCS, nous présentons deux formalismes adaptés à l'étude de propriétés thermodynamiques et de transport dans les supraconducteurs non homogènes : le formalisme de Bogoliubov-de Gennes (BdG) et le formalisme des fonctions de Green quasi-classiques. Le formalisme BdG permet de comprendre les mécanismes de scattering microscopiques qui gouvernent le transport dans les hétérostructures N/S. Le principal mécanisme est la réflexion d'Andreev sur une interface S/N, et la formation d'états liés d'Andreev dans les jonctions S/N/S. Puis, nous présentons les cas importants d'une interface S/F et d'une jonction Josephson S/F/S. Dans un ferromagnétique, le champ d'échange favorise l'alignement des spins dans la même direction et sépare les bandes de spins opposés. L'interaction d'échange est donc antagoniste à l'appariement BCS qui favorise l'antialignement des spins au sein des paires de Cooper singulet de spin. Dans les hétérostructures S/F, cette compétition entre le ferromagnétisme et la supraconductivité conduit à un effet de proximité à très courte portée, et la possibilité d'une transition zero-pi dans laquelle le courant critique change de signe en fonction des paramètres champ d'échange et/ou de longueur du ferromagnétique.

Cette partie introductive est suivie par une série de chapitres consacrés à l'exposition des résultats de recherche originaux de cette thèse.

Le second chapitre traite de la formations des états liés d'Andreev et de l'effet Josephson associé dans des jonctions ballistiques entre "spin-split" (SS) supraconducteurs dont la densité d'états est fortement affectée par un champ magnétique extérieur, ou bien des champs d'échange. Ces champs d'échange peuvent être obtenus en mettant en contact des films minces supraconducteurs avec des isolants ferromagnétiques. La densité d'état dépendante de spin a pour origine l'interaction d'échange entre les électrons de conduction et les forts moments magnétiques localisés dans l'isolant ferromagnétique. L'utilisation d'isolants ferromagnétiques a l'avantage de suppléer à l'application de champs magnétiques externes, qui devraient être très élevés pour obtenir un effet similaire. Nous considérons des jonctions Josephson SS/N/SS dans lesquels l'orientation du champ d'échange peut être contrôlée individuellement dans chaque supraconducteur. Nous avons démontré qu'il est possible d'augmenter le courant critique Josephson en augmentant l'amplitude des champs d'échange, lorsque ceux-ci sont alignés de manière antiparallèle. Les états liés d'Andreev (ELA) n'avaient pas été étudiés en détail dans ce type de jonctions. Nous avons donc analysé leurs propriétés spectrales, et démontré que pour des champs d'échange de même sens, on a généralement la suppression des ELA pour certains intervalles de la différence de phase supraconductrice. En général, le courant Josephson est porté en partie par les ELA et en partie par le continuum des états d'énergie au-dessus du gap.

Dans le chapitre 3, nous avons étudié la génération de corrélations triplet de longue portée (CTLP) dans des ferromagnétiques diffusifs et évalué comment elles affectent l'effet Josephson. En théorie, ces corrélations triplet à longue portée (CTLP) peuvent être engendrées par la présence simultanée de couplage spin-orbite (CSO) et d'un champ d'échange uniforme, mais cela n'a pas encore été confirmé expérimentalement. Nous proposons des designs de jonctions favorables pour mettre en évidence ces CTLP, et nous calculons le courant Josephson pour deux types de CSO. Dans une hétérostructure S/F avec un champ d'échange uniforme, les paires de Cooper singulet peuvent pénétrer le ferromagnétique et sont partiellement converties en paires triplet mais ayant une projection du spin total nulle le long de l'axe unique défini par le champ d'échange. Dans un monodomaine ferromagnétique diffusif, les corrélations singulet et triplet du condensât supraconducteur décroissent à l'échelle de la longueur magnétique, qui dépend de l'énergie d'échange. Pour les supraconducteurs conventionnels et les champs d'échange typiques, cette longueur magnétique est bien plus courte que la longueur thermique caractérisant la décroissance des corrélations supraconductrices du système non magnétique. En revanche, les composantes triplet avec une projection du spin total non nulle, ne sont pas affectées par l'effet de pair breaking du champ d'échange et décroissement lentement sur une échelle spatiale comparable à la longueur thermique. De telles CTLP peuvent être générées par des inhomogénéités du champ d'échange, ou bien par la présence d'un couplage spin-orbite (CSO) dans un champ d'échange homogène.

La présence de CTLP a été vérifiée expérimentalement en utilisant des champs d'échange inhomogènes dans des hétérostructures S/F. En revanche, la génération de CTLP par le couplage spin-orbite en champ d'échange uniforme n'a pas encore été mise en évidence expérimentalement. Récemment, des jonctions Josephson avec un champ magnétique dans le plan et du spin-orbite ont été réalisées expérimentalement mais le courant Josephson mesuré ne montre pas de signes de CTLP. En effet dans de telles jonctions S/F/S verticales, la condition pour la formation de CTLP est très restrictive. En particulier pour qu'un couplage spin-orbite de type Rashba puisse générer des CTLP l'aimantation uniforme doit posséder une composante hors du plan. Ceci est un scénario défavorable car un tel champ d'échange peut créer aussi des vortex dans le supraconducteur ce qui complique l'interprétation des résultats expérimentaux. Plus souhaitable pour l'observation des CTLP est la géométrie latérale, dans laquelle les courants ont aussi une composante le long de l'interface entre S et F. Dans ce chapitre 3, nous récapitulons les bases de l'effet de proximité sous l' influence de champ d'échange et de couplage spin-orbite dans des hétérostructures diffusives. Nous démontrons que les jonctions latérales sont les dispositifs favorables pour l'observation de courants Josephson sur de longues distances. Nous proposons deux types de jonctions réalistes pour des expériences futures sur la génération de LRTCs, et nous calculons le courant Josephson correspondant pour deux types de couplage spin-orbite, Rashba et Dresselhaus.

Nous avons traité deux géométries de jonctions. Le premier type de jonctions est constitué d'un pont ferromagnétique reliant deux électrodes supraconductrices, le fort couplage spin-orbite provenant de couches de métaux lourds intercalées entre les électrodes S et le pont ferromagnétique. Dans le second type de jonctions, le champ d'échange et le couplage spin-orbite coexistent sur toute la longueur du pont. Ce second scénario peut être réalisé au moyen d'un pont semi-conducteur 2D placé dans un champ magnétique externe. Nous présentons des solutions analytiques des équations d'Usadel linéarisées, et le courant Josephson pour le premier type de jonctions. Ces résultats analytiques sont complétés par des calculs numériques sur les deux types de géométries de jonctions. L'ensemble des résultats, analytiques et numériques, montrent que l'intensité et le signe du courant Josephson peuvent être contrôlés en changeant le champ d'échange et le couplage spin-orbite. Au delà de l'application possible comme valves supraconductrices, notre travail montre que les jonctions latérales peuvent être utilisées comme détecteurs de l'effet de proximité triplet à longue portée induit par la combinaison d'un couplage spin-orbite et d'un champ d'échange uniforme.

Nous avons aussi étudié un autre phénomène d'équilibre, à savoir les courants de spin d'équilibre (CSE). Dans le chapitre 4, nous montrons qu'un nanofil avec du couplage spin-orbite et brisant l'invariance par renversement du temps par un champ Zeeman conduit à un courant d'équilibre bulk qui se manifeste par une polarisation de spin (transverse au champ Zeeman) aux bords de l'échantillon.

Les courants de spin sont détectés indirectement en mesurant, par exemple, des voltages avec une électrode ferromagnétique, ou par magnetoresistance de Hall de spin, induite par une accumulation de spin. En revanche les CSE n'induisent pas d'accumulation de spin et ne peuvent donc pas être détectées par ces méthodes. En effet, les CSE n'étant pas des courants de transport semblent inobservables, bien que certaines propositions théoriques les aient reliés à des couples mécaniques détectables. Pour ces raisons, l'interprétation des CSE est toujours sujette à débat.

Dans le chapitre 4, nous démontrons la correspondance entre les CSE dans des nanofils avec spin-orbite et une polarisation de spin transverse plus simple à mesurer sans ambiguïté. Cette correspondence est présente pour tout système (quasi-) unidimensionel en interaction, à condition que les interactions electron-electron soient indépendantes de spin. Les CSE apparaissent par application d'un champ magnétique B avec une composante perpendiculaire au spin-orbite, introduisant une levée de dégénérescence Zeeman $h = g\mu_B B$. Nous montrons que les CSE sont toujours accompagnés par une accumulation de spin qui est transverse au champ Zeeman et au champ spin-orbite. Cette accumulation de spin transverse peut être comprise comme une redistribution de la densité de spin en réponse à un courant DC. Ainsi la mesure d'une telle densité de spin transverse serait une mise en évidence des CSE dans le nanofil. Cette accumulation de spin existe non seulement dans l'état normal mais aussi quand le nanofil est dans l'état supraconducteur (par exemple par proximité avec un supraconducteur). Nous avons mis en évidence une connexion entre l'existence des CSE et la réponse paramagnétique anormale d'un supraconducteur. Les nanofils semi-conducteurs avec spin-orbite, tels que InAs et InSb, en contact avec des supraconducteurs, ont été explorés très activement dans les dernières années, essentiellement comme plateformes possibles pour la création de modes de Majorana et de supraconductivité topologique. Aussi bien les CSE et les modes de Majorana nécessitent une composante du champ Zeeman perpendiculaire au spin-orbite. Dans le contexte de la recherche des fermions de Majorana, plusieurs travaux théoriques ont déjà fait le lien entre la polarisation de spin aux bords du fil et la transition topologique. Dans ce chapitre, nous démontrons que la polarisation de spin transverse aux bords est une propriété universelle qui existe pour toutes les valeurs du champ d'échange h, y compris très loin de la transition topologique. Ainsi la détection de cette polarisation ne sera pas à relier à l'existence de modes de Majorana, mais à la présence des CSE.

Dans le dernière partie de cette thèse, nous avons étudié des propriétés de transport dans des semimétaux de Weyl (SMW). Il s'agit d'une nouvelle classe de matériaux qui possèdent des quasiparticules à dispersion linéaire à proximité de points spéciaux de la zone de Brillouin appelés points de Weyl, ainsi que des états de surface très spéciaux appelés arcs de Fermi. Nous avons démontré un effet de filtrage de chiralité à l'interface entre deux SMW distincts. La possibilité de filtrer un degré de liberté de spin est au coeur du calcul. Par exemple, les transistors de l'électronique numérique standard reposent sur le filtrage de la charge électrique pour controller le courant, tandis que la spintronique exploite le spin des porteurs de charges pour coder information. Dans les métaux ayant des quasiparticules de Dirac ou Weyl à dispersion linéaire, tels que le graphène 2D et les SMWs 3D, il existe d'autres degrés de libertés qui sont couplés au mouvement des charges et peuvent servir de supports alternatifs au calcul et à l'électronique du futur.

Dans le graphène, à deux dimensions, les quasiparticules de Dirac existent dans des zones restreintes, appelées les vallées, autour de deux vecteurs d'ondes bien précis. Ce degré de liberté de vallée peut être utilisé pour coder de l'information à condition de pouvoir peupler sélectivement une seule vallée. On parle alors de valléetronique.

A trois dimension, les quasiparticules de Weyl sont localisées autour de noeuds de Weyl qui apparaissent par paires de chiralités opposées. La chiralité est un degré de liberté quantique qui indique si l'impulsion de la quasiparticule pointe dans la même direction que le spin ou bien dans la direction opposée. Par analogie avec le filtrage de vallée, un filtre de chiralité pourrait être utilisé pour coder de l'information, avec une protection topologique additionnelle. Dans ce dernier chapitre, nous rappelons brièvement les équations de Dirac et de Weyl qui décrivent les fermions de spin 1/2, respectivement massifs (Dirac) et de masse nulle (Weyl).

Nous présentons ensuite le modèle le plus simple de liaisons fortes qui réalise les fermions de Weyl en matière condensée. Utilisant ce modèle, nous proposons une réalisation simple d'un filtre de chiralité tridimensionnel. Le filtre consiste en une interface entre deux différents semimétaux de Weyl, dans lequels les noeuds de Weyl de chiralités opposées de part et d'autre de l'interface sont séparés en énergie et en impulsion.

La condition générale de transmission ou de blocage entre noeuds de même chiralité réside dans la conservation de l'impulsion transverse des quasiparticules. Notre proposition de filtre de chiralité n'exige pas de réglage du dopage, de barrières de potentiels ou de champs externes. Nous avons calculé la conductance différentielle à travers une interface qui peut être mesurée expérimentalement. Nous avons identifié divers régimes de transport correspondant à la transmission d'aucune chiralité ou d'une seule chiralité. Bien sûr, il existe aussi un régime plus standard où les deux chiralités peuvent franchir l'interface.

General introduction

It has been known for millennia that “The totality is not... a mere heap, but the whole is other than the sum of the parts.” Aristotle’s famous sentence applies perfectly to the physics of mesoscopic superconducting heterostructures. Bringing multiple different materials into contact multiplies the possibilities to manipulate the transport and equilibrium properties in these hybrids. Superconductors are especially interesting candidates to link with other materials. When brought into contact they form more than just a mechanical connection with other materials: the superconductivity can leak far beyond the contact region. In general, this makes it possible to observe superconductivity simultaneously with other interesting phases of condensed matter, but the consequences on the system properties depend strongly on the type of superconductivity and the altered material. In this thesis we will be concerned mainly with hybrids of conventional superconductors and materials subject to magnetic and spin-orbit coupling fields.

Superconductivity is a macroscopic quantum phenomenon characterized by a vanishing resistivity and the expulsion of external magnetic fields below a critical temperature. In 1911 H. Kamerlingh Onnes was the first to reach temperatures low enough to experimentally observe superconductivity in a mercury sample [1]. A phenomenological theoretical description for the electrodynamics of superconductors (S) has been provided by F. and H. London in 1935 [2] and generalized by Ginzburg and Landau in 1950 [3]. Finally in 1957 a microscopic description was provided by J. Bardeen, L. N. Cooper and J. R. Schrieffer [4] known as BCS theory. They showed that the normal Fermi gas is unstable under arbitrarily weak attractive interactions between electrons about the Fermi energy. The attraction between electrons responsible for superconductivity was found to be mediated by electron-phonon interactions. In this case it is favorable for electrons with opposite momenta and spins to bind into pairs, the so-called Cooper pairs. This is referred to as s-wave or conventional pairing, as the total angular momentum of the paired electrons forming the superconducting ground-state is zero. Materials exhibiting this pairing mechanism are called conventional superconductors. Many elements that display superconductivity, like Al or Nb, belong to this type. In the 1980’s several new classes of superconductors were discovered, in particular organic [5], heavy-fermion [6], and copper-oxide superconductors [7], and the search is still ongoing. In many of these new classes the pairing mechanisms are not fully understood, the pairing has unconventional symmetry and the critical temperature T_c can be much higher then in conventional superconductors. For conventional superconductors the currently highest experimentally observed T_c is about 39 K [8]. In contrast, for the high temperature superconductors like the copper-oxide superconductor YBaCuO, T_c lies at 93 K [9], and the currently highest experimentally measured T_c of 203 K has been observed in sulfur hydride systems under extremely high pressure [10].

Although for conventional superconductors, it is necessary to achieve relatively low temperatures to enter the superconducting state, they are an essential part for a range of practical applications. On a big scale they are used as ideal conductors to create strong magnetic fields, as needed in particle accelerators or for magnetic resonance imaging. On a small scale, constant advancement in the fabrication and miniaturization of high quality superconducting heterostructures, involving normal metals (N), ferromagnets (F), semi-conductors, materials with strong spin-orbit coupling (SOC) or two-dimensional (2D) electron gases, has opened the path to study many interesting phase coherent effects and has made superconductors the basis for various future emerging technologies, for example quantum simulation [11] and quantum computation [12, 13]. Conventional superconductors are used as an essential building block in nanoscale devices where the quantum nature of the macroscopic superconducting state is exploited, for example in high precision magnetometers, so-called Superconducting QUantum Interference Devices (SQUIDs) [14], high precision current detectors or to realize qubits as building block of quantum computation, like the Cooper pair box [15], the Transmon [16] or Fluxonium [17]. In general, in such heterostructures the non superconducting components in contact with the superconductor acquire some properties of the latter, what is known as the proximity effect. Superconducting correlations are not necessarily bound to the superconductor and penetrate the normal conducting materials on the length scale of the characteristic size of Cooper pairs, the superconducting coherence length, which itself strongly depends on the normal conducting material.

One of the most prominent manifestations of the proximity effect is the Josephson effect [18]. The groundstate of a superconductor is described by a macroscopic quantum wavefunction that will have a phase in general. In 1962 Brian Josephson predicted that phase coherent tunneling of Cooper pairs between two superconductors, that are separated by a thin insulating barrier and differ in the phase of their individual macroscopic wave function, leads to a zero resistance current at zero voltage. This effect is known as the dc-Josephson effect and is a direct proof of the macroscopic character of the superconducting ground state. Further Josephson predicted that at applied voltage, the coherent tunneling of Cooper pairs leads to a quickly alternating current, which is known as the ac-Josephson effect. Both effects where confirmed experimentally shortly after their discovery [19, 20].

Other phenomena related to the proximity effect have their origin in the spin state of the Cooper pairs. In a singlet superconductor, as the name suggests, the paired electrons have opposite spin. As a consequence the coherence length can get strongly altered by spin-active fields. A prominent example is the manipulation of the proximity effect inside a ferromagnet or in a normal conductor under presence of an external magnetic field. The exchange field in a ferromagnet splits the previously degenerate bands in energy and consequently a parallel alignment of the spins is energetically favorable. In the case of an external magnetic field the equivalent situation is played be the Zeeman interaction. Both counter the conventional pairing mechanism that prefers anti-parallel orientation of the spins, thus in principle ferromagnetism and superconductivity are two strongly competing phases. Indeed, at S/F interfaces the proximity effect is strongly suppressed [21]. In the ferromagnet the superconducting correlations decay on a much shorter length scale and are accompanied by spatial oscillations. The competition between both phases can be used to control the proximity effect. For example in S/F/S junctions, the oscillations of the superconducting correlations can cause a reversal of the maximal dc-Josephson current depending on the junction length and the strength of the exchange field [22–26].

Another interesting effect is the generation of long ranged triplet correlations in S/F/S heterostructures with inhomogeneous ferromagnets or multilayered ferromagnets connecting the superconductors [27–29]. Triplet correlations with spin projections perpendicular to a present exchange field/Zeeman field are not vulnerable to the spin-splitting and thus decay on a length scale comparable to the one of a non-magnetic system. Supercurrents carried by such triplet pairs can be in a highly polarized state. This makes them an ideal candidate for spintronics applications [29, 30], where the precise control and manipulation of the spin degree of freedom is a highly sought after property for signal transmission, processing and storage.

Besides the generation of triplet correlations through inhomogeneous ferromagnets there exist theoretical proposals to use SOC active compounds as a substitute [31, 32]. Of particular importance are SOC fields of the Rashba [33] and Dresselhaus [34] type. Rashba SOC is present in systems with broken structural inversion symmetry, e.g. at interfaces, whereas Dresselhaus SOC is present in systems lacking bulk inversion symmetry, i.e. the crystal structure of the material is not inversion symmetric [35]. Both types of SOC can be described as a momentum dependent, time-reversal preserving, effective magnetic field and are equally able to rotate the carrier spin to avoid the short range decay of the superconducting correlations. They introduce new possibilities of control over the spin degree of freedom, especially in a one-dimensional/two-dimensional electron gas, where the strength of the Rashba and Dresselhaus SOC can be tuned by applying a gate voltage [36, 37].

The study of the interplay of SOC, magnetic fields and superconducting correlations is also of great relevance for the realization of Majorana Fermions in condensed matter systems. Majorana Fermions were first predicted by Ettore Majorana in 1937 [38] as real solutions of the Dirac equation and are elementary particles that are their own antiparticles. In the context of high energy physics their existence has not been confirmed, however after many decades Kitaev demonstrated that Majorana Fermions could be realized as quasiparticle excitations in a solid state system [39]. Due to their non-abelian statistics [40] Majorana Fermions are considered as potential building block for topological quantum computation [41]. Many different devices have been suggested to host and detect Majorana Fermions [42–44]. A promising scheme consists of a one-dimensional quantum wire with strong Rashba SOC, e.q. InAs or InSb wires, proximized by a conventional superconductor and subject to a magnetic field [45]. Experiments in such systems report a zero-bias conductance peak as signatures of the Majorana Fermions [46, 47]. Alternative explanations question the unambiguousness of these results [48–50]. Potential alternative signatures for the presence of Majorana physics are on demand and could be found in the various magneto-electric effects that rise due to the interplay of the different spin-fields and superconductivity [51–53].

The above mentioned effects were studied under the assumption of a non-relativistic, quadratic dispersion for the quasiparticle excitations. At first glance this is not surprising as the typical excitation energies in condensed matter systems are far below the rest mass of the electron. A relativistic description of the involved physics doesn't seem necessary. However, in contrast to a free Fermion, in solid state systems electrons move through a periodic crystal. The symmetries of the crystal impose restrictions on the quasiparticle states and can lead to effective low-energy descriptions that correspond to the Dirac equation [54]. A recently discovered material class that exhibits Dirac physics is Weyl semimetals (WSM) [55–57]. WSMs are three-dimensional materials, characterized by the appearance of pairwise linear band crossings. These band crossings are protected by the internal symmetries of the crystal and are called Weyl nodes. The low-energy physics around the Weyl nodes is described by the Weyl Hamiltonian and each node is characterized by its chirality, which is the projection of the spin onto the direction of motion of the quasiparticle. So at each Weyl node the direction of motion of a quasiparticle is locked to its spin, which can have drastic consequences on the proximity effect between a WSM and a conventional superconductor. For example at a magnetic WSM/S interface the proximity effect is not just suppressed but is completely blocked [58]. The chirality represents a currently unused quantum degree of freedom that can be exploited to encode and transmit information [59–64]. It is therefore desirable to further understand how superconductivity introduces additional options of manipulating this degree of freedom.

Outline of the thesis

This thesis studies the interplay between spin-active fields and superconducting correlations in various heterostructures. Each chapter of the main work is dedicated to a different system. Each system creates effects that have been predicted theoretically - both by this work and previous studies - but not observed until now.

- Chapter 1 is a brief introduction to the theory of transport in superconducting mesoscopic systems. We recap basic elements of the BCS theory, the Bogoliubov-de Gennes (BdG) formalism and the quasi-classical Green's function formalism, which are extensively used throughout this thesis. We derive basic properties of bulk superconductors and study basic transport phenomena in heterostructures involving superconductors with the aid of the scattering formalism.

The chapters that follow form the main part of the thesis and present original research.

- Chapter 2 is devoted to the Andreev bound state formation and the resulting Josephson effect in ballistic junctions involving spin-split superconductors. In such systems it is possible to increase the critical Josephson current by increasing the magnitude of the exchange field. This is a rather counterintuitive result considering the pair breaking nature of the spin-splitting fields. The dependence of the Andreev bound states on the phase difference between the superconducting banks has not been investigated so far and we analyze the spectral properties of this junction type within the BdG formalism.
- Chapter 3 turns to diffusive superconducting systems and discusses the generation of long range triplet correlations (LRTC) in strong ferromagnets through SOC. We propose two types of realistic Josephson junctions, which represent the most favorable setup to observe this currently unrealized possibility to generate LRTC and determine the signature of these correlations, a long-ranged Josephson current.
- Chapter 4 is dedicated to the interplay of superconductivity, Rashba SOC and a homogeneous exchange field in a 1D wire for a wide range of parameters and regimes. We show a universal

correspondence between equilibrium spin currents in the bulk and spin polarization transverse to the magnetic field at the edges of the wire. Such edge polarization has been suggested by some authors as a signature of Majorana zero modes. We show that this not true in general and emphasize the link to hitherto undetected and long debated theoretical concept of equilibrium spin currents.

- Chapter 5 leaves the superconducting regime and studies the ballistic transport through interfaces between WSMs. The aim of this part of my work was to consider the proximity effect between WSMs and superconductors. It turned out that interfaces between WSMs are already very exciting by themselves. In this chapter we propose a way to filter the charge current based on the chirality of the quasiparticles in such structures, thus exploring the well defined chiral degree of freedom as a potential candidate for signal processing and computation.

Chapter 1

Mesoscopic superconductivity

This chapter is a brief reminder on the formalisms used in this thesis. The first section introduces the BCS theory and derives basic results for the bulk properties of conventional superconductors. Based on the BCS theory two formulations of the latter are deduced that are able to treat transport in superconducting heterostructures. The Bogoliubov de Gennes (BdG) equation and the Green-Gor'kov equation. Then we turn to the scattering formalism to present basic transport phenomena in superconducting heterostructures on a microscopic level. Finally we derive the quasi-classical transport formalism in the clean and dirty limit from the Green-Gor'kov equation. This chapter enables the reader to reproduce the findings in the chapters that follow.

1.1 Elements of BCS theory

We start from the BCS effective Hamiltonian which leads to the formation of Cooper pairs [65]

$$\mathcal{H}^{\text{eff}}_{\text{BCS}} = \int d\mathbf{x}\Psi^\dagger(\mathbf{x})h(\hat{\mathbf{p}})\Psi(\mathbf{x}) + \int d\mathbf{x}\frac{V(\mathbf{x})}{4}\left[(\Psi^T i\sigma_2\Psi)^\dagger(\Psi^T i\sigma_2\Psi)\right](\mathbf{x}) \tag{1.1}$$

where $h(\hat{\mathbf{p}})$ is some time independent classic Hamiltonian that only depends on the momentum operator $\hat{\mathbf{p}} = -i\hbar\nabla_{\mathbf{x}}$, $V(\mathbf{x}) < 0$ is an attractive interaction and a function of space in general. The matrices σ_i are the Pauli matrices represented by

$$\sigma_1 = \begin{pmatrix} 0 & 1 \\ 1 & 0 \end{pmatrix},\ \sigma_2 = \begin{pmatrix} 0 & -i \\ i & 0 \end{pmatrix},\ \sigma_3 = \begin{pmatrix} 1 & 0 \\ 0 & -1 \end{pmatrix}, \tag{1.2}$$

and we define $\sigma_0 := \hat{1}$ as the identity. Through-though the thesis we will use the indices (x, y, z) and $(1, 2, 3)$ interchangeably to label the Pauli matrices. For the case we are in a direct product space, where each subspace is spanned by the Pauli matrices and the identity, the basis of the second subspace will be denoted by τ_i. The spinors Ψ and $\Psi^\dagger$ are

$$\Psi = \begin{pmatrix} \psi_\uparrow \\ \psi_\downarrow \end{pmatrix}, \quad \Psi^\dagger = \begin{pmatrix} \psi_\uparrow^\dagger & \psi_\downarrow^\dagger \end{pmatrix}. \tag{1.3}$$

The operators $\psi_\alpha^\dagger(\mathbf{x}), \psi_\alpha(\mathbf{x})$ are fermionic creation and annihilation operators at position x where α is some internal degree of freedom, i.e. the spin. They obey the usual anti-commutation relations

$$\begin{aligned} \left\{\psi_\alpha^\dagger(\mathbf{x}), \psi_\beta(\mathbf{y})\right\} &= \delta_{\alpha,\beta}\delta(\mathbf{x}-\mathbf{y}), \\ \{\psi_\alpha(\mathbf{x}), \psi_\beta(\mathbf{y})\} &= 0. \end{aligned} \tag{1.4}$$

Following Bardeen, Cooper and Schrieffer, who realized that an attractive interaction between electrons leads to formation of Cooper pairs, we decouple the interaction term by a mean-field approximation assuming that thermal averages of two creation or annihilation operators can be non-vanishing. This leads to the following mean field Hamiltonian

$$\mathcal{H}_{\text{BCS}}^{\text{mf}} = \int d\mathbf{x} \Psi^\dagger(\mathbf{x}) h(\hat{\mathbf{p}}) \Psi(\mathbf{x}) - \int d\mathbf{x} \left[\Delta(\mathbf{x})\psi_\uparrow^\dagger(\mathbf{x})\psi_\downarrow^\dagger(\mathbf{x}) + \Delta^*(\mathbf{x})\psi_\downarrow(\mathbf{x})\psi_\uparrow(\mathbf{x})\right], \tag{1.5}$$

where we introduced the superconducting order parameter $\Delta(x) = |V(\mathbf{x})| \langle\psi_\downarrow(\mathbf{x})\psi_\uparrow(\mathbf{x})\rangle$. Here $\langle\cdots\rangle$ denotes the thermal average of an operator which is defined by

$$\langle\cdots\rangle = \text{Tr}[e^{-\beta\mathcal{H}}\cdots]/\text{Tr}[e^{-\beta\mathcal{H}}], \tag{1.6}$$

where Tr denotes the trace of an operator and $\beta = 1/k_B T$. Note that terms corresponding to products of two thermal averages have been neglected as they only lead to a constant shift of the ground-state energy. By construction the Hamiltonian (1.5) describes a non-interacting system, where electron and hole degrees of freedom are coupled. Let us turn to to the bulk excitation spectrum described by this Hamiltonian. As the system is translational invariant we apply a Fourier transformation to Hamiltonian (1.5). For simplicity we assume that the kinetic part is trivial in spin space and quadratic in momentum $h(\hat{\mathbf{p}}) = \hat{\mathbf{p}}^2/2m - \mu$ with m as the effective mass and μ denoting the chemical potential. The equivalent Hamiltonian in momentum space can be written as [66]

$$\mathcal{H}_{\text{BCS}}^{\text{mf}} = \sum_{\mathbf{k},\sigma} \xi_{\mathbf{k}} c_{\mathbf{k},\sigma}^\dagger c_{\mathbf{k},\sigma} + \sum_{\mathbf{k}} \left[\Delta_{\mathbf{k}} c_{\mathbf{k},\uparrow}^\dagger c_{-\mathbf{k},\downarrow}^\dagger + \Delta_{\mathbf{k}}^* c_{-\mathbf{k},\downarrow} c_{\mathbf{k},\uparrow}\right], \tag{1.7}$$

where $\xi_{\mathbf{k}} = \mathbf{k}^2/2m - \mu$ is the kinetic energy measured from the Fermi energy and we assumed that the attractive interaction binds electrons/holes of opposite spin and momenta which leads to the gap equation

$$\Delta_{\mathbf{k}} = -\frac{1}{N} \sum_{\mathbf{k}\mathbf{k}'} V_{\mathbf{k},\mathbf{k}'} \left\langle c_{-\mathbf{k}',\downarrow} c_{\mathbf{k}',\uparrow}\right\rangle. \tag{1.8}$$

We diagonalize the Hamiltonian by the so-called Bogoliubov transformation [67]. The Bogoliubov transformation introduces new fermionic operators $\gamma, \gamma^\dagger$ which are linear combinations of the original

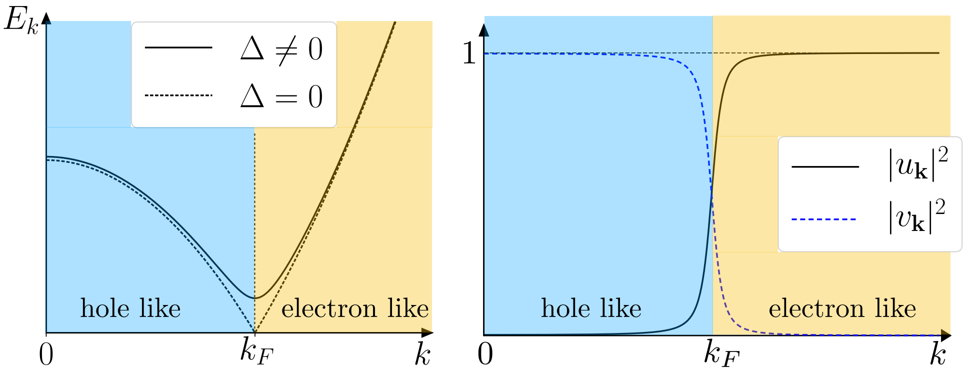

FIGURE 1.1: Quasiparticle excitation spectrum for vanishing and finite order parameter and composition of the quasiparticles below and above the Fermi energy in a superconductor

electron creation and destruction operators,

$$\begin{aligned}\gamma_{\mathbf{k},\uparrow} &= u^*_{\mathbf{k}} c_{\mathbf{k},\uparrow} - v_{\mathbf{k}} c^\dagger_{-\mathbf{k},\downarrow},\\ \gamma^\dagger_{-\mathbf{k},\downarrow} &= v^*_{\mathbf{k}} c_{\mathbf{k},\uparrow} + u_{\mathbf{k}} c^\dagger_{-\mathbf{k},\downarrow}.\end{aligned} \tag{1.9}$$

Demanding that the new operators obey fermionic commutation relations one can show that the coefficients of the transformation, also referred to as coherence factors, fulfill $|u_{\mathbf{k}}|^2 + |v_{\mathbf{k}}| = 1$. The inverse transformation reads

$$\begin{aligned}c_{\mathbf{k},\uparrow} &= u_{\mathbf{k}} \gamma_{\mathbf{k},\uparrow} + v_{\mathbf{k}} \gamma^\dagger_{-\mathbf{k},\downarrow},\\ c^\dagger_{-\mathbf{k},\downarrow} &= -v^*_{\mathbf{k}} \gamma_{\mathbf{k},\uparrow} + u^*_{\mathbf{k}} \gamma^\dagger_{-\mathbf{k},\downarrow}.\end{aligned} \tag{1.10}$$

The Hamiltonian written in terms of the new operators is

$$\mathcal{H}_{\mathrm{BCS}} = E_{\mathrm{BCS}} + \sum_{\mathbf{k}\sigma} E_{\mathbf{k}} \gamma^\dagger_{\mathbf{k}\sigma} \gamma_{\mathbf{k}\sigma}, \tag{1.11}$$

and the resulting quasiparticle excitation spectrum

$$E_{\mathbf{k}} = \sqrt{\xi^2_{\mathbf{k}} + |\Delta|^2}. \tag{1.12}$$

The quasiparticles, usually called Bogolons, are superpositions of electron- and hole-like states, which can be deduced from the amplitude of the coherence factors

$$|u_{\mathbf{k}}| = \frac{1}{\sqrt{2}}\sqrt{1 + \frac{\xi_k}{E_k}} \xrightarrow{\Delta\to 0} \Theta\left(\xi_k\right), \tag{1.13}$$

$$|v_{\mathbf{k}}| = \frac{1}{\sqrt{2}}\sqrt{1 - \frac{\xi_k}{E_k}} \xrightarrow{\Delta\to 0} \Theta\left(-\xi_k\right), \tag{1.14}$$

in combination with the spectrum which are shown in Fig. 1.1. In the limit of vanishing order parameter the Bogolons are holes for energies below the Fermi energy and electrons above as expected for a normal metal. When the order parameter is finite the nature of the Bogolons depends on the energy and ranges from mostly hole-like far below the Fermi energy to mostly electron like far above the Fermi energy. At the Fermi energy $|u_{\mathbf{k}}|^2 = |v_{\mathbf{k}}|^2 = 1/2$, i.e. the excitations are exactly half hole half electron. In contrast to the normal metal superconductivity opens a gap of magnitude Δ_{k_F} in the excitation spectrum thus no quasiparticle excitations are possible below this threshold. This reflects the fact that it costs energy to break a Cooper pair in the BCS condensate ground state to create two Bogolons. To determine the gap energy, inserting the Bogoliubov transformation into the definition for $\Delta_{\mathbf{k}}$ leads to

$$\Delta_{\mathbf{k}} = -\frac{1}{N}\sum_{\mathbf{k'}} V_{\mathbf{kk'}} \frac{\Delta_{\mathbf{k'}}}{2E_{\mathbf{k'}}} \tanh\left(\frac{\beta}{2}E_{\mathbf{k'}}\right). \tag{1.15}$$

We make some approximations that allow to obtain analytical results. As $\xi_{\mathbf{k}}$ is isotropic it is possible to convert the sum over $\mathbf{k}$ into an integral over energy

$$\frac{1}{N}\sum_{\mathbf{k}} \approx \int \frac{d\mathbf{k}}{(2\pi)^3} \approx \int_{-\infty}^{\infty} \mathcal{N}(\xi+\mu)d\xi \tag{1.16}$$

with $\mathcal{N}(\varepsilon)$ being the density of states. Assuming that pairing is constant, $\mathbf{k}$ independent $V_{\mathbf{kk'}} = V_0$, and active only in a small window (Debye energy) around the Fermi energy, and that the DOS is almost constant

$$\int_{-\infty}^{\infty} \mathcal{N}(\xi+\mu)d\varepsilon \approx \mathcal{N}_0 \int_{-\omega_c}^{\omega_c} d\xi \tag{1.17}$$

where $\mathcal{N}_0$ is the normal state DOS at the Fermi energy and ω_c is a cut-off energy. The gap equation becomes

$$\Delta \;=\; -\frac{V_0\mathcal{N}_0}{2}\int_{-\omega_c}^{\omega_c} d\xi \frac{\Delta}{\sqrt{\xi^2+\Delta^2}} \tanh\left(\frac{\beta}{2}\sqrt{\xi^2+\Delta^2}\right) \tag{1.18}$$

that can be solved numerically (Fig.1.2). For $T = 0$ analytical solutions are possible. We have

$$\Delta_0 \;=\; -\frac{V_0\mathcal{N}_0}{2}\int_{-\omega_c}^{\omega_c} d\varepsilon \frac{\Delta}{\sqrt{\xi^2+\Delta^2}} = g\mathcal{N}_0\Delta_0 \mathrm{Arsinh}\frac{\omega_c}{\Delta_0}, \tag{1.19}$$

so

$$\sinh\frac{1}{\mathcal{N}_0V_0} = \frac{\omega_c}{\Delta_0} \quad\Rightarrow\quad \Delta_0 = \omega_c\frac{1}{\sinh\frac{1}{\mathcal{N}_0V_0}}. \tag{1.20}$$

In the weak coupling limit ($\mathcal{N}_0V_0 \ll 1$) we obtain the usual zero temperature gap

$$\Delta_0 = 2\omega_c e^{-\frac{1}{\mathcal{N}_0V_0}}, \tag{1.21}$$

and the relation with the critical temperature $\Delta_0\beta_c \approx 1.76$. In a similar way one obtains the BCS density

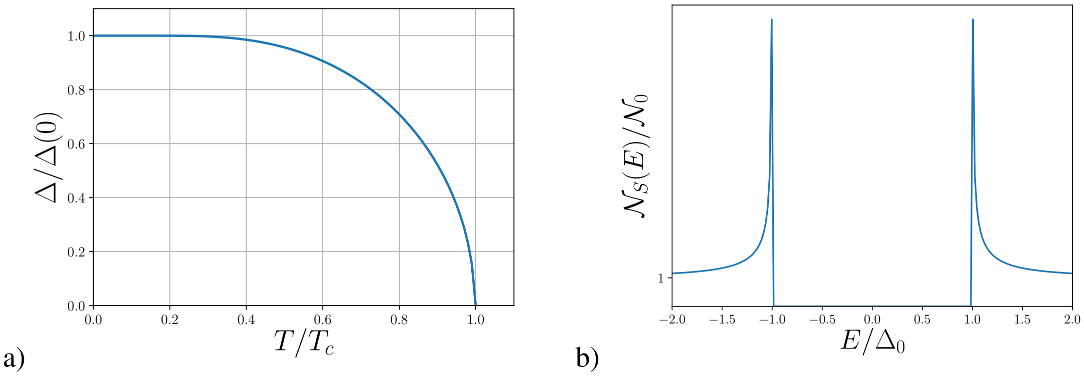

FIGURE 1.2: a) Numerical obtained temperature dependence of the BCS gap. b) Density of states of a superconductor.

of state (DOS) of a superconductor

$$\mathcal{N}_S(E) = \frac{1}{N}\sum_{\mathbf{k}} \delta(E - E_{\mathbf{k}}) \approx \begin{cases} \mathcal{N}_0 \frac{E}{\sqrt{E^2 - \Delta_0^2}} & , E > \Delta_0 \\ 0 & , E < \Delta. \end{cases} \tag{1.22}$$

As expected there are no quasiparticle states in the gap and the DOS shows a square root divergence at the edge of the gap as shown in Fig. 1.2 b).

1.1.1 Bogoliubov - de Gennes equations

To study inhomogeneous superconducting systems on the level of the BCS mean field theory, we need to formulate the BCS theory in real space. As the BCS Hamiltonian describes non-interacting Bogolons, it is sufficient to study single-particle excitations. In the following, we construct a Schrödinger like equation for the eigenstates of the BCS Hamiltonian in the electron-hole basis instead of the Bogolon operators. This will lead to the Bogoliubov-de Gennes (BdG) Hamiltonian which allows to study the single particle excitations within the framework of first-quantization in systems with heterojunctions, interfaces etc. We start from the equation of motion for the electron and hole operators,

$$\begin{aligned} \partial_t c^\dagger_{\mathbf{k},\uparrow} &= \frac{i}{\hbar}\left(\xi_{\mathbf{k}} c^\dagger_{\mathbf{k},\uparrow} - \Delta^*_{\mathbf{k}} c^\dagger_{-\mathbf{k},\downarrow}\right), \\ \partial_t c_{-\mathbf{k},\downarrow} &= \frac{i}{\hbar}\left(-\xi_{\mathbf{k}} c_{-\mathbf{k},\downarrow} - \Delta^*_{\mathbf{k}} c^\dagger_{-\mathbf{k},\downarrow}\right), \end{aligned} \tag{1.23}$$

and insert the Bogoliubov transformed operators (1.10). Calculating the time-derivative of the Bogolon operators on the left side

$$\partial_t \gamma^\dagger_{\mathbf{k},\uparrow} = -\frac{i}{\hbar} E_{\mathbf{k}} \gamma^\dagger_{\mathbf{k},\uparrow}, \quad \partial_t \gamma_{-\mathbf{k},\downarrow} = \frac{i}{\hbar} E_{\mathbf{k}} \gamma_{-\mathbf{k},\downarrow}, \tag{1.24}$$

and gathering terms with $\gamma^{\dagger}_{\mathbf{k},\uparrow}$, $\gamma_{-\mathbf{k},\downarrow}$ respectively we obtain

$$\begin{pmatrix} \xi_{\mathbf{k}} & \Delta_{\mathbf{k}} \\ \Delta^*_{\mathbf{k}} & -\xi_{\mathbf{k}} \end{pmatrix} \begin{pmatrix} u_{\mathbf{k}} \\ v^*_{\mathbf{k}} \end{pmatrix} = E_{\mathbf{k}} \begin{pmatrix} u_{\mathbf{k}} \\ v^*_{\mathbf{k}} \end{pmatrix} . \tag{1.25}$$

The eigenvalues of the matrix on the left hand side are $\pm E_k$, thus it has exactly the same positive excitation spectrum as $\mathcal{H}^{\mathrm{mf}}_{\mathrm{BCS}}$. One can show that its eigenstates are the one of the Bogolon creation and annihilation operators. Then

$$\mathcal{H}_{\mathrm{BdG}}(\mathbf{k}) = \begin{pmatrix} \xi_{\mathbf{k}} & \Delta_{\mathbf{k}} \\ \Delta^*_{\mathbf{k}} & -\xi_{\mathbf{k}} \end{pmatrix} \tag{1.26}$$

is the desired first quantized form of the $\mathcal{H}^{\mathrm{mf}}_{\mathrm{BCS}}$ in $\mathbf{k}$ space also called the BdG Hamiltonian. Performing a Fourier-transformation back to the real space representation of $\mathcal{H}_{\mathrm{BdG}}$ gives

$$\mathcal{H}_{\mathrm{BdG}}(\mathbf{x}) = \begin{pmatrix} H_0(\mathbf{x}) & \Delta(\mathbf{x}) \\ \Delta^*(\mathbf{x}) & -H_0(\mathbf{x}) \end{pmatrix} , \tag{1.27}$$

where $H_0(\mathbf{x}) = -\hbar^2\partial^2_{\mathbf{x}}/2m - \mu + V(x)$. The Schrödinger-like equation for the Bogolons is

$$\mathcal{H}_{\mathrm{BdG}}(\mathbf{x})\Psi\left(\mathbf{x}\right) = E\Psi\left(\mathbf{x}\right) , \tag{1.28}$$

and is referred to as the BdG equation. In principle, we can now model different spatial variations of the gap parameter $\Delta(\mathbf{x})$. On a first glance, what changed is that now the solutions are spinors

$$\Psi(\mathbf{x}) = \begin{pmatrix} \psi_1(\mathbf{x}) \\ \psi_2(\mathbf{x}) \end{pmatrix} \tag{1.29}$$

in electron-hole space. However we also need to keep in mind that in an exact calculation, the gap has to be determined self-consistently. To study many general effects of the superconducting pairing it is usually sufficient to assume that $\Delta(\mathbf{x})$ is some given function for which self-consistency is fulfilled.

1.1.2 Gor'kov equation

The BCS theory can be translated in the language of Green's functions. In this section we derive the equation of motion for the Green's function of a superconducting system, which is named after Gor'kov as the Gor'kov equation, who together with Abrikosov was one of the main heads behind this reformulation [68]. Furthermore, Gor'kov was able to show that the phenomenological Ginzburg and Landau theory [3] follows from the Gor'kov equation for temperatures close to the critical temperature [69].

Let us define the central object of this section, the Green-Gor'kov matrix

$$\begin{aligned}\mathbf{G}(\xi_1,\xi_2) &= \frac{1}{i\hbar}\left\langle \hat{T}\left[\begin{pmatrix} \Psi(\xi_1) \\ -[\mathcal{T}\Psi(\xi_1)] \end{pmatrix} \otimes \left(\Psi(\xi_2)^\dagger\; [\mathcal{T}\Psi(\xi_2)]^\dagger\right)\right]\right\rangle \\ &= \begin{pmatrix} G(\xi_1,\xi_2) & F(\xi_1,\xi_2) \\ -\bar{F}(\xi_1,\xi_2) & \bar{G}(\xi_1,\xi_2) \end{pmatrix}, \end{aligned} \tag{1.30}$$

where $\xi_i = (\mathbf{x}_i, t_i)$ represents a space-time point and

$$\hat{T}\left[\psi(\xi_1)\psi^\dagger(\xi_2)\right] = \begin{cases} \psi(\xi_1)\psi^\dagger(\xi_2) & , t_2 < t_1 \\ -\psi^\dagger(\xi_2)\psi(\xi_1) & , t_2 > t_1 \end{cases} \tag{1.31}$$

the time ordering operator for fermionic field operators. The upper two sub-matrices in Eq. (1.30) are the normal and anomalous Green's function

$$G\left(\xi_1,\xi_2\right) = \frac{1}{i\hbar}\left\langle \hat{T}\begin{pmatrix} \psi_\uparrow\psi_\uparrow^\dagger & \psi_\uparrow\psi_\downarrow^\dagger \\ \psi_\downarrow\psi_\uparrow^\dagger & \psi_\downarrow\psi_\downarrow^\dagger \end{pmatrix}(\xi_1,\xi_2)\right\rangle, \tag{1.32}$$

$$F\left(\xi_1,\xi_2\right) = \frac{1}{i\hbar}\left\langle \hat{T}\begin{pmatrix} \psi_\uparrow\psi_\downarrow & -\psi_\uparrow\psi_\uparrow \\ \psi_\downarrow\psi_\downarrow & -\psi_\downarrow\psi_\uparrow \end{pmatrix}(\xi_1,\xi_2)\right\rangle \tag{1.33}$$

respectively. As we have seen in the previous sections, the BCS interaction couples electron- and hole-like states and holes can be viewed as time reversed electrons. The equations of motion for the Green's function of a superconductor will necessarily include correlators between states and time reversed states. It will become handy later to define the time reversal operator for spin-1/2 quasiparticles $\mathcal{T} = i\sigma_2\mathcal{K}$ with $\mathcal{K}$ the complex conjugation operator. The time reversal operator $\mathcal{T}$ has the property $\mathcal{T}^2 = -1$ and $\mathcal{T} = -\mathcal{T}^{-1}$. The Green-Gor'kov matrix respects particle-hole symmetry where the particle-hole operator is defined as

$$\mathcal{P} = \mathcal{K}\tau_2\sigma_2 = \begin{pmatrix} 0 & \mathcal{T} \\ \mathcal{T}^{-1} & 0 \end{pmatrix} \tag{1.34}$$

with $\mathcal{P}^2 = 1$ and $\mathcal{P} = \mathcal{P}^{-1}$. The τ_i are the Pauli matrices that span the particle-hole space. Applying the particle hole transformation onto the Green-Gor'kov matrix gives

$$\mathcal{P}\mathbf{G}(\xi_1,\xi_2)\mathcal{P} \;= \begin{pmatrix} \mathcal{T}\bar{G}\mathcal{T}^{-1} & \mathcal{T}\bar{F}\mathcal{T}^{-1} \\ -\mathcal{T}F\mathcal{T}^{-1} & \mathcal{T}G\mathcal{T}^{-1} \end{pmatrix} = \mathbf{G}(\xi_1,\xi_2) \tag{1.35}$$

where $\mathcal{T}F\mathcal{T}^{-1} = \bar{F}$ and $\mathcal{T}G\mathcal{T}^{-1} = \bar{G}$ have been used. This shows that G and F are the only two independent components of the Green-Gor'kov matrix.

The equation of motion for the Green-Gor'kov matrix, follows from evaluating the Heisenberg equation of motion for the field operators $i\hbar\partial_t\psi = [\psi, \mathcal{H}]$ with the Hamiltonian $\mathcal{H}^{\text{mf}}_{\text{BCS}}$ (1.5). The resulting equations can be cast into matrix form, the Gor'kov equation:

$$\mathbf{G}_0^{-1}(\xi_1)\mathbf{G}\left(\xi_1,\xi_2\right) = \delta\left(\xi_1 - \xi_2\right) \tag{1.36}$$

where

$$\mathbf{G}_0^{-1}(\xi_1) = i\hbar\tau_3\partial_{t_1} - \boldsymbol{\xi}\left(\hat{\mathbf{p}}_1\right) + \Delta\left(\mathbf{x}_1\right), \tag{1.37}$$

$$\boldsymbol{\xi}\left(\hat{\mathbf{p}}\right) = \left(\begin{array}{cc} h\left(\hat{\mathbf{p}}\right) & 0 \\ 0 & \mathcal{T}h\left(\hat{\mathbf{p}}\right)\mathcal{T}^{-1} \end{array}\right), \;\; \boldsymbol{\Delta}(\mathbf{x}) = \left(\begin{array}{cc} 0 & \Delta(\mathbf{x}) \\ -\Delta(\mathbf{x})^* & 0 \end{array}\right) \tag{1.38}$$

and $\Delta(\mathbf{x}) = i\hbar V(\mathbf{x})\mathrm{Tr}\left[F\left(\xi_2 \to \xi_1\right)\right]$. Note that we assumed that the kinetic energy operator only depends on the momentum operator. For completeness, repeating the procedure for the case when the derivatives are taken with respect to ξ_2 leads to the conjugate equation

$$\mathbf{G}\left(\xi_1,\xi_2\right)\left(\mathbf{G}_0^{-1}(\xi_2)\right)^\dagger = \delta\left(\xi_1 - \xi_2\right) \tag{1.39}$$

where

$$\left(\mathbf{G}_0^{-1}(\xi_2)\right)^\dagger = -i\hbar\tau_3\partial_{t_2}^\dagger - \boldsymbol{\xi}^*\left(\hat{\mathbf{p}}_2\right) + \boldsymbol{\Delta}\left(\mathbf{x}_2\right) \tag{1.40}$$

and the daggered partial derivative is acting on expressions to its left hand side. We will need it later to derive quasi-classical transport equations.

The physical information contained in the BdG or Gor'kov equations is equivalent. Each of the formulations has its advantages and disadvantages. In contrast to the previous BdG formalism, the solutions of the Gor'kov equations are two point correlators, i.e. Green's functions. To study non-homogeneous systems, like interfaces or junctions the Gor'kov Green's function is a rather complicated object to deal with. An advantage of the Green's function formulation gets obvious when applying diagrammatic techniques, for example when treating disordered systems.

It is possible to simplify the Gor'kov equations to a equation of motion for functions that only depend on one spatial variable in the so called quasi-classical limit. In this thesis the Gor'kov equation will be the starting point to generalize these quasi-classical transport equations to a SU(2) gauge covariant formulation in order to describe interaction between particles and spin fields.

1.2 Basic transport phenomena in mesoscopic systems involving superconductors

In this section we will use the previously introduced Bogoliubov-de Gennes Hamiltonian to discuss basic scattering phenomena at boundaries between normal and superconducting regions with the aid of minimal examples. We start with the Andreev reflection as the microscopic explanation for the charge

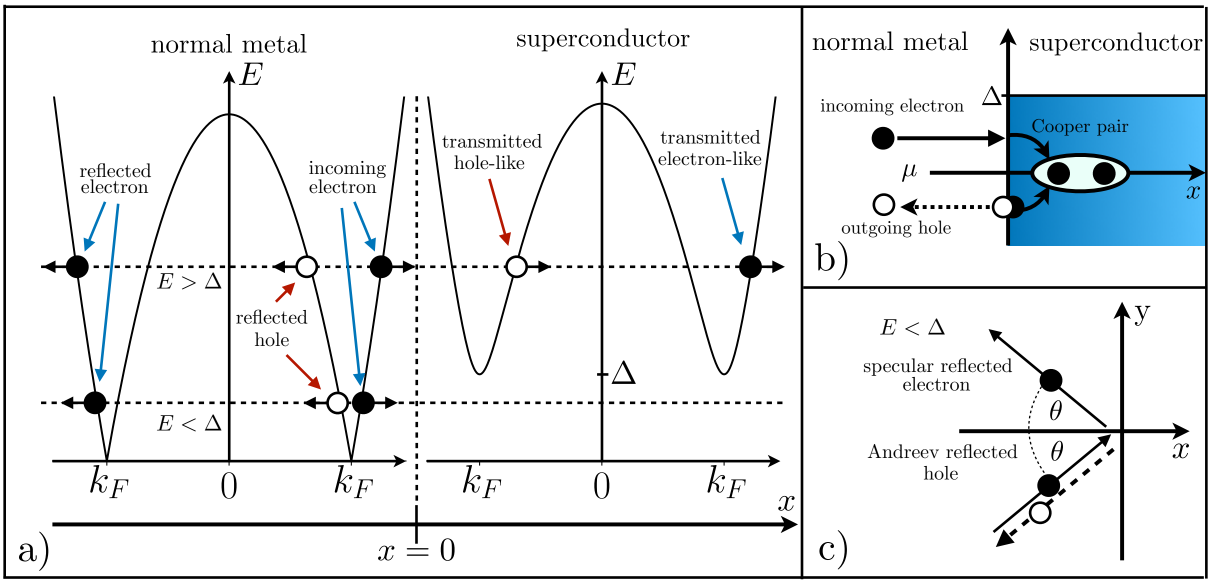

FIGURE 1.3: a) Excitation spectrum and possible quasiparticle solutions and their propagation direction on both sides of the interface. b) Electron with sub gap energy can not enter the superconductor, pairs up with a electron below the Fermi energy to enter the condensate and leaves behind a hole. c) Paths of the reflected quasiparticles.

transfer at such boundaries and explain how these lead to the formation of Andreev bound states and the Josephson effect in S/N/S junctions. Finally we explore how these effects are altered under the presence of a homogeneous exchange field. This section will allow the reader to fully reproduce the findings of chapter 2.

1.2.1 Andreev reflection and N/S interface - Proximity effect

The Andreev reflection is a process that appears at a N/S interface and is an explanation for the finite sub-gap charge transport. It also provides insight into the difference between the BCS many particle gap, and a single particle gap, because a quasiparticle can enter the superconductor with an energy below the gap, only because of the presence of the many-body condensate.

Let us assume a planar system in the x-y plane, with a N/S interface located at $x = 0$ and translational invariant in the y direction. We model the order parameter as a step-function $\Delta\left(\mathbf{x}\right) = \Theta(x)\Delta_0$ and a add δ-like normal scattering barrier at the interface by setting $V(\mathbf{x}) = H\delta(x)$. Let us determine the possible propagating solutions in the different regions.

In the normal region $x < 0$ the possible solutions for a given quasiparticle energy E and transverse momentum k_y are

$$\psi_e^\pm = \begin{pmatrix} 1 \\ 0 \end{pmatrix} e^{\pm ik_e x} e^{ik_y y}, \text{ and } \psi_h^\pm = \begin{pmatrix} 0 \\ 1 \end{pmatrix} e^{\pm ik_h x} e^{ik_y y}. \tag{1.41}$$

In the superconductor $x > 0$ we find the solutions

$$\psi_{qe}^{\pm} = \begin{pmatrix} ue^{i\frac{\varphi}{2}} \\ ve^{-i\frac{\varphi}{2}} \end{pmatrix} e^{\pm iq_e x} e^{ik_y y}, \text{ and } \psi_{qh}^{\pm} = \begin{pmatrix} ve^{i\frac{\varphi}{2}} \\ ue^{-i\frac{\varphi}{2}} \end{pmatrix} e^{\pm iq_h x} e^{ik_y y}, \tag{1.42}$$

where

$$u = \sqrt{\frac{E+\Omega}{2E}}, \quad v = \sqrt{\frac{E-\Omega}{2E}}, \quad \Omega = \sqrt{E^2 - \Delta_0^2}, \tag{1.43}$$

and $e^{i\varphi} = \frac{\Delta_0}{|\Delta_0|}$ is the phase of the order parameter. We parametrize the in-plane Fermi wave vector of the circular Fermi surface by angle θ, $\mathbf{k}_F = k_F(\cos\theta, \sin\theta)$. For small excitations about the gap energy and when the gap is much smaller then the Fermi energy, $E, \Delta_0 \ll \mu$, we can approximate

$$k_e = k_F \cos\theta + \frac{E}{\hbar v_F \cos\theta}, \quad k_h = k_F \cos\theta - \frac{E}{\hbar v_F \cos\theta} \tag{1.44}$$

$$q_e = k_F \cos\theta + \frac{\Omega}{\hbar v_F \cos\theta}, \quad q_h = k_F \cos\theta - \frac{\Omega}{\hbar v_F \cos\theta}. \tag{1.45}$$

which is usually referred to as the Andreev or quasi-classical approximation. From these single particle solutions we can construct the solution across the interface. For an incoming electron from the normal region we have two possible solutions that propagate away from the interface on each side of the junction, by calculating the group velocity of the excitations $v_g(\mathbf{k}) = \partial_{\mathbf{k}} E_{\mathbf{k}}$. The Ansatz in the normal region and superconducting regions reads

$$\Psi_N(x) = \psi_e^+(x) + r_{eh}\psi_h^+(x) + r_{ee}\psi_e^-(x), \tag{1.46}$$

$$\Psi_S(x) = t_{ee}\psi_{qe}^+(x) + t_{eh}\psi_{qh}^-(x) \tag{1.47}$$

respectively. The coefficients $r_{eh}, r_{ee}, t_{ee}, t_{eh}$ are the probability amplitudes for electron-hole-, electron-electron reflection, electron-hole-, electron-electron transmission respectively and are determined by boundary conditions for the wave function at the interface

$$\Psi_N(0^-) = \Psi_S(0^+), \tag{1.48}$$

$$\partial_x \Psi_N(0^-) - \partial_x \Psi_S(0^+) = \frac{2mH}{\hbar^2} \Psi_N(0). \tag{1.49}$$

A scheme of the Ansatz for the different regions of the junction is shown in Fig. 1.3. Solving the system of equations resulting from the boundary conditions we find the coefficients [70]

$$r_{ee} = \frac{(Z^2 + iZ)(u^2 - v^2)}{\gamma}, \quad r_{eh} = -\frac{uv}{\gamma} e^{-i\varphi}, \quad t_{ee} = \frac{(iZ - 1)u}{\gamma} e^{-i\frac{\varphi}{2}}, \quad t_{eh} = -\frac{iZv}{\gamma} e^{-i\frac{\varphi}{2}}, \tag{1.50}$$

where we used the approximation $k_e, k_h, q_e, q_h \approx k_F \cos\theta$, and introduced $Z = H/(\hbar v_F \cos\theta)$ and $\gamma = (u^2 + Z^2(u^2 - v^2))$. In Fig. 1.4 we plot the probabilities for the different processes resulting from an electron impinging at the interface at normal incidence, $R_{ab} = |r_{ab}|^2$, $T_{ab} = |t_{ab}|^2$, where $a, b \in \{e, h\}$. The probability for the reflection of a electron into a hole is always present for energies below or slightly above to the superconducting gap and vanishes at higher energies. Such a process is usually called Andreev reflection [71] and is responsible for the charge transport across SN interfaces for energies below the gap energy. One might think that no charge transfer is possible, as quasiparticles with energies smaller then the gap can not enter the superconductor due to the vanishing DOS. However, Δ is a many particle gap representing the tendency for electrons to form Cooper pairs. Inside the superconductor, the electron-like quasiparticle solution is evanescent, thus its charge must transfer to the other side of the interface. When penetrating the superconductor, the incoming electron can pair up with a electron below the Fermi-energy to form a Cooper pair, which gets absorbed by the condensate. During this a hole excitation is left behind, and leaves into the normal metal as sketched in Fig. 1.3 b). As the electrons can only enter the condensate in pairs, with each Andreev reflection a total charge of $2e$ is transferred into the superconductor. Inspection of the Ansatz shows another peculiarity. Within the Andreev approximation of small excitation- and gap-energies with respect to E_F, the reflected hole traces back exactly the path of the incoming electron (Fig. 1.3 c). The Andreev reflection competes with the usual specular reflection of electrons, as can be seen in Fig. 1.4. For vanishing normal barrier $Z = 0$, quasiparticles with energy below the gap get perfectly Andreev reflected. Increasing the barrier strength Z leads to a strong suppression of the Andreev reflection as the electrons are hindered to enter the superconductor and thus can not be absorbed by the condensate. Let us now calculate some observables from these coefficients.

Current and conductance at finite voltage

For small applied bias between a normal and superconductor lead connected by some constriction, for example a short wire, the current can be related to the reflection and transmission coefficients. Within the generalized Landauer-Büttiker formalism to superconducting systems introduced by BTK [70], the current is given by

$$I_{NS} = 2\mathcal{N}_0 e v_F \mathcal{A} \int_{-\infty}^{\infty} \left[f_0\left(E - eV\right) - f_0(E)\right]\left[1 + R_{eh} - R_{ee}\right] dE. \tag{1.51}$$

Here f_0 is the Fermi distribution at equilibrium, $\mathcal{N}_0$ is the normal density of states at the Fermi energy and $\mathcal{A}$ is the cross section of the link between the leads. In the normal metal $R_{eh} = 0$ due to absence of Andreev scattering processes and $1 - R_{ee} = T_{ee} = \frac{1}{1+Z^2}$ due to conservation of probability current. Thus the current between normal metals connected by a point contact with a scattering barrier gets

$$I_{NN} = \frac{2\mathcal{N}_0 e^2 v_F \mathcal{A}}{1 + Z^2} V = \frac{V}{R_N}. \tag{1.52}$$

For small voltages at $T = 0$ it follows that the differential conductance $G = \frac{\partial I}{\partial V}$ behave like

$$\frac{G_{NS}}{G_{NN}} = 2\frac{1 + Z^2}{(1 + 2Z^2)^2}. \tag{1.53}$$

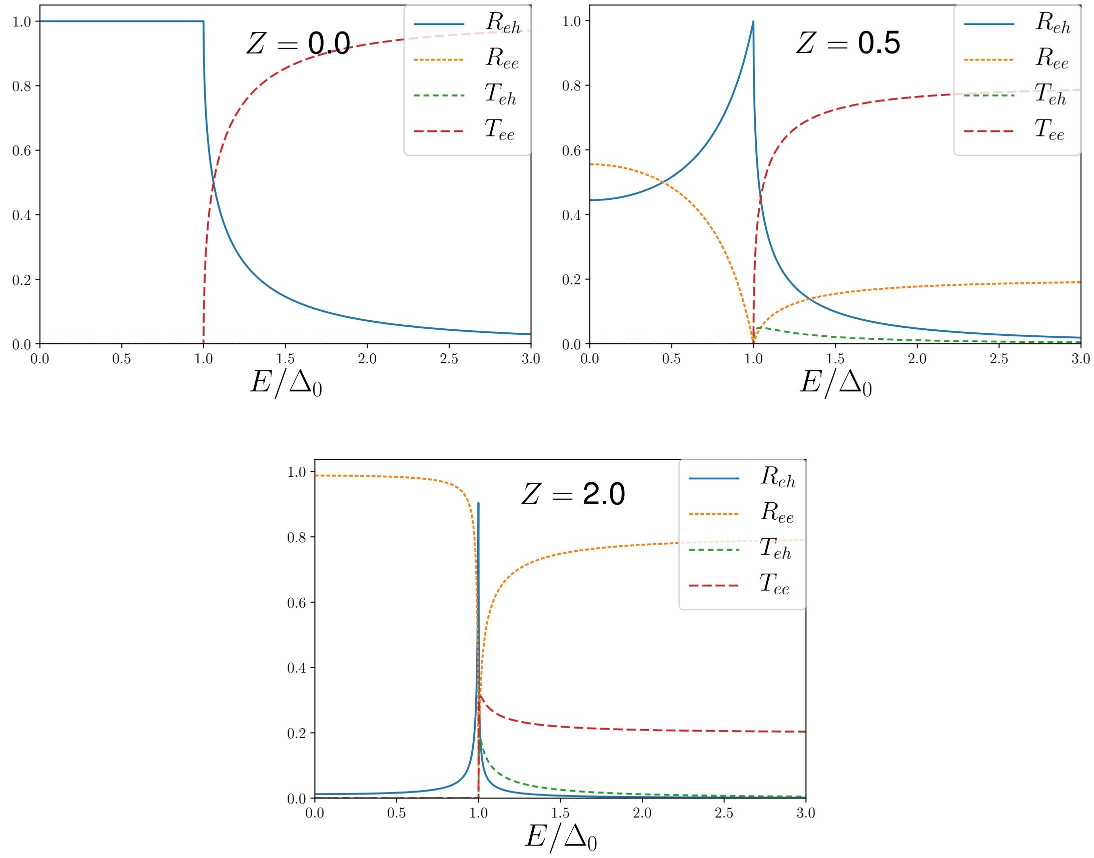

FIGURE 1.4: Reflection and transmission probabilities for different normal barrier strengths Z for a particle with incidence angle normal to the interface.

The current and the differential conductance are shown in Fig.1.5. For a ballistic link where $Z = 0$, the current for Voltages below the gap and the conductance are exactly twice the quantities in the normal state. This is as expected when only Andreev processes contribute to the charge transfer. Electrons pass the interface in pairs only. In the tunneling limit, when $Z \gg 1$, the sub gap current and conductance are strongly reduced due to the suppression of the Andreev reflection. The cusp at the the gap energy stems from the singularity of the density of states of the superconductor at the gap edge.

1.2.2 Josephson effect and Andreev bound states in S/N/S junctions

In general, the order parameter of the superconducting state is a complex quantity. It will therefore have a phase which is unobservable due to the nature of measurement within the quantum mechanical framework, where only phase differences between quantum states are of relevance. If two superconductors are brought into contact separated by a tunnel junction (thin insulating layer) or a weak link (normal metal constriction), the two subsystems maintain their own phase of the order parameter, let us say φ_L and φ_R. The coupling between the two superconductors leads to interference of the phases making the phase difference an observable quantity. Such a device is called a Josephson junction and was named after

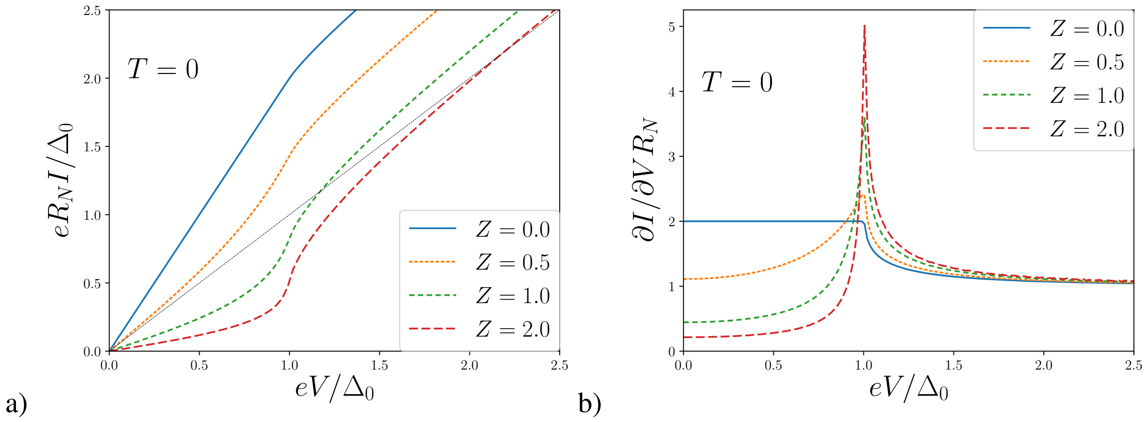

a) b)

FIGURE 1.5: a) Current and b) differential conductance for different normal barrier strengths Z.

B. D. Josephson, whose striking prediction was that the macroscopic phase difference $\varphi = \varphi_L - \varphi_R$ drives a zero-voltage supercurrent

$$j(\varphi) \propto \sin\varphi \tag{1.54}$$

between the two superconductors [18]. This is called the dc-Josephson effect. He also predicted the time evolution

$$\partial_t \varphi = \frac{2eV}{\hbar} \tag{1.55}$$

of the phase difference if a voltage V is applied across the junction, which leads to a quickly alternating current and is known as the ac-Josephson effect.

In this work we will be only interested in the dc-Josephson effect, and we will now link its appearance to the solutions of the BdG equation in a clean S/N/S junction. It will allow us to describe a wide range of Josephson devices including the tunnel junction case studied by Josephson originally.

If no voltage is applied between the two superconductors, an electron in the normal region with energy below the gap energy, is Andreev reflected as a hole at one interface. It is then Andreev reflected as an electron at the other interface thus returning to its initial state. This leads to the formation of so called Andreev bound states as shown schematically in Fig. 1.6. In the case of a clean interface, only Andreev reflection processes take place and a Cooper pair is emitted into the right superconductor for every reflection at the right interface. On the other side of the normal region the reverse process takes place. A Cooper pair is absorbed from the left superconductor for every reflection at the left interface. This corresponds to a equilibrium supercurrent through the device. Thus, Andreev bound states offer a microscopic description of the Josephson effect.

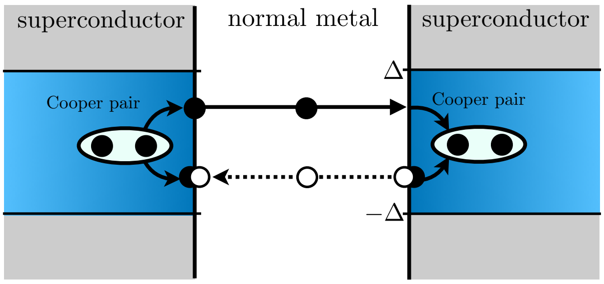

FIGURE 1.6: Andreev bound state in a SNS junction.

Bound state energies

The condition for the formation of an Andreev bound state depicted in Fig. 1.6 can be obtained by constructing the wave function $\Psi_{SNS}(x)$ across the junction. Wa take the simple case of a single mode with zero transverse momentum in a junction of length L with the center of the normal region at $x = 0$. This corresponds to the Ansatz

$$\Psi_{SNS}(x) = \begin{cases} t_{hh}\begin{pmatrix} ve^{i\varphi_{L/2}} \\ ue^{-i\varphi_{L/2}} \end{pmatrix} e^{iq^h x}, & x < -\frac{L}{2} \\ r_{he}\begin{pmatrix} 1 \\ 0 \end{pmatrix} e^{ik^e x} + r_{eh}\begin{pmatrix} 0 \\ 1 \end{pmatrix} e^{ik^h x}, & |x| < \frac{L}{2} \\ t_{ee}\begin{pmatrix} ue^{i\varphi_{R/2}} \\ ve^{-i\varphi_{R/2}} \end{pmatrix} e^{iq^e x}, & x > \frac{L}{2} \end{cases} \tag{1.56}$$

The solvability condition for the system of equations resulting from the condition of continuity at $x = \pm\frac{L}{2}$ yields

$$E = \pm\frac{\hbar v_F}{L}\left[\frac{\varphi}{2} \mp \arcsin\frac{E}{|\Delta_0|} + \pi\left(n \pm \frac{1}{2}\right)\right], \quad n \in \mathbb{Z}. \tag{1.57}$$

When the junction is short compared to the coherence length of the superconductor $L \ll \xi_0 = \frac{\hbar v_F}{\Delta_0}$ the above equation reduces to the pair of bound state energies

$$E = \pm|\Delta_0|\cos\left(\frac{\varphi}{2}\right). \tag{1.58}$$

In the expressions Eq.(1.57), (1.58) , the normal scattering is not included in the calculation. The case of vanishing scattering potential is physically not very relevant as it would mean the existence of a bulk superconductor with spatially sharp separated regions of different phases of superconducting condensate. In realistic systems normal scattering appears for example due to surface roughness of the interface. Including the scattering potential as previously in Sec. 1.2.1 generalizes the short junction result Eq.(1.58) to

$$E = \pm\Delta\sqrt{\frac{1+2Z^2+\cos\varphi}{2+2Z^2}} = \pm\Delta\sqrt{1-\sin^2\frac{\varphi}{2}\tau}, \tag{1.59}$$

where we expressed the barrier strength Z through the transmission τ of the barrier, $\tau = 1/\left(1+Z^2\right)$. The effect of a finite temperature can be included by assuming the weak-coupling temperature dependence of the gap $\Delta = \Delta_0\sqrt{1-(T/T_C)^2}$.

Josephson current

Being a equilibrium current, the dependence of the Josephson current on the phase difference can be calculated varying the thermodynamic potential, the free energy F of the system, after the phase difference [65, 66]

$$j = \frac{2e}{\hbar}\frac{\partial F}{\partial\varphi}. \tag{1.60}$$

The total free energy of the system is

$$F[\Delta,\Delta^*] = \frac{1}{|V_0|}\int d^3\mathbf{r}\,|\Delta(\mathbf{r})|^2 + F_{BCS}[\Delta,\Delta^*] \tag{1.61}$$

After determining the free Energy F_{BCS} of a superconductor defined through the grand canonical partition sum $F_{\text{BCS}}[\Delta,\Delta^*] = -\frac{1}{\beta}\ln Tr\left[e^{-\beta\mathcal{H}_{\text{BCS}}^{\text{mf}}}\right]$ we obtain

$$F[\Delta,\Delta^*] = \frac{1}{|V_0|}\int d^3\mathbf{r}\,|\Delta(\mathbf{r})|^2 + \text{Tr}\left[\hat{h}(\hat{\mathbf{p}})\right] - \frac{2}{\beta}\sum_n \ln\left(2\cosh\frac{\beta E_n}{2}\right) \tag{1.62}$$

where n is a index labeling the states of the system. The first two terms are φ-independent and will not contribute to the current. Inserting $F[\Delta,\Delta^*]$ into Eq. (1.60) gives the current phase relationship for the Josephson current [65, 72]

$$j = -\frac{2e}{\hbar}\sum_{n,E_n<\Delta}\tanh\left(\frac{\beta E_n}{2}\right)\frac{\partial E_n}{\partial\varphi} - \frac{2e}{\hbar}\frac{2}{\beta}\int_\Delta^\infty dE\ln\left[2\cosh\left(\frac{\beta E}{2}\right)\right]\frac{\partial\mathcal{N}(E)}{\partial\varphi}. \tag{1.63}$$

The first term corresponds to discrete excitations below the gap, in our case the Andreev bound states. The second term comes from the continuous spectrum above the gap energy.

As an example we treat the case of a short ballistic junction that hosts a single mode. In that case it can be shown that the contribution to the current Eq. (1.63) from the continuum states can be neglected [73]. Inserting the positive branch of the bound state energy Eq. (1.59) into Eq. (1.63) gives

$$j = \frac{e\Delta}{2\hbar}\tanh\left[\frac{\beta}{2}\Delta\sqrt{1-\tau\sin^2\frac{\varphi}{2}}\right]\frac{\tau\sin\varphi}{\sqrt{1-\tau\sin^2\frac{\varphi}{2}}}. \tag{1.64}$$

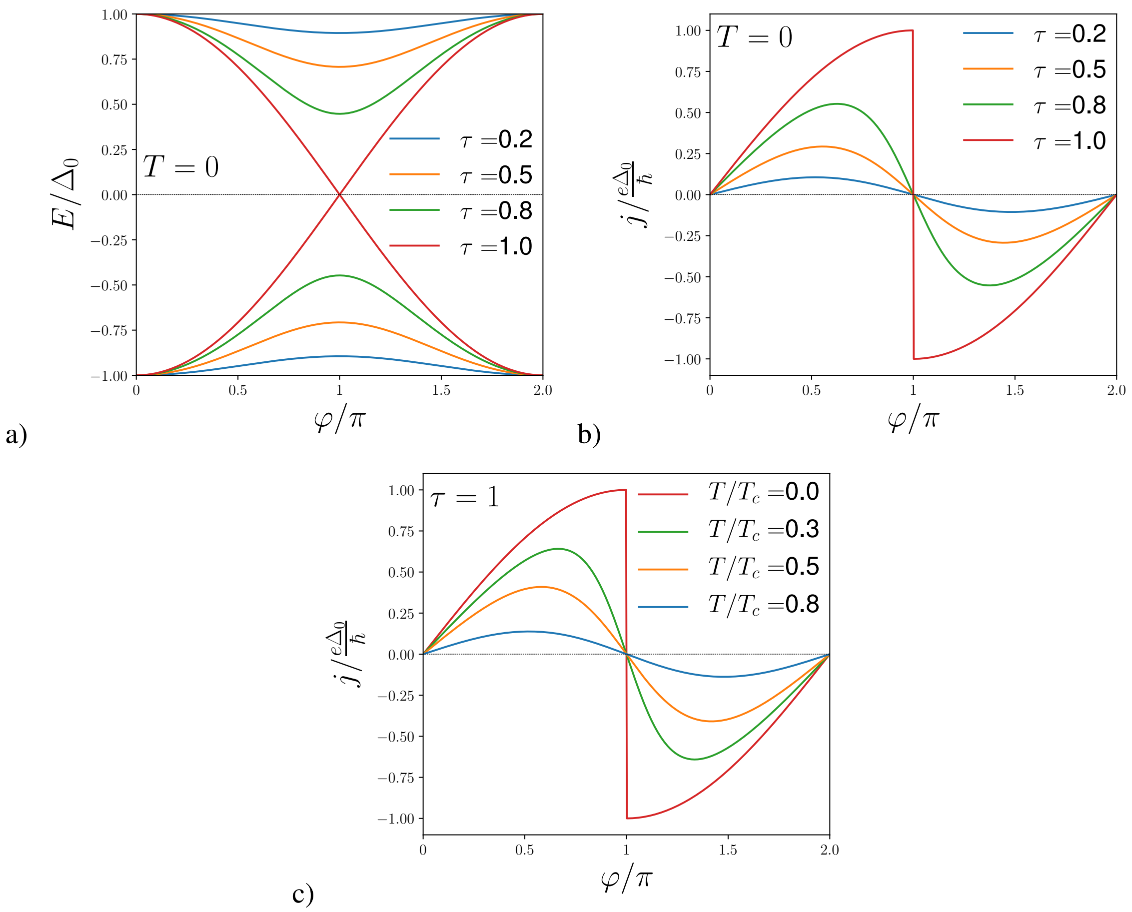

FIGURE 1.7: a) Andreev bound state energy in a short junction for different barrier transmissivities τ at zero temperature. Josephson current at b) zero temperature and c) at perfect transmission and varying the temperature.

The Andreev bound state energies and the corresponding Josephson current phase relationships are shown in Fig. 1.7. At perfect transmission $\tau = 1$, the ballistic limit, and low temperatures the two possible Andreev bound states are decoupled and the current shows a saw tooth like dependence on the phase difference. Allowing for backscattering in the normal region, $0 < \tau < 1$, a right moving electron/hole can be reflected back into a left moving electron/hole which couples the two ballistic Andreev bound states. As a consequence the Andreev spectrum gaps out at the crossing at $\varphi = \pi$. In the tunneling limit, when τ is small, the current shows the expected $\sin\varphi$ behavior as predicted by Josephson. Close to T_c, the higher harmonics of the current phase relation are suppressed and the current becomes sinusoidal.

Quasi-classical Green's function of a junction and the BdG formalism - Furusaki-Tsukada formula

Calculating the equilibrium charge current from the thermodynamic expression Eq. (1.63) can get a quite tedious task, for example when sub-gap states and continuum states contribute to the current. The quasi-classical Green's function of the junction contains the full spectral information of the system and we will introduce it formally in Sec. 1.4. For now we will show that for a ballistic system, the letter can be constructed by combining direct products of the BdG solutions for the junction [74, 75]. The current can then be related to components of the Green's function and expressed through the Andreev reflection probability amplitudes as shown by Furusaki and Tsukada [76]. This demonstrates the equivalence of the Green's function and BdG formulation, and also emphasizes their individual strengths. The BdG formulation provides a microscopic picture of the individual quasiparticle processes by combining single particle solutions. On the other hand, once we know the Green's function of the system, it contains the whole spectral information of the system and observables can be calculated from it usually in a straightforward way. We introduce this formalism as we make great use of it in chapter 2.

Let us assume a ballistic structure with a interface between a superconductor for $x < 0$, and a normal conductor for $x > 0$, that is perpendicular to the transport direction x. The retarded Green's function $G^r(x, x', E, k_{\|})$ is interpreted as the probability amplitude for quasiparticles, with energy E and conserved transverse momentum $k_{\|}$, to propagate from x' to x. The Green's function thus can be constructed by summing up over all possible single particle propagators, which represents all possible quasiparticle trajectories. There are two ways to do so. We can sum up probabilities for a quasiparticle to arrive at x, having started at x' in a specific state, or we can sum up probabilities for a quasiparticle starting at x' to arrive at x in a specific state. In a bulk these are identical, but due reflections at the interface the arriving (starting) quasiparticle, can be in a different state from the starting (arriving) quasiparticle. The first way is valid for $x' < x < 0$ and the second for $x < x' < 0$. Let us have a look at the particular example, when an electron is created at x' and propagates towards the interface to the point $x > x'$. The three single particle propagators for each path correspond to

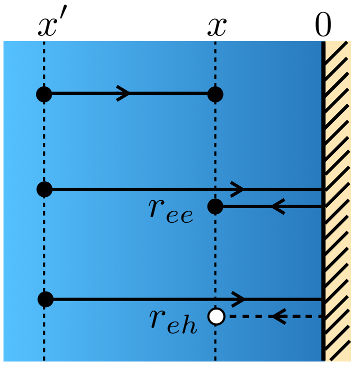

$$\begin{pmatrix} ue^{i\varphi_L} \\ v \end{pmatrix} e^{iq_e x} \otimes \left[\begin{pmatrix} ue^{i\varphi_L} \\ v \end{pmatrix} e^{iq_e x'} \right]^{\dagger},$$

$$r_{ee} \begin{pmatrix} ue^{i\varphi_L} \\ v \end{pmatrix} e^{-iq_e x} \otimes \left[\begin{pmatrix} ue^{i\varphi_L} \\ v \end{pmatrix} e^{iq_e x'} \right]^{\dagger},$$

$$r_{eh} \begin{pmatrix} ve^{i\varphi_L} \\ u \end{pmatrix} e^{iq_h x} \otimes \left[\begin{pmatrix} ue^{i\varphi_L} \\ v \end{pmatrix} e^{iq_e x'} \right]^{\dagger},$$

so this branch $G^r_e(x, x', E, k_{\|})$ of the full Green's function $G^r(x, x', E, k_{\|})$ is the direct product of the BdG solution in the left superconductor and the incoming quasiparticle wave function,

$$G^r_e(x, x', E, k_{\|}) = C_1 \left[\psi^+_{qe}(x) + r_{ee}\psi^-_{qe}(x) + r_{eh}\psi^+_{qh}(x) \right] \otimes \left[\psi^+_{qe}(x') \right]^{\dagger}. \tag{1.65}$$

For the case when $x < x' < 0$ we repeat the construction for a electron-like quasiparticle created at x' and the possible resulting states at x. The different paths correspond to

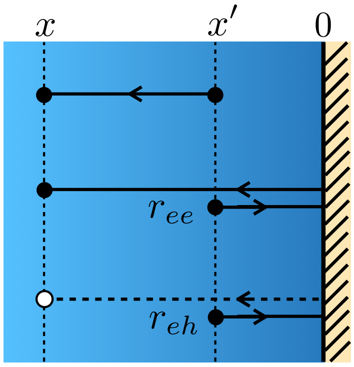

$$\begin{pmatrix} ue^{i\varphi_L} \\ v \end{pmatrix} e^{-iq_e x} \otimes \left[\begin{pmatrix} ue^{i\varphi_L} \\ v \end{pmatrix} e^{-iq_e x'} \right]^\dagger ,$$

$$r_{ee} \begin{pmatrix} ue^{i\varphi_L} \\ v \end{pmatrix} e^{-iq_e x} \otimes \left[\begin{pmatrix} ue^{i\varphi_L} \\ v \end{pmatrix} e^{iq_e x'} \right]^\dagger ,$$

$$r_{eh} \begin{pmatrix} ve^{i\varphi_L} \\ u \end{pmatrix} e^{iq_h x} \otimes \left[\begin{pmatrix} ue^{i\varphi_L} \\ v \end{pmatrix} e^{iq_e x'} \right]^\dagger ,$$

and the Ansatz for this Green' function branch is

$$G_e^r(x, x', E, k_\parallel) = C_1' \left(\psi_{qe}^-(x) \otimes \left[\psi_{qe}^-(x) \right]^\dagger + \left[r_{ee}\psi_{qe}^-(x) + r_{eh}\psi_{qh}^+(x) \right] \otimes \left[\psi_{qe}^+(x') \right]^\dagger \right) . \tag{1.66}$$

The construction of $G_h^r(x, x', k_\parallel)$, when starting in a hole state is equivalent. The remaining constants C_i, C_i' of the full Green's function Ansatz $G^r(x, x', E, k_\parallel) = G_e^r(x, x', k_\parallel) + G_h^r(x, x', k_\parallel)$ are then fixed by the conditions [75, 77]

$$G^r(x, x', E, k_\parallel)|_{x=x'+0^+} = G^r(x, x', E, k_\parallel)|_{x=x'-0^+} , \tag{1.67}$$

$$\partial_x G^r(x, x', E, k_\parallel)|_{x=x'+0^+} - \partial_x G^r(x, x', E, k_\parallel)|_{x=x'-0^+} = \frac{2m}{\hbar}\hat{\sigma}_3 . \tag{1.68}$$

The full expression reads,

$$\begin{aligned} &G^r(x, x', E, k_\parallel) = -\frac{imE}{\hbar^2\Omega} \times \\ &\frac{1}{q_e} \left[e^{iq_e|x-x'|} + r_{ee}e^{-iq_e(x+x')} \begin{pmatrix} u^2 & uve^{i\varphi_L} \\ uve^{i\varphi_L} & v^2 \end{pmatrix} + r_{eh}e^{i(q_h x - q_e x')} \begin{pmatrix} uv & v^2e^{i\varphi_L} \\ u^2e^{-i\varphi_L}e^{i\varphi_L} & uv \end{pmatrix} \right] + \\ &\frac{1}{q_h} \left[e^{-iq_h|x-x'|} + r_{hh}e^{iq_h(x+x')} \begin{pmatrix} v^2 & uve^{i\varphi_L} \\ uve^{i\varphi_L} & u^2 \end{pmatrix} + r_{he}e^{i(q_h x' - q_e x)} \begin{pmatrix} uv & u^2e^{i\varphi_L} \\ v^2e^{-i\varphi_L}e^{i\varphi_L} & uv \end{pmatrix} \right] . \end{aligned} \tag{1.69}$$

The poles of the Green's function give direct access to the whole spectrum of the Josephson junction: the discrete Andreev bound states coincide with poles of the Andreev reflection coefficients, while branch cuts provide the continuum part of the spectrum.

Calculating the equation of motion for the Green's function and combining it with the equation of continuity for the charge density we get the current in terms of the retarded Green's function

$$j = \frac{e\hbar}{2im} \int dE \sum_{k_\parallel} \lim_{x' \to x} (\partial_x - \partial_{x'}) \, \mathrm{Tr} \left[G^r(x, x', E, k_\parallel) \right] . \tag{1.70}$$

Evaluating the trace and conversion to Matsubara frequency space $E \to i\omega_n$ to include a temperature dependence for the equilibrium current, we obtain the Furusaki-Tsukada formula [76]

$$j = \frac{e\Delta}{2\hbar}\frac{1}{\beta}\sum_{k_{\parallel}}\sum_{\omega_n}\frac{(q_e + q_h)}{\Omega_n}\left(\frac{r_{eh}\left(\varphi,\omega_n,k_{\parallel}\right)}{q_e} - \frac{r_{he}\left(\varphi,\omega_n,k_{\parallel}\right)}{q_h}\right), \tag{1.71}$$

with $\Omega_n = \sqrt{\omega_n^2 + \Delta^2}$. Formula (1.71) relates the charge current to the Andreev reflection coefficients for each channel, which are labeled by the transverse momentum $k_{\parallel}$. As usual these are found by calculating the solutions of the BdG equation across the junction. Thus naturally this formula includes contributions to the current above and below the gap energy, and can be applied to a wide range of ballistic junction scenarios. Note that in the last step of the calculation we have evaluated the expression at the interface $x = 0$, which is a short-cut and is equivalent to a full self-consistent evaluation of the current. For details we refer to Furusaki and Tsukadas original work [76].

Josephson effect and different junction types

The size, geometry, the involved materials and of course external parameters like the temperature will set the conditions for the formation of Andreev bound states and Andreev reflection processes, and thus the number of modes contributing to the Josephson current. Oversimplifying, what is left to do is to count the modes in the correct way for each setup. We will now categorize different junction types. Two classes can be distinguished with regards to the ratio of the length L of the region separating the superconductors and the coherence length ξ_0. Short junctions for which $\xi_0 \gg L$ and long junctions $\xi_0 \ll L$.

A further distinction is made regarding the ratio of the length of the mean free path l and ξ_0. The mean free path is the length of the classical path that a quasiparticle travels without changing its traveling direction due to scattering at impurities. In a dirty/diffusive junction, scattering is very frequent and $l \ll \xi_0$ with the diffusive coherence length $\xi_0 = \sqrt{\frac{\hbar D}{\Delta}}$ where $D = v_F\tau^2/\text{dim}$ is the diffusion constant, with dim as the dimension of the system and the scattering time $\tau = l/v_f$. In a clean junction $l \gg \xi_0$ and $\xi_0 = \frac{\hbar v_F}{\Delta}$. We need to include disorder in our description of the superconducting state in order to describe dirty systems, which we will do in Sec. 1.4.6. For now we will be mainly concerned with clean systems and only present some previous results on dirty systems.

Junctions can also be categorized depending on the realization of the coupling between the superconducting electrodes. In his original work Josephson considered a tunnel junction, where a thin vacuum or insulating layer separates the superconductors but still allows for exchange of quasiparticles, as shown in Fig. 1.8 a). It is also possible to connect the two electrodes via a normal conducting constriction, which is referred to as a weak link. There are many possibilities of weak links like narrow bridges, wires or point contacts. Weak links can be further characterized by comparing the minimal width W of the constriction with the Fermi wavelength λ_F. When $W \sim \lambda_F$ the contact region hosts only a few conduction channels. Such system is called a quantum point contact [73, 78]. If $W \gg \lambda_F$ one speaks of a classic (point) contact [79].

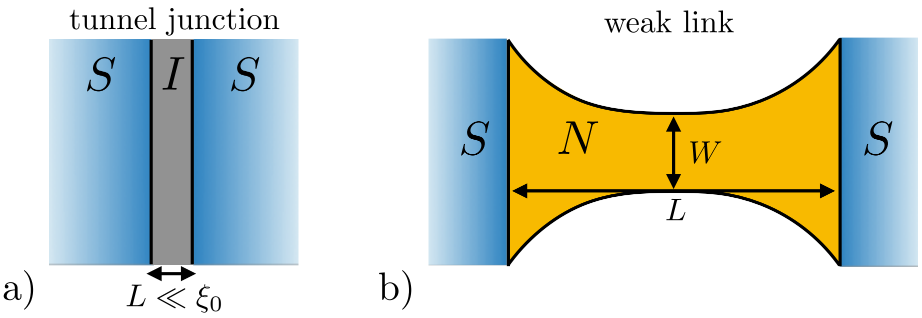

FIGURE 1.8: a) Scheme of a tunnel junction, two superconductors (S) are separated by a thin insulating layer (I) and b) Scheme of a Josephson weak link, a constriction made of a normal conductor (N) of length L and maximal width W connects two Ss.

Short junctions

For wide planar junctions like a tunneling junction, the width of the contact between the two superconductors is far above the Fermi wavelength. In that case, Josephson found that the current is sinusoidal and proportional to the normal state conductance

$$j(\varphi) = \frac{\pi \Delta G_N}{2e} \tanh\left[\frac{\beta}{2}\Delta_0\right] \sin\varphi. \tag{1.72}$$

The temperature dependence in the above formula has been determined by Ambegaokar and Baratoff [80]. The critical current $j_c = \max\left[j(\varphi)\right]$ fulfills $j_c R_N = \frac{\pi\Delta_0}{2e}$, where $R_N = 1/G_N$ is the normal state resistance of the contact. It is determined by size of the gap and characteristics of the normal state which reflects once more the fact that the non superconducting barrier is the bottle neck for the Cooper pair transfer from one side of the junction to the other.

A short and diffusive classic link was treated by Kulik and Omelyanchuk [81] solving the Usadel Eq. (1.152). The current in that case is given by

$$j = \frac{\pi \Delta G_N}{e} \operatorname{arctanh}\left(\sin\frac{\varphi}{2}\right) \cos\frac{\varphi}{2} \tag{1.73}$$

and shows a increase of the critical current by a factor of 1.32 when compared to the tunnel junction. The Josephson current in a ballistic classical superconducting point contact was obtained by the same authors [79] using the Eilenberger Eq. (1.147). In that case the critical current is twice the value of the tunnel junction at $T = 0$ and the current phase relationship reads

$$j(\varphi) = \frac{\pi \Delta G_N}{e} \sin\frac{\varphi}{2} \quad \varphi \in \left[-\pi, \pi\right]. \tag{1.74}$$

The case of a quantum point contact has been investigated by Beenakker and van Houten within the BdG formalism [73]. They found that the current is given by

$$j = N\frac{e\Delta}{\hbar} \tanh\left[\frac{\beta}{2}\Delta\cos\frac{\varphi}{2}\right] \sin\frac{\varphi}{2}, \tag{1.75}$$

thus it is proportional to number of modes $N \approx \frac{A}{\lambda_F^2}$ where A is the cross-section of the link. At zero temperature the result of Bennakker and van Houten is equivalent with the one of Kulik Eq. (1.74), what demonstrates that the classic result holds also in the quantum limit. The current is proportional to the normal state conductance which itself is related to the number of open conductance channels. However, varying the width of the junction in the case of a quantum point contact leads to measurable conductance steps because of the small amount of modes. This behavior has been confirmed in many experiments, for example on break junctions [82, 83].

The above results can be linked to the one channel result for short junctions Eq.(1.64). For a general short link between two superconductors the current will be carried by some number of channels with different transmissions. Thus at $T = 0$ in general

$$j = \frac{e\Delta}{2\hbar} \sum_{i=1}^{N} \frac{\tau_i \sin\varphi}{\sqrt{1 - \tau_i \sin^2\left(\frac{\varphi}{2}\right)}}, \tag{1.76}$$

where τ_i is the transmission of each channel. In a tunneling junction all the transmissions are small $\tau_i \ll 1$ and we can approximate

$$j \approx \frac{e\Delta}{2\hbar} \sum_{i=1}^{N} \tau_i \sin\varphi = \frac{\Delta\pi}{2eR_N} \sin\varphi \tag{1.77}$$

and recover the result by Josephson Eq. (1.72). Here we used the relation by Landauer and Büttiker [84], $G_N = G_0 \sum_i \tau_i$, where $G_0 = 2e^2/h$, which states that the normal state conductance is the conductance of each individual channel. The result for a ballistic contact by Bennakker follows by setting $\tau_i = 1$ for all channels. As mentioned before, to describe dirty weak links it is necessary to include disorder in the theory. Nevertheless it is possible to model such constrictions with the formula Eq.(1.76) by using a ensemble of channels determined by a distribution function [85].

Long junctions

The current in a long ballistic weak link was obtained first by Ishii [75] from the quasi classical Green's function of the junction constructed from solutions of the BdG equation [74], as we showed in the previous Sec. 1.2.2. The Andreev reflection amplitudes for electron- and hole-like quasiparticle states in a junction of finite length are given by

$$r_{eh}^i(\varphi) = r_{he}^i(-\varphi) = \frac{\Delta\left[e^{i\Phi_i} - e^{i\varphi}\right]}{(E+\Omega)\, e^{i\varphi} - (E-\Omega)\, e^{i\Phi_i}} \tag{1.78}$$

where we $\Phi_i = (k_i^e - k_i^h)L$ is the phase difference between electron- and hole-like quasiparticles in the i-th conduction channel after passing the junction. Inserting these into the Furusaki-Tsukada formula (1.71), and after analytical continuation $E \to i\omega_n$ and $\Phi_i(E \to i\omega_n) = i\tilde{\Phi}_i$, we obtain the current

$$j = \frac{2e\Delta^2}{\hbar\beta} \sum_{i=1}^{N} \sum_{n} \frac{\sin\varphi}{(2\omega_n^2 + \Delta^2)\cosh\left(\tilde{\Phi}_i\right) + 2\omega_n\Omega_n \sinh\left(\tilde{\Phi}_i\right) + \Delta^2\cos\varphi}. \tag{1.79}$$

This versatile expression reduces to all previous ballistic short junction limits. At zero temperature and $L \gg \xi_0$ it can be approximated

$$j \approx \frac{e}{\pi L} \sum_{i=1}^{N} v_i \varphi \tag{1.80}$$

where $v_i = \frac{\hbar\sqrt{k_F^2 - k_y^{i\,2}}}{m}$ is the quasiparticle velocity in transport direction of in the channel i. The current carried by each channel is inverse proportional to the time that the quasiparticles need to pass the junction and linearly dependent on the "potential difference" φ that drives the supercurrent. This leads to the characteristic sawtooth shape with jumps at $\varphi = (2n+1)\pi$. For finite temperature and/or finite back scattering the current phase relationship smears out and one recovers the known sinusoidal dependence (see Fig. 1.7 b), c) comparable to the tunnel junction case [65].

1.3 Heterostructures involving Ferromagnets

Conventional superconductivity and ferromagnetism are two strongly competing phases of matter. Superconductors are ideal diamagnets and actively expel magnetic fields, which is known as the Meißner-Ochsenfeld effect [86]. Clearly, screening the external magnetic field, so that it vanishes inside the superconductor must be energetically favorable. Consequently one can infer that at some critical field strength one can overcome this energetic advantage so that the superconductivity breaks down. Indeed There are two mechanisms that lead to a breaking of the Cooper pairs in a conventional superconductor, due to the presence of a magnetic field, namely the paramagnetic- and the orbital pair breaking effect.

The orbital pair breaking effect is a consequence of the opposite momentum of the electrons forming the Cooper pairs. From a classical point of view, the Lorentz force, resulting from the movement of the electrons in the magnetic field, points in opposite direction for each of the paired electrons and tears them apart.

The paramagnetic pair breaking originates in the opposite spin of the paired electrons. In a magnetic field, the spins of the electrons will try to align with the magnetic field. Increasing the magnetic field, so that the corresponding Zeeman energy exceeds the binding energy of the Cooper pair, one of the electrons will flip the spin eventually and the pair will break. Only taking into account the paramagnetic effect, the critical field of a superconductor has been determined by Clogston and Chandrasekhar [87, 88] and is given by $H_c = \frac{\Delta_0}{\mu_B\sqrt{2}}$ at $T = 0$. Above this limit there are two possibilities for the superconductivity to survive. The first is the existence of an attractive interaction between electrons of equal spin, like in triplet superconductors [89]. The other possibility proposed in 1964 by Fulde and Ferrel [90] and independently by Larkin and Ovchinnikov [91] is that, instead of flipping the spin, the Cooper pairs acquire a finite center-of-mass momentum. Such state would be characterized by a spatially oscillating order parameter and was named after its discoverers as the FFLO state. For decades there has been no evidence for the experimental realization of the FFLO state, and only recently experiments on layered organic superconductors proved its existence [92, 93].

Heterostructures between superconductors and ferromagnets, represent a unique way of probing the interplay of both phases. The proximity effect is strongly suppressed due to the exchange splitting of the bands inside the ferromagnet [21], furthermore the exchange field introduces an additional magnetic length scale in the system which leads to interference effects between quasiparticles with opposite spin. The latter leads to the reversal of the critical current in a S/F/S junction [22–26]. In the following we demonstrate these effects in the ballistic systems studied in Sec. 1.2.1 and Sec. 1.2.2, by replacing the normal region by a ferromagnet. To model the spin splitting of the bands in the ferromagnet, we consider the Stoner model, in which the motion of conduction electrons inside the ferromagnet can be described by an effective single-particle Hamiltonian with an exchange interaction. It is included in our theoretical description by adding the term

$$\mathcal{H}_{\text{ex}} = -\sum_{\mathbf{k}} \sum_{\alpha,\beta} c^\dagger_{\mathbf{k},\alpha} \left(\boldsymbol{\sigma} \cdot \mathbf{h}\right)_{\alpha,\beta} c_{\mathbf{k},\beta} \tag{1.81}$$

to the Hamiltonian $\mathcal{H}^{\text{mf}}_{\text{BCS}}$ (1.7), where we defined $\mathbf{h} = g\mu_B \mathbf{H}_{\text{ex}}$ with $\mathbf{H}_{\text{ex}}$ being the exchange field. The derivation of the BdG equation for the spin-full case is performed along the same path as shown in Sec. 1.1.1 making use of a spin-generalized Bogoliubov transformation. In the following we use the convention

$$c_{\mathbf{k},\sigma} = \sum_{\sigma'} (u_{\mathbf{k},\sigma,\sigma'} \gamma_{\mathbf{k},\sigma'} + v^*_{-\mathbf{k},\sigma,\sigma'} \gamma^\dagger_{-\mathbf{k},\sigma'}). \tag{1.82}$$

A detailed derivation can be found in App. A.1, where obtain the spin generalized BdG equation

$$\begin{pmatrix} \underline{\underline{\xi}} & \underline{\underline{\Delta}}(\mathbf{x}) \\ -\underline{\underline{\Delta}}^*(\mathbf{x}) & -\underline{\underline{\xi}}^* \end{pmatrix} \begin{pmatrix} \underline{u} \\ \underline{v} \end{pmatrix} (\mathbf{x}) = E \begin{pmatrix} \underline{u} \\ \underline{v} \end{pmatrix} (\mathbf{x}). \tag{1.83}$$

The underlined and doubly underlined characters indicate vectors and matrices in spin space respectively. We defined $\underline{\underline{\xi}} = H_0(\mathbf{x})\hat{1} - \boldsymbol{\sigma}\mathbf{h}$ and $\underline{u} = (u \uparrow, u_\downarrow)^{\mathrm{T}}$, $\underline{v} = (v \uparrow, v_\downarrow)^{\mathrm{T}}$. In the case of singlet pairing the pairing matrix is given by

$$\underline{\underline{\Delta}}(\mathbf{x}) = i\sigma_y \Delta(\mathbf{x}). \tag{1.84}$$

If the order parameter Δ is zero one obtains the normal single-particle Hamiltonian to describe a ferromagnetic region, whereas setting the exchange field h to zero we describe the superconductor. This allows to model S/F interfaces. If both parameters are finite we describe the case of a spin-split superconductor which we cover in more detail in chapter 2.

1.3.1 Andreev reflection at the S/F interface

First, we study the influence of a finite exchange field in the normal region on the Andreev reflection at a S/F interface. As we already demonstrated, Andreev reflection processes are the microscopic explanation for the sub-gap conductivity at interfaces between normal metals and superconductors. During a Andreev reflection, a incoming electron with spin up is reflected into a hole of opposite spin. In normal metals, due to the spin degeneracy of the energy levels, no spin effects occur with the Andreev reflection. In a ferromagnet, the energy band is split. Plane wave solutions describing quasiparticles from the majority- and minority-spin Fermi surfaces to a given excitation energy, show a miss-match of the quasiparticle wave vectors, which is proportional to the energy difference $2h$ of the bands. The corresponding Andreev reflection process is shown schematically in Fig. 1.9. The situation of reflections between bands of different spin is similar to a potential step tunneling problem. Consequently the Andreev scattering at the superconducting gap is imperfect, not retro-reflective and normal specular backscattering takes place even at a clean S/F interface. Another way to interpret this is that a incoming electron can not enter the condensate as there is no partner of exactly opposite spin and momentum at a given excitation energy, which makes the formation of Cooper pairs less effective.

In the following example of a S/F interface we choose the exchange field finite in the left half space $h(x) = h\Theta(-x)$ and parallel to the z-axis. In the ferromagnet the two spin species are decoupled and the BdG Hamiltonian is block diagonal. We do not include a normal scattering barrier as we already know that it suppresses Andreev reflection. The individual subsystems are

$$\mathcal{H}_\sigma\psi_\sigma(x) = \begin{pmatrix} \hat{\xi} - h(x) & \sigma\Delta(x) \\ \sigma\Delta^*(x) & -\hat{\xi} - \sigma h(x) \end{pmatrix} \begin{pmatrix} u_\sigma(x) \\ v_{-\sigma}(x) \end{pmatrix} = E \begin{pmatrix} u_\sigma(x) \\ v_{-\sigma}(x) \end{pmatrix}, \tag{1.85}$$

and labeled by $\sigma = \uparrow, \downarrow = \pm$. The kinetic term is given by $\hat{\xi} = -\frac{\hbar^2}{2m}\partial_x^2 - \mu + \frac{(\hbar k_\parallel)^2}{2m}$ with the chemical potential μ, that is assumed to be constant in the system. We define a step function like order parameter $\Delta(x) = \Delta\Theta(x)$. The solution of the BdG Eq. (1.85) across the interface for a given energy E and transverse momentum $\mathbf{k}_\parallel$ obtained as in the previous sections, and leads to the following Ansatz for an injected spin-up electron in the ferromagnet region:

$$\Psi_{e,\uparrow}(x) := \begin{cases} \begin{pmatrix} 1 \\ 0 \end{pmatrix} e^{ik_{e,\uparrow}x} + r_{ee}^{\uparrow} \begin{pmatrix} 1 \\ 0 \end{pmatrix} e^{-ik_{e,\uparrow}x} + r_{eh}^{\uparrow} \begin{pmatrix} 0 \\ 1 \end{pmatrix} e^{ik_{h,\downarrow}x}; & x < 0 \\ t_{ee}^{\uparrow} \begin{pmatrix} u \\ v \end{pmatrix} e^{iq_e x} + t_{eh}^{\uparrow} \begin{pmatrix} v \\ u \end{pmatrix} e^{-iq_h x}; & x > 0, \end{cases} \tag{1.86}$$

with the coherence factors u, v as in Eq.(1.43). Within the Andreev approximation the wave vectors are given by

$$k_{e,\sigma} = \sqrt{k_{F,x}^2 + \frac{2m}{\hbar^2}(E + \sigma h)}, \quad k_{h,-\sigma} = \sqrt{k_{F,x}^2 - \frac{2m}{\hbar^2}(E + \sigma h)}, \quad q_{e(h)} = k_{F,x} \pm \frac{\Omega}{\hbar v_{F,x}} \tag{1.87}$$

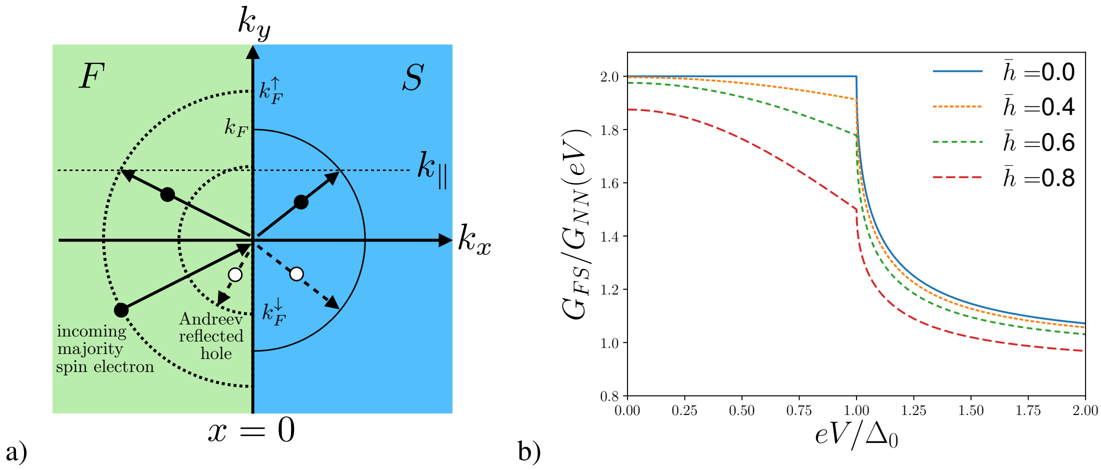

FIGURE 1.9: a) Possible propagating quasiparticle solutions for given excitation energy $E > \Delta$ and transverse momentum $k_{\|}$ at a S/F interface. The Andreev reflection is not perfectly retroreflective due to the exchange splitting of the bands in the F. b) Differential conductance for a single channel FS interface varying the exchange field $\bar{h} = h/\mu$ at $T = 0$.

where we defined the effective Fermi momentum $k_{F,x} = \mu - \frac{(\hbar k_{\|})^2}{2m}$. The probability amplitudes for each process are obtained by solving the resulting system of equations from demanding continuity of the wave-function and its derivative at $x = 0$. This gives the following expression for the normal and Andreev reflection coefficients [21]

$$r_{ee}^{\uparrow} = \frac{\left(\bar{k}_{e,\uparrow} - 1\right)\left(\bar{k}_{h,\downarrow} + 1\right)u^2 - \left(\bar{k}_{e,\uparrow} + 1\right)\left(k_{\bar{k},\downarrow} - 1\right)v^2}{\left(\bar{k}_{e,\uparrow} + 1\right)\left(\bar{k}_{h,\downarrow} + 1\right)u^2 - \left(1 - \bar{k}_{e,\uparrow}\right)\left(1 - \bar{k}_{h,\downarrow}\right)v^2}, \tag{1.88}$$

$$r_{eh}^{\uparrow} = \frac{4\bar{k}_{e,\uparrow}uv}{\left(\bar{k}_{e,\uparrow} + 1\right)\left(\bar{k}_{h,\downarrow} + 1\right)u^2 - \left(1 - \bar{k}_{e,\uparrow}\right)\left(1 - \bar{k}_{h,\downarrow}\right)v^2}. \tag{1.89}$$

In the above expression we ignored terms of the order $\frac{E}{\mu}$ and introduced the normalized wave vectors

$$\bar{k}_{e,\sigma/h,-\sigma} = \frac{k_{e,\sigma/h,-\sigma}}{k_{F,x}} \approx \sqrt{1 \pm \bar{h}} \tag{1.90}$$

with $\bar{h} = \frac{h}{\mu \cos^2 \vartheta}$. The coefficients in case of an incident electron of opposite spin are obtained from the ones above by substituting $\uparrow \leftrightarrow \downarrow$. For vanishing exchange field $\bar{k}_{e,\uparrow} = \bar{k}_{h,\downarrow} = 1$ and the normal reflection amplitude $r_{ee} = 0$, so clearly the exchange splitting introduces normal reflection to the system. The probabilities for the Andreev and normal reflection are

$$R_{eh}^{\sigma} = \frac{\bar{k}_{h,-\sigma}}{\bar{k}_{e,\sigma}}|r_{eh}^{\sigma}|^2 \text{ and } R_{ee}^{\sigma} = |r_{ee}^{\sigma}|^2, \tag{1.91}$$

respectively. Note that the prefactor of the Andreev reflection probability accounts for the different group velocities of electron and hole solutions in the ferromagnet. As for the N/S interface we can calculate the differential conductivity of the interface by using the extension of the BTK formula to the spin-full case. The differential conductance for a single mode in the case of direct incidence $k_{F,x} = k_F$ is given by [21, 94]

$$\frac{G_{FS}}{G_{NN}}(eV) = \frac{1}{2}\sum_{\sigma}\left(1 + R^{\sigma}_{eh}(eV) - R^{\sigma}_{ee}(eV)\right) \tag{1.92}$$

where we have normalized it by the normal state conductance. The conductivity for small bias voltage and different values of the exchange field is shown in Fig. 1.9 b), and is clearly reduced compared to the zero field case.

1.3.2 S/F/S junction and current reversal

We will now study the reversal of the critical Josephson current due to the presence of the exchange field, which is usually called a 0-π transition. The name refers to the change of the ground state of the system that is found by minimizing the Free energy with respect to the phase difference φ between the superconductors, as previously shown in Sec. 1.2.2.

For the S/N/S junction, the minimum of the Free energy is always at $\varphi = 0$ and such junction are called 0-junctions. In a S/F/S junction the ferromagnet introduces a difference of the wave vectors between spin-up and spin-down quasiparticles, corresponding to a new magnetic length scale on which quasiparticle wave functions from different spin sectors oscillate and interfere. From another point of view this is the equivalent to oscillations of the pair correlations that penetrate the ferromagnet from the superconductors. Depending on the length of the junction and the strength of the exchange field these oscillations can result in a additional π phase-shift between the ground state wave functions of the two superconducting leads. Consequently the global minimum of the Free energy of the system will shift from 0 to π as function of φ. According to the thermodynamical relation Eq. (1.60) such a shift will result in a reversal of the critical current.

Let us go back to the microscopic picture where a Cooper pair from the condensate on one side of the junction absorbs a incoming hole, simultaneously releasing an electron into the normal region (see Fig. 1.6). For the bound state formation there are now four distinct possibilities, we can start an electron or hole in the left, either in a spin up or spin down state. Constructing the wave functions for the possible bound states, only considering Andreev reflection processes for simplicity (Andreev approximation), gives the following condition for bound state energies of a SFS junction,

$$E = \pm\frac{\hbar v_F}{d}\left(\frac{\varphi}{2} \pm \arccos\frac{E}{|\Delta|} + \pi n\right) - \sigma h; \quad n \in \mathbb{Z}. \tag{1.93}$$

If the exchange field/Zeeman splitting is of the same magnitude as the excitation energy, for a short junction $(d \to 0)$ we can neglect it and we obtain the result for a clean S-N-S junction. If the excitation energies around the gap energy and $\Delta \ll h$, for short junctions when $\frac{L}{\xi_0} \to 0$ the term $\frac{LE}{\hbar v_F}$ goes much faster to zero than $\frac{Lh}{\hbar v_F}$ and we can set the lefthand side of Eq.(1.93) to zero. The resulting four branches of the bound state energies are

$$E = \pm\Delta\cos\left(\frac{\varphi + \sigma\eta}{2}\right) \text{ where } \eta = \frac{2hL}{\hbar v_F} = \frac{2L}{\xi_h} \tag{1.94}$$

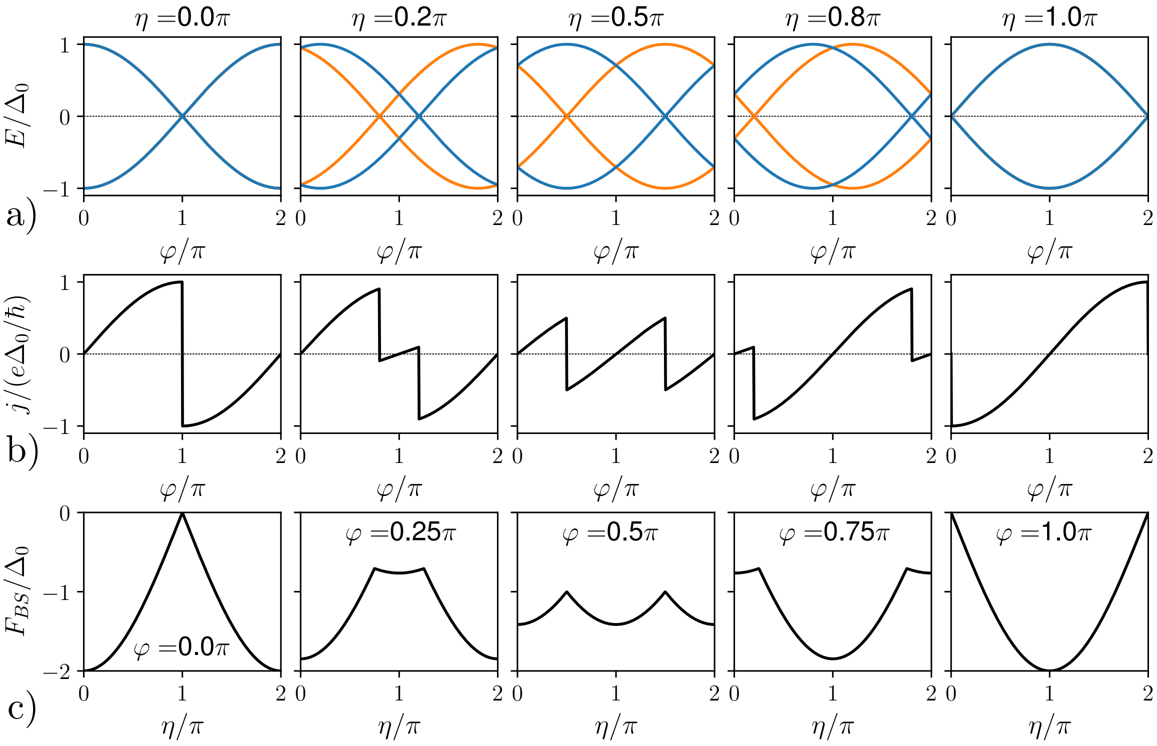

FIGURE 1.10: Panel a) shows Andreev bound state spectra and panel b) the Josephson current as function of the phase difference φ for different values of junction lengths L with respect to the magnetic decay length ξ_h. From left to right the junction changes its ground state from a 0-state to a π-state. Panel c) shows the contribution of the Andreev bound states to the Free energy of the system as function of η varying φ from left to right. All plots are for temperature $T = 0$.

and we introduced the ballistic magnetic decay length ξ_h.

The exchange field in the intermediate region causes a spin dependent phase shift of the bound state energies by η with respect to φ as shown in Fig. 1.10 a). Calculating the Josephson current from these gives

$$j = \frac{e\Delta}{\hbar} \sum_{\sigma} \tanh\left[\frac{\Delta\beta}{2} \cos\left(\frac{\varphi + \sigma\eta}{2}\right)\right] \sin\left(\frac{\varphi + \sigma\eta}{2}\right) \tag{1.95}$$

which is depicted in Fig. 1.10 b) for different values of η. There we also plot the free energy contribution from the bound states F_{BS} as function of the phase shift η for different values of φ. Clearly, the global minimum of the free energy shifts from $\varphi = 0$ to $\varphi = \pi$ when η approaches π, which is accompanied by a reversal of the current phase relationship. Comparing the energy of the 0-state with the energy of the π-state in Fig. 1.10 c) one can deduce that the π state is the ground state of the system whenever $\pi/2 < |\eta \mod 2\pi| < 3/2\pi$, thus in principle we get a repeated switching of the current by increasing the exchange interaction continuously. We need to keep in mind though that due to introduced approximations we neglected the normal scattering which is strongly enhanced by increasing the exchange field, and therefore will lower the critical Josephson current.

1.4 Quasi-classical theory for superconducting systems

In this section we derive quasi-classic transport like (Boltzman-like) equations for superconducting systems with linear in momentum spin-orbit coupling fields. We start from the Gor'kov equations and include spin-orbit coupling by a SU(2) gauge covariant formulation of the latter. In contrast to the Bogoliubov-de Gennes formalism, the quasi-classical equations can be extended to describe disorder, however they are not suited to deal with inhomogeneous systems straightaway. We simplify them using the fact that in conventional superconducting systems, the typical excitation energies are very small against the Fermi energy, which leads us to the Eilenberger equation. The Eilenberger equation can be further simplified in the so-called dirty limit, when the mean free path of the system is much smaller then the coherence length. Collisions between quasiparticles are so frequent that the system appears to be almost isotropic in momentum space. Thus the Green's function of the system has only a weak dependence on the momentum direction, which leads us to the Usadel equation.

1.4.1 Quantum phase space dynamics and Wigner transformation

In classical many-particle physics the Boltzmann equation describes the dynamics of the phase-space distribution function $f(\mathbf{r}, \mathbf{p}, t)$. In quantum mechanics, the coordinates $\mathbf{r}$ and $\mathbf{p}$ are replaced by hermitian operators which have to obey the Heisenberg uncertainty principle and are thus not known exactly simultanously. To obtain a phase-space like formulation of many body quantum mechanics it is necessary to determine the quantum mechanical correspondent object to the phase-space distribution function. We will now link the Green's functions to the so-called Wigner function which is obtained by a mixed coordinate Fourier transformation. Here, we demonstrate that the Wigner function shows some similarities to a particle density in phase space, which will motivate the Wigner transformation of the Gor'kov equation in the following sections.

We start from the lesser Green's function $G^{<}(\xi_1, \xi_2) = i\langle \psi^{\dagger}(\mathbf{x}_2, t_2)\, \psi(\mathbf{x}_1, t_1)\rangle$ which describes the probability amplitude for a particle to be found at point ξ_1 when initially at ξ_2. To change to a momentum space representation of the Green's function we have to perform a Fourier transformation for the field operators, that is defined in the standart way

$$\Psi(\mathbf{p}_i, \omega_i) = \int d\mathbf{x}_i \int dt_i e^{i(\omega_i t_i - \mathbf{p}_i \mathbf{x}_i/\hbar)} \Psi(\mathbf{x}_i, t_i). \tag{1.96}$$

Analogous we define mixed coordinate Fourier transformations within a center of mass coordinate system where

$$\mathbf{x}_{1,2} = \mathbf{x} \pm \frac{\mathbf{r}}{2}, t_{1,2} = T \pm \frac{t}{2} \tag{1.97}$$

Applying a Fourier transform with respect to the relative coordinates,

$$G^{<}(\mathbf{p}, \omega, \mathbf{x}, T) = \int d\mathbf{r} \int dt e^{-i\mathbf{p}\mathbf{r}/\hbar} e^{i\omega t} G^{<}(\mathbf{r}, t, \mathbf{x}, T) \tag{1.98}$$

and defining the Wigner function as

$$f(\mathbf{p},\omega,\mathbf{x},T) = -iG^{<}(\mathbf{p},\omega,\mathbf{x},T) \tag{1.99}$$

it follows that

$$\int \frac{d\omega}{2\pi} \int \frac{d\mathbf{p}}{(2\pi\hbar)^d} f(\mathbf{p},\Omega,\mathbf{x},T) = -i\mathbf{G}^{<}(\mathbf{r}=0,t=0,\mathbf{x},T) = \langle \psi^\dagger(\mathbf{x},T)\,\psi(\mathbf{x},T)\rangle \tag{1.100}$$

which is the particle density. Furthermore

$$\begin{aligned}\int \frac{d\omega}{2\pi} \int d\mathbf{x} f(\mathbf{p},\omega,\mathbf{x},T) &= -i\int d\mathbf{x}\int d\mathbf{r} e^{-i\mathbf{p}\mathbf{r}/\hbar} G^{<}(\mathbf{r},t=0,\mathbf{x},T)\\ &= \int d\mathbf{x}\int d\mathbf{r} e^{-i\mathbf{p}\mathbf{r}/\hbar}\left\langle \psi^\dagger\left(\mathbf{x}-\frac{\mathbf{r}}{2},T\right)\psi\left(\mathbf{x}+\frac{\mathbf{r}}{2},T\right)\right\rangle\\ &= \int d\mathbf{x}_1\int d\mathbf{x}_2 e^{-i\mathbf{p}(\mathbf{x}_1-\mathbf{x}_2)/\hbar}\left\langle \psi^\dagger(\mathbf{x}_2,T)\,\psi(\mathbf{x}_1,T)\right\rangle\\ &= \langle \psi^\dagger(\mathbf{p},T)\,\psi(\mathbf{p},T)\rangle \end{aligned} \tag{1.101}$$

which is the particle density in momentum space. This suggests the interpretation as phase space distribution. However, the defined quantity can be negative in contrast to the classical phase space distribution function, thus this analogy is not fully true.

Our goal is to derive a transport-like equation for the quantum analogon of the phase space distribution, but unlike in the above example, we want to keep the time dependence intact. Therefore we apply the mixed coordinate Fourier transformation with respect to the relative spatial difference $\mathbf{r}$, which is referred to as Wigner transformation [95, 96]. As an example, the Wigner transformed lesser Green-Gor'kov Eq.(1.30) reads

$$\mathbf{G}(\mathbf{p},\mathbf{x},t_1,t_2) = \int d\mathbf{r} e^{-i\mathbf{p}\mathbf{r}/\hbar}\mathbf{G}(\mathbf{r},\mathbf{x},t_1,t_2). \tag{1.102}$$

1.4.2 Gradient expansion and quasi-classical transport equation

We now derive the quasi-classical transport equation from an quasi-classical expansion of the Wigner transformed Green-Gor'kov equation. The Wigner transformed Gor'kov Eq. (1.36) reads (unaltered variables are not repeated)

$$\left[i\hbar\tau_3\partial_{t_1} - \boldsymbol{\xi}\left(\mathbf{p}-\frac{i\hbar}{2}\partial_{\mathbf{x}}\right) + \boldsymbol{\Delta}\left(\mathbf{x}+\frac{i\hbar}{2}\partial_{\mathbf{p}}\right)\right]\mathbf{G}(\mathbf{p},\mathbf{x}) = \delta(t_1,t_2). \tag{1.103}$$

This implies that the Wigner transformation is implying transformation of the operators $\hat{\mathbf{p}} \to \mathbf{p} - i\hbar\partial_{\mathbf{x}}/2$ and $\hat{\mathbf{x}} \to \mathbf{x} + i\hbar\partial_{\mathbf{p}}/2$ which is called a Bopp-substitution [96]. For the other Gor'kov equation where the operators act on the second variable we have

$$\mathbf{G}(\mathbf{p},\mathbf{x})\left[-i\hbar\tau_3\partial_{t_2}^\dagger - \boldsymbol{\xi}\left(\mathbf{p}+\frac{i\hbar}{2}\partial_{\mathbf{x}}\right) + \boldsymbol{\Delta}\left(\mathbf{x}-\frac{i\hbar}{2}\partial_{\mathbf{p}}\right)\right] = \delta(t_1,t_2). \tag{1.104}$$

We now perform a quasi-classical expansion of the two equations, i.e. an expansion up to first order in $\hbar/(p_c x_c)$ with p_c and x_c as the characteristic momentum and characteristic length scale of the system. The characteristic momentum of the superconductor is the Fermi momentum p_F and the characteristic length scale is the coherence length ξ_0. Therefore the quasi-classical expansion is valid under the condition

$$\frac{\hbar}{p_F \xi_0} \sim \frac{\Delta}{E_F} \ll 1 \tag{1.105}$$

which is the case in conventional superconductors where the gap energy is usually much smaller then the Fermi energy. Expanding up to first order yields the following two equations,

$$\left[i\hbar\tau_3\partial_{t_1} - \boldsymbol{\xi} + \boldsymbol{\Delta}\right]\mathbf{G}\left(\mathbf{p},\mathbf{x}\right) + \frac{i\hbar}{2}\partial_{\mathbf{p}}\boldsymbol{\xi}\;\partial_{\mathbf{x}}\mathbf{G}\left(\mathbf{p},\mathbf{x}\right) + \frac{i\hbar}{2}\partial_{\mathbf{x}}\boldsymbol{\Delta}\;\partial_{\mathbf{p}}\mathbf{G}\left(\mathbf{p},\mathbf{x}\right) \approx \delta(t_1,t_2), \tag{1.106}$$

$$\mathbf{G}\left(\mathbf{p},\mathbf{x}\right)\left[-i\hbar\tau_3\partial_{t_2}^{\dagger} - \boldsymbol{\xi} + \boldsymbol{\Delta}\right] - \frac{i\hbar}{2}\partial_{\mathbf{x}}\mathbf{G}\left(\mathbf{p},\mathbf{x}\right)\partial_{\mathbf{p}}\boldsymbol{\xi} - \frac{i\hbar}{2}\partial_{\mathbf{p}}\mathbf{G}\left(\mathbf{p},\mathbf{x}\right)\partial_{\mathbf{x}}\boldsymbol{\Delta} \approx \delta(t_1,t_2). \tag{1.107}$$

The transport like equation is obtained by subtracting Eqs.(1.106) and (1.107) which gives

$$i\hbar\left(\tau_3\partial_{t_1}\mathbf{G} + \partial_{t_2}\mathbf{G}\tau_3\right) + \frac{i\hbar}{2}\left\{\partial_{\mathbf{p}}\boldsymbol{\xi}, \partial_{\mathbf{x}}\mathbf{G}\right\} - \left[\boldsymbol{\xi} - \boldsymbol{\Delta}, \mathbf{G}\right] + \frac{i\hbar}{2}\left\{\partial_{\mathbf{x}}\boldsymbol{\Delta}, \partial_{\mathbf{p}}\mathbf{G}\right\} = 0. \tag{1.108}$$

This equation together with the sum of Eqs. (1.106) and (1.107) are the starting point of quasi-classical transport theory in superconductors. An convenient and equivalent way to obtain these expressions is by using the Moyal product [97], also referred to as gradient expansion. We denote the Wigner transform of some operator convolution as $W[A \circ B]$ then

$$W\left[\mathbf{G}_0^{-1} \circ \mathbf{G}\right] = \mathbf{G}_0^{-1}\left(\mathbf{p},\mathbf{x}\right) \star \mathbf{G}\left(\mathbf{p},\mathbf{x}\right) \tag{1.109}$$

where the Moyal product is defined as

$$\star := \exp\left(-\frac{i}{2\hbar}\left(\partial_{\mathbf{p}}^{\dagger}\partial_{\mathbf{x}} - \partial_{\mathbf{x}}^{\dagger}\partial_{\mathbf{p}}\right)\right). \tag{1.110}$$

This formula is valid for any product of operators and we will use it in the following section, where we generalize the obtained transport Eq. (1.108) to include interactions with spin fields.

1.4.3 Gauge covariant Gor'kov equation

In this section we obtain the gauge covariant formulation of the Gor'kov equation with respect to local U(1) and SU(2) gauge transformations. The corresponding gauge fields can be interpreted as coupling to electromagnetic and spin-fields respectively. This will allow us to extend the transport formalism from Sec. 1.4.2 to matter-field interactions.

The Hamiltonian $\mathcal{H}_{\text{BCS}}$ is invariant under local U(1) and SU(2) gauge transformations which are equivalent to a local change of phase by $\alpha(x)$ where x is some spacetime point:

$$\Psi(x) \mapsto e^{i\alpha(x)}\Psi(x); \quad \Psi^\dagger(x) \mapsto e^{-i\alpha(x)}\Psi^\dagger(x), \tag{1.111}$$

or a local spin rotation around the axis $\mathbf{n}(x)$ by angle $\beta(x)$:

$$\Psi(x) \mapsto e^{i\mathbf{n}\boldsymbol{\sigma}\beta}\Psi(x); \quad \Psi^\dagger(x) \mapsto \Psi^\dagger(x)e^{-i\mathbf{n}\boldsymbol{\sigma}\beta}. \tag{1.112}$$

The superconducting interaction part $\mathcal{H}_{\text{BCS}}$ of the Hamiltonian contains pairs of daggered and undaggered operators, thus the U(1) invariance is easy to show. For the SU(2) invariance we assume that the rotation in spin space can be decomposed into subsequent rotations

$$e^{i\mathbf{n}\boldsymbol{\sigma}\beta} = e^{i\sigma_1 X(\beta)}e^{i\sigma_2 Y(\beta)}e^{i\sigma_3 Z(\beta)} \tag{1.113}$$

with some functions X, Y, Z to be determined. With this the terms in $\mathcal{H}_{\text{BCS}}$ transform like

$$\left(\Psi^T i\sigma_2\Psi\right) \mapsto \left(\Psi^T e^{i\sigma_3 Z(\beta)}e^{-i\sigma_2 Y(\beta)}e^{i\sigma_1 X(\beta)}i\sigma_2 e^{i\sigma_3 Z(\beta)}e^{i\sigma_2 Y(\beta)}e^{i\sigma_1 X(\beta)}\Psi\right) = \left(\Psi^T i\sigma_2\Psi\right) \tag{1.114}$$

and the gauge invariance is demonstrated.

We will here generically denote gauge transformations as mappings with the unitary operator $U(\xi)$ in the case of an Abelian, as well as non-Abelian gauge field. Under a gauge transformation the field operator transform like $\Psi(\xi) \mapsto U(\xi)\Psi(\xi), \ \Psi^\dagger(\xi) \mapsto U(\xi)^\dagger\Psi^\dagger(\xi)$ and consequently the Green Gor'kov matrix equation transforms as

$$\mathbf{G}\left(\xi_1, \xi_2\right) \mapsto \mathbf{U}(\xi_1)\mathbf{G}\left(\xi_1, \xi_2\right)\mathbf{U}^\dagger(\xi_2); \text{ with } \mathbf{U}(\xi) = \begin{pmatrix} U(\xi) & 0 \\ 0 & \mathcal{T}U(\xi)\mathcal{T}^{-1} \end{pmatrix}. \tag{1.115}$$

Inserting the gauge transformed Green-Gor'kov matrix into the Gor'kov equation, the differential operators in the Gor'kov equation will also act onto the local transformation $U(\xi)$. In order to make the Gor'kov equation gauge covariant we need to cancel the additional appearing terms. Therefore we define the covariant derivative $D\left(\xi\right) = \partial_\xi - iA(\xi)$ introducing a generic gauge field A which has to transform according to

$$\begin{aligned} &\Psi(\xi) \mapsto U(\xi)\Psi(\xi) \\ &A(\xi) \mapsto U(\xi)A(\xi)U^\dagger(\xi) + iU(\xi)\partial_\xi U(\xi)^\dagger. \end{aligned} \tag{1.116}$$

Then the covariant derivative transform like Ψ as the name suggest, i.e. $D\Psi \mapsto UD\Psi$ whenever $\Psi \mapsto U\Psi$.

Following this prescription we obtain the gauge-covariant Gor'kov equation

$$\mathbf{G}_0^{-1}(\xi_1)\mathbf{G}\left(\xi_1, \xi_2\right) = \delta\left(\xi_1 - \xi_2\right) \tag{1.117}$$

with the covariantly defined operator

$$\mathbf{G}_0^{-1} = i\hbar\tau_3\mathbf{D}_0(\xi) - \boldsymbol{\xi}\left(-i\hbar\mathbf{D}_i(\xi)\right) + \boldsymbol{\Delta}(\xi) \tag{1.118}$$

where

$$\mathbf{D}_\mu = \partial_\mu - i\begin{pmatrix} \mathcal{A}_\mu & 0 \\ 0 & \mathcal{T}\mathcal{A}_\mu\mathcal{T}^{-1} \end{pmatrix} = \partial_\mu - i\mathbf{A}_\mu \tag{1.119}$$

with time-like ($\mu = 0 = t$) and space-like ($\mu = x, y, z$) covariant operators and we defined the gauge-potential $\mathbf{A}_\mu = (\mathbf{A}_0, \mathbf{A})$ in the Nambu-spin space. For the anticipated quasi-classical transport equation we also need the Gor'kov equation where the differential operator is acting on ξ_2,

$$\mathbf{G}(\xi_1, \xi_2)\left[\mathbf{G}_0^{-1}(\xi_2)\right]^\dagger = \delta(\xi_1 - \xi_2) \tag{1.120}$$

with

$$\left[\mathbf{G}_0^{-1}(\xi)\right]^\dagger = -i\hbar\tau_3\mathbf{D}_0^\dagger(\xi) - \boldsymbol{\xi}\left(-i\hbar\mathbf{D}_i^\dagger(\xi)\right) + \boldsymbol{\Delta}(\xi)\,. \tag{1.121}$$

Resulting charge and current densities

The gauge covariant reformulation introduces couplings to gauge fields which will alter the conserved quantities in our system, the charge and current densities which we will now determine. The action S of our system is

$$S[\boldsymbol{\psi}, A_\mu] = \int d\xi \boldsymbol{\psi}^\dagger\left[i\hbar\tau_3\mathbf{D}_0(\xi) - \boldsymbol{\xi}\left(-i\hbar\mathbf{D}_i(\xi)\right) + \boldsymbol{\Delta}(\xi)\right]\boldsymbol{\psi} \text{ where } \boldsymbol{\psi} = \begin{pmatrix} \Psi \\ \mathcal{T}\Psi \end{pmatrix} \tag{1.122}$$

is a spinor in Nambu-Spin space in accordance with the defined basis of the Green-Gor'kov matrix Eq.(1.30). Note that we sum over repeated indices. Varying the action after the field operators results in the covariant equation of motion for the field operators, the Gor'kov Eqs. (1.117)- (1.120). The charge and current densities are obtained varying the action of our system after the new dynamical variables of the system, the gauge fields. The gauge fields in the covariant derivatives $\mathcal{A}_\mu$ appear always with their time reverse $\mathcal{T}\mathcal{A}_\mu\mathcal{T}^{-1}$. For each component of the gauge fields there exist only two possibilities for their behavior under time-reversal $\mathcal{T}\mathcal{A}_\mu\mathcal{T}^{-1} = \pm\mathcal{A}_\mu$, either they are even or odd. If we deal with a Abelian U(1) gauge field describing electromagnetism, the space- and time-like components of the field are even under time reversal. On the other hand for a non-Abelian SU(2) gauge field describing spin fields, the space and time-like components of the field are odd under time reversal. Other cases will not be of relevance in the following.

We expand the matrix $\mathcal{A}_\mu$ as

$$\mathcal{A}_\mu = g\mathcal{A}_\mu^a\gamma^a \tag{1.123}$$

where g is the charge associated to the corresponding gauge field and γ^a are matrices that reflect the degree of freedom for this type of charge. For electromagnetic fields the charge $g = -e$ and has no internal degree of freedom thus $\gamma^a = \delta^{a1}$ (we could have defined any index to be "the one" here). For the SU(2) case we keep g to denote the SU(2) coupling constant and we have $\gamma^a = \sigma^a$. With the above expansion, variation after time like components gives

$$j_0^a = \frac{\delta S}{\delta \mathcal{A}_0^a} = g\boldsymbol{\psi}^\dagger \boldsymbol{\gamma}^a \boldsymbol{\psi} \;\; \text{with} \;\; \boldsymbol{\gamma}^a = \begin{pmatrix} \gamma^a & 0 \\ 0 & \mathcal{T}\gamma^a\mathcal{T}^{-1} \end{pmatrix}. \tag{1.124}$$

Repeating the procedure for the space like components assuming only quadratic terms in the dispersion $\boldsymbol{\xi}(\mathbf{p}) = \frac{p^2}{2m}$ gives

$$j_i^a = \frac{\delta S}{\delta \mathcal{A}_i^a} = -i\frac{g\hbar}{2m}\boldsymbol{\psi}^\dagger \left(\boldsymbol{\gamma}^a \mathbf{D}_i - \mathbf{D}_i^\dagger \boldsymbol{\gamma}^a\right)\boldsymbol{\psi} \tag{1.125}$$

One can show that these defined densities and current densities fulfill the covariant continuity equation [98]

$$\mathbf{D}_t \mathbf{j}_0 + \mathbf{D}_i \mathbf{j}_i = 0. \tag{1.126}$$

The expectation value of the densities (1.124) and (1.124) can be linked to the components of the Green-Gor'kov matrix. Taking into account all the possible parity combinations with respect to time reversal symmetry of the gauge fields, we define

$$\rho_e(\mathbf{x}, t) = \frac{ie\hbar}{2} \lim_{\mathbf{x}' \to \mathbf{x}} \operatorname{Tr}\left[\mathbf{G}(\mathbf{x}, \mathbf{x}', t, t + 0^+)\right] \tag{1.127}$$

$$j_i(\mathbf{x}, t) = -e\frac{\hbar^2}{4m} \lim_{\mathbf{x}' \to \mathbf{x}} \operatorname{Tr}\left[\tau_3 \mathbf{D}_i(\mathbf{x})\mathbf{G}(\mathbf{x}, \mathbf{x}', t, t + 0^+) - \mathbf{G}(\mathbf{x}, \mathbf{x}', t, t + 0^+)\mathbf{D}_i^\dagger(\mathbf{x}')\tau_3\right] \tag{1.128}$$

as the electric charge density and charge current density and

$$\rho_s^a(\mathbf{x}, t) = -\frac{ig\hbar}{4} \lim_{\mathbf{x}' \to \mathbf{x}} \operatorname{Tr}\left[\tau_3 \sigma^a \mathbf{G}(\mathbf{x}, \mathbf{x}', t, t + 0^+)\right] =: s^a(\mathbf{r}, t) \tag{1.129}$$

$$j_i^a(\mathbf{x}, t) = \frac{g\hbar}{8m} \lim_{\mathbf{x}' \to \mathbf{x}} \operatorname{Tr}\left[\sigma^a \mathbf{D}_i(\mathbf{x})\mathbf{G}(\mathbf{x}, \mathbf{x}', t, t + 0^+) - \mathbf{G}(\mathbf{x}, \mathbf{x}', t, t + 0^+)\mathbf{D}_i^\dagger(\mathbf{x}')\sigma^a\right] \tag{1.130}$$

for the spin and spin current densities, where the trace is taken in Nambu and spin space. The observables now must be expressed in terms of the Wigner transformed Green's functions. We refer for that to Refs. [99, 100] and we continue with the derivation of the transport equation.

1.4.4 Gauge covariant quasi-classical equation

In the last section we extended the Gor'kov equation to the case when the charge carriers interact with electromagnetic or spin fields. In the next step we derive quasi-classical transport equations from these gauge-covariant equations. We generalize the Wigner transform to the gauge-covariant Wigner transform in the case of non-Abelian gauge fields and apply it to the Gor'kov equations.

Gauge covariant Wigner transformation

The gauge covariant Wigner transform has been introduced already quite some time ago in the eighties in high-energy physics to study quark-gluon plasma [101, 102]. Within the last decade it has been rediscovered in order to describe spin interactions in normal [99] and superconducting systems [32, 100]. To motivate it we start from the previously introduced Wigner representation (see Eq. (1.98)) of the Green-Gor'kov matrix

$$\mathbf{G}\left(\mathbf{p},\mathbf{x},\omega,T\right)=\int dt d\mathbf{r} e^{i(\omega t-\mathbf{p}\mathbf{r}/\hbar)}\mathbf{G}\left(\mathbf{x}+\frac{\mathbf{r}}{2},\mathbf{x}-\frac{\mathbf{r}}{2},T+\frac{t}{2},T-\frac{t}{2}\right). \tag{1.131}$$

Equivalently we can rewrite the transformed Green's function using translation operators

$$\mathbf{G}\left(\mathbf{p},\mathbf{x},\omega,T\right)=\int d\mathbf{r} e^{i(\omega t-\mathbf{p}\mathbf{r}/\hbar)/2}e^{(t\partial_T+\mathbf{r}\partial_\mathbf{x})/2}\mathbf{G}\left(\mathbf{x},\mathbf{x},T,T\right)e^{-\left(t\partial_T^\dagger+\mathbf{r}\partial_\mathbf{x}^\dagger\right)/2} \tag{1.132}$$

where $\partial_i, \partial_i^\dagger$ - operators act on the first field operator to the right, left respectively. Under a U(1) or SU(2) gauge transformations of Eq. (1.131), exponentials will appear at different space-time points and are not compensated, thus the above Wigner transformed Green's function does not transform covariantly. However, the equivalent definition Eq. (1.132) indicates that the covariant transform can be obtained by substituting the normal derivatives in the translational operators by covariant ones. We define the covariant generalization of the Wigner representation

$$\mathbf{G}\left(\mathbf{p},\mathbf{x},\omega,T\right)=\int d\mathbf{r} e^{i(\omega t-\mathbf{p}\mathbf{r}/\hbar)}e^{(t\mathbf{D}_T+\mathbf{r}\mathbf{D}_\mathbf{x})/2}\mathbf{G}\left(\mathbf{x},\mathbf{x},T,T\right)e^{-\left(t\mathbf{D}_T^\dagger+\mathbf{r}\mathbf{D}_\mathbf{x}^\dagger\right)/2} \tag{1.133}$$

with $\mathbf{D}_\mu^{(\dagger)}=\partial_\mu\mp i\frac{\mathbf{A}_\mu}{\hbar}$ where the un-/daggered operators act on the first field to their right, left respectively.

The covariant generalization of the Wigner transformation with respect to SU(2) gauge transformations Eq. (1.102) follows directly from the Eq. (1.133) by only including space-like transformations. Using the relationship [101]

$$e^{\mathbf{r}\mathbf{D}_\mathbf{x}/2}\Psi(\mathbf{x})=\mathbf{W}\left(\mathbf{x},\mathbf{x}+\mathbf{r}/2\right)\Psi(\mathbf{x}+\mathbf{r}/2) \tag{1.134}$$

we can rewrite the definition of the gauge covariant Wigner transform as

$$\mathbf{G}\left(\mathbf{p},\mathbf{x}\right)=\int d\mathbf{r} e^{-i\mathbf{p}\mathbf{r}/\hbar}\mathbf{W}\left(\mathbf{x},\mathbf{x}+\frac{\mathbf{r}}{2}\right)\mathbf{G}\left(\mathbf{x}+\frac{\mathbf{r}}{2},\mathbf{x}-\frac{\mathbf{r}}{2}\right)\mathbf{W}\left(\mathbf{x}-\frac{\mathbf{r}}{2},\mathbf{x}\right), \tag{1.135}$$

where we introduced the parallel transport/Wilson link operator

$$\mathbf{W}\left(\mathbf{b},\mathbf{a}\right)=P\exp\left(i\int_\mathbf{a}^\mathbf{b}d\mathbf{z}\mathbf{A}\left(\mathbf{z}\right)\right)=P\exp\left(i\int_0^1 ds\left[\left(\mathbf{b}-\mathbf{a}\right)\mathbf{A}\left(s\right)\right]\right), \tag{1.136}$$

with P the path ordering operator and the path of the integration $\mathbf{z}(s)$ is along the straight line between endpoints $\mathbf{z}\left(s\right)=\mathbf{a}+\left(\mathbf{b}-\mathbf{a}\right)s,\quad s\in\left[0,1\right]$. This expression transforms locally covariantly under SU(2) rotations $\mathbf{U}\left(\mathbf{x}\right)$

$$\mathbf{G}\left(\mathbf{p},\mathbf{x}\right)\mapsto\mathbf{U}\left(\mathbf{x}\right)\mathbf{G}\left(\mathbf{p},\mathbf{x}\right)\mathbf{U}^{\dagger}\left(\mathbf{x}\right). \tag{1.137}$$

thanks to the action of the Wilson link operators that connect the positions of the field operators with the center of mass coordinates.

Gauge covariant transport like equation

All the components that we used to derive the transport like Eq.(1.108) are now defined covariantly. From here on we can now follow through the steps as we did for the case of vanishing fields to include a linear in momentum spin-orbit coupling. We have to change to the generalized Wigner representation Eq.(1.133) of the gauge covariant Gor'kov equations and then perform a quasi-classical expansion. The detailed derivation involves lengthy differential geometric proofs as shown in [100–102].

We will here take a short cut by deriving the desired quasi-classical equation in the case of homogeneous fields as done in in Ref. [32]. It is easier to follow and can be generalized to the case of non-homogeneous fields at the end of the calculation. As for the case with no gauge fields we Wigner transform the gauge covariant Gor'kov Eq.(1.36) and its conjugate in the space coordinates and expand up to first order in gradients which gives

$$\mathbf{G}_0^{-1}\left(\mathbf{p},\mathbf{x}\right)\star\mathbf{G}\left(\mathbf{p},\mathbf{x}\right)\approx\mathbf{G}_0^{-1}\mathbf{G}-\frac{i\hbar}{2}\left(\partial_{\mathbf{p}}\mathbf{G}_0^{-1}\partial_{\mathbf{x}}\mathbf{G}-\partial_{\mathbf{x}}\mathbf{G}_0^{-1}\partial_{\mathbf{p}}\mathbf{G}\right) \tag{1.138}$$

$$\mathbf{G}\left(\mathbf{p},x\right)\star\left[\mathbf{G}_0^{-1}\left(\mathbf{p},\mathbf{x}\right)\right]^{\dagger}\approx\mathbf{G}\left[\mathbf{G}_0^{-1}\right]^{\dagger}-\frac{i\hbar}{2}\left(\partial_{\mathbf{p}}\mathbf{G}\partial_{\mathbf{x}}\left[\mathbf{G}_0^{-1}\right]^{\dagger}-\partial_{\mathbf{x}}\mathbf{G}\partial_{\mathbf{p}}\left[\mathbf{G}_0^{-1}\right]^{\dagger}\right). \tag{1.139}$$

The quasi-classical transport equation is obtained by subtracting both equations giving

$$i\hbar\left(\tau_3\partial_{t_1}\mathbf{G}+\partial_{t_2}\mathbf{G}\tau_3\right)+\frac{i\hbar}{2m}\left\{\mathbf{p}-\mathbf{A},\partial_{\mathbf{x}}\mathbf{G}\right\}+\left[\tau_3A_0+\frac{\mathbf{pA}}{m}+\check{\Delta}+\check{\Sigma},\mathbf{G}\right]=0, \tag{1.140}$$

where we assumed a spatially constant order parameter $\check{\Delta}$, and used that $\mathbf{p}$, $\mathbf{A}^2\propto\mathbb{1}$. Note that we also extended the free propagator by self energy term $\check{\Sigma}$ that will allow us to introduce disorder to the system.

This equation is not gauge covariant as we used the usual Wigner transform. To change to the full gauge covariant picture, we can use the relation between the gauge covariantly transformed and usual Green's function (1.135) which gets drastically simplified in the case of homogeneous fields, as the Wilson link operators $\mathbf{W}$ are then matrix exponentials of the SU(2) gauge fields $\mathbf{W}(\mathbf{x}_1,\mathbf{x}_2)=\exp(i/2\cdot(\mathbf{x}_1-\mathbf{x}_2)\,\mathbf{A})$, thus

$$\tilde{\mathbf{G}}=e^{\mathbf{A}\partial_{\mathbf{p}}/2}\check{\mathbf{G}}e^{\mathbf{A}\partial_{\mathbf{p}}^{\dagger}/2} \tag{1.141}$$

Here we introduced the gauge covariantly transformed Green's function $\tilde{\mathbf{G}}$. Substituting this relation into Eq.(1.140), expanding the shift operators and keeping only terms up to first order in gradients and second order in fields $\mathcal{A}_k$ gives the following fully gauge covariant equation [32],

$$i\hbar\left(\tau_3\partial_{t_1}\tilde{\mathbf{G}}+\partial_{t_2}\tilde{\mathbf{G}}\tau_3\right)+\frac{i\hbar}{m}p_i\tilde{\nabla}_i\tilde{\mathbf{G}}+\left[\tau_3\mathcal{A}_0+\check{\Delta}+\check{\Sigma},\tilde{\mathbf{G}}\right]-\frac{i}{2\hbar}\left\{\tau_3\mathcal{F}_{0i}+\frac{p_i}{m}\mathcal{F}_{ij},\frac{\partial\tilde{\mathbf{G}}}{\partial p_j}\right\}=0 \tag{1.142}$$

where

$$\mathcal{F}_{0i}=-i\left[\mathcal{A}_0,\mathcal{A}_i\right],\ \mathcal{F}_{ij}=-i\left[\mathcal{A}_i,\mathcal{A}_j\right] \tag{1.143}$$

are the SU(2) field strength tensors and $\tilde{\nabla}_i\cdot=\partial_i\cdot-i\left[\cdot,\mathcal{A}_i\right]$ is the covariant derivative.

This equation is true for homogeneous fields, but let us add without proof that the case of spacially smoothly varying fields can be obtained by inserting the terms that contain space variations in the full expression of the SU(2) field tensor $\mathcal{F}_{\mu\nu}=\partial_\mu\mathcal{A}_\nu-\partial_\nu\mathcal{A}_\mu-i\left[\mathcal{A}_\mu,\mathcal{A}_\nu\right]$. We now have an fully gauge covariant equation where the SOC is included in terms of the covariant derivative and the field tensor$\mathcal{F}_{\mu\nu}$. The covariant derivative is linear in SOC fields and describes the momentum dependent spin precession due to the latter. The fourth term in Eq.(1.142) involving components of the field strength tensor involves higher orders in the SOC fields and leads to coupling between spin and charge degrees of freedom and the spin Hall effect.

1.4.5 Eilenberger equation

The transport equation for $\tilde{\mathbf{G}}\left(\mathbf{p}\right)$ derived in the previous section can be further simplified by recalling that within the BCS theory, superconductivity only takes place at very low temperatures. Therefore typical quasiparticle excitation energies are located within a very narrow energy window of the size $k_\mathrm{B}T_c$ around the Fermi energy where T_c is the critical temperature of the superconducting phase (in conventional superconductors $T_c/T_F\approx10^{-4}$). This motivates the definition of the quasiparticle energy integrated Green's function or so called ξ-integrated Green's function. Let us have a look at the integral $\int\frac{d^3p}{(2\pi\hbar)^3}\tilde{\mathbf{G}}\left(\mathbf{p}\right)$ which can be approximated in the following way

$$\int\frac{d^3p}{\left(2\pi\hbar\right)^3}\tilde{\mathbf{G}}\left(\mathbf{p}\right)=\int\frac{d\Omega_p}{4\pi}\int\frac{dpp^2}{2\pi^2\hbar^3}\tilde{\mathbf{G}}\left(\mathbf{p}\right)\approx\int\frac{d\Omega_p}{4\pi}\int\frac{dpp_F^2}{2\pi^2\hbar^3}\tilde{\mathbf{G}}\left(p,\mathbf{n}\right)=\int\frac{d\Omega_p}{4\pi}\mathcal{N}_0\int d\xi\tilde{\mathbf{G}}\left(\xi,\mathbf{n}\right) \tag{1.144}$$

where $\xi=v_F\left(p-p_F\right)$ is the linearized spectrum around the Fermi energy and $\mathcal{N}_0$ is the density of states at the Fermi level. In the last steps we assumed that the Green's function is peaked in a small window around the Fermi momentum. For small momenta we linearize the spectrum and we assume that the density of states is constant within a small window around the Fermi energy, thus we can pull it out of the integration. This motivates the definition of the ξ-integrated Green's function

$$\check{\mathbf{g}}\left(\mathbf{n},\mathbf{x}\right)=\frac{i}{\pi}\int d\xi\tilde{\mathbf{G}}\left(\xi,\mathbf{n}\right) \tag{1.145}$$

that now only depends on the Fermi momentum direction $\mathbf{n}$ and the center of mass (of course time as well in general). The prefactor is chosen for convenience in later explicit calculations of $\mathbf{g}$. The equation of motion for this simplified Green's function is the generalized Eilenberger equation [103]

$$i\hbar\left(\tau_3\partial_{t_1}\breve{\mathbf{g}}+\partial_{t_2}\breve{\mathbf{g}}\tau_3\right)+i\hbar v_F n_i\tilde{\nabla}_i\breve{\mathbf{g}}+\left[\tau_3\mathcal{A}_0+\check{\Delta},\breve{\mathbf{g}}\right]-\frac{i}{2\hbar m}\left\{n_i\mathcal{F}_{ij},\frac{\partial\breve{\mathbf{g}}}{\partial n_j}\right\}=-\left[\check{\Sigma},\breve{\mathbf{g}}\right] \tag{1.146}$$

which is directly obtained by ξ-integration of Eq.(1.142). The ξ integration of the self-energy term corresponds to the expression on the right hand side. If we assume elastic and isotropic scattering of randomly distributed non magnetic impurities, within the Born approximation the self energy is given by $\check{\Sigma}=i\hbar\langle\breve{\mathbf{g}}\rangle/(2\tau)$. Here τ is the scattering time, and $\langle\ldots\rangle$ is the angular average over quasiparticle momenta at the Fermi surface.

1.4.6 Usadel equation

We now turn to he diffusive limit of the quasi-classical transport equation, that applies in a dirty superconductor. A quasiparticle traveling through a dirty superconductor will frequently scatter of impurities and change its traveling direction. This frequent scattering into random directions leads to a direction averaging. For conventional/s-wave superconductors this justifies the assumption that the quasiparticle propagator will have only a weak direction dependence. We now obtain a closed equation of motion for the isotropic part of the Green's function $\breve{g}_0$, the Usadel equation.

We start from the Eilenberger equation in equilibrium [104, 105]

$$\hbar v_F n_i\tilde{\nabla}_i\breve{\mathbf{g}}+\left[\check{\Omega},\breve{\mathbf{g}}\right]-\frac{1}{2\hbar m}\left\{n_i\mathcal{F}_{ij},\frac{\partial\breve{\mathbf{g}}}{\partial n_j}\right\}=-\frac{\hbar}{2\tau}\left[\langle\breve{\mathbf{g}}\rangle,\breve{\mathbf{g}}\right] \tag{1.147}$$

where $\check{\Omega}=(\omega_n-i\mathcal{A}_0)-i\check{\Delta}$ with the Matsubara frequencies $\omega_n=(2n+1)\pi$.

As stated in Ref. [105], assuming that the scattering time τ is much smaller than any other characteristic timescale of our system, for an asymptotic expansion up to $\mathcal{O}(\tau^2)$ it is sufficient to include the first two moments (the s and p-wave part)

$$\breve{\mathbf{g}}\left(\mathbf{n}\right)\approx\breve{g}_0+n_k\breve{g}_k \tag{1.148}$$

with $\breve{g}_k\ll\breve{g}_0$. Taking the angular average of Eq. (1.147), as well as the angular average of Eq. (1.147) multiplied by n_i gives

$$\frac{\hbar v_F}{d}\tilde{\nabla}_i\breve{g}_i+\left[\check{\Omega},\breve{g}_0\right]=0 \tag{1.149}$$

$$\tau\hbar v_F\tilde{\nabla}_i\breve{g}_0+\tau\left[\check{\Omega},\breve{g}_i\right]-\frac{\tau}{2\hbar m}\left\{\mathcal{F}_{ij},\breve{g}_j\right\}=-\frac{\hbar}{2}\left[\breve{g}_0,\breve{g}_k\right]. \tag{1.150}$$

These equations are solved assuming the normalization condition $\breve{\mathbf{g}}^2=1$, and that the fields $\mathcal{A}_\mu$ vanish at infinity. With these solutions it is possible to express the anisotropic part of the Green's function $\breve{g}_i$ in terms of $\check{g}_0$. The detailed derivation can be found in Ref. [105] and we will just present the result

$$\check{g}_i = -\tau v_F \check{g}_0 \tilde{\nabla}_i \check{g}_0 - \frac{v_F \tau^2}{2m} \left\{ \mathcal{F}_{ij}, \tilde{\nabla}_j \check{g}_0 \right\} - i\tau^2 v_F \left[\tau_3 \mathcal{F}_{i0}, \check{g}_0 \right]. \tag{1.151}$$

Inserting this result into Eq. (1.149) we obtain the Usadel equation [106] in the case of linear in momentum spin fields

$$-D\tilde{\nabla}_k \left(\left(\check{g}_0 \tilde{\nabla}_i \check{g}_0 \right) + \frac{\tau}{2m} \left\{ \mathcal{F}_{ij}, \tilde{\nabla} \check{g}_0 \right\} + i\tau \left[\tau_3 \mathcal{F}_{i0}, \check{g}_0 \right] \right) + \left[\left(\omega_n - i\mathcal{A}_0 \right) \tau_3 - i\check{\Delta}, \check{g}_0 \right] = 0 \tag{1.152}$$

where $D = v_F^2 \tau / \mathrm{dim}$ is the diffusion coefficient and dim is the dimension on the system.

Linearized Usadel equation

The Usadel Eq. (1.152) is a non-linear differential equation. To simplify analytical calculations, we can overcome this difficulty by changing to the linearized form of the Usadel equation. The linearization is valid when either the system temperature is close to the critical temperature, or the proximity effect is weak. In both cases the amplitude of the anomalous part of the Green's function is small compared to the normal part and we can expand $\check{g}_0 \approx \mathrm{sign}(\omega_n)\tau_3 + i\tau_2 \hat{f}$. Within this limit the Usadel equation becomes

$$-\mathrm{sgn}(\omega_n) D \tilde{\nabla}^2 f_0 - \frac{\tau D}{2m} \left\{ \tilde{\nabla}_i \mathcal{F}_{ij}, \tilde{\nabla}_j f_0 \right\} + \left\{ \omega_n - i\mathcal{A}_0, f_0 \right\} + 2i\Delta \mathrm{sgn}(\omega_n) = 0. \tag{1.153}$$

When dealing with heterostructures between superconductors and other materials, we need to know the boundary conditions for the anomalous Green's function. The boundary conditions for the field free case have been determined by Kupriyanov and Lukitchev [107]. In the linearized case and for general spin-fields reads [31, 32]

$$\mathcal{N}_i \left[\tilde{\nabla}_i f_0 + \frac{\tau \mathrm{sgn}(\omega_n)}{2m} \left\{ \mathcal{F}_{ij}, \tilde{\nabla}_j f_0 \right\} \right]_{x_0} = -\gamma f_{\mathrm{BCS}} \tag{1.154}$$

where x_0 is the position of a interface between the bulk superconductor, described by the bulk Green's function f_{BCS}, and the non superconducting region. The interface is characterized by the normal vector $\mathcal{N}_i$ of its surface and its transparency γ.

Conclusion

We have introduced the transport formalisms that will be used through though this thesis. Based on minimal examples we described basic transport phenomena in superconducting hybrid structures, like the Andreev reflection, Andreev bound state formation and the 0-π transition. This will be of particular importance in the next chapter where we investigate the Andreev spectra in Josephson junctions where the superconductors are subject to an intrinsic exchange interaction.

Chapter 2

Josephson junction with spin-split superconductors[†]

Superconductors with spin-split density of states have attracted particular interest since the pioneering works of Tedrow and Merservey, in which Zeeman splitting in superconductors was used to determine the spin-polarization of ferromagnetic metals [108, 109]. Such spin-splitting can be achieved either by applying an external magnetic field or in thin superconducting films in contact with ferromagnetic insulators (FI) at zero field [110, 111]. The spin-split density of states found in superconducting films originates from the exchange interaction between the conduction electrons of the superconductor and the large localised magnetic moments of the FI [112]. In order to obtain large spin-splittings, the use of FIs has the advantage of avoiding the application of high magnetic fields. The spectrum of a conventional superconductor in this case shows two BCS-like densities of states shifted by the energy $2h$, where h is the effective exchange field induced in the superconductor film. Here we denote them as spin-split superconductors (SS).

There has been a resurgence of interest in SS because of several theoretical studies proposing them as absolute spin-valves [113], heat-valves [114] and thermoelectric elements [115–117]. Moreover, superconducting heterostructures with spin-splitting fields have attracted the interest from theorists and experimentalists in the last years, mainly motivated by the possible detection of Majorana fermions [43, 47, 118] and elaboration of complex S-FI heterostructures [119–121], where S denotes a BCS superconducting lead.

One striking effect in such structures is the enhancement of the critical Josephson current in a FI-S/I/FI-S junction by increasing the amplitude of the spin-splitting field [122–124]. Here I denotes an insulating tunneling barrier. This phenomenon has been demonstrated experimentally in Ref. [125].

In order to understand the supercurrent in ballistic Josephson junctions it is important to analyze the spectral properties of these weak links [126, 127]. In a short ballistic superconductor-normal metal-superconductor (S/N/S) junction with equal gaps and at low temperatures, tunneling through Andreev

---

[†] This chapter has been published: "Andreev spectrum of a Josephson junction with spin-splitt superconductors", B. Bujnowski, D. Bercioux, F. Konschelle, J. Cayssol and F.S. Bergeret, Europhysics Letters **115**, 67001 (2016)

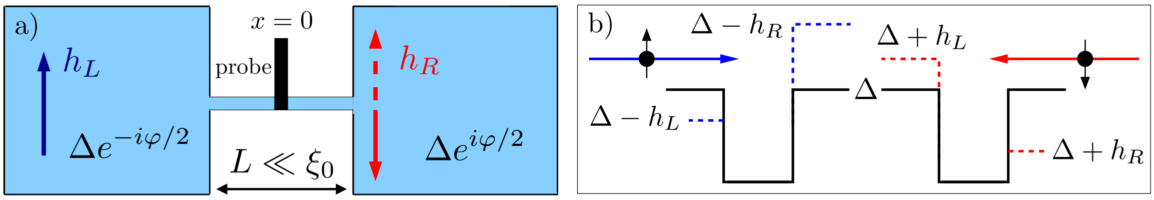

FIGURE 2.1: (a): Schematic diagram of the junction. Two SS electrodes with intrinsic exchange fields h_{L}, h_{R} separated by a ballistic weak link. A tunneling probe is situated at $x = 0$. (b) Sketch of the effective gaps for spin up/down electron when the left/right exchange fields $h_{\mathrm{L}}/h_{\mathrm{R}}$ are configured so that $-h_R > h_L > 0$.

bound states (ABSs) is the dominant contribution to the Josephson current [128]. The dependence of the ABSs on the phase difference between the superconducting banks in SS/I/SS junctions remains unexplored so far.

In the following we investigate in detail a single-channel Josephson weak link connecting two spin-split superconducting leads. We focus on the dependence of sub-gap states on the superconducting phase difference across a ballistic SS/I/SS junction with a tunneling barrier of arbitrary strength. We extend the results [122–124] by demonstrating that any deviation from the case of equal exchange fields leads to the complete disappearance of the ABSs in a finite range of the superconducting phase bias φ defined by a critical phase φ_c such that $|\varphi| < \varphi_c$. This phenomenon originates in the spin dependent asymmetry of the gaps in the left and right SS electrodes. As a consequence, within these interval the Josephson current is carried exclusively by states in the continuous part of the spectrum. The value of φ_c does not depend on the transmissivity of the junction and hence it is robust against imperfections.

2.1 SS/I/SS junction

We consider a Josephson junction consisting of two bulk SSs connected by a ballistic weak link (see Fig. 2.1 a)). We model the weak link as a δ-function scattering potential with strength U. The corresponding Bogoliubov-de Gennes equation for quasiparticle states with energy E reads

$$\begin{pmatrix} \hat{H}_0(\mathbf{r}) & \hat{\Delta}(\mathbf{r}) \\ \hat{\Delta}^\dagger(\mathbf{r}) & -\hat{H}_0^{\mathrm{T}}(\mathbf{r}) \end{pmatrix} \Psi(\mathbf{r}) = E\Psi(\mathbf{r}), \tag{2.1}$$

where

$$\hat{H}_0(\mathbf{r}) = -\frac{\hbar^2}{2m}\nabla_{\mathbf{r}}^2 - \mu + U\delta(x) - [\Theta(-x)h_{\mathrm{L}} + \Theta(x)h_{\mathrm{R}}]\,\hat{\sigma}_z, \quad \text{and} \tag{2.2}$$

$$\hat{\Delta}(\mathbf{r}) = \mathrm{i}\hat{\sigma}_y\Delta[\mathrm{e}^{-\mathrm{i}\varphi/2}\Theta(-x) + \Theta(x)\mathrm{e}^{\mathrm{i}\varphi/2}]. \tag{2.3}$$

The temperature dependent gap is modeled by the interpolation formula

$$\Delta = \Delta(T) \cong \Delta_0 \tanh(1.74\sqrt{(T_c/T) - 1}) \tag{2.4}$$

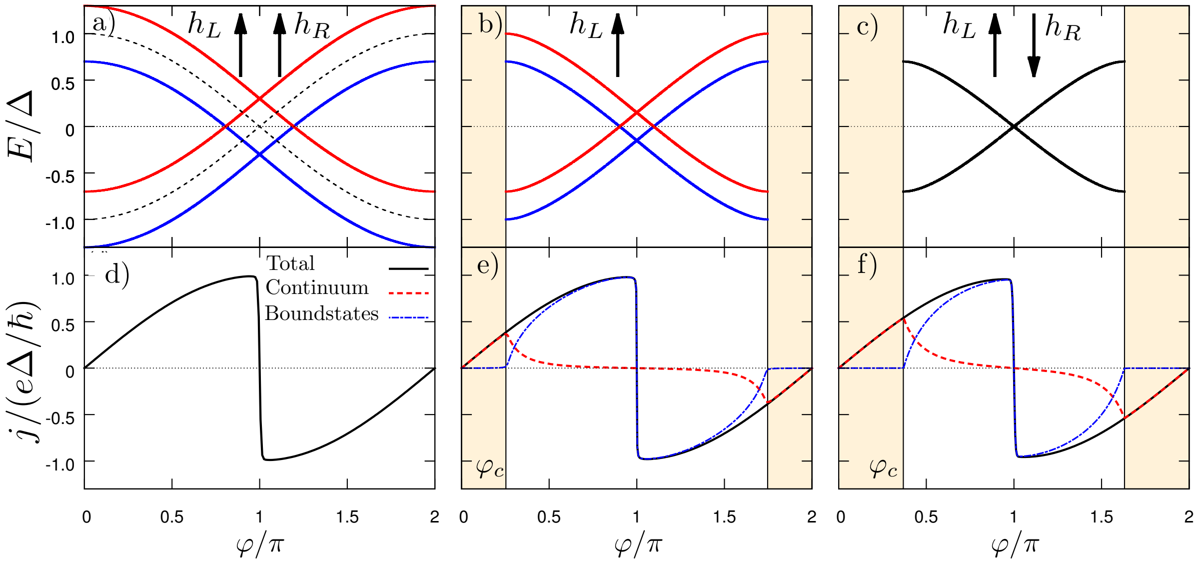

FIGURE 2.2: Top panels (a) - (c) show Andreev bound state energies for (a) non-magnetic case (black dashed line) and parallel orientation of the exchange fields ($h_{\mathrm{L}} = h_{\mathrm{R}} = 0.3\Delta$), (b) one side of the junction with zero exchange field ($h_{\mathrm{L}} = 0.3\Delta, h_{\mathrm{R}} = 0$) and (c) anti-parallel orientation of the exchange fields ($h_{\mathrm{L}} = -h_{\mathrm{R}} = 0.3\Delta$). The coloured regions correspond to the interval $|\phi| < \phi_{\mathrm{C}}$ where there is no formation of Andreev bound states. The panels (d)-(f) show the corresponding current phase relationships. Where applicable we separated the continuum and bound state contribution to the total current (dashed red and dash-dotted blue lines). All plots are for $\tau = 1$ and the current versus phase relationships are calculated at $T/T_c = 0.01$.

, where T_c is the critical temperature for superconductivity. In Eq. (2.3), φ is the phase difference between the order parameters of the superconductors, $\Theta(x)$ is the Heaviside step function, and $\delta(x)$ is the Dirac delta function. We assume weak exchange fields so that the Clogston-Chandrasekhar criterion, $|h_{\mathrm{L,R}}| < \Delta_0/\sqrt{2}$, is fulfilled, where Δ_0 is the BCS gap at zero temperature and zero exchange field[87, 88]. We restrict ourselves to symmetric electrodes (in the absence of exchange fields) with equal gap magnitudes, chemical potentials and effective masses on both sides of the junction. The only asymmetry originates from the exchange fields in the left (L), right (R) superconducting leads, which are assumed to be collinear, though with arbitrary values h_{L} and h_{R}. In this case the boundstate spectra can be obtained analytically.

2.1.1 Andreev bound states

We solve Eq. (2.1) separately in the L and R region to construct the wave function across the junction and determine the Andreev boundstate energies. In the bulk SS we obtain plane-wave solutions with

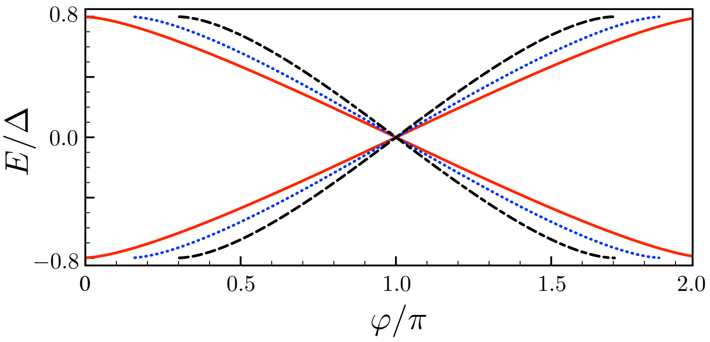

FIGURE 2.3: Discrete part of the spectrum of a SS/N/SS junction as a function of the phase across the junction in the anti-parallel configuration ($h_{\rm L} = -h_{\rm R} = 0.2$) for three different lengths of the junction: $L = 0$ dashed-black line, $L = 0.3\xi$ dotted-blue line and $L = 0.6\xi$ solid-red line.

$\psi^{\nu}_{\boldsymbol{k},e(h),\sigma}(\boldsymbol{r}) = \phi^{\nu}_{e(h),\sigma}\mathrm{e}^{\mathrm{i}\boldsymbol{k}^{e,(h)}_{\sigma}\boldsymbol{r}}$ for electron-like (hole-like) quasiparticles with spin σ. The spinors are

$$\phi^{\nu}_{e,\uparrow} = (u^{\nu}_{\uparrow}\mathrm{e}^{\mathrm{i}\phi_{\nu}}, 0, 0, v^{\nu}_{\uparrow})^{\mathrm{T}}, \tag{2.5a}$$

$$\phi^{\nu}_{h,\uparrow} = (v^{\nu}_{\uparrow}\mathrm{e}^{\mathrm{i}\phi_{\nu}}, 0, 0, u^{\nu}_{\uparrow})^{\mathrm{T}}, \tag{2.5b}$$

$$\phi^{\nu}_{e,\downarrow} = (0, -u^{\nu}_{\downarrow}\mathrm{e}^{\mathrm{i}\phi_{\nu}}, v^{\nu}_{\downarrow}, 0)^{\mathrm{T}}, \tag{2.5c}$$

$$\phi^{\nu}_{h,\downarrow} = (0, -v^{\nu}_{\downarrow}\mathrm{e}^{\mathrm{i}\phi_{\nu}}, u^{\nu}_{\downarrow}, 0)^{\mathrm{T}}\,. \tag{2.5d}$$

Here we have introduced the coherence factors $u^{\nu}_{\sigma} = \sqrt{(E^{\nu}_{\sigma} + \Omega^{\nu}_{\sigma})/2E^{\nu}_{\sigma}}$, $v^{\nu}_{\sigma} = \sqrt{(E^{\nu}_{\sigma} - \Omega^{\nu}_{\sigma})/2E^{\nu}_{\sigma}}$, where $\Omega^{\nu}_{\sigma} = \sqrt{E^{\nu\,2}_{\sigma} - \Delta^2}$ and $E^{\nu}_{\sigma} = E + \sigma h_{\nu}$, $(\nu = \mathrm{L}, \mathrm{R})$.

We use these piecewise solutions to construct the wave function ansatz for a spin-σ electron-like quasiparticle incident from the left SS with wavevector $\boldsymbol{k}^{\mathrm{e}}_{\sigma}$. In the following we consider a narrow wire constriction, and provide the corresponding single channel calculations. Therefore, the wave function ansatz reads:

$$\begin{aligned}\Psi_{e,\sigma}(\boldsymbol{r}) &= \Theta(-x)\Big\{\psi^{\mathrm{L}}_{\boldsymbol{k},e,\sigma} + \sum_{\sigma'=\uparrow\downarrow}\big[r^{\sigma\sigma'}_{eh}\psi^{\mathrm{L}}_{\boldsymbol{k},h,\sigma'} + r^{\sigma\sigma'}_{ee}\psi^{\mathrm{L}}_{-\boldsymbol{k},e,\sigma'}\big]\Big\}\\ &+ \Theta(x)\Big\{\sum_{\sigma'=\uparrow\downarrow}[t^{\sigma\sigma'}_{e}\psi^{\mathrm{R}}_{\boldsymbol{k},e,\sigma'} + t^{\sigma\sigma'}_{h}\psi^{\mathrm{R}}_{-\boldsymbol{k},h,\sigma'}]\Big\}.\end{aligned} \tag{2.6}$$

For $x < 0$, Eq. (2.6) describes the superposition of an incident electron-like quasiparticle with an Andreev reflected hole-like quasiparticle with amplitude $r^{\sigma\sigma'}_{eh}$ and a reflected electron-like quasiparticle with amplitude $r^{\sigma\sigma'}_{ee}$. For $x > 0$, electron-like and hole-like quasiparticles are transmitted with probability amplitudes $t^{\sigma\sigma'}_{ee}$ and $t^{\sigma\sigma'}_{eh}$, respectively. The ansatz for an incident hole-like spin σ quasiparticle $\Psi_{h,\sigma}(\boldsymbol{r})$ is analogous with probability amplitudes $r^{\sigma\sigma'}_{he}$, $r^{\sigma\sigma'}_{hh}$ etc. We work within the Andreev approximation by assuming that $\mu \gg \max{(E, \Delta, |h_{\nu}|)}$, so that the electron and hole quasiparticle wavevectors can be regarded as approximately equal in magnitude, $k^{e}_{\sigma} \approx k^{h}_{\sigma} \approx k_{\mathrm{F}}$.

The probability amplitudes in Eq. (2.6) for the various processes are calculated requiring the continuity of the wave function and a finite jump of the derivative at the interface. In particular the Andreev reflection amplitudes [71] read

$$r_{eh}^{\sigma\sigma} = \frac{\Delta\left(E_{\sigma}^{\mathrm{L}}\cos\varphi - E_{\sigma}^{\mathrm{R}}\right) + \mathrm{i}\Delta\sin\varphi\Omega_{\sigma}^{\mathrm{L}}}{E_{\sigma}^{\mathrm{L}}E_{\sigma}^{\mathrm{R}} - \Delta^2\cos\varphi + (1+2Z^2)\Omega_{\sigma}^{\mathrm{L}}\Omega_{\sigma}^{\mathrm{R}}} \quad \text{and} \quad r_{he}^{\sigma\sigma}(\varphi) = r_{eh}^{\sigma\sigma}(-\varphi). \tag{2.7}$$

We introduced the dimensionless strength of the scattering potential $Z = 2mU/k_{\mathrm{F}}\hbar^2$ [70]. The parameter Z is related to the transmission τ of the barrier as $\tau = 1/(1+Z^2)$.

The the discrete Andreev bound state (ABS) spectrum coincides with the poles of the Andreev reflection coefficients. We start by analyzing the spectrum of a short junction with a perfect transmission coefficient ($\tau = 1$), thereby recovering the well-known phase dependence of the ABS energy in a short S/N/S junction without spin-splitting fields (Fig. 2.2 a), black-dashed line). In the case of parallel exchange fields equal in magnitude ($h_{\mathrm{L}} = h_{\mathrm{R}}$) we find a splitting of the ABS energy-phase relationship of magnitude $|h_{\mathrm{L}}+h_{\mathrm{R}}|$ between spin-up and spin-down quasiparticles (Fig. 2.2 a), red and blue solid-lines).

By lowering the value of one of the exchange fields while keeping the other fixed, the ABSs disappear within finite intervals of the phase difference φ (Figs. 2.2 b), 2.2 c)). Moreover this behaviour is independent of the transmission of the barrier. The minimal phase difference $\varphi_c = \arccos(1 - |h_{\mathrm{L}} - h_{\mathrm{R}}|/\Delta)$ for which bound-states exist depends only on the difference between the exchange fields. In short, the ABSs are found only in the interval $\varphi \in [\varphi_c, 2\pi - \varphi_c]$. At the same time we observe a reduction of the gap.

One can provide a physical interpretation for the reduction of the gap and disappearance of ABS for some phase ranges: For illustration we consider a spin-up quasiparticle with positive energy coming from the left electrode [c.f. Fig. 2.1 b)], in the parameter regime with $h_{\mathrm{L}} > 0 > h_{\mathrm{R}}$, $|h_{\mathrm{R}}| > |h_{\mathrm{L}}|$. This quasiparticle encounters a reduced gap in the left SS of magnitude $\Delta - h_{\mathrm{L}}$ and an enhanced gap of magnitude $\Delta - h_{\mathrm{R}}$ in the right SS. If the quasiparticle energy is higher than the energy of the left gap and lower than the right one, it can be Andreev reflected only at the right SS and ABSs can not be formed. The process for a spin-down quasiparticle incoming from the right electrode is analogous. The same picture applies for quasiparticles with energies $E < 0$ and can be modified to any case of collinear orientation of the exchange fields. This scenario is very similar to the case of a junction between two superconductors with gaps different in magnitude [129], where the existence of the ABSs was shown to be set by the smaller gap, but was completely spin independent. In the case of SSs leads, the distinct exchange fields induce the asymmetry between the gaps, which is different for spin up or spin down quasiparticles (Fig. 2.1 b)).

The above results where obtained for short weak links, i.e. for $L \ll \hbar v_{\mathrm{F}}/\Delta$, where L is the length of the normal region separating the two superconducting leads, and v_{F} is the Fermi velocity. We now discuss whether the previous picture (spin dependent reduced gaps and disappearance of ABS) holds for longer junctions. For arbitrary lengths of the junction and a fully transparent link ($U = 0$), the critical phase can be obtained by analyzing the Bohr-Sommerfeld quantization condition for the SS/N/SS junction, where we assume no magnetic field in the normal region [65]:

$$2\frac{EL}{\hbar v_{\mathrm{F}}} \pm \varphi - \sum_{\nu=\{\mathrm{L,R}\}} \arccos\left(\frac{E+\sigma h_{\nu}}{\Delta}\right) = 2n\pi\,, \tag{2.8}$$

with $n \in \mathbb{Z}$. Note that the spin-splitting of the gaps (being a bulk property of the SS leads) is independent of the length L. In the short junction limit ($L \ll \hbar v_{\mathrm{F}}/\Delta$), one recovers the critical phase $\varphi_c = \arccos(1-|h_{\mathrm{L}} - h_{\mathrm{R}}|/\Delta)$ introduced earlier. From Eq. (2.8) we can also infer the dependence of the critical phase on the length L of the weak link: φ_c decreases as the length L is increased, and $\varphi_c \to 0$, for lengths exceeding the superconducting coherence length $\xi = \hbar v_{\mathrm{F}}/\Delta$ (Fig. 2.3). Indeed in the long junction limit, even if the highest ABS merges into the continuum, there are other ABS (with lower energies) which are still defined for all values of the phase. Note that the study of ABSs associated with the Bohr-Sommerfeld quantization condition Eq. (2.8) can be generalized to the case of a spin-active weak link using the formalism developed in Ref. [130].

2.1.2 Local density of states

Direct insight about states for all phases can also be obtained by calculating the local density of states (LDOS) of the junction. The LDOS at the tunneling barrier can be related to the $(1,1)$ component of the retarded Green's function Eq. (2.10) [77], using the formula

$$\rho(E,x) = \sum_\sigma \rho_\sigma(E,x) = -\lim_{x' \to x} \frac{1}{\pi} \mathrm{Im}[G^r_{11}(x,x',E)]. \tag{2.9}$$

The complete Green's function of the junction can be built from the scattering solutions Eq. (2.6) [74] as introduced in Sec. 1.2.2. The retarded Green's function in the left superconductor ($x < 0$) reads:

$$\begin{aligned} G^r(x,x',E) =& \sum_\sigma \mathcal{A}^\nu_\sigma \left\{ \left[r^{\sigma\sigma}_{eh} \mathrm{e}^{\mathrm{i}k_{\mathrm{F}}(x-x')} + r^{\sigma\sigma}_{he} \mathrm{e}^{-\mathrm{i}k_{\mathrm{F}}(x-x')} \right] \times \begin{pmatrix} u^\nu_\sigma v^\nu_{\bar\sigma} & {v^\nu_{\bar\sigma}}^2 \mathrm{e}^{\mathrm{i}\varphi_\nu} \\ {u^\nu_\sigma}^2 \mathrm{e}^{-\mathrm{i}\varphi_\nu} & u^\nu_\sigma v^\nu_{\bar\sigma} \end{pmatrix} \right. \\ &+ \left[\mathrm{e}^{\mathrm{i}k_{\mathrm{F}}|x-x'|} + r^{\sigma\sigma}_{ee} \mathrm{e}^{-\mathrm{i}k_{\mathrm{F}}(x+x')} \right] \begin{pmatrix} {u^\nu_\sigma}^2 & u^\nu_\sigma v^\nu_{\bar\sigma} \mathrm{e}^{\mathrm{i}\varphi_\nu} \\ u^\nu_\sigma v^\nu_{\bar\sigma} \mathrm{e}^{-\mathrm{i}\varphi_\nu} & {v^\nu_{\bar\sigma}}^2 \end{pmatrix} \\ &+ \left. \left[\mathrm{e}^{-\mathrm{i}k_{\mathrm{F}}|x-x'|} + r^{\sigma\sigma}_{hh} \mathrm{e}^{\mathrm{i}k_{\mathrm{F}}(x+x')} \right] \begin{pmatrix} {v^\nu_{\bar\sigma}}^2 & u^\nu_\sigma v^\nu_{\bar\sigma} \mathrm{e}^{\mathrm{i}\varphi_\nu} \\ u^\nu_\sigma v^\nu_{\bar\sigma} \mathrm{e}^{-\mathrm{i}\varphi_\nu} & {u^\nu_\sigma}^2 \end{pmatrix} \right\}, \end{aligned} \tag{2.10}$$

where $\mathcal{A}^\nu_\sigma = -\frac{\mathrm{i}mE^\nu_\sigma}{\hbar^2 k_{\mathrm{F}} \Omega^\nu_\sigma}$. It carries the complete information about the system and allows the computation of the phase dependent local density of states and the Josephson current [128, 131]. The spectrum of the Josephson junction is directly related to the poles of the Green's function: the discrete Andreev bound states coincide with poles of the Andreev reflection coefficients Eq. (2.7), while the branch cuts of Eq. (2.7) provide the continuum part of the spectrum. In our case, the corresponding spin-resolved LDOS (2.9) reads

$$\rho_\sigma(E) = \frac{m}{\pi \hbar^2 k_{\mathrm{F}}} \mathrm{Re} \left[\left(\frac{2E^\nu_\sigma + (r^{\sigma\sigma}_{eh} + r^{\sigma\sigma}_{he})\Delta}{2\Omega^\nu_\sigma} \right) \right], \tag{2.11}$$

where the atomic scale oscillations of $\rho(E)$ are assumed to be averaged out [132]. In Fig. 2.4 we show the LDOS contributions from spin-σ quasiparticles in the cases of parallel and anti-parallel orientations of the exchange fields and perfect transmission $\tau = 1$.

In the parallel case and $\varphi = 0$, we obtain (as expected) the spectrum of a bulk SS with the two spin-split BCS densities of states with coherence peaks at $E = \pm(\Delta + \sigma h)$ (Fig. 2.4 a)). For a finite phase difference between the SSs, spin-split ABSs appear. The peaks corresponding to hole- and electron-like quasiparticles with spin σ are centered around $E = \sigma|h_\nu|$ (red (blue) lines in the left column in Fig. 2.4) and merge at this energy when approaching $\varphi = \pi$.

In the anti-parallel case and $|\varphi| < \varphi_c$ (see Fig. 2.4 f) and 2.4 g)) the spectrum deviates drastically from the BCS-like spectrum and no BCS coherent peaks are observed. At the critical value of the phase φ_c these peaks appear at energies $\pm(\Delta - |h_\nu|)$. The two peaks corresponding to ABSs merge into a single peak at $\varphi = \pi$ (Fig. 2.4 j)).

For imperfect transmission ($\tau < 1$) and parallel configuration of the exchange fields ($h_\mathrm{R} = h_\mathrm{L} = h$) (Fig. 2.5 a) the energy difference between the spin polarized ABSs remains the same as in the $\tau = 1$ case In contrast, in the anti-parallel case there is no splitting of the ABSs. In both cases there are avoided energy crossings at $\varphi = \pi$ due to finite backscattering. Noticeably, neither the spin-splitting nor the critical phase φ_c are τ-dependent.

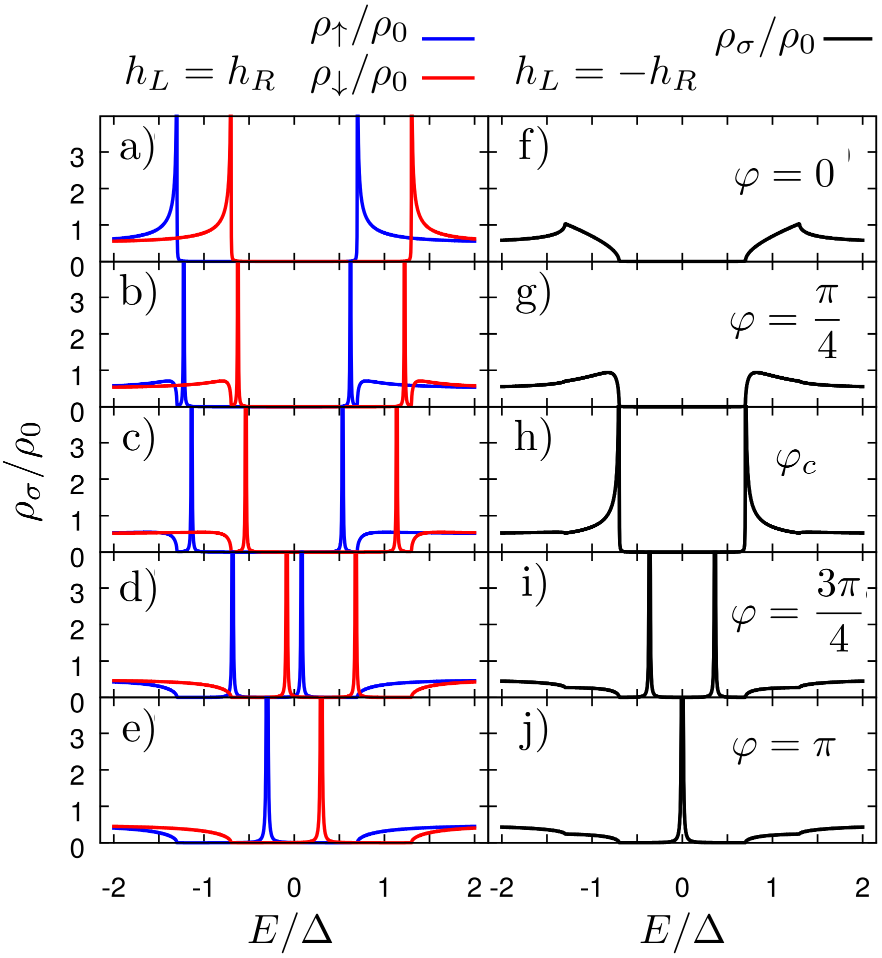

FIGURE 2.4: LDOS of the junction $\rho(E)$ divided by the normal state LDOS $\rho_0(E)$, for parallel (left column) and anti-parallel (right column) orientation of the exchange fields of magnitude $|h_{L,R}|/\Delta = 0.3$. The phase difference gradually increases from the top panels where $\varphi = 0$ through φ_c to the bottom panels with $\varphi = \pi$. All plots are for $\tau = 1.0$.

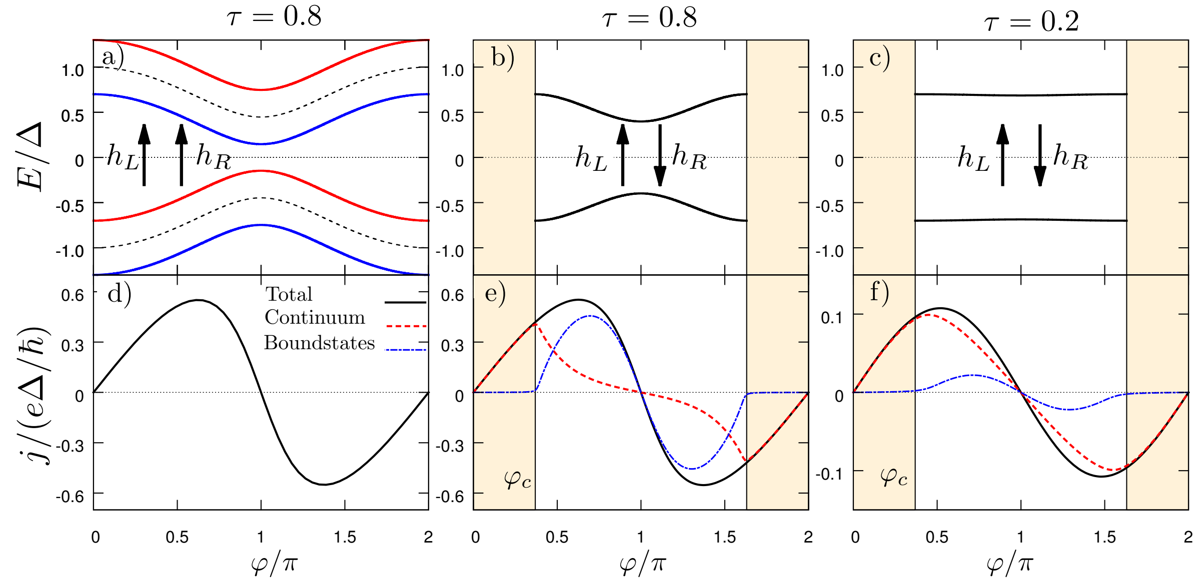

FIGURE 2.5: Andreev bound state energies for (a) non magnetic case (black dashed) and parallel orientation of the exchange fields ($h_\mathrm{L} = h_\mathrm{R} = 0.3\Delta$), and b)-c) anti-parallel orientation of the exchange fields ($h_\mathrm{L} = -h_\mathrm{R} = 0.3\Delta$). For panels a),b) $\tau = 0.8$ and for c) $\tau = 0.2$. The colored regions correspond to the intervals with no formation of Andreev bound states. Panels d)-f) show the corresponding current phase relationships separated into the continuum states (red dashed line) and bound states contribution (blue dash-dotted line) to the total current. All plots are for $T/T_c = 0.01$.

2.1.3 Current-phase relation

To understand how the absence of ABSs influence the Josephson current in the non-parallel case for $|\varphi| < \varphi_c$, we numerically evaluate the Josephson current through the junction using the real time representation of the Furusaki-Tsukada formula Eq. (1.71) [76, 78] that we introduced in Sec. 1.2.2. It reads

$$I = \frac{\mathrm{i}e\hbar}{8\pi m}\int_{-\infty}^{\infty} dE \tanh\left(\frac{\beta E}{2}\right) \lim_{x'\to x=0^+}\left(\frac{\partial}{\partial x} - \frac{\partial}{\partial x'}\right) \mathrm{Tr}\left[G^r(x,x',E) - G^a(x,x',E)\right], \tag{2.12}$$

Tr[...] is the trace in Nambu-spin space and $G^{r/a}$ is the retarded/advanced Green's function from Eq. (2.10).

In the lower panels of Fig. 2.2 current phase relations are shown for different orientations of the exchange fields and perfect transmission of the barrier ($\tau = 1$). The current phase relations show the well-known sawtooth shape Fig. 2.2 d)- f). Lowering the transmission, the current phase relationships become sinusoidal and one recovers the usual current-phase relation of a tunneling junction, see Figs. 2.5 d) - f). We also verified the enhancement of the critical current with respect to the non-magnetic case by the presence of anti-parallel exchange fields in the low transmission limit and low temperatures [122, 123] as shown in Figs. 2.6 a) - b).

The total current is the sum of two contributions: one originating from the ABS (I_ABS) and the other from states in the continuous spectrum (I_Cont). These are shown in the lower panels of Figs. 2.2 and 2.5.

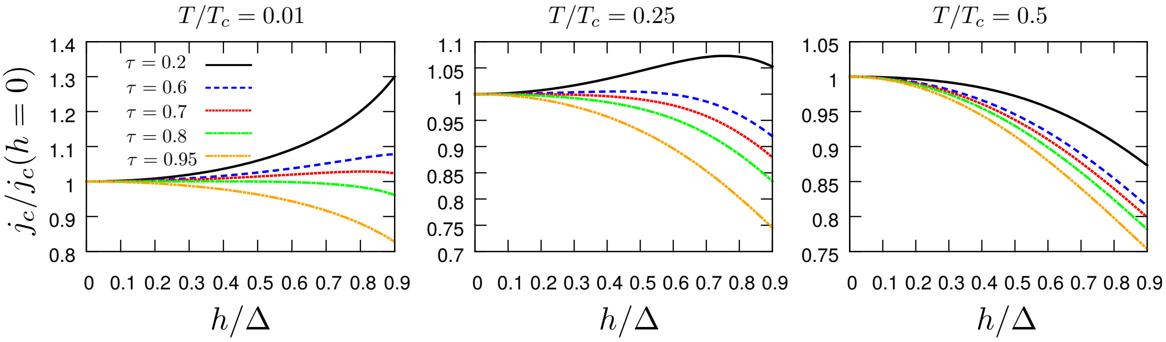

FIGURE 2.6: Critical current normalized by zero field critical current for anti-parallel orientation of the exchange fields $h_L = -h_R = h$ as function h for various temperatures T and transmissions τ.

In the parallel configuration with identical exchange fields the Josephson current is carried exclusively by the ABSs. In contrast, if the exchange fields are different both I_{ABS} and I_{Cont} contribute to the current. The vanishing contribution from the discrete spectrum for $|\varphi| < \varphi_c$ is compensated by a finite I_{Cont} (see Figs. 2.2 e) and 2.2 f) for $\tau = 1$ and in Figs. 2.5 e) and 2.5 f) for $\tau < 1$). In other words, current from tunneling through ABSs is only present for $\varphi \notin (-\varphi_c, \varphi_c)$ and gets reduced by lowering the transmission of the junction. High enough exchange interactions and low transmission can lead to a current dominated by contributions from continuum states, as shown in Fig. 2.5 f). This is consistent with the results of Chtchelkatchev *et al.* [123] where the critical current is shown to be purely due to the states of the continuous spectrum in the case of high magnitudes of the anti-parallel exchange fields and sufficiently low transmissions.

2.1.4 Conclusion

We have presented a detailed study of the spectrum and current-phase relation of a Josephson junction consisting of a short weak link connecting two superconducting leads with a spin-split density of states. We have shown that for collinear orientations of the exchange fields, any deviation from the case of equal fields leads to finite intervals of phases without Andreev bound states. These intervals are independent of the transmission of the junction and are characterized by a critical phase-difference $\varphi_c = \arccos(1 - |h_{\text{L}} - h_{\text{R}}|/\Delta)$ for which ABSs disappear by merging within the continuum.

When the phase difference is in the range $|\varphi| < \varphi_c$, the Josephson current is therefore completely carried by states in the continuous part of the spectrum. Outside this range the current is a superposition of the contributions from the ABS and the continuous spectrum. For perfect transmission the current is mainly due to tunneling through the ABSs (Fig. 2.2 e)), whereas for low transmission the current is totally due to excitations from the continuous part of the spectrum (Fig. 2.5 f)). Hence changing the transmission of the junction allows to tune the origin of the current.

Chapter 3

Josephson triplet junctions with spin-orbit coupling

This chapter is dedicated to the study of the Josephson current in heterostructures in the diffusive regime with spin-orbit coupling (SOC) of Rashba and Dresselhaus type, and how to control it via external fields. In this chapter the units are chosen so that $k_\mathrm{B} = \hbar = 1$.

The interplay between superconductivity and ferromagnetism leads to triplet superconducting correlations [27–31, 133, 134]. The simplest setup for the generation of a triplet component is a superconductor (S)-ferromagnet (F) heterostructure with a homogeneous exchange field (Sec. 1.3). The singlet Copper pairs can penetrate the ferromagnet, and due to the local exchange field, are partially converted into triplet pairs with the total spin projection zero with respect to the exchange field. Oscillations of the triplet correlations in the F region lead to the well understood effect of the reversal of the critical current in S/F/S Josephson junctions, a 0-π transition [22–26]. In a diffusive monodomain F, both singlet and triplet correlations decay on the magnetic length scale $\xi_h = \sqrt{D/h}$, where h is the magnitude of the exchange field and D is the diffusion constant. For conventional superconductors and typical exchange field strengths, ξ_h is much shorter than the thermal length scale of decay $\xi_\omega \approx \sqrt{D/T}$ in a non-magnetic system. On the other hand, triplet components with finite spin projection, are not affected by its pair breaking effect and would decay on a length scale comparable to ξ_ω. Such long-range triplet components (LRTC) can be generated due to inhomogeneities of the exchange field [27–29] or due to the presence of SOC under a homogeneous exchange field [31, 32]. The prediction of LRTCs in S/F hybrid structures has stimulated several experimental work that confirmed their existence [120, 135–144]. The fabrication of devices exhibiting long-range Josephson currents has become a routine nowadays which paves the path for new spintronic applications.

On the contrary, the LRTC generation based on the interplay of SOC and exchange fields has not been observed yet. More recently, transverse vertical heterostructures with in-plane magnetic fields and SOC materials have been experimentally explored but no evidence for an LRTC was found [145–147]. In accordance with previous theoretical works [31, 32], in such vertical multilayered S/F/S junctions the condition for the generation of an LRTC is quite restrictive. For example, in order for a pure Rashba SOC to generate the LRTC, the magnetization has to have an out-of-plane component. This is a rather unfavorable scenario as such exchange fields can create vortices in the superconductor and thus complicate the interpretation of experimental results.

More suitable for the observation of LRTC induced by the SOC are lateral structures, where currents have also a component flowing in the direction parallel to the hybrid interface [31, 32, 148–150].

The next Sec. 3.1 recapitulates the basics on the proximity effect under influence of spin-fields in diffusive heterostructures. Based on that, we demonstrate that lateral junctions are the favorable setup to study long ranged Josephson currents due to SOC. The reader familiar with the topic of long ranged triplet correlations can skip this introductory section. In Sec. 3.2 the Josephson current is determined in two types of realistic, lateral junctions with the focus on the control of possible 0-π transitions.

3.1 Generation of long range triplet components

3.1.1 Long range proximity effect at diffusive S/F interfaces

We first study the proximity effect at a diffusive S/N and S/F interface lying in the y-z-plane. We assume that the proximity effect is weak, e.g. the case of an interface with low transparency, in which the linearized Usadel Eq.(1.153) is valid:

$$D\nabla^2\hat{f} - 2|\omega_n|\hat{f} - i\text{sign}(\omega_n)\left\{\hat{h},\hat{f}\right\} - i\Delta(x)\hat{1}\hat{f} = 0. \tag{3.1}$$

Here D is the diffusion constant, ω_n is the Matsubara frequency and $\hat{h} = \hat{\sigma}^a h^a$ is the exchange field. Symbols with a $\hat{}$ stand for operators in spin space and $\hat{\sigma}^a$ are the Pauli matrices. The Einstein summation convention is used to sum over repeated indices. The general form of the condensate function in spin space is

$$\hat{f} = f_s\hat{1} + f_t^a\hat{\sigma}^a, \tag{3.2}$$

where f_s is the singlet component and f_t^a are the triplet components. In our representation the short (long)-range triplet component corresponds to the component parallel (orthogonal) to the exchange or Zeeman field. At the interface between the S and the N the anomalous Green's function obeys the Kupriyanov-Lukichev boundary condition (1.154)

$$\left[\mathcal{N}_i\nabla_i\hat{f}\right]_{S/N} = -\gamma f_{\text{BCS}}\hat{1}. \tag{3.3}$$

The system is translational invariant in the y and z direction, thus the problem is effectively one dimensional. Deep in the bulk of the superconductor, in the linearized limit, the anomalous Green's function is given by $f_{\text{BCS}} = -i\frac{\Delta}{|\omega_n|}$. In a realistic calculation, the spatial dependence of $\Delta(x)$ has to be determined self consistently. We assume a potential step like gap function $\Delta(x) = \Delta(1-\Theta(x))$. Therefore, in the normal metal region ($x > 0$) the solution of Eqs.(3.1) and (3.3) is given by

$$\hat{f}(x) = \frac{\gamma}{\kappa} f_{\text{BCS}}\, e^{-\kappa_\omega x} \hat{1}, \tag{3.4}$$

where $\kappa_\omega = \sqrt{2|\omega_n|/D}$, i.e. the bulk solution decays on a length scale $\xi_\omega = 1/\kappa_\omega$, that is set by the temperature of the system since $|\omega_n| \propto T$. In diffusive systems at very low temperatures, this length scale can be much larger then the coherence length $\xi_0 = \sqrt{D/\Delta}$ and the mean free path. This shows that the proximity effect in diffusive systems is not affected by disorder due to elastic scattering at non-magnetic impurities.

Homogeneous exchange field

In the presence of the exchange field $\hat{h}$ the in spin space structure of $\hat{f}$ becomes relevant. The exchange field causes a singlet-triplet conversion at the interface. For a time independent and homogeneous exchange field pointing along the z-direction, $\hat{h} = h\hat{\sigma}^z$ the Usadel Eq.(3.1) in the bulk F region reduces to

$$\begin{aligned}
\partial_x^2 f_s - \kappa_\omega^2 f_s - 2i\text{sign}(\omega_n)\frac{h}{D} f_t^z &= 0, \\
\partial_x^2 f_t^z - \kappa_\omega^2 f_t^z - 2i\text{sign}(\omega_n)\frac{h}{D} f_s &= 0.
\end{aligned} \tag{3.5}$$

The solution in the F region reads

$$\begin{pmatrix} f_s \\ f_t^z \end{pmatrix} = \frac{\gamma}{2} f_{\text{BCS}} \left[\begin{pmatrix} 1 \\ 1 \end{pmatrix} \frac{e^{-\lambda^+ x}}{\lambda^+} + \begin{pmatrix} -1 \\ 1 \end{pmatrix} \frac{e^{\lambda^- x}}{\lambda^-} \right], \tag{3.6}$$

with $\lambda^\pm = \sqrt{\frac{2|\omega_n| \pm 2i\text{sign}(\omega_n)h}{D}}$. In typical systems, the energy h of the exchange field is much larger than the thermal energy T. In that case we can approximate $\lambda^\pm \approx (i \pm 1)/\xi_h$, thus the superconducting correlations f_s and f_t^z decay and oscillate on the magnetic length scale $\xi_h = \sqrt{D/h}$ in the F region. The proximity effect is strongly suppressed compared to the case without the exchange field.

Linear domain wall at the interface

Interestingly, the suppression of the proximity effect can be avoided. It follows from Eq.(3.1) that a triplet component of $\hat{f}$ which anticommutes with the exchange field, i.e. a component perpendicular to $\hat{h}$, will experience damping on the thermal length scale instead on the magnetic one. This can be accomplished by introducing a inhomogeneous exchange field, as first discussed in Ref. [27], in the context of a Bloch domain wall located at the S/F interface.

Let us briefly demonstrate the appearance of a long range component. We assume a superconductor for $x < 0$ and for $0 < x < w$ a linear domain wall of the form

$$\hat{h}(x) = h \left[\sin(Qx)\, \hat{\sigma}^y + \cos(Qx)\, \hat{\sigma}^z \right]. \tag{3.7}$$

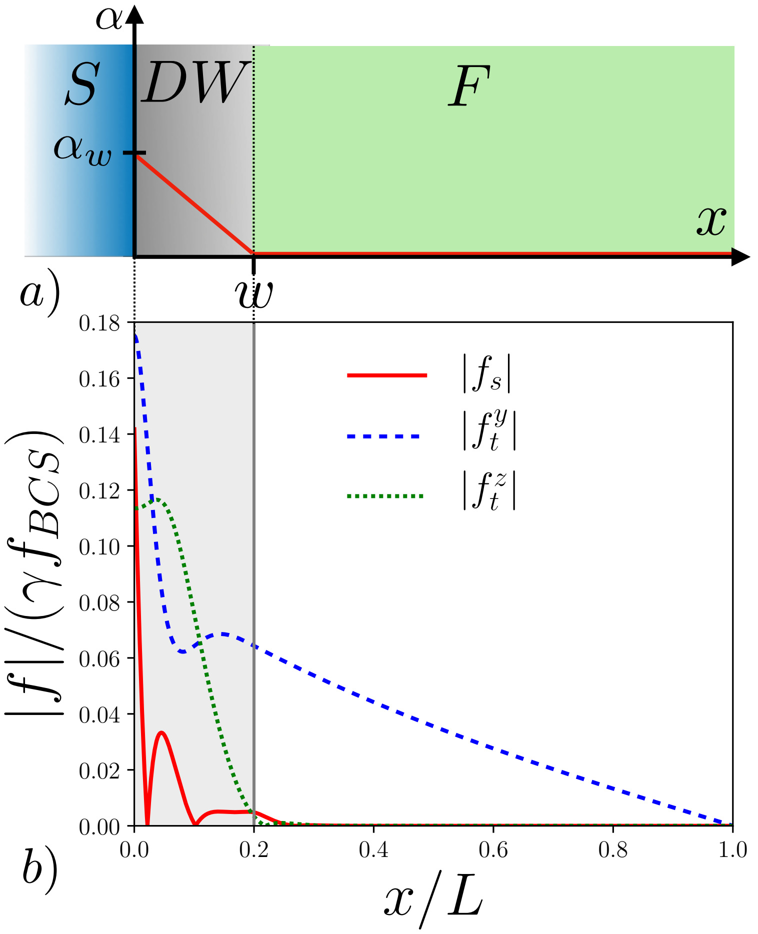

FIGURE 3.1: a) Geometrical setup used for the numerical study of an interface between a superconductor (S) a linear domain wall (DW) of width $w/L = 0.2$ and a ferromagnet (F) of length L. The angle between the exchange field and the z-axis is α. In the numerical solution we chose the exchange field in the homogeneous F region $x > w$ to point along the z-direction. Towards the S, the orientation of the exchange field is rotated by a total angle $\alpha_w = \pi/2$. b) Numerically obtained absolute value of the singlet and triplet components normalized by their bulk value, for the Matsubara frequency $\omega_{n=0} = \pi T$ and exchange field of magnitude $h/\Delta = 10$. The calculation was done for $T/\Delta = 0.01$ and all lengths are in units of $\xi_0 = \sqrt{D/\Delta}$.

The magnetization rotates around the x-axis with a wave vector Q. For $x > w$ we have a homogeneous ferromagnet with exchange field orientation $\hat{h}(w)$. In order to solve the resulting Eq.(3.1) in the domain wall region we introduce a SU(2) local gauge transformation $\mathcal{U}(x) = e^{-\frac{i}{2}Qx\hat{\sigma}^x}$ that removes the coordinate dependence from the domain wall. Inserting

$$\hat{f} = \mathcal{U}^{-1}(x)\hat{\tilde{f}}\mathcal{U}(x) \tag{3.8}$$

into the Usadel equation gives the following equation for the transformed Green's function

$$D\partial_x^2\hat{\tilde{f}} + iDQ\left[\hat{\sigma}^x, \partial_x\hat{\tilde{f}}\right] + \frac{DQ^2}{2}\left(\hat{\sigma}^x\hat{\tilde{f}}\hat{\sigma}^x - \hat{\tilde{f}}\right) - 2|\omega_n| - i\text{sign}\left\{h\hat{\sigma}^z, \hat{\tilde{f}}\right\} = 0. \tag{3.9}$$

As can be inferred from the second and third term in Eq.(3.9) there exist two distinct mechanisms to generate triplet components of the anomalous Green's function. The second term linear in Q is the rotation of the spin due to spin precession. The third term proportional to Q^2 is the diffusive spin relaxation. It rescales the thermal decay length, is a tensorial quantity in general and can be anisotropic. If triplet superconducting correlations penetrate a region with anisotropic spin relaxation, the triplet component with the lowest decay rate is favored and the total spin will rotate into this direction. Writing out Eq.(3.9) by components in spin space gives:

$$D\partial_x^2 \tilde{f}_s - 2i\,\mathrm{sign}(\omega_n) h \tilde{f}_t^z - 2|\omega_n| \tilde{f}_s = 0, \tag{3.10}$$

$$D\partial_x^2 \tilde{f}_t^x - 2|\omega_n| \tilde{f}_t^x = 0, \tag{3.11}$$

$$D\partial_x^2 \tilde{f}_t^y + 2DQ\tilde{f}_t^z - DQ^2 \tilde{f}_t^y - 2|\omega_n| \tilde{f}_t^y = 0, \tag{3.12}$$

$$D\partial_x^2 \tilde{f}_t^z - 2DQ\tilde{f}_t^y - DQ^2 \tilde{f}_t^z - 2|\omega_n| \tilde{f}_t^y - 2i\,\mathrm{sign}(\omega_n) h \tilde{f}_s = 0. \tag{3.13}$$

From this one infers that the component $\tilde{f}_t^y$ does not couple to the exchange field. Thus if generated, it decays on the thermal length scale in the region $x > w$ where $Q = 0$.

To obtain a analytical solution for Eq.(3.9) in the F-region, we seek for a perturbative solution up to first order in Q which is justified as long as $DQ^2 \ll T$. In this example the exchange field in the homogeneous region $x > w$ points along the z-axis and rotates towards the S/F interface by an angle α_w as shown in Fig. 3.1 a). In zeroth order in Q, the homogeneous case, the solution of the system is given by Eq.(3.6). The first order correction to $\tilde{f}_t^y$ is determined from

$$D\partial_x^2 \tilde{f}_t^y - 2|\omega_n| \tilde{f}_t^y = +2DQ\tilde{f}_t^z, \tag{3.14}$$

together with the boundary conditions between the S/F and between the domain wall and a semi-infinite F-region given by

$$\left[\partial_x \tilde{f}_t^y + Q\tilde{f}_t^z\right](0^+) = 0, \tag{3.15}$$

$$\hat{f}(w - 0^+) = \hat{f}(w + 0^+), \tag{3.16}$$

$$\partial_x \hat{f}(w - 0^+) = \partial_x \hat{f}(w + 0^+). \tag{3.17}$$

Under the approximation $T \ll h$ and $\xi_h \ll w$ as well as only a small rotation of the magnetization in the domain wall $Qw \ll 1$ one finds that in the region of the homogenous exchange field $x > L$

$$f_t^y(x) = \mathrm{sign}(\omega_n) iQ\xi_h\xi_\omega\gamma f_{\mathrm{BCS}} e^{-\kappa_\omega x}. \tag{3.18}$$

This component is long range as it decays on the thermal length scale. Details of the calculation are shown in the App. A.4 and an exact solution of the problem can be found in Ref. [27].

The full numerical solution of the system for a finite F region, is shown in Fig. 3.1 b). In the domain wall region, the triplet components parallel and perpendicular to the homogeneous exchange field in the F region get generated, and decay on a length scale of the order of ξ_h. The decay of the triplet components perpendicular to the x-direction, varies along x due to the rotation of the exchange field. In

$x > w$, the component of the anomalous Green's function perpendicular to the exchange field is f_t^y, and it decays on a much longer length scale compared to f_s and f_t^z as expected.

3.1.2 Long range triplet components from spin-orbit coupling

The derivation in the previous section reveals another interesting result. As ruled out in Ref. [32], the gauge transformed Eq. (3.9) can be brought into the form

$$D\tilde{\nabla}_x^2 \hat{\tilde{f}}_t - 2|\omega_n|\hat{\tilde{f}} - i\text{sign}(\omega_n)\left\{h\hat{\sigma}^z, \hat{\tilde{f}}\right\} = 0. \tag{3.19}$$

Here $\tilde{\nabla}_x \cdot = \partial_x \cdot + i\frac{Q}{2}\left[\hat{\sigma}^x, \cdot\right]$ is the covariant derivative introduced in Sec. 1.4 in the context of SU(2) gauge invariant transport Eq. (1.142), and is equivalent to a linear in momentum SOC with the field component $\hat{A}_x = -Q/2\hat{\sigma}^x$. This shows the gauge equivalence of a linear domain wall in a S/F heterostructure and a superconductor with linear in momentum SOC under presence of a homogeneous exchange field. It follows that heterostructures involving SOC fields are also able to restore the long-range decay behavior by generating triplet components perpendicular to the exchange field.

We now turn to systems with homogeneous exchange fields and SOC with linear in momentum and spatially constant SOC. In this case the linearized Usadel Eq. (1.153) reads

$$D\tilde{\nabla}^2 \hat{f} - 2|\omega_n|\hat{f} - i\text{sign}(\omega)\left\{\hat{h}, \hat{f}\right\} = 0, \tag{3.20}$$

with $\tilde{\nabla}_k = \partial_k - i[\hat{A}_k, \dots]$, where $\hat{A}_k = \frac{\hat{\sigma}^a}{2}\mathcal{A}_k^a$ describe the SOC fields. In its linearized form, the corresponding Kupriyanov-Lukichev boundary conditions generalized for materials with SOC at an S/X interface (1.154) read :

$$\mathcal{N}_i\left[\tilde{\nabla}_i \hat{f}\right]_{S/X} = -\gamma f_{\text{BCS}}\hat{1}, \tag{3.21}$$

where X denotes any non-superconductor material and $f_{\text{BCS}} = \frac{\Delta e^{i\varphi}}{\sqrt{\Delta^2 - \omega_n^2}}$ is the anomalous Green's function in the bulk S region with the amplitude of the superconducting order parameter Δ and its phase φ in the S region. Due to the gauge equivalence it is just the system of equations and boundary conditions (3.1)-(3.3) we used for the domain wall problem by replacing the normal spatial derivative by its covariant formulation. Writing out the equations for the components of $\hat{f}$ gives

$$D\left[\partial_k^2 f_s\right] - 2|\omega_n|f_s - 2i\text{sign}(\omega_n)f_t^a h^a = 0, \tag{3.22}$$

$$D\left[\partial_k^2 f_t^a + 2\mathcal{C}_k^{ab}\left(\partial_k f_t^b\right) - \Gamma^{ab} f_t^b\right] - 2|\omega_n|f_t^a - 2i\text{sign}(\omega_n)f_s h^a = 0. \tag{3.23}$$

From these equations we recognize the two distinct mechanisms that generate triplet correlations in systems with spatially homogenous spin fields. The spin precession, corresponding to the terms proportional to spin precession tensor $\mathcal{C}_k^{ab} = \varepsilon^{acb}\mathcal{A}_k^c$, and spin relaxation, corresponding to the terms proportional to the Dyakonov-Perel (DP) spin relaxation tensor $\Gamma^{ab} = \mathcal{A}_k^c\mathcal{A}_k^c\delta_{a,b} - \mathcal{A}_k^a\mathcal{A}_k^b$.

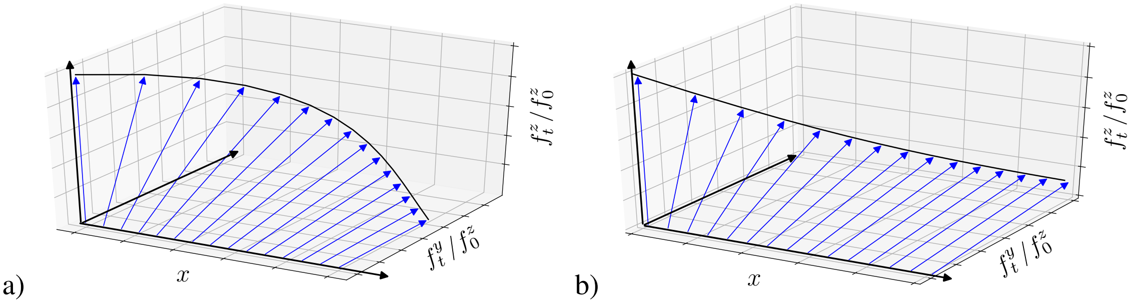

FIGURE 3.2: Rotation of the polarization of the triplet components for a) spin precession and isotropic spin relaxation and b) pure anisotropic spin relaxation ($\beta/\alpha = 1/3$) at $T = 0$.

Let us briefly illustrate the two effects through minimal examples. In our example the triplet components are polarized in the z-direction in spin space at $x = 0$, $\hat{f} = f_0^z \hat{\sigma}^z$, and we are interested in the spatial variation of the triplet components in the x-direction. We first focus on the spin precession mechfanism and choose the SOC fields $\hat{\mathcal{A}}_k = \delta_k^a \alpha$, which corresponds to an isotropic SOC, and thus a isotropic spin relaxation. In this case, the Eqs. (3.22), (3.23) read

$$D\partial_x^2 f_t^y - D2\alpha\partial_x f_t^z - 2\left|\omega_n\right| f_t^y - 2D\alpha^2 f_t^y = 0, \tag{3.24}$$

$$D\partial_x^2 f_t^z + D2\alpha\partial_x f_t^y - 2\left|\omega_n\right| f_t^z - 2D\alpha^2 f_t^z = 0. \tag{3.25}$$

This system is easily solved in the case when the thermal energy is much smaller than the spin relaxation energy, $T \ll D\alpha^2$, giving

$$f_t^y(x) = \sin\left(\alpha x\right) e^{-\alpha x} f_0^z, \tag{3.26}$$

$$f_t^z(x) = \cos\left(\alpha x\right) e^{-\alpha x} f_0^z. \tag{3.27}$$

We see that the precession rotates the polarization around the x-axis in a helical way accompanied by an isotropic decay. In this example the choice of the x-direction to track the evolution of the initial polarization is arbitrary as the system is isotropic. The evolution in z-direction is trivial as there $\mathcal{C}_z^{za} = 0$ so there is no rotation of the polarization due to precession. In a realistic situation the polarization rotates around the direction of the spin inhomogeneity in space.

Now let us turn to the generation of triplet components through spin relaxation. Therefore we need to the latter to be non-isotropic. Let us choose the SOC fields $\mathcal{A}_z^y = \alpha$ and $\mathcal{A}_z^z = \beta$ and assume the same situation as above otherwise. The spin precession terms in the Eqs. (3.22), (3.23) vanish and we are left to solve the coupled system of equations

$$D\partial_x^2 f_t^y - \left(2\left|\omega_n\right| + D\beta^2\right) f_t^y + D\alpha\beta f_t^z = 0, \tag{3.28}$$

$$D\partial_x^2 f_t^z - \left(2\left|\omega_n\right| + D\alpha^2\right) f_t^z + D\alpha\beta f_t^y = 0, \tag{3.29}$$

together with the boundary condition $\hat{f}|_{x=0} = f_0^z \hat{\sigma}^z$. In the limit of very low temperatures $T \to 0$ we obtain the solution

$$f_t^y = f_0^z \frac{\alpha\beta}{\alpha^2 + \beta^2}(1 - e^{-\kappa x}), \tag{3.30}$$

$$f_t^z = f_0^z \left(\frac{\beta^2}{\alpha^2 + \beta^2} + \frac{\alpha^2}{\alpha^2 + \beta^2} e^{-\kappa x} \right), \tag{3.31}$$

where $\kappa = \sqrt{\alpha^2 + \beta^2}$. The result shows that the initial z polarization of the correlations turns towards the direction with the lowest relaxation rate. This is the case as long as the initial polarization has a component perpendicular to the principle axis of the spin relaxation tensor. The spatial variation of the absolute value of the polarizations for both cases are shown schematically in Fig. 3.2.

Spin precession and relaxation for Rashba and Dresselhaus SOC - transversal vs lateral structures

The condition for the generation of LRTCs due to spin precession is the existence of a SOC field component $\hat{\mathcal{A}}_k$ that does not commute with the exchange field and with a spatial component along the spin inhomogeneity. Within the gauge covariant formulation this is equivalent to a finite SU(2) field tensor component

$$\mathcal{F}_{k,0} = \partial_k \hat{\mathcal{A}}_0 - i \left[\hat{\mathcal{A}}_k, \hat{\mathcal{A}}_0 \right] \neq 0. \tag{3.32}$$

This is the SU(2) analogon of the electric field tensor [31, 32] and we will therefore call it the SU(2) electric field. In the DW problem $\mathcal{F}_{k,0}$ was finite due to the spatial variation of the exchange field, while for the case of a homogeneous exchange field, the SOC field has to have components perpendicular to the exchange field.

The LRTC generation due to spin relaxation is possible as long as the DP tensor couples the triplet component with spin parallel to the exchange field to the components of $\hat{f}$ that are perpendicular to the exchange field. This corresponds to the condition

$$\left[\left[\hat{\mathcal{A}}_k, \left[\hat{\mathcal{A}}_k, \hat{h} \right] \right], \hat{h} \right] \neq 0. \tag{3.33}$$

We now explore the dependence of the LRTC generation on the geometry of the heterostructure under the presence of Rashba and Dresselhaus SOC. We consider two basic arrangements of the interface, a transversal and lateral heterostructure.

Transversal structure

We start by studying the setup shown in Fig. 3.3 a). For simplicity we assume a interface between a S and a homogeneous F with finite SOC. In a more realistic setup the individual fields could be arranged in separate layers of F and SOC materials, similar to the DW problem shown in Fig. 3.1, but replacing

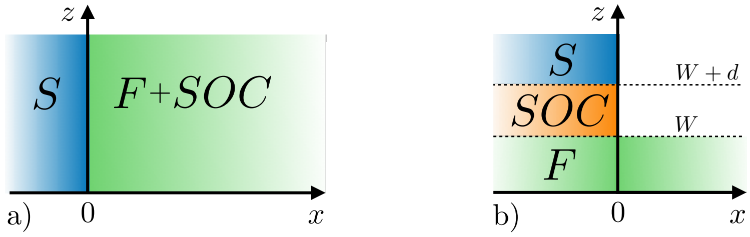

FIGURE 3.3: Scheme of the considered interface geometries, a) transversal interface and b) lateral interface.

the DW region by a SOC active layer. The structure chosen to be translational invariant in the y-z plane, thus the Rashba and Dresselhaus SOC are described by the fields

$$\hat{\mathcal{A}}_y = \alpha/2\hat{\sigma}^z - \beta/2\hat{\sigma}^y, \tag{3.34}$$

$$\hat{\mathcal{A}}_z = \beta/2\hat{\sigma}^z - \alpha/2\hat{\sigma}^y, \tag{3.35}$$

where α, β are the strengths of the Rashba and Dresselhaus SOC, respectively. As the structure is inhomogeneous in x-direction, combining the definition of the fields and Eq. (3.32) we see that there is no generation of triplet components due to spin precession effects ($\mathcal{F}_{x,0} = 0$). The remaining possibility is the generation via spin relaxation. For the above choice of SOC fields the condition (3.33) yields

$$\left[\left(\alpha^2 + \beta^2\right)\left(h^a\hat{\sigma}^a + h^x\hat{\sigma}^x\right) + 2\alpha\beta\left(h^y\hat{\sigma}^z + h^z\hat{\sigma}^y\right), h^a\hat{\sigma}^a\right] \neq 0. \tag{3.36}$$

It follows that if all exchange field components are finite, an LRTC is generated for any choice of α, β. In a more realistic structure this situation could be achieved by using multiple thin layers (below the magnetic decay length) with different orientations of the exchange field or by using a intrinsically inhomogeneous F. However, this again makes the SOC fields obsolete as this case is similar to the DW problem where we know that spin precession generates LRTCs. Therefore we consider homogeneous exchange fields in the following.

A finite exchange field component perpendicular to the interface can induce vortices at the interface which complicates the experimental situation. A more favorable setup is to have a ferromagnet with a parallel orientation of the exchange field with respect to the interface, $h^x = 0$. In this case the left hand side of Eq. (3.36) is finite only in the case when both, Dresselhaus and Rashba SOC are finite and if $h^y \neq h^z$.

Lateral structure

We now consider the case of a lateral structure as shown in Fig. 3.3 b). A superconductor and a thin SOC active layer are stacked on top of a ferromagnetic bar. The SOC field is finite only in the SOC layer

$$\mathcal{A}_k^a(x,z) = \Theta(W + d - z)\Theta(z - W)\Theta(-x)\mathcal{A}_k^a, \tag{3.37}$$

with constant $\mathcal{A}_k^a$. The Rashba and Dresselhaus SOC are defined by the fields

$$\hat{\mathcal{A}}_x = \beta/2\sigma^x - \alpha/2\sigma^y, \tag{3.38}$$

$$\hat{\mathcal{A}}_y = \alpha/2\sigma^x - \beta/2\sigma^y. \tag{3.39}$$

The exchange field has only finite components in the x-y plane,

$$\hat{h}(x,z) = h^x\hat{\sigma}^x + h^y\Theta(z)\Theta(W-z). \tag{3.40}$$

The structure is translational invariant in the y-direction. We are interested if LRTCs are generated in the F bar and their evolution along the positive x-direction. Without loss of generality we can assume that the thickness d of the SOC interlayer and the bridge W is small against the typical length on which $\hat{f}$ changes. This reduces the initial two-dimensional problem to an effective one dimensional one. Within this simplification we have a fully proximized homogeneous F with SOC coupling with an interface at $x = 0$ to a plain F. Now calculating the SU(2) electric field in direction of the spin field inhomogeneity,

$$\mathcal{F}_{x,0} = (\alpha h^x + \beta h^y)\,\hat{\sigma}^z, \tag{3.41}$$

shows that in lateral structures LRTCs appear already due to spin precession. Evaluating the condition (3.36) gives

$$\left[\left(\alpha\beta h^x + \alpha^2 h^y\right)\hat{\sigma}^x + \left(\alpha\beta h^y + \beta^2 h^x\right)\hat{\sigma}^y, h^x\hat{\sigma}^x\right] \neq 0, \tag{3.42}$$

which is finite if $h_x,\ \beta > 0$ or $h_y,\ \alpha > 0$. Clearly the lateral setup is the less restrictive geometry to generate potential LRTCs with respect to the choice of SOC and exchange field parameters. Even more importantly they allow for the interplay of both effects as we will show in the following section in a rigorous way.

3.2 Switchable Josephson current in junctions with spin-orbit coupling[*]

Motivated by the previous possibilities regarding the generation of the LRTC, in this section we study two types of lateral junctions that are good candidates for their detection and offer multiple possibilities to control the Josephson current through the spin fields. We will refer to those candidates as type 1 and type 2 junctions. The type 1 junction consists of two superconducting electrodes on top of a ferromagnetic film, as shown in Fig. 3.4 a). Between the two materials we assume there is an interlayer with a finite SOC. We refer to this junction as type 1 junction. The type 2 junction, shown in Fig. 3.4 b), consists of a similar lateral geometry, but the SOC is finite in the bridge region. Whereas type 1 junctions may correspond to junctions with a heavy metal interlayer, type 2 junctions describe, for example, a lateral Josephson junction made of a 2D electron gas in the presence of a Zeeman field and SOC. We assume that in both junctions the distance between the superconductor electrodes is larger than the magnetic

---

[*] This section has been submitted in form of an article to Physical Review B: "Switchable Josephson current in junctions with spin-orbit coupling", B. Bujnowski, R. Biele and F.S. Bergeret, (2019)

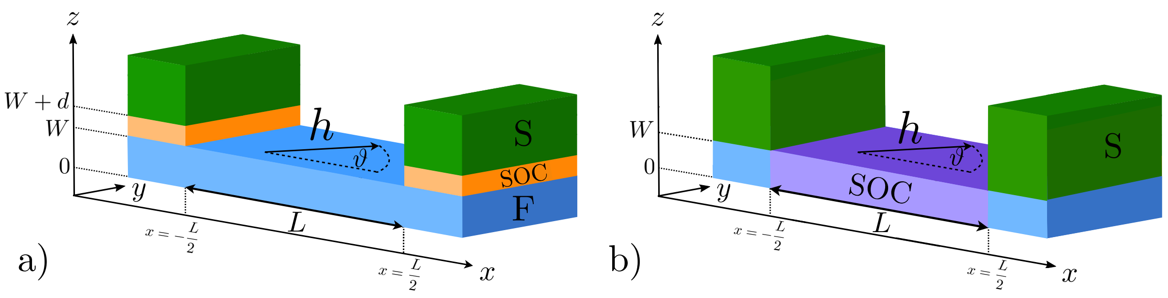

FIGURE 3.4: Schematic setup for the two junction types considered. a) The junction of type 1 consists of two superconductors with thin layers of a spin orbit coupling active material (SOC) that sit on top of a ferromagnet (F) bar separating them. The magnetization **h** is lying in the $x - y$ plane. b) For the junction of type 2 the SOC material is only present in the bridge region connecting the two superconductors.

decay length, such that the Josephson current is only carried by LRTC. We proceed as follows. With the help of an analytical solution for type 1 junctions in the case of small SOC presented in Sec. 3.2.2, we show that in leading order of the SOC coupling, i.e. only taking into account the spin precession effect, the junction remains in the 0-state independently of the direction of the exchange field. The next leading order contribution to the current is due to the inhomogeneous spin relaxation with a negative sign, such that for certain directions of the exchange field the junction can switch to the π-state. In junctions of type 1 this only occurs if both, the Rashba and Dresselhaus SOC are finite. In Sec. 3.2.3 we present numeric calculations of the current for arbitrary SOC strength that confirm these findings. In addition, the numeric calculations reveal that type 2 junctions allow for $0 - \pi$ transitions in a wider range of SOC parameters. Specifically the transition can be induced by a pure Rashba or Dresselhaus SOC by changing their strengths. This is a new possibility to induce 0-π transition by tuning the Rashba SOC strength, which is experimentally achievable by gating the SOC active material.

3.2.1 Basic equations for diffusive lateral Josephson junction with SOC

As before, we assume that the proximity effect, i.e. the induced superconducting correlations in the bridge, is weak and that the system is in the diffusive regime so we describe the spectral properties of the junction by the linearized Usadel equation generalized to linear in momentum SOC Eq. (3.20). In order to describe hybrid interfaces between the superconductor and a substrate we use the boundary conditions (3.21). For the case of an boundary to the vacuum (V) we use the boundary condition

$$\mathcal{N}_i \left[\tilde{\nabla}_i \hat{f}\right]_{X/V} = 0, \tag{3.43}$$

which corresponds to no charge current flow at the boundary. We are interested in determining the Josephson current density in the bridge region for the different structures depicted in Fig. 3.4. Including the effect of spatially constant spin active fields, it can be expressed as [103]

$$j = ie\pi\mathcal{N}_0 DT\sum_{\omega_n}\mathrm{Tr}\left\{\hat{f}\tilde{\nabla}\hat{\bar{f}} - \hat{\bar{f}}\tilde{\nabla}\hat{f}\right\}, \tag{3.44}$$

where $\mathcal{N}_0$ is the density of states and $\hat{\bar{f}} = \hat{\sigma}^y \hat{f}^* \hat{\sigma}^y$.

We now adapt the basic Eqs. (3.20) and (3.21) to the specific cases of type 1 and 2 junctions. The junctions in Fig. 3.4 are translational invariant in the y-direction. We define a step function like order parameter along the x-direction with amplitude Δ, and a phase difference of the order parameters φ between both superconductors,

$$\Delta(x, z) = \Theta(z - (W + d))\Theta(|x| - L/2)\Delta e^{i\frac{\varphi}{2}\mathrm{sign}(x)}. \tag{3.45}$$

The SOC fields are finite only in the SOC layers thus for the junction type 1,

$$\mathcal{A}_k^a(x, z) = \Theta(W + d - z)\Theta(z - W)\Theta(|x| - L/2)\mathcal{A}_k^a, \tag{3.46}$$

and for the junction type 2 with the SOC in the bridge region (Fig.3.4 b)),

$$\mathcal{A}_k^a(x, z) = \Theta(W - z)\Theta(z - W)\Theta(L/2 - |x|)\mathcal{A}_k^a \tag{3.47}$$

with constant $\mathcal{A}_k^a$ in both cases. We restrict ourselves to SOC of the Rashba and Dresselhaus type defined by the fields (3.38), (3.39). Rashba SOC corresponds to terms proportional to α while Dresselhaus SOC corresponds to terms proportional to β. For both junction types the exchange field has only finite components in the x-y plane and is present in the F-region,

$$\hat{h}(x, z) = h(\cos\vartheta\hat{\sigma}^x + \sin\vartheta\hat{\sigma}^y)\Theta(z)\Theta(W - z), \tag{3.48}$$

where $h = \sqrt{h^a h^a}$.

To distinguish components that are parallel and perpendicular to the exchange field, *i.e.* short - and long-range components, it is convenient to rotate Eqs. (3.20) and (3.21) by the unitary transformation $\mathcal{U} = e^{i\hat{\sigma}^x\frac{\vartheta}{2}}$. After the rotation the exchange field is fixed along the x-axis,

$$\mathcal{U}\hat{h}\mathcal{U}^\dagger = h\hat{\sigma}^x. \tag{3.49}$$

Thus the long-range triplet components are those polarized in y and z direction. Assuming for simplicity, that the thickness d of the SOC interlayers (if present) and the bridge W is small against the typical length on which $\hat{f}$ changes, we can integrate the Usadel equation along the z-direction [32].

Here we illustrate how the z-integration is carried out. Besides the first term in Eq. (3.20) all other terms do not contain a spatial derivative in the z-direction. Therefore the integration results simply in the averaged value of f. Integration of the first term leads to

$$\begin{aligned}\int_0^{W+d} \tilde{\nabla}_k^2 \hat{f} dz &= \int_0^{W+d} dz \left(\left(\partial_x^2 + \partial_z^2\right) \hat{f} - 2i \left[\hat{A}_x, \partial_x \hat{f}\right] - \left[\hat{A}_k, \left[\hat{A}_k, \hat{f}\right]\right]\right) \\ &\approx \gamma f_{\text{BCS}} + (W+d)\partial_x^2 \hat{f} - 2id \left[\hat{A}_x, \partial_x \hat{f}\right] - d \left[\hat{A}_k, \left[\hat{A}_k, \hat{f}\right]\right]. \end{aligned} \tag{3.50}$$

In the first step, we have used the translational invariance in y-direction and our choice of the SOC, which is step-like constant. In the second step, we use the continuity of $\hat{f}$ in the z-direction and the boundary condition Eq. (3.21) at the interface at $z = W + d$ as well as the boundary condition with the vacuum Eq.(3.43). This result holds also for junction type 2 by setting $d = 0$.

This reduces the initial two dimensional problem to an effective one-dimensional one. The z-integration causes an averaging of the couplings that differs for the two junction types. We therefore present the final equations separately for the two types.

Usadel equations for type 1 lateral junction

After performing the z-integration, and the rotation of Eq. (3.20), the resulting system of equations for the rotated anomalous Green's function $\hat{\tilde{f}} = \mathcal{U} \hat{f} \mathcal{U}^\dagger$ is

$$D\left[\partial_x^2 \tilde{f}_s\right] - 2|\omega_n| \tilde{f}_s - 2i\text{sign}(\omega_n)\bar{h}\tilde{f}_t^x = -D\bar{\gamma} f_{\text{BCS}} e^{-i\text{sign}(x)\frac{\varphi}{2}}, \tag{3.51}$$

$$D\left[\partial_x^2 \tilde{f}_t^a + 2\bar{\mathcal{C}}_x^{ab}\left(\partial_x \tilde{f}_t^b\right)\right] - 2|\omega_n|\tilde{f}_t^a - D\bar{\Gamma}^{ab}\tilde{f}_t^b = \delta_{x,a} 2i\text{sign}(\omega_n)\bar{h}\tilde{f}_s, \tag{3.52}$$

where we introduced the components of the averaged spin precession tensor

$$\bar{\mathcal{C}}_k^{ab} = \varepsilon^{acb} \mathcal{A}_k^c \tfrac{d}{W+d}, \tag{3.53}$$

and averaged Dyakonov-Perell (DP) spin relaxation tensor

$$\bar{\Gamma}^{ab} = \left(\mathcal{A}_k^c \mathcal{A}_k^c \delta_{a,b} - \mathcal{A}_k^a \mathcal{A}_k^b\right) \tfrac{d}{W+d}. \tag{3.54}$$

The averaged coupling constants are defined as $\bar{h}^a = h^a W/(W+d)$, $\bar{\alpha} = \alpha d/(W+d)$, $\bar{\beta} = \beta d/(W+d)$ and $\bar{\gamma} = \gamma/(W+d)$. The spatial dependence of the SOC fields, exchange field and order parameter in x-direction is not repeated explicitly, and is as in the definition Eqs. (3.45), (3.46) and (3.48). In the rotated system the non vanishing spin-precession tensor elements are

$$\bar{\mathcal{C}}_x^{xz} = -\bar{\mathcal{C}}_x^{zx} = -\bar{\alpha}\cos(\vartheta) - \bar{\beta}\sin(\vartheta), \tag{3.55}$$

$$\bar{\mathcal{C}}_x^{yz} = -\bar{\mathcal{C}}_x^{zy} = \bar{\alpha}\sin(\vartheta) - \bar{\beta}\cos(\vartheta). \tag{3.56}$$

The non-zero elements of the DP spin relaxation tensor are

$$\bar{\Gamma}^{xx}(\vartheta) = \bar{\Gamma}^{yy}(-\vartheta) = \left(\bar{\alpha}^2 + \bar{\beta}^2 + \bar{\alpha}\bar{\beta}\sin(2\vartheta)\right)\frac{W+d}{d}, \tag{3.57}$$

$$\bar{\Gamma}^{zz}(\vartheta) = \bar{\Gamma}^{xx}(\vartheta) + \bar{\Gamma}^{yy}(\vartheta), \tag{3.58}$$

$$\bar{\Gamma}^{xy}(\vartheta) = \bar{\Gamma}^{yx}(\vartheta) = 2\bar{\alpha}\bar{\beta}\cos(2\vartheta)\,\frac{W+d}{d}. \tag{3.59}$$

The solution of Eqs. (3.51)-(3.52) and its covariant derivative are continuous at the boundaries $x = \pm L/2$ between the different regions thus:

$$\partial_x \tilde{f}_s\big|_{x=\pm\frac{L}{2}+0^-} = \partial_x \tilde{f}_s\big|_{x=\pm\frac{L}{2}+0^+}, \tag{3.60}$$

$$\partial_x \tilde{f}_t^a\big|_{x=\pm\frac{L}{2}+0^\mp} = \left[\partial_x \tilde{f}_t^a + \bar{\mathcal{C}}_x^{ab}\tilde{f}_t^b\right]_{x=\pm\frac{L}{2}+0^\pm}. \tag{3.61}$$

The Eqs. (3.51), (3.52) together with the boundary conditions (3.60) and (3.61) fully determine the condensate within the limits of the mentioned approximations. Finally, the current in the bridge region is given by

$$j = 4\pi e\mathcal{N}_0 DT\sum_{\omega_n}\mathrm{Im}\left[\tilde{f}_s^*\partial_x\tilde{f}_s - (\tilde{f}_t^i)^*(\partial_x\tilde{f}_t^i)\right]. \tag{3.62}$$

Usadel equations for type 2 lateral junction

For the junction type 2 the SOC coupling and the exchange field are finite over the whole bridge thickness so there is no averaging of the spin fields. Consequently $\bar{h}^a = h$, $\bar{\alpha} = \alpha$, $\bar{\beta} = \beta$ and $\bar{\gamma} = \gamma/W$. Thus the z-integrated Usadel equation is like in Eqs. (3.51) and (3.52) where now

$$\bar{\mathcal{C}}_k^{ab} = \mathcal{C}_k^{ab} = \varepsilon^{acb}\mathcal{A}_k^c, \tag{3.63}$$

and the DP spin-relaxation tensor

$$\bar{\Gamma}^{ab} = \Gamma^{ab} = \mathcal{A}_k^c\mathcal{A}_k^c\delta_{a,b} - \mathcal{A}_k^a\mathcal{A}_k^b. \tag{3.64}$$

The spatial dependence of the SOC fields is now given by Eq. (3.47). The solution of this system of equations is continuous and fulfills

$$\partial_x \tilde{f}_s\big|_{x=\pm\frac{L}{2}+0^-} = \partial_x \tilde{f}_s\big|_{x=\pm\frac{L}{2}+0^+}, \tag{3.65}$$

$$\left[\partial_x \tilde{f}_t^a + \mathcal{C}_x^{ab}\tilde{f}_t^b\right]_{x=\pm\frac{L}{2}+0^\mp} = \partial_x \tilde{f}_t^a\big|_{x=\pm\frac{L}{2}+0^\pm}. \tag{3.66}$$

Thus for type 2 junctions, the condensate function is determined from Eqs. (3.51)-(3.52) and Eqs. (3.65)-(3.66). Finally the current through the junction is given by

$$j = 4\pi e \mathcal{N}_0 D T \sum_{\omega_n} \mathrm{Im}\left[\tilde{f}_s^* \partial_x \tilde{f}_s - (\tilde{f}_t^i)^* (\partial_x \tilde{f}_t^i) + (\tilde{f}_t^z)^* \left(\alpha \tilde{f}_t^x + \beta \tilde{f}_t^y\right)\right]. \tag{3.67}$$

3.2.2 The Josephson current in type 1 junctions: analytical solution

We focus on the case when the exchange interaction is the dominant energy scale, $D\alpha^2, D\beta^2, D\alpha\beta, T \ll h$. The junction is larger than the magnetic length, ξ_h, and hence the current is solely determined by the LRTC, $\tilde{f}_t^y$ and $\tilde{f}_t^z$. The other two components decay over ξ_h in the F region.

We solve the Eqs. (3.51) and (3.52) perturbatively up to second order in the SOC fields $\mathcal{A}_k^a$. In zeroth order only the singlet and triplet component parallel to the field, $\tilde{f}_{t,0}^x$, are finite. Their explicit form is given in App. B, Eq. (A.42). It is determined by

$$\partial_x^2 \tilde{f}_{t,1}^z - \frac{2|\omega_n|}{D} \tilde{f}_{t,1}^z = -2\bar{\mathcal{C}}_x^{zx} \left(\partial_x \tilde{f}_{t,0}^x\right). \tag{3.68}$$

In first order in the SOC, the component $\tilde{f}_t^z$ appears as a consequence of the precession term. The component $\tilde{f}_t^y$ appears in second order and satisfies:

$$\partial_x^2 \tilde{f}_{t,2}^y - \frac{2|\omega_n|}{D} \tilde{f}_{t,2}^y = -2\bar{\mathcal{C}}_x^{yz} \left(\partial_x \tilde{f}_{t,1}^z\right) + \Gamma_{yx}(\vartheta) f_{t,0}^x. \tag{3.69}$$

The explicit expressions for these components are given in App. A.5, Eqs. (A.49), (A.53). From these solutions we obtain the current density in the F region. The current density Eq. (3.44) is only due to the contribution of the long-range components $\tilde{f}_t^z$ and $\tilde{f}_t^y$ in Eq. (3.67). The maximum value of the Josephson current, i.e. the critical current j_c, is obtained at $\varphi = \pi/2$:

$$j_c = j\left(\varphi = \tfrac{\pi}{2}\right) = \pi e \mathcal{N}_0 D T \sum_{\omega_n} |f_x^b|^2 e^{-\kappa_\omega L} \left(\frac{\left(\bar{\alpha}\cos\vartheta + \bar{\beta}\sin\vartheta\right)^2}{2\kappa_\omega} - \frac{8\bar{\alpha}^2\bar{\beta}^2\cos^2 2\vartheta}{\kappa_\omega^3} \right) \tag{3.70}$$

where

$$f_x^b = -iD\gamma \frac{f_{\mathrm{BCS}}}{2} \frac{\mathrm{sign}(\omega_n)\bar{h}}{|\omega_n|^2 + \bar{h}^2} \overset{T \ll h}{\approx} -i\frac{\gamma\,\mathrm{sign}(\omega_n)\xi_{\bar{h}}^2}{2} f_{\mathrm{BCS}} \tag{3.71}$$

is the value of $\tilde{f}_t^x$ for zero SOC, in the F region below the superconducting electrodes far from the interface. The first term on the r.h.s of Eq. (3.70) is the lowest correction in the SOC which stems from the precession term in Eq. (3.68) which generates the long-range component $\tilde{f}_t^z$ from rotation of the short-range $\tilde{f}_{t,0}^x$. It is a positive contribution (0-junction) and depends on the direction of the exchange field. For $\vartheta = 0$ and the considered configuration, it is only finite if the Rashba SOC is nonzero (*cf.* with the numerical results shown in Fig. 3.5).

In the second order of the SOC, the contribution to the current is the negative second term in Eq. (3.70), and it is due to the spin relaxation term Γ_{yx} in Eq. (3.69), that leads to a finite $\tilde{f}_t^y$ component. This contribution is only finite if both Rashba and Dresselhaus type of SOC are present. This explains why in the case of a pure Rashba or Dresselhaus SOC the current does not change sign as a function of ϑ (see numerical results shown in Fig. 3.5 a-b,d-e).

Thus, the sign and magnitude of the critical current is determined by two competing contributions, namely spin precession and anisotropic spin-relaxation [32], which in turn depend strongly on the direction of the applied Zeeman field. For example the contribution due to spin-precession is zero whenever the SU(2) electric field strength in transport direction $\mathcal{F}_{x,0}(\vartheta) = -i\left[\hat{\mathcal{A}}_x, \hat{h}(\vartheta)\right]$ vanishes. This confirms previous theoretical investigations that identified $\mathcal{F}_{k,0}$ as the generator of the LRTC [31, 32]. According to Eq. (3.70), $\mathcal{F}_{x,0}(\vartheta) = 0$, for $\vartheta_0 = \arctan\left(-\frac{\alpha}{\beta}\right) + n\pi$. For this value of ϑ the second negative term dominates provided that $\cos 2\vartheta_0 \neq 0$, and leads to a change of sign of the critical current, a 0-π transition.

For either pure Rashba or pure Dresselhaus SOC the dependence of the critical current on ϑ is simply shifted by $\pi/2$ for the same magnitude of the SOC parameter. This can be already inferred from Eq. (3.20), which is symmetric when interchanging $\alpha \leftrightarrow \beta$ and $x \leftrightarrow y$ for the coordinate labels in spin space.

Eq. (3.70) is valid for a symmetric junction, i.e. a junction of type 1 with the same SOC at both electrodes. In the case that the left (L) and right (R) electrodes have different values for the Rashba and Dresselhaus SOCs $\alpha_{L/R}$ and $\beta_{L/R}$ it is possible to obtain a change of the critical current sign solely due to spin precession effects. Namely, the critical current up to first order in the SOC fields reads

$$j_c = \pi e \mathcal{N}_0 D T \sum_{\omega_n} \frac{|f_x^b|^2}{\kappa_\omega} e^{-\kappa_\omega L} (\bar{\alpha}_L \cos\vartheta + \bar{\beta}_L \sin\vartheta)(\bar{\alpha}_R \cos\vartheta + \bar{\beta}_R \sin\vartheta) \ . \tag{3.72}$$

By inspecting Eq. (3.72), we see that the current reversal appears every-time the SU(2) electric field strength disappears in the left or right lead $\mathcal{F}_{x,0}^{L/R} = 0$, as long as $\alpha_L\beta_R \neq \alpha_R\beta_L$. When all couplings are finite this takes place at the angles $\vartheta_0^{L/R} = \arctan\left(-\frac{\alpha_{L/R}}{\beta_{L/R}}\right) + n\pi$. The interval, where the current is reversed with respect to the symmetric case, is maximized when there is only Rashba SOC in one lead and only Dresselhaus SOC in the other as then $j_c \propto \alpha\beta \sin(2\vartheta)$.

To summarize this section, for low SOC strength, the current due spin precession effects is the dominant contribution to the critical current. If the S-electrodes are symmetric and only one type of SOC is active, the current can be switched on and off by rotating the exchange field in the x-y plane, but no 0-π transition takes place. A reversal of the current only appears if both SOC types are finite and originates in a competition between the spin-precession- and the spin-relaxation effects. A current reversal only due to spin-precession effects can be achieved by choosing leads with different SOC parameters.

3.2.3 Numerical results

In this section we compute numerically the Josephson current for both types of junctions with finite S-electrodes. The total length of the system is $L_{tot} = 2L_S + L$, where L_S is the length of the S-electrode,

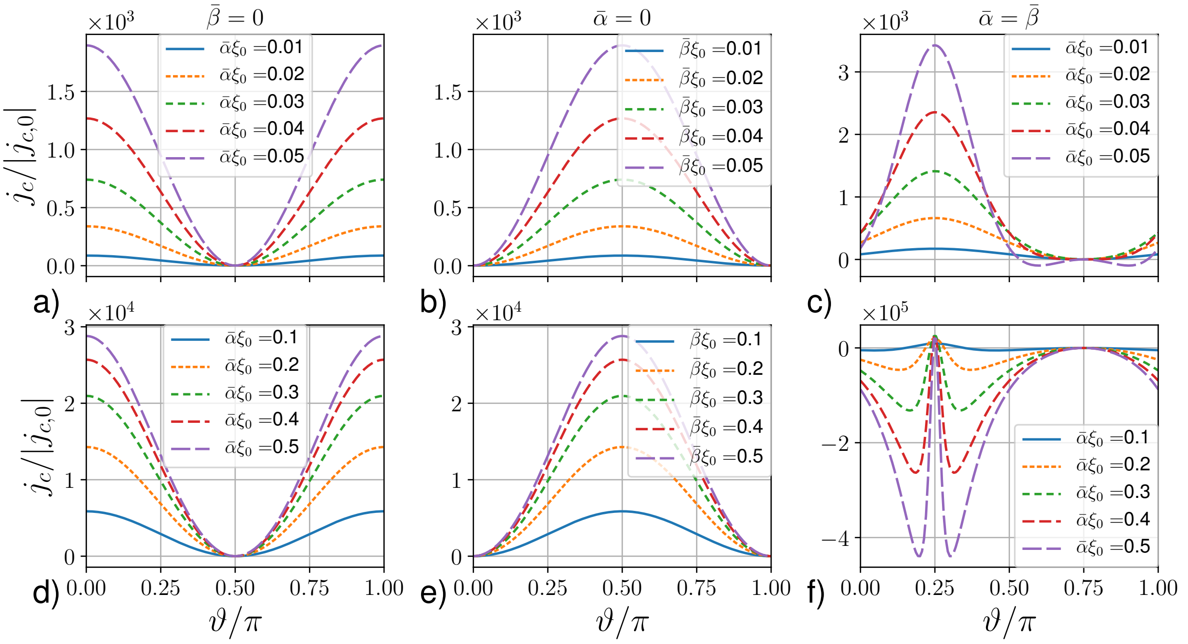

FIGURE 3.5: Numerically results for the critical current j_c, normalized by the critical current for vanishing SOC fields $j_{c,0}$, as function of the orientation of an in-plane exchange field parametrized by the angle ϑ for junction of type 1. Different curves correspond to different values of the SOC parameters. In all plots we set $\bar{h} = 10\Delta$, $L = 5\xi_0$, $T = 0.01\Delta$ and the thickness of the SOC and F layer are chosen such that $d/W = 1$.

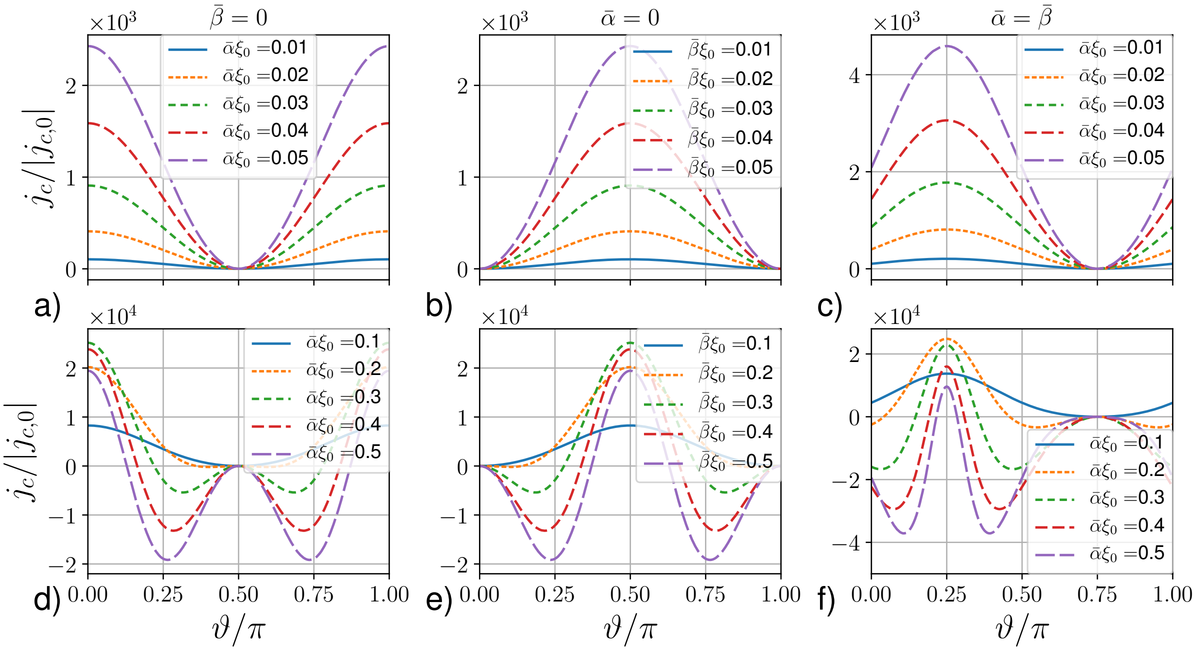

FIGURE 3.6: Numerical results for the critical current critical current j_c, normalized by the critical current for vanishing SOC fields $j_{c,0}$, as function of the orientation of an in-plane exchange field parametrized by the angle ϑ for junction of type 2. Different curves correspond to different values of the SOC parameters. In all plots we set $\bar{h} = 10\Delta$, $L = 5\xi_0$, $T = 0.01\Delta$.

and is set to $L_{tot} = 10L$. The systems of Eqs. (3.51), (3.52) is complemented by the boundary condition Eq. (3.43) at the outer interfaces:

$$\tilde{\nabla}_x \hat{f}|_{x=\pm L_{tot}/2} = 0. \tag{3.73}$$

The resulting critical current density for the junction type 1 is shown in Fig. 3.5 a) - f) and for junction type 2 in Fig. 3.6 a) - f). For low SOC strengths and any of the studied SOC types and junction types, the current vanishes when the SU(2) electric field strength vanishes in accordance with the theory [31]. Indeed, the critical current for both setups and small SOC show qualitatively identical behavior (Figs. 3.5 a) - c), 3.6 a) -c)), in very good agreement with the analytical result for the junction type 1 (Eq. (3.70). This implies that at the level of spin-precession effects both junctions behave similarly. As expected, the critical current curves for the case of pure Rashba or Dresselhaus SOC are shifted by $\pi/2$ when comparing curves of corresponding SOC strengths.

When increasing the SOC strength for junction type 1 we observe the competition between the two LRTC generating mechanisms. Comparing upper and lower panels of Fig. 3.5 we see that the current changes sign at sufficiently large SOC strengths, only when Rashba and Dresselhaus SOC are finite. For the special case when $\alpha = \beta$, for exchange field orientation $\vartheta = \pi/4$ there is no 0-π transition as the spin relaxation contribution vanishes and at $\vartheta \neq 3/4\pi$ both contributions simultaneously, which is depicted in Fig. 3.5 f).

By further increase of the SOC the numerical results shown in Fig. 3.5 f) differ qualitatively from the analytic ones: there is a strong increase of the critical current in two negative dips around $\vartheta = \pi/4$. The two negative dips move closer to $\vartheta = \pi/4$ by increasing the SOC strength. Also there is a flattening of the curve at $\vartheta = 3/4$.

The $0 - \pi$ transition due to spin precession effect in junction type 1 with asymmetric SO interaction obtained analytically in the previous section is confirmed by the numerics as shown in Fig. 3.7. In particular, the points of current reversal as function of ϑ are in agreement with the analytical result, Eq. (3.72).

The case of large SOC in type 2 junctions is shown in Fig. 3.6 d) - f). We clearly see that 0-π transitions are possible for any choice of SOC. The case when $\alpha, \beta \neq 0$ is qualitatively similar to junction type 1. In contrast, for junction 2, $0 - \pi$ transitions are possible for pure Rashba or Dresselhaus SOC when increasing the SOC strength, as shown in Fig. 3.6 c), d) and Fig. 3.8. Our results, regarding the current sign reversal, are similar to the results of Ref. [149], where a one dimensional junction with a pure Rashba has been studied. Similarly to the one dimensional case, our results for two dimensional SOC, show that the direction of the current can be inverted by tuning the strength of the Rashba SOC, which can be done by a voltage gate if the bridge region is a two-dimensional electron gas with asymmetric quantum well structure in a semiconductor. Such a gate has also been suggested in Ref. [148] for creation of a long ranged spin-triplet helix in a ballistic ferromagnetic Josephson junction.

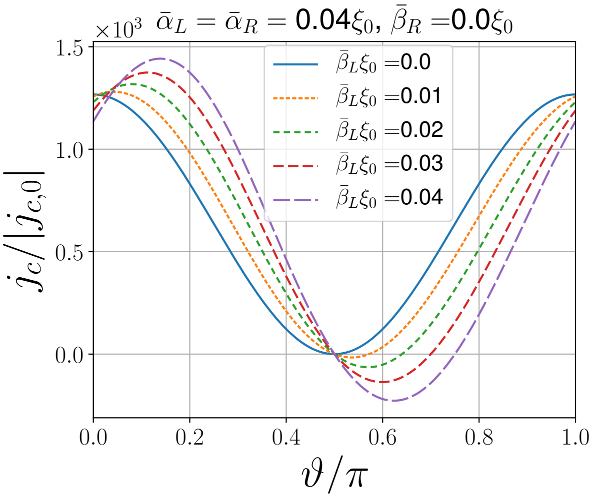

FIGURE 3.7: Numerical results for the critical current as function of the orientation of an in-plane exchange field for an asymmetric junction of type 1. We set $\bar{h} = 10\Delta$, $L = 5\xi_0$, $T = 0.01\Delta$ and $d/W = 1$.

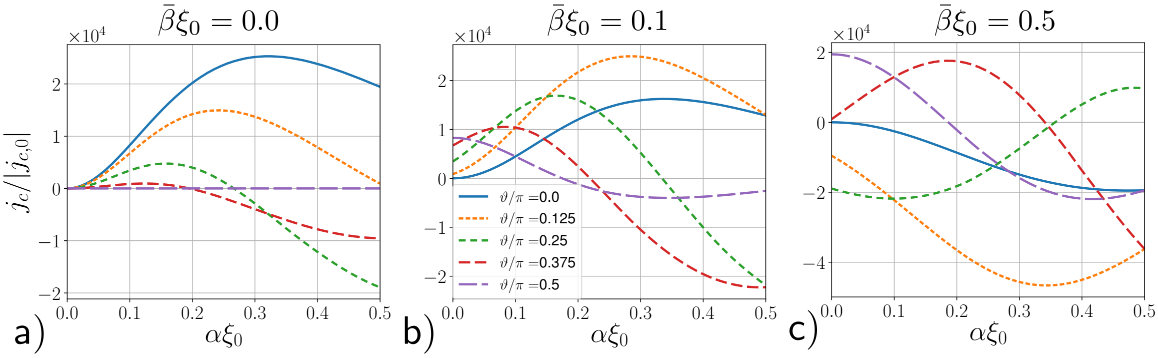

a)

FIGURE 3.8: Critical current for a junction of type 2 as function of the Rashba SOC strength α. The Dresselhaus SOC parameter β is increased from panel a) to panel c). Different curves correspond to different orientations of the exchange field. In all plots we set $\bar{h} = 10\Delta$, $L = 5\xi_0$, $T = 0.01\Delta$

3.2.4 Conclusion

In this chapter we introduced in a compact form the mechanisms leading to the generation of LRTCs in S/F and S/F/SOC hybrid junctions. We then studied the effects of Rashba and Dresselhaus SOC interaction in two types of diffusive lateral Josephson junctions. In type 1 junctions the bridge linking the superconducting electrodes is a F and the SOC fields originated from heavy metal interlayers placed between the S leads and the F bridge. In type 2 junctions the exchange field and SOC fields were finite over the whole bridge. In a realistic setup, this can be realized by a 2D semiconducting bridge in an external magnetic field. We presented analytical results of the linearized Usadel equation for the Josephson current for junction type 1, obtained by a perturbative expansion in the SOC. These analytical results where complemented by numerical calculations for both junction types. Analytical and numerical results showed good qualitative agreement and demonstrated that the magnitude and sign of the Josephson current can be controlled by varying the direction of the exchange field as well as tuning the strengths of the SOC. Besides their relevance for application as supercurrent valves we demonstrated that these lateral junctions can be used as detectors for the long-range proximity effect induced by SOC and a homogeneous exchange field.

Chapter 4

Equilibrium spin-currents and edge spin accumulation in wires with spin-orbit coupling[†]

Spin currents have been a subject of intensive investigations in several branches of condensed matter physics [30, 151–153]. In 2003 Rashba himself demonstrated that any system described by the standard two-dimensional Rashba Hamiltonian may support spin currents even in thermodynamical equilibrium [154]. Such equilibrium spin currents (ESC) in materials with spin-orbit coupling (SOC) have attracted a great deal of attention [152, 155–159] . However, the interpretation of the ESC in remained under debate for a while because in the presence of SOC the spin is not conserved in a customary sense. The theoretical controversy can be removed by treating the SOC as an external SU(2) gauge field [98, 160], but from the experimental point of view ESC still remain elusive.

In this chapter, we demonstrate a correspondence between ESC in nanowires with SOC and a transverse spin polarization induced at the edges of the wires as schematically shown in Fig. 4.1. Contrary to ESC, spin polarization can be experimentally detected. The correspondence we found, is universal in the sense that it holds for any (quasi) one-dimensional many-body system, provided the particle-particle interaction is spin-independent. Specifically, ESC appear when a magnetic field B with a component perpendicular to the SOC is applied, inducing a Zeeman splitting field, $h = g\mu_B B$. We show that this bulk ESC is always accompanied with an edge spin accumulation that is transverse to both, the Zeeman field and SOC. Hence, a measurement of the transverse spin density would be an unequivocal evidence of ESC in nanowires. Interesting, this transverse edge spin accumulation shows up not only in the normal state [161], but also when the nanowire has a superconducting gap Δ in its density of states induced, for example, by the proximity to a superconductor. In other words, we find a connection between the existence of ESC and an anomalous paramagnetic response of a superconductor that generalizes the well-established theory of the Knight-shift in superconductors [162–164].

[†] This chapter has been submitted in form of an article to Physical Review B: "Correspondence between bulk equilibrium spin-currents and edge spin accumulation in wires with spin-orbit coupling", I.V. Tokatly, B. Bujnowski and F.S. Bergeret, (2019)

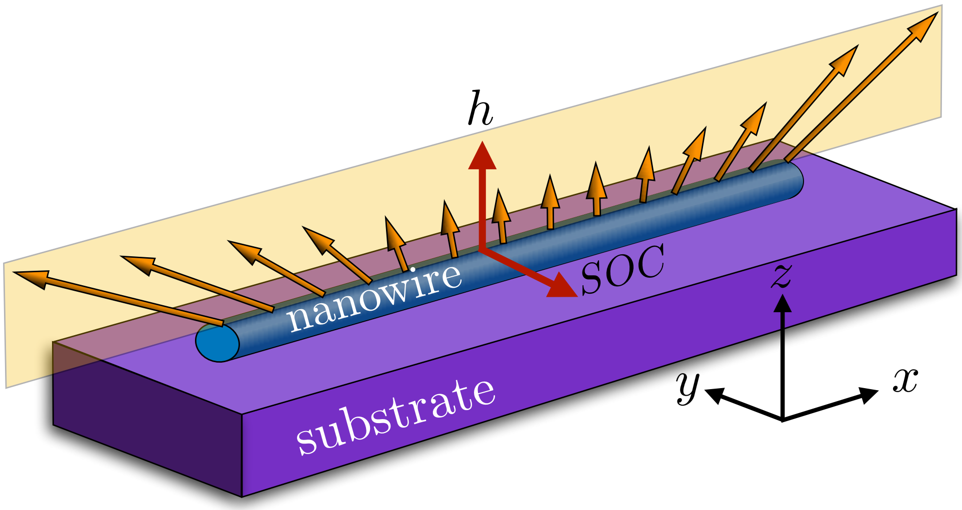

FIGURE 4.1: Schematic view of the system under consideration: A nanowire with spin-orbit coupling in a Zeeman field perpendicular to the substrate. Due to existence of an equilibrium spin current a transverse-to-the-field component of the magnetization, localized at the edges, is induced. The orange arrows represent the total induced spin. Its transverse component has opposite sign at both edges of the wire

Semiconducting nanowires with spin-orbit coupling, as InAs and InSb, contacted to conventional superconductors, have been intensively explored in recent years, mainly due to the possibility of creating Majorana zero modes and topological superconductivity in these systems [43, 45–47, 51, 52, 165–171]. It is worth noticing that both, the ESC and Majorana zero modes, require a component of the Zeeman field perpendicular to the SOC. In the context of Majorana fermions, several theoretical works have made a connection between the spin polarization induced at the edges of the wire and the the topological transition when $h = \sqrt{\mu^2 + \Delta^2}$ [51, 172–174], where μ is the chemical potential. In this chapter we show that the transverse edge spin polarization is a universal property of nanowires supporting ESC and it exists at all values of h, including those far below the topological transition. Therefore its detection cannot be associated straightaway to Majorana zero modes [51, 161], but, as we will see, to the existence of ESC.

Specifically, we show that as a function of the Zeeman field h, the total spin accumulation shows in general a cusp at $h = \sqrt{\mu^2 + \Delta^2}$. Interestingly, when $\Delta \ll \mu$, the transverse spin accumulation shows in addition a sharp maximum at $h \approx \Delta$ and can be much larger than the magnitude at the cusp when $h = \mu$. We analyze in detail this maximum of the spin accumulation and show its robustness against disorder. Finally we present analytical results for the spatial distribution of the magnetic moment induced as a response to the Zeeman field. We find that the transverse susceptibility close to the edge of the wire can be much larger than the longitudinal one, for small values of the SOC.

4.1 Bulk boundary correspondence

We consider the setup shown Fig. 4.1, where a nanowire is deposited on a substrate. The wire has an intrinsic SOC which, as usual, is assumed to be linear in momentum and determined by the symmetry of the structure. In addition, a Zeeman/exchange field h is applied perpendicular to the substrate and thus to the SOC. Without loss of generality let the wire be oriented along the x-axis, Rashba SOC along the y axis and a Zeeman field along the z-axis. The many-body Hamiltonian modeling the system reads:

$$H = \sum_{n=1}^{N} \left[\frac{\hat{\mathbf{p}}_n^2}{2m} + \alpha \hat{p}_n^x \sigma_n^y + h\sigma_n^z + V_c(\mathbf{r}_n^{\perp}, x_n) \right] + H_{int} \; , \tag{4.1}$$

where the index n labels the particles, $\hat{p}_n^k = -i\partial_{x_n^k}$ with $k = x, y, z$ are components of the momentum operator of nth particle, α is the strength of the SOC, $V_c(\mathbf{r}^{\perp}, x)$ is a confinement potential, $\mathbf{r}^{\perp} = (y, z)$, and H_{int} describes a spin-independent interaction.

The main observables we are interested here are the spin density $\mathbf{s} = (s^x, s^y, s^z)$, and components of the spin current density $\mathbf{j}_k = (j_k^x, j_k^y, j_k^z)$ By defining the spin current operator in the standard way [98, 152, 155, 157],

$$\hat{j}_k^a(\mathbf{r}) = \frac{1}{4} \sum_{n=1}^{N} \left\{ \left\{ \frac{\partial H}{\partial \hat{p}_n^k}, \sigma_n^a \right\}, \delta(\mathbf{r} - \mathbf{r}_n) \right\}, \tag{4.2}$$

and using the Hamiltonian (4.1) we obtain the following equation of motion for the spin density [98] (see Eq.(1.126))

$$\partial_t \mathbf{s} + \partial_{x^k} \mathbf{j}_k + \alpha \, \hat{\mathbf{y}} \times \mathbf{j}_x + h \, \hat{\mathbf{z}} \times \mathbf{s} = 0. \tag{4.3}$$

Here the third term is the spin-orbit torque, while the last term is the spin torque due to the Zeeman field.

Let us now concentrate on the equilibrium state. The Hamiltonian in (4.1) is real and therefore its eigenfunctions can be chosen real. This implies that in equilibrium there is no component of the spin density parallel to the SOC, $s^y(\mathbf{r}) = 0$. Similarly, we find that the system can only support an equilibrium spin current $j_k^y(\mathbf{r})$ polarized along the y-axis. Therefore in equilibrium the spin-orbit torque vanishes and the y-component of spin continuity equation (4.3) takes the form

$$\partial_{x^k} j_k^y(\mathbf{r}) + h s^x(\mathbf{r}) = 0. \tag{4.4}$$

Finally, by integrating this equation over the wire cross-section we simplify it as follows

$$\partial_x J_x^y(x) + h S^x(x) = 0 \; , \tag{4.5}$$

where $\mathbf{S}(x)$ is the line spin density along the wire, and $J_x^y(x)$ is the ESC flowing through the wire cross-section. Equation (4.5) shows that ESC in the bulk of the system may exist only if the x-component of the spin is accumulated at the edges. In other words, Eq. (4.5) establishes a correspondence between the bulk property of the system, the ESC, and the net spin accumulation transverse to the Zeeman field at the edge of a finite system. An example of this correspondence has been obtained in Ref. [161] for a non-interacting finite 1D wire contacted to leads.

In a semi-infinite wire, where all particles are confined in the right half-space, the spin accumulation at the left edge is obtained by integrating Eq.(4.5)

$$\bar{S}^x \equiv \int_{-\infty}^{+\infty} S^x(x) = -\frac{1}{h} J_x^y(\infty)\ . \tag{4.6}$$

This equation is of particular interest: On one hand it connects the ESC on the right hand side, which is a rather theoretical object [154], with a measurable quantity, the edge spin polarization (left hand side). On the other hand it provides a direct way to determine the edge spin accumulation by calculating a bulk property, the ESC, independently of boundary conditions. Clearly, for a finite wire, the transverse spin accumulation at opposite edges is equal in magnitude but oriented in the opposite direction, as shown schematically in Fig. 4.1. In the following we will use this relation to compute the transversal spin accumulation in normal and superconducting wires.

4.2 Spin current of a normal conductor

As a first example we consider a one-channel normal ballistic wire described by the 1D version of Hamiltonian (4.1) with $H_{int} = V_c = 0$ [161]. The spin current can be written as

$$J_x^y = \int \frac{dk}{2\pi} \mathrm{Tr}\left[\sigma^y \hat{v}_x \hat{\rho}_k\right] \tag{4.7}$$

with the velocity operator $\hat{v}_x = \frac{\partial H}{\partial \hat{p}_x} = \frac{k}{m} + \alpha\hat{\sigma}^y$ and the equilibrium density matrix written in terms of the projectors on the two eigenstates $E_k^{\pm} = \xi_k \pm E_k$

$$\hat{\rho}_k = \sum_{i=\pm} \rho_k^i f(E_k^i),\ \rho_k^{\pm} = \frac{1}{2}\left(\mathbb{1} \pm \frac{\alpha k \hat{\sigma} y + h\hat{\sigma}^z}{E_k}\right)\ , \tag{4.8}$$

where $\xi_k = k^2/2m - \mu$, $E_k = \sqrt{\alpha^2 k^2 + h^2}$ and $f(E)$ is the Fermi distribution function. We focus on the case $T = 0$ and $\mu, \alpha, h > 0$. Introducing the Fermi momenta for the two spin split bands

$$k^{\pm} = \sqrt{2m\left[m\alpha^2 + \mu \mp \sqrt{\left(m\alpha^2 + \mu\right)^2 + h^2 - \mu^2}\right]}\ , \tag{4.9}$$

the current can be expressed as the sum of the contributions from the two bands:

$$J_x^y = J_x^{y,-} + \Theta(\mu - h) J_x^{y,+}\ , \tag{4.10}$$

where $+, -$ labels the upper, lower band respectively. The two contributions are

$$J_x^{y,\pm} = \frac{\alpha k^{\pm}}{\pi} \pm \frac{1}{2m\pi}\left[\frac{k^{\pm}}{\alpha}\sqrt{(\alpha k^{\pm})^2 + h^2} - \frac{h^2}{\alpha^2}\ln\left(\sqrt{\frac{(\alpha k^{\pm})^2}{h^2} + 1} + \frac{\alpha}{h}k^{\pm}\right)\right]. \tag{4.11}$$

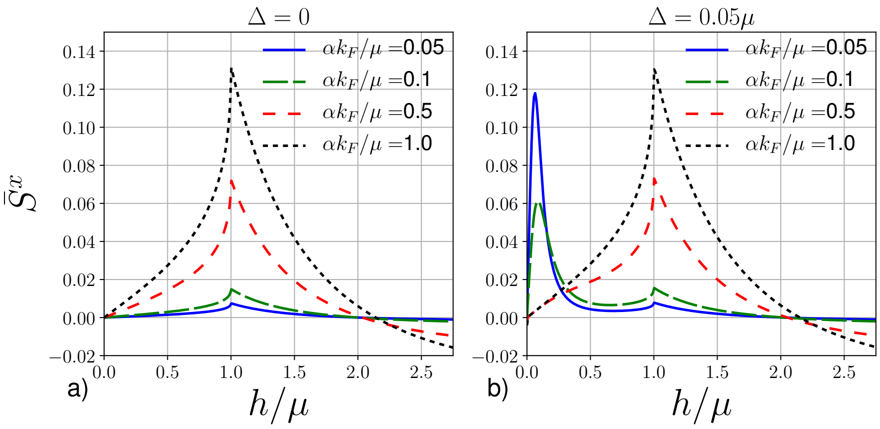

FIGURE 4.2: Transverse spin accumulation as function of the Zeeman field $h = g\mu_B B$ for various values of the SOC strength, αk_F in the a) normal and b) superconducting case at $T = 0$.

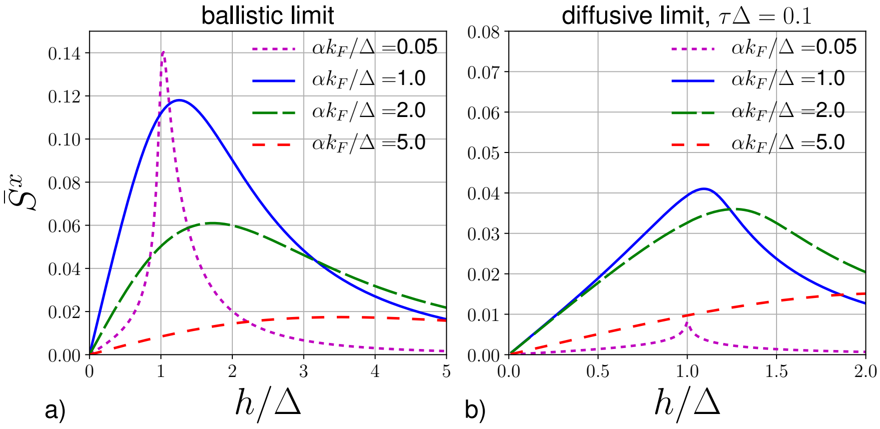

FIGURE 4.3: Spin accumulation calculated in the quasi-classical limit as function of the Zeeman field for various values of αk_F in the a) ballistic and b) diffusive limit at $T = 0$. In the diffusive limit we have chosen $\Delta\tau = 0.1$.

Clearly the ESC is finite only if both, the SOC and Zeeman field, are finite. The transverse spin accumulation can be computed by substituting Eq. (4.11) into Eq. (4.6). The result is shown in Fig. 4.2 a). By increasing h from zero towards μ, the spin current increases monotonically. At $h = \mu$, $k^+ = 0$and for larger values of h the upper band does not contribute to the current. This results in a cusp-like maximum in the spin current, also obtained in Ref. [161] for a normal wire [*].

4.3 Spin current for superconducting wire

Now we assume that the wire is placed on top of a superconductor so that it is fully proximized.

---

[*] Notice that the expression (4.6) makes a connection between the bulk spin-current and the total transverse spin. The spatial distribution of the latter has to be computed by solving the full boundary value problem. In a normal wire this was done in Ref. [161].

4.3.1 Ballistic case

We start by examining the case of a clean wire. As customary, the system is described by the Bogoliubov de Gennes (BdG) Hamiltonian, which can be obtained from Eq. (4.1) after extension to the Nambu-Spin space:

$$\mathcal{H} = \left(\frac{\hat{p}_x^2}{2m} - \mu + \alpha \hat{p}_x \hat{\sigma}^y \right) \tau_z + h\hat{\sigma} z + \Delta \tau_x \tag{4.12}$$

where Δ is the SC order parameter, and τ_j are the Pauli matrices in the Nambu space. This Hamiltonian leads to a four bands spectrum

$$E_{\pm i} = \pm \sqrt{\xi_k^2 + (\alpha k)^2 + h^2 + \Delta^2 + (-1)^i 2Q} \,, \tag{4.13}$$

with $i = 1, 2$ and $Q = \sqrt{(\xi_k^2 + \Delta^2)h^2 + \xi_k^2 \alpha^2 k^2}$. In this case the spin current can be written as

$$J_x^y = \int \frac{dk}{2\pi} \sum_{i=\pm 1, \pm 2} \mathrm{Tr} \left[P_i \hat{J}_x^y \right] f(E_i) \,, \tag{4.14}$$

where $P_i = \prod_{j \neq i} \frac{\mathcal{H} - E_j}{E_i - E_j}$ is the projection operator to the eigenstate $|n_i\rangle$ of the BdG Hamiltonian and $\hat{J}_x^y = \left(\frac{k}{m} \hat{\sigma} y + \alpha \right) \tau_z$ the spin current operator written in Nambu-spin space. Explicit evaluation of this expression at $T = 0$ gives:

$$\begin{aligned} J_x^y = {} & \frac{\alpha}{2\pi} \int dk \left\{ 1 - \frac{\xi_k}{2} \sum_{i=1,2} \left[\frac{1}{E_i} \left(1 + (-1)^i \frac{E_k^2}{Q} \right) \right] \right\} \\ & - \frac{\alpha}{2\pi} \int dk \left\{ \frac{k^2}{2m} \sum_{i=1,2} \left[\frac{1}{E_i} \left(1 + (-1)^i \frac{\xi_k^2}{Q} \right) \right] \right\} . \end{aligned} \tag{4.15}$$

It is important to note that this expression is rather general and valid for arbitrary values of the parameters. The numerical evaluation of the integral can be performed straightforwardly and shows two prominent features as seen in Fig. 4.2 b). The first one is the same cusp-like local maximum, as in the normal case, which now appears at $h = \sqrt{\mu^2 + \Delta^2}$. This value corresponds to the critical Zeeman field above which the wire is in the topological phase. It is worth mentioning that this cusp-like feature is obtained, practically, over the whole range of parameters. Only when $\mu \to 0$, and $m\alpha^2 \gg \Delta$, the transverse spin does not show a maximum at $h = \Delta$ and the discontinuity in the slope of S^x at $h = \Delta$ is smoothed out [174]. In this work we are not interested in zero chemical potential limit and focus on cases when $\mu \gg \Delta, m\alpha^2$.

The second second prominent feature as seen from Fig. 4.2 b) is the maximum that appears at values of $h \ll \mu$ and that for small enough values of α is located at $h \approx \Delta$. Interestingly, by lowering α the peak first gets narrow and simultaneously increases in magnitude exceeding by far the local maximum at the topological transition. Further decrease of α reduces the height of the peak until the spin current, and thus the spin accumulation, vanish when $\alpha \to 0$.

4.3.2 Quasi-classical limit

Since this maximum in the spin accumulation occurs at values of the fields much smaller than μ we can investigate the behavior of the transverse spin-accumulation at small α within the quasi-classical approach [175]. The spin current within this approach is given by [103],

$$J_x^a = \frac{i\pi\mathcal{N}_0}{2} T \sum_{\omega_n} \mathrm{Tr}\langle v_F \hat{\sigma}^a \check{g} \rangle . \tag{4.16}$$

Here $\check{g}$ is the quasi-classical Green's function that is obtained from the Gor'kov Green's function by the ξ-integration [175] $\check{g} = i/\pi \int d\xi \check{G}(k, \omega_n)$, $\langle \cdots \rangle$ is the average over the Fermi surface, T the temperature, $\mathcal{N}_0 = 1/(2\pi v_F)$ is the 1D density of states at the Fermi level, $\omega_n = (2n+1)\pi T$ are the Matsubara frequencies and v_F, k_F denote the Fermi velocity, Fermi momentum respectively.

To obtain the quasi-classical Green's function we start from the Gor'kov Eq. (1.36). After a Fourier transformation in time and space (assuming a constant Δ) these are

$$\begin{aligned}
&[\mathbf{i}\omega_n - \hat{\varepsilon}_k]\, \hat{\mathbf{G}}(k, \omega_n) + \Delta \hat{\mathbf{F}}(k, \omega_n) = \mathbb{1} \\
&[-\mathbf{i}\omega_n - \hat{\varepsilon}_k^c]\, \hat{\mathbf{F}}(k, \omega_n) - \Delta^* \hat{\mathbf{G}}(k, \omega_n) = 0.
\end{aligned} \tag{4.17}$$

where

$$\begin{aligned}
\hat{\varepsilon}_k &= \xi + h\hat{\sigma}_z + \alpha k \hat{\sigma}_y \\
\hat{\varepsilon}_k^c &= \xi - h\hat{\sigma}_z + \alpha k \hat{\sigma}_y .
\end{aligned} \tag{4.18}$$

and $\xi = k^2/2m - \mu$. Solving this algebraic equation for $\hat{\mathbf{G}}$ we find for its components in spin space

$$G_i = \frac{\tilde{G}_i}{(\xi - \xi_1)(\xi + \xi_1)(\xi - \xi_1^*)(\xi + \xi_1^*)} \tag{4.19}$$

with the linearized dispersions

$$\begin{aligned}
\pm\xi_1 &= \pm\mathbf{i}\sqrt{(\omega_n^2 + \Delta^2 - \alpha^2 k_F^2 - h_z^2 + 2\mathbf{i}\sqrt{\alpha^2 k_F^2 (\omega_n^2 + \Delta^2) + h^2\omega_n^2}} \\
\pm\xi_1^* &= \mp\mathbf{i}\sqrt{(\omega_n^2 + \Delta^2 - \alpha^2 k_F^2 - h_z^2 - 2\mathbf{i}\sqrt{\alpha^2 k_F^2 (\omega_n^2 + \Delta^2) + h^2\omega_n^2}}
\end{aligned} \tag{4.20}$$

and

$$\begin{aligned}
\tilde{G}_0 &= -\xi_k^3 - \mathbf{i}\omega_n \xi_k^2 - \xi_k - \mathbf{i}\omega_n \left(h^2 + \alpha^2 k_F^2 + \Delta^2 + \omega_n^2\right) \\
\tilde{G}_x &= 0 \\
\tilde{G}_y &= -\alpha k_F \left((\omega_n - \mathbf{i}\xi_k)^2 + \alpha^2 k_F^2 + h^2 + \Delta^2\right) \\
\tilde{G}_z &= -h \left(h^2 + \alpha^2 k_F^2 - \Delta^2 + (\omega_n - \mathbf{i}\xi_k)^2\right) .
\end{aligned} \tag{4.21}$$

To obtain the quasi-classical limit we are left with calculating the integral

$$g_i(\omega_n) = \frac{\mathbf{i}}{\pi}\int d\xi_k \frac{\tilde{G}_i}{(\xi_k-\xi_1)(\xi_k+\xi_1)(\xi_k-\xi_1^*)(\xi_k+\xi_1^*)}. \tag{4.22}$$

Using the contour consisting of two half circles above and below the real axis with opposite orientation (Eilenberger contour)

$$g_i(\omega_n) = \frac{\mathbf{i}}{4\mathrm{Im}\left[\xi_1^2\right]}\left(\frac{\tilde{G}_i(\xi_1)+\tilde{G}_i(-\xi_1)}{\xi_1} + \frac{\tilde{G}_i(\xi_1^*)+\tilde{G}_i(-\xi_1^*)}{\xi_1^*}\right). \tag{4.23}$$

then

$$g_y(\omega_n) = -\frac{\mathbf{i}\alpha k_F}{R}\mathrm{Im}\left[\frac{w_n^2+\Delta^2+\mathbf{i}R}{\sqrt{w_n^2+\Delta^2-h^2-\alpha^2k_F^2+2\mathbf{i}R}}\right] \tag{4.24}$$

with $R = \sqrt{h^2\omega_n^2+\alpha^2(\omega_n^2+\Delta^2)}$.

At $T\to 0$ we obtain for the spin current

$$J_x^y = \int\frac{d\omega}{\pi}\mathrm{Im}\left[\frac{\alpha k_F\left(\omega^2+\Delta^2+iR\right)}{R\sqrt{\omega^2+\Delta^2-h^2-\alpha^2k_F^2+2iR}}.\right] \tag{4.25}$$

From this expression and Eq. (4.6) we compute the dependence $S^x(h)$ around $h=\Delta$, which is shown in Fig. 4.3 a). As expected, in this range of parameters, the quasi-classical result agrees with the exact calculation (*cf.* Fig. 4.2 b). In particular, the peak is more pronounced for small values of SOC and washes out with increasing SOC strength. At $h=\Delta$ and for $\alpha k_F/\Delta \ll 1$ the integral can be approximated keeping only leading order terms in $(\alpha k_F)/\Delta$

$$J_x^y \approx \frac{2\alpha k_F}{\pi}\int_0^\infty d\omega\mathrm{Im}\left[\frac{\Delta^2}{\sqrt{2i}R^{\frac{3}{2}}}\right]. \tag{4.26}$$

With $\alpha k_F/\Delta \ll 1$ we can approximate $R\approx\Delta\sqrt{\omega^2+(\alpha k_F)^2}$, and the integrand becomes

$$J_x^y \approx -2\sqrt{\frac{\alpha k_F\Delta}{\pi}}\frac{\Gamma(5/4)}{\Gamma(3/4)}. \tag{4.27}$$

For finite temperature the integral converts into a sum over Matsubara frequencies

$$J_x^y = \alpha k_F T\sum_n \mathrm{Im}\frac{\omega_n^2+\Delta^2+iR}{R\sqrt{\omega_n^2+\Delta-h^2-(\alpha k_F)^2+2iR}} \tag{4.28}$$

Following the derivation as for $T=0$, if $h=1$ and $a\ll 1, T$ we can approximate the sum so that

$$J_x^y \approx 2\alpha k_F T\sum_{n=0}^{\infty}\mathrm{Im}\frac{\Delta^2}{\sqrt{2i}R^{3/2}} = -\alpha k_F T\sqrt{\Delta}\sum_{n=0}^{\infty}\frac{1}{(\omega_n^2)^{3/4}} = -\frac{\alpha k_F}{\pi^{3/2}}\sqrt{\frac{\Delta}{T}}\sum_{n=0}^{\infty}\frac{1}{|2n+1|^{3/2}}. \tag{4.29}$$

4.3.3 Diffusive limit

So far we have considered a pure ballistic situation. It is however known that s-wave superconductivity is insensitive against elastic disorder, and therefore one would expect to obtain qualitative similar results for a disorder superconducting nanowire supporting ESC. Notice that in this case the wire is a multiband wire described by Hamiltonian Eq. (4.1) which can be considered as a quasi-one dimensional wire when its lateral dimensions are much shorter than the superconducting coherence length but larger than the elastic mean free path. In this case the spin current can be written in terms of the isotropic in momentum quasi-classical Green's function [105] that we introduced in Eq. (1.148). Here we will denote it by $\breve{\mathfrak{g}}$ for better distinguishability. Then the spin current is given by

$$J_x^y = -i\frac{\pi D}{2}\mathcal{N}_0 T\sum_{\omega_n}\mathrm{Tr}\left\{\hat{\sigma}^y\breve{\mathfrak{g}}\tilde{\nabla}_x\breve{\mathfrak{g}}\right\}, \tag{4.30}$$

where $D = v_F^2\tau$ is the diffusion constant in 1D, τ is the momentum relaxation time, $\tilde{\nabla}_x\cdot = \partial_x\cdot - i(\kappa_\alpha/2)\left[\hat{\sigma}^y,\cdot\right]$, and $\kappa_\alpha = 2m\alpha$ is the inverse of the spin precession length. To find $\breve{\mathfrak{g}}$ we solve the Usadel equation for a bulk system [105]

$$\frac{1}{2}\left[\hat{\Gamma}\breve{\mathfrak{g}},\breve{\mathfrak{g}}\right] - \left[\left(\hat{\omega}_n - ih\hat{\sigma}_z\right)\tau_3 + \Delta\tau_1,\breve{\mathfrak{g}}\right] = 0 \tag{4.31}$$

where $\hat{\Gamma}\breve{\mathfrak{g}} = \left[\hat{\sigma}^y,\left[\hat{\sigma}^y,\breve{\mathfrak{g}}\right]\right]/4\tau_\alpha$, and $1/\tau_\alpha = D\kappa_\alpha^2$ is the inverse Dyakonov-Perel spin relaxation time. The Green's function has to fulfill the normalization condition $\breve{\mathfrak{g}}^2 = \mathbb{1}$.

The matrix structure of the quasi-classical Green's functions entering the Usadel equation is $\breve{\mathfrak{g}} = \hat{\mathfrak{g}}\tau_3 + \hat{\mathfrak{f}}\tau_1$ and for a Zeeman field in z-direction the matrices $\hat{\mathfrak{g}}$ and $\hat{\mathfrak{f}}$ are diagonal in the spin space with components $\mathfrak{g}^\pm$ and $\mathfrak{f}^\pm$ respectively.

At $T = 0$ the expression for the equilibrium spin current, Eq. (4.30), reduces to

$$J_x^y = -\frac{\alpha k_F}{\Delta}\Delta\tau\int\frac{d\omega}{\pi}\left(1 - \mathfrak{g}^+\mathfrak{g}^- - \mathfrak{f}^+\mathfrak{f}^-\right);. \tag{4.32}$$

Substituting in this equation the solution of Eq. (4.31) and after using our correspondence, Eq. (4.6) one obtains the transverse spin accumulation as shown in Fig. 4.3 b). Thus, also in the diffusive limit we find a maximum S^x at $h \approx \Delta$ for small values of SOC.

In the limit $T \ll 1/\tau_\alpha \ll h \sim \Delta$ we obtain that, within logarithmic accuracy, the spin current of Eq. (4.32) is given by

$$J_x^y \approx \frac{2}{3}\frac{\alpha k_F}{\pi}\Delta\tau\log\left(\Delta\tau_\alpha\right)\ . \tag{4.33}$$

Thus, in the diffusive case the peak in the spin-current at $h = \Delta$ for small values of the SOC is reduced by a factor $\sim \delta\log\delta$, with $\delta = \Delta\tau\sqrt{\frac{\alpha k_F}{\Delta}} \ll 1$, with respect to the pure ballistic case, *cf.* Eq. (4.27). This explains the difference between the peak heights in Figs. 4.3 a) - b), for $k_F\alpha = 0.05\Delta$. Notice however that this difference is not that pronounced for larger values of the SOC.

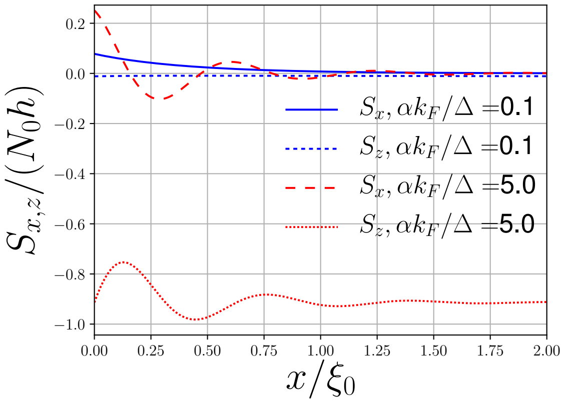

FIGURE 4.4: Spatial dependence of the mangetization parallel (M_z) and perpendicular (M_x) to the exchange field for a semi-infinite wire at $T = 0$ and different values of SOC.

4.3.4 Spatial distribution of the Magnetization

Previously, we have used the general expression Eq. (4.6) to relate the bulk ESC to the transverse spin-polarisation, $\bar{S}^x$ in a finite wire (see Fig. 4.1). We understand that $\bar{S}^x$ accumulates at the edge and decays from the edge towards the bulk, but the exact spatial distribution has to be determined in each particular case. In the normal state the dependence $S^x(x)$ was computed numerically in Ref. [161] for a wire connected to two leads and for values of h of the order of $|\mu|$. Here we focus on the superconducting state in the relevant quasiclassical regime, $h \ll \mu$, for which the Eilenberger equation holds

$$\pm v_F \partial_x \check{g}_\pm = i \left[\pm \alpha p_F \hat{\sigma}^y + \tau_3 \left(i\omega_n + h\hat{\sigma}^z\right) + i\tau_2 \Delta, \check{g}_\pm\right] \ . \tag{4.34}$$

Here $\check{g}_\pm$ denotes the the Green's functions for both propagation directions $\pm v_F$. We assume that the wire extends over the region $x > 0$. At the edge, $x = 0$ no current flows and the boundary condition imposes that $\check{g}_+(0) = \check{g}_-(0)$. We focus here on the spin susceptibility, *i.e.* the magnetic linear response of the system in the presence of a small Zeeman field. In other words we compute the spatial dependence of the spin in linear order in h. To this end we perform perturbation theory and write the solution of Eq. (4.34) as $\check{g}_\pm(x) = \check{g}_{\text{BCS}} + \delta\check{g}_\pm(x)$ where $\check{g}_{\text{BCS}} = (\omega_n \tau_3 + \Delta\tau_2)/E$ and $E = \sqrt{\omega_n^2 + \Delta^2}$. The spin density, is then obtained from

$$\delta S_j = \pi i T N_0 \frac{1}{8} \sum_{\omega_n} \text{Tr}\left[\tau_3 \hat{\sigma}^j \delta\check{g}^s\right] , \tag{4.35}$$

where $\delta\check{g}^s = \delta\check{g}_+ + \delta\check{g}_-$. Specifically, we obtain

$$\delta\check{g}^s = \frac{2h\Delta\check{g}_{\text{BCS}}\tau_1}{E^2 + (\alpha k_F)^2}\left[\hat{\sigma}^z + \frac{\alpha k_F}{E} e^{-\left(i\hat{\sigma}^y \kappa_\alpha + \frac{2E}{v_F}\right)x}\right] . \tag{4.36}$$

The detailed calculation can be found in the App.A.6.

$$\frac{S_x}{S_0} = \Delta^2 \pi T \sum_{\omega_n} \frac{\alpha k_F \cos(\kappa_\alpha x)}{E^2\left(E^2 + (\alpha k_F)^2\right)} e^{-\frac{2Ex}{v_F}} , \tag{4.37}$$

$$\frac{\delta S_z}{S_0} = \Delta^2 \pi T \sum_{\omega_n} \frac{E + \alpha k_F \sin(\kappa_\alpha x) e^{-\frac{2Ex}{v_F}}}{E^2 (E^2 + (\alpha k_F)^2)} , \tag{4.38}$$

where $S_0 = h\mathcal{N}_0$ is the Pauli paramagnetic term. This is a remarkable result that shows that in a finite system, besides the longitudinal response $S_z = \delta S_z - S_0$, there is a finite transverse magnetisation M_x accumulated at the edge of the sample which decays toward the bulk over the superconducting coherence length. At low temperatures, the ratio S_x/S_z at the edge of the sample, $x = 0$, is proportional to $\Delta/\alpha k_F$ and therefore the transverse magnetisation can be much larger than S_z provided $\alpha p_F \ll \Delta$. This result generalises the well-established theory of paramagnetic response of superconducting systems with intrinsic SOC [164]. The full spatial dependence of $S_{x,z}(x)$ is shown in Fig. 4.4.

4.3.5 Conclusion

In summary, we have demonstrated a universal correspondence between equilibrium spin currents and a transverse spin accumulation in wires with SOC and a perpendicular Zeeman field. Such spin accumulation appears in both normal and superconducting state. In the normal state the total edge spin is maximized for values of h of the order of the chemical potential μ. More interestingly, in the superconducting state the effect can be maximized at values of the SOC and Zeeman energy much smaller than μ. We demonstrated that this effect is robust against disorder and manifest in a hitherto unknown transverse magnetic susceptibility in finite systems.

Chapter 5

Weyl semimetal interfaces as chiral valves

The previous chapters focused on superconducting heterostructures, where the normal state dispersion was quadratic in momentum. Within the last months of my thesis, the aim was to study the proximity effect in heterostructures between superconductors and the recently discovered Weyl semimetals (WSM) [55–57]. WSMs are a new exciting material class exhibiting a pseudo-relativistic linear dispersion around so-called Weyl points in the Brillouin zone and unusual surface states called Fermi arcs, that are a consequence of the topological structure of the bulk dispersion. As preliminary work I studied the ballistic transport properties of WSM heterostructures in the normal state. This led to the discovery of an interesting filtering effect that is the topic of this chapter. The extension to interfaces with superconductors will be the subject of future work.

The possibility of filtering quantum mechanical degrees of freedom is the essence of computation. For instance, transistor-based electronics relies on the filtering of electric charge to control the flow of current, while spintronics relies on filtering the spin-up or spin-down projection to encode information [176–178]. In metals where the low-energy quasiparticles behave as pseudo-relativistic particles, such as two-dimensional graphene and three-dimensional WSMs [54], there exist additional degrees of freedom which can serve as alternatives for computation. In two-dimensions, Dirac quasiparticles are excitations around specific quasiparticle momenta known as valleys, with linear dispersion relations. By selectively populating a single valley this degree of freedom may be used to encode information, a possibility referred to as valleytronics [179, 180].

In three-dimensions, Weyl quasiparticles are excitations with a linear dispersion around pairwise occuring Weyl nodes at arbitrary points in momentum space of opposite chirality. The chirality is a quantum-mechanical degree of freedom that refers to whether the quasiparticle momentum is pointing parallel or anti-parallel to its spin. Similarly to the valley filter, a chirality filter may be used to encode information.

This chapter is organized as follows. In Sec. 5.1 we recall the Dirac equation and the Weyl equation that describe relativistic massive and massless spin $1/2$ fermions respectively. Based on this, we make the connection to solid-state realizations of such fermions and introduce the minimal model describing these quasiparticles. We then use this model in Sec. 5.2 to study the ballistic transport properties of an interface between two Weyl semimetals.

5.1 Dirac materials and Weyl semimetals

In 1928 Dirac succeeded in finding a formulation of single particle quantum mechanics in accordance with special relativity. The theory had to be be Lorentz invariant, thus in such a relativistic wave equation time and space derivatives had to appear at the same order. Also for the particle density to be positive definite, the time derivative had to be first order. Dirac wrote the Ansatz ($\hbar = c = 1$)

$$i\partial_t \Psi = (\boldsymbol{\alpha}\hat{\mathbf{p}} + \beta m)\,\Psi. \tag{5.1}$$

Here $\boldsymbol{\alpha}$ and β are Hermitian operators that are spatially constant and only act on inner degrees of freedom. Demanding that the spectrum of the Hamiltonian agrees with the classically know relationship $E^2 = \mathbf{p}^2 + m^2$ implies that the operators α_i and β obey the following conditions:

$$\alpha_i^2 = \beta^2 = \hat{1}, \tag{5.2}$$

$$\{\alpha_i, \alpha_j\} = 0, \tag{5.3}$$

$$\{\alpha_i, \beta\} = 0. \tag{5.4}$$

Using these relationships allows to rewrite the Dirac Eq.(5.1) in a way that highlights its covariance. Multiplying β from the left and defining the matrices $\gamma^0 = \beta$, $\gamma^i = \beta\alpha^i$ and casting them into a four-vector γ^μ gives

$$(i\gamma^\mu \partial_\mu - m)\,\Psi = 0. \tag{5.5}$$

The conditions (5.2)-(5.4) imply that the matrices γ^μ satisfy the Dirac algebra

$$\{\gamma^\mu, \gamma^\nu\} = 2g^{\mu\nu}, \tag{5.6}$$

where $g^{\mu\nu} = \mathrm{diag}(1, -1, -1, -1)$ is the Minkowski metric tensor. There exist infinitely many representations for the γ^μ matrices, however it can be shown that the smallest possible representation is in terms of 4×4 matrices [181]. In the following we will use the chiral representation,

$$\gamma^0 = \begin{pmatrix} 0 & \hat{1} \\ \hat{1} & 0 \end{pmatrix} = \hat{1} \otimes \tau_x, \quad \gamma^i = \begin{pmatrix} 0 & \sigma^i \\ -\sigma^i & 0 \end{pmatrix} = i\sigma^i \otimes \tau_y. \tag{5.7}$$

The introduced τ_i matrices are the same as the Pauli matrices σ^i but operate in the chiral subspace. In a 4-dimensional representation, the wave function Ψ must be a 4-vector (Dirac spinor)

$$\Psi = (\psi_1, \psi_2, \psi_3, \psi_4)^{\mathrm{T}} := (\Psi_-, \Psi_+)^{\mathrm{T}}. \tag{5.8}$$

We decomposed the Dirac spinor into Ψ^- and Ψ^+ which are its projections onto to the two chiral subspaces. In this chiral basis the Dirac equation reads

$$(i\partial_t - \boldsymbol{\sigma}\hat{\mathbf{p}})\,\Psi^+ = m\Psi^- \tag{5.9}$$

$$(i\partial_t + \boldsymbol{\sigma}\hat{\mathbf{p}})\,\Psi^- = m\Psi^+, \tag{5.10}$$

so a finite mass mixes both subspaces.

In the massless limit the two equations decouple into two Weyl equations [182]

$$i\partial_t \begin{pmatrix} \Psi^- \\ \Psi^+ \end{pmatrix} = \begin{pmatrix} \mathcal{H}^- & \hat{0} \\ \hat{0} & \mathcal{H}+ \end{pmatrix} \begin{pmatrix} \Psi^- \\ \Psi^+ \end{pmatrix} \tag{5.11}$$

with the Weyl Hamiltonians $\mathcal{H}^\tau = \tau\boldsymbol{\sigma}\mathbf{p}$ where $\tau = \pm 1$. The quasiparticles described by the decoupled spinors Ψ^- and Ψ^+ are Weyl fermions with left-handed and right-handed chirality, respectively. The chirality is a symmetry of the Hamiltonian (5.11), as can be seen by defining the chirality operator

$$\gamma^5 = i\gamma^0\gamma^1\gamma^2\gamma^3 = -\hat{1}\otimes\tau_z. \tag{5.12}$$

It anti-commutes with all the other matrices γ^μ and commutes with the Hamiltonian (5.11). The spinors $(\Psi^-, 0, 0)^{\mathrm{T}}$ and $(0, 0, \Psi^+)^{\mathrm{T}}$ are eigenstates of γ^5 with eigenvalues ± 1 which correspond to their left- or right-handedness. Besides this rather mathematical introduction of the chirality as a conserved quantity in the massless case, it is the sign of the spin projection along the direction of the momentum of the particle.

From a particle physics perspective, all fermions are Dirac fermions and Weyl fermions have not been discovered as elementary particles. However, in solid-state systems, Weyl fermions can exist as low-energy excitations around certain points in three-dimensional momentum space. Materials exhibiting such linear band dispersions described by the Weyl Eqs. (5.11) are called Weyl semimetals, and the points in momentum space where these bands cross are called Weyl nodes.

In a solid-state system the realization of a vanishing mass term is rather unrealistic and the Weyl fermions would gap out as shown in Fig. 5.1 a). Nevertheless there exist ways to protect the linear band crossings, even in presence of a mass term. One possibility is by imposing additional symmetries. This leads to the case of a Dirac semi-metal, where two doubly degenerate Dirac cones exist at the same point in momentum space, but the Weyl fermions remain decoupled. Another possibility is to break one of the two inherent symmetries of the Dirac and Weyl Hamiltonian, inversion symmetry $\mathcal{I}$ or time-reversal symmetry $\mathcal{T}$. This splits the previously degenerate Dirac cones and gives rise to two Weyl nodes that are separated in energy and momentum space.

The low-energy physics for these cases is encoded in the minimal Hamiltonian

$$\mathcal{H}(\mathbf{k}) = \begin{pmatrix} \mathcal{H}^+(\mathbf{k}) & m \\ m & \mathcal{H}^-(\mathbf{k}) \end{pmatrix}, \tag{5.13}$$

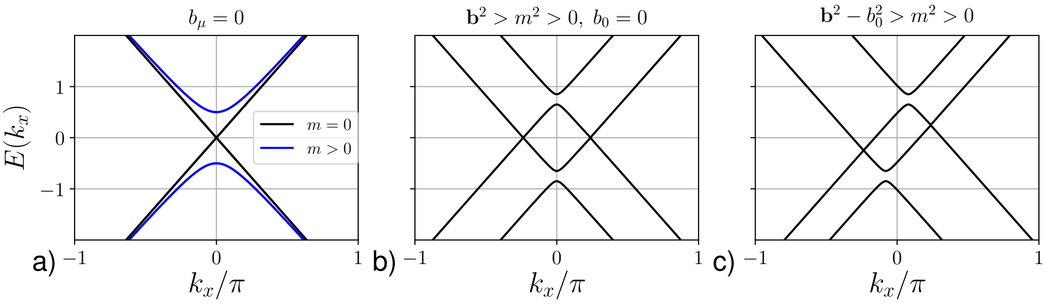

FIGURE 5.1: Dispersions of the minimal model Eq. (5.13) for the different gapless cases. a) Dispersion of the Dirac equation in the gapless and massive case. b) Splitting of the Dirac cones due to time reversal symmetry breaking fields. c) Time-reversal and inversion symmetry breaking fields shift the nodes in momentum and energy space.

where each block

$$\mathcal{H}^\tau(\mathbf{k}) = \tau b_0 + \boldsymbol{\sigma}.(\tau\mathbf{k} - \mathbf{b}) - \mu\,, \tag{5.14}$$

describes the dynamics of a Weyl fermion around the node $\tau = \pm 1$ in $\mathbf{k}$-space, where we set the Fermi velocity to unity, $v_F = 1$. Further μ is the chemical potential and, as in the Dirac Eq. (5.5), the parameter m describes an eventual coupling between the two Weyl nodes. The terms proportional to the parameters b_0 and $\mathbf{b}$, correspond to the $\mathcal{I}$ and $\mathcal{T}$ breaking fields, respectively. In general, the parameters are specific to a given WSM, and can be tuned, to some extent, by applying strains or modifying the internal magnetization of the material. We gather the parameters within a 4-vector notation $b_\nu = (b_0, \mathbf{b})$. The case of interest is when the system is gapless, which is true as long as $b_\nu b^\nu = -b_0^2 + \mathbf{b}^2 > m^2$. Then the Weyl node separation in 4-notation reads:

$$\delta\mathbf{K}_\nu = 2b_\nu\sqrt{1 - \frac{m^2}{|b_\mu b^\mu|}}. \tag{5.15}$$

Clearly the terms proportional to $\mathbf{b}$ cause Weyl node seperations in momentum space, what is schematically shown for the massive case in Fig. 5.1 b). The term proportional to b_0 is responsible for shifts of the Weyl nodes in energy space, as shown in Fig. 5.1 c), and can for example appear due to the presence of inversion breaking SOC [183].

In Sec.5.2, we mainly investigate the case of completely decoupled Weyl nodes, namely $m = 0$. Then the electronic spectrum is given by:

$$E_\tau(\mathbf{k}) = \tau b_0 - \mu \pm |\,\mathbf{k} - \tau\mathbf{b}\,|\,, \tag{5.16}$$

describing conical dispersion around nodes located at $\mathbf{k} = \pm\mathbf{b}$, and are also shifted in energy by $2b_0$. The chemical potential μ and the energy shift b_0 set the sizes of the Fermi surfaces which consist in two spheres of radius $\mu_\tau = \mu - \tau b_0$, centered at $\tau\mathbf{b}$. Depending on the relative values of the chemical potential, energy shift $2b_0$ and momentum shift $2\mathbf{b}$, these Fermi spheres might merge into a single Fermi surface through a Lifshitz transition. In this work, we avoid such a situation, thereby keeping always two well-separated Fermi spheres (Fig. 5.2).

5.2 Weyl semimetals and chiraltronics

The controlled population of a single chirality is experimentally challenging. One of the main proposals in this direction is to design interfaces that, upon varying an external parameter can transmit one, none or both chiralities. Under specific conditions a barrier between electron and hole doped materials, a p-n junction, can act as a chirality filter. For example, two Weyl quasiparticles with linear dispersion relations tilted in a given direction, known as a tilted Weyl cone, allows perfect transmission of a single chirality at particular incident angles [60]. This is possible since the tilt determines the existence of states across the barrier that conserve the momentum parallel to the interface; in its absence both chiralities would be transmitted with equal probability [59]. However, doping metals is experimentally challenging and therefore p-n junctions composed of WSMs have not been experimentally realized.

An alternative proposal to achieve a chirality filter is to use strain engineering. Mechanical strain acts for low-energy Weyl quasiparticles as an emergent chirality dependent pseudo-electromagnetic field [184]. Wave packets of different chiralities subject to these fields can trace out different trajectories, enabling the filter [185]. Although analogues of strain coupling to Weyl dispersions have been achieved in Weyl acoustic metamaterials [186] and photonic systems [187], the required strain profiles to achieve a chirality filter in electronic systems is far from being realized. In this work we propose a simpler alternative to design a three-dimensional chirality filter. The filter is based on interfacing two distinct chiral WSMs, for which the Weyl nodes are separated in energy and momentum. Due to the difference in Weyl node separation across the interface, the two chiralities may experience different transmission probabilities. Depending on the difference of the Weyl node separation on both sides of the interface and the bias voltage, it is possible to achieve transition of one, none or both chiralities. The filtering does not require differences in doping [59, 60], potential barriers [61, 62], or external fields [63, 64].

5.2.1 Interface between two Weyl/Dirac materials

We consider a planar interface between two WSMs (WSM_1/WSM_2), each one being described by a generic model Eq. (5.13) with its own parameters. The shift parameters are denoted $(b_{0,L}, \mathbf{b}_L)$ (resp. $(b_{0,R}, \mathbf{b}_R)$) for the material located in the half-space $x < 0$ (resp. $x > 0$). The general condition for transmission/blocking at the nodes between same chirality $\tau = \pm$ is that the projections of the Fermi surfaces around the nodes in WSM_1 and WSM_2 onto the interface plane have to overlap/be disjunct. This geometric condition is particularly simple in the massless case when the Fermi surfaces are spheres. Then the sum of the radii of the Fermi spheres, attached to the nodes of a distinct chirality on both sides of the interface must be bigger/smaller then their Weyl node separation in momentum space, i.e.

$$\left|\mu_L + E - \tau b_0^L\right| + \left|\mu_R + E - \tau b_0^R\right| \gtrless \left|(\mathbf{b}_L - \mathbf{b}_R)_{\|}\right| . \tag{5.17}$$

Here $\mathbf{a}_{\|}$ stands for a vector component parallel to the interface. If the shift between the Weyl nodes is purely perpendicular to the interface, the projections of the Fermi surface onto the interface plane always overlap, and the chirality filtering will not work. In the following, we assume a planar interface in the y-z plane located at $x = 0$. We introduce $\mathbf{b}_{L/R} = \mathbf{B} \mp \mathbf{\Delta b}/2$, and restrict ourselves to the case of momentum-space node-shifts purely orthogonal to the transport direction. For simplicity, we take the difference between the node separations on both sides of the interface along $\mathbf{e}_y$, i.e.

$$\mathbf{b}_{L/R} = (B \mp \Delta b/2)\,\mathbf{e}_y. \tag{5.18}$$

Scattering properties for decoupled nodes

We start from the case $m = 0$, when the Weyl nodes are decoupled and it is possible to obtain analytical results for the transmission probability of quasiparticles across the interface constructing the scattering wave functions of the system. In the following, we assume x as the transport direction and an interface in the y-z plane. A sharp interface is assumed for calculations but the main qualitative result, namely chirality filtering, pertains for a smooth one (smooth in the x direction). The components of the momenta parallel to the interface, $\mathbf{k}_\parallel = (k_y, k_z)$, are good quantum numbers due to the translational invariance within the y-z plane. For a given excitation energy E and (k_y, k_z), the plane wave solutions traveling in positive x-direction at the $\tau = \pm$ Weyl node have the form

$$\psi(\mathbf{r}) = \begin{pmatrix} 1 \\ s^\tau \alpha^\tau e^{is^\tau \varphi^\tau} \end{pmatrix} e^{is^\tau q_x^\tau x} e^{i\mathbf{k}_\parallel \mathbf{r}_\parallel}\,, \tag{5.19}$$

and the ones traveling in the negative $-x$ direction read

$$\psi(\mathbf{r}) = \begin{pmatrix} 1 \\ -s^\tau \alpha^\tau e^{i-s^\tau \varphi^\tau} \end{pmatrix} e^{-is^\tau q_x^\tau x} e^{i\mathbf{k}_\parallel \mathbf{r}_\parallel}\,, \tag{5.20}$$

where

$$q_x^\tau = \sqrt{(k^\tau)^2 - (q_y^\tau)^2 - (q_z^\tau)^2} = k^\tau \cos\varphi^\tau \sin\vartheta^\tau, \tag{5.21}$$

$$q_y^\tau = k_y - \tau b_y = k^\tau \sin\vartheta^\tau \sin\varphi^\tau, \tag{5.22}$$

$$q_z^\tau = k_z - \tau b_z = k^\tau \cos\vartheta^\tau, \tag{5.23}$$

$k^\tau = |E + \mu^\tau|$ are the radii of the Fermi spheres, $\mu^\tau = \mu - \tau b_0$ and $\alpha^\tau = \frac{\sin\vartheta^\tau}{\tau s^\tau + \cos\vartheta^\tau}$ and $s^\tau = \mathrm{sign}(E + \mu^\tau)$. The solutions are parametrized individually for each node by spherical coordinates with the origin placed at the node point with angles $\varphi^\tau \in (-\pi/2, \pi/2)$, $\vartheta^\tau \in [0, \pi)$ as shown in Fig. 5.2

From these spinors, we now construct the scattering states across the interface. As an example, the wave function for a conduction band electron injected from the left (L) Weyl node and transmitted to the conductance band in the right (R) Weyl node of the same chirality $\tau = +$ for a given energy $E > -\mu_L, -\mu_R$ and parallel momentum $\mathbf{k}_\parallel$ reads for $x < 0$:

$$\Psi_L^+(x) = \frac{e^{i\mathbf{k}_\parallel \mathbf{r}_\parallel}}{\sqrt{\alpha_L^+ \cos\varphi_L^+}} \begin{bmatrix} e^{iq_{x,L}^+ x} + r e^{-iq_{x,L}^+ x} \\ \alpha_L^+ \left(e^{iq_{x,L}^+ x + i\varphi_L^+} - r e^{-iq_{x,L}^+ x - i\varphi_L^+} \right) \end{bmatrix}, \tag{5.24}$$

(5.25)

and for $x > 0$:

$$\Psi^{+}_{R}(x) = \frac{e^{i\mathbf{k}_{\parallel}\mathbf{r}_{\parallel}}r}{\sqrt{\alpha^{+}_{R}\cos\varphi^{+}_{R}}}t\begin{bmatrix} 1 \\ \alpha^{+}_{R}e^{i\varphi^{+}_{R}} \end{bmatrix}e^{iq^{+}_{x,R}x}. \tag{5.26}$$

Each solution is normalized to carry unit probability flux. Solving the system of equations obtained by imposing continuity of the scattering wave function across the interface for both nodes, $\Psi^{\tau}_{L}(x=0) = \Psi^{\tau}_{R}(x=0)$, we get the probability for transmission between the nodes

$$T^{\tau} = \frac{4s^{\tau}_{L}s^{\tau}_{R}\alpha^{\tau}_{L}\alpha^{\tau}_{R}\cos\varphi^{\tau}_{L}\cos\varphi^{\tau}_{R}}{(\alpha^{\tau}_{L})^{2} + (\alpha^{\tau}_{R})^{2} + 2s^{\tau}_{L}s^{\tau}_{R}\alpha^{\tau}_{L}\alpha^{\tau}_{R}\cos\left(s^{\tau}_{L}\varphi^{\tau}_{L} + s^{\tau}_{R}\varphi^{\tau}_{R}\right)}\,. \tag{5.27}$$

. This expression for the transmission probability holds as long as there exist propagating solutions on both sides of the interface, i.e. for given energy E and injection angles $\varphi^{\tau}_{L}, \vartheta^{\tau}_{L}$ the momentum $q^{\tau}_{x,R} = \sqrt{(E+\mu^{\tau}_{R})^{2} - (k_{y} - \tau b_{y,R})^{2} - k^{2}_{z}}$ is a real quantity.

Chiral filtering

We here further illustrate the geometric criterion in reciprocal space given in Eq. (5.17), for reaching complete chirality filtering, namely the total blocking of a given chirality while the opposite chirality is (partially) transmitted. This chirality filtering relies on transverse momentum conservation. For the ballistic regime and the interface described above, the system is invariant by any translation in the y-z plane. Therefore the components k_y and k_z of the momenta are good quantum numbers and are conserved across the interface. Momentum conservation parallel to the interface implies the following Snell-Descartes type laws :

$$k^{\tau}_{L}\cos\vartheta^{\tau}_{L} = k^{\tau}_{R}\cos\vartheta^{\tau}_{R} \tag{5.28}$$

$$k^{\tau}_{L}\sin\varphi^{\tau}_{L}\sin\vartheta^{\tau}_{L} = k^{\tau}_{R}\sin\varphi^{\tau}_{R}\sin\vartheta^{\tau}_{R} + \tau\Delta b\,, \tag{5.29}$$

where the norms of the electron wave vectors $k^{\tau}_{(R,L)}$ and the different angles are defined below.

The norm of the electron wave vector in the material at right ($x > 0$) is given by :

$$k^{\tau}_{R} = |E + \mu - \tau b_{0,R}|\,, \tag{5.30}$$

for the chirality τ, and a similar equation is obtained, in the left-side material, for k^{τ}_{L} by the substitution $b_{0,R} \to b_{0,L}$.

The injection angle on the left the transmission angles are defined by :

$$\varphi^{\tau}_{R} = \arctan\left(\frac{q_{y,R}}{q_{x,R}}\right), \quad \vartheta^{\tau}_{R} = \arccos\left(\frac{k^{\tau}_{L}}{k^{\tau}_{R}}\cos\vartheta^{\tau}_{L}\right) \tag{5.31}$$

which implies injection angles above which there is no real solution of the above equations and thus no transmission.

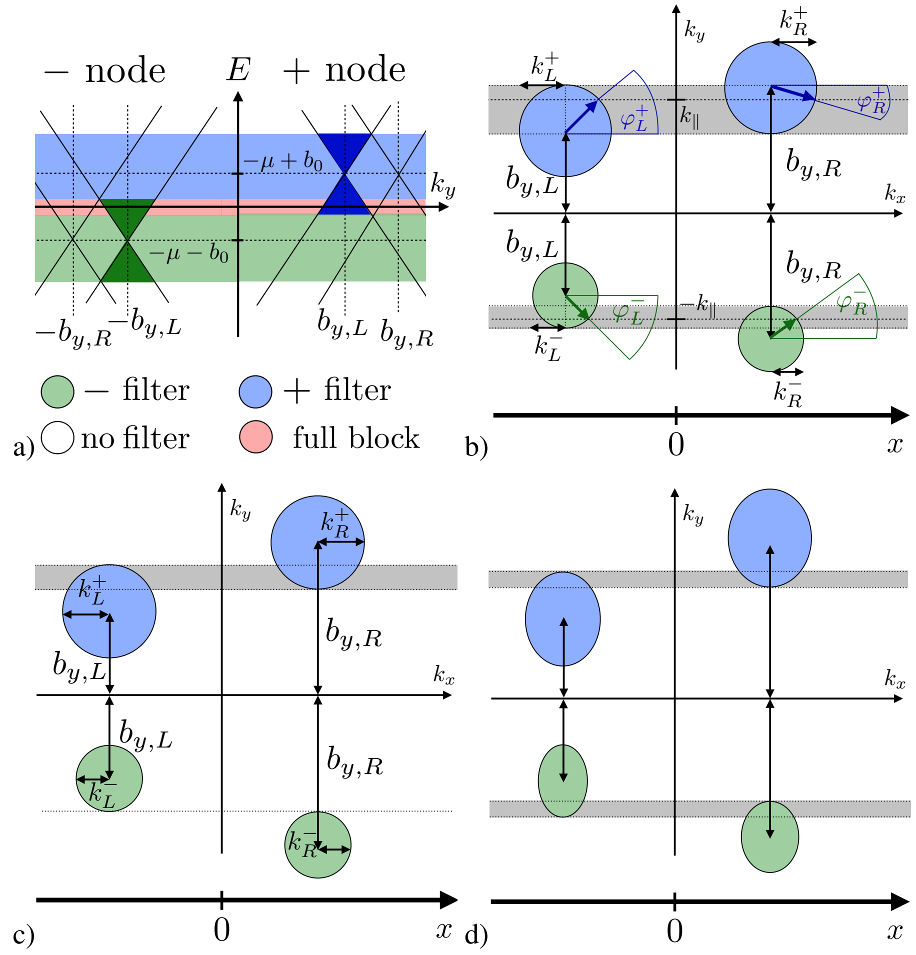

FIGURE 5.2: a) Projection of the band structure around the nodes as function of k_y onto the interface. Full colored hourglass shapes mark the energy windows where transmission is blocked between nodes of equal chirality. Blue/green shaded regions mark the Energy windows for which chiral filtering appears. The red shaded region corresponds to a full blockage of transmission. b) Scheme of the Fermi spheres for finite relative shift in k_y direction and same finite shift in energy b_0 between the nodes on both sides of the interface when all quasiparticle momenta are in the plane $k_z = 0$. Grey regions mark the states on the spheres that overlap when projected onto the interface and thus contribute to transport. Colored arrows attached to the center of the spheres are the group velocity vectors for excitations with a certain momentum component parallel to the interface. c) Situation when one chirality is blocked. d) A finite mass distorts the spheres to ellipsoids and shifts them towards the origin.

Ballistic transmission is only possible if there is an outgoing state with the same (k_y, k_z) as the incident electron. In the following we show that a certain choice of shift parameters b_ν can lead to energy windows in which the conductance between nodes of only one chirality is finite.

Therefore, the criterion for the blocking of the fermions with energy E and chirality τ can be written as

$$k_L^\tau + k_R^\tau = |E + \mu_L^\tau| + |E + \mu_R^\tau| < |\Delta b| \, . \tag{5.32}$$

This means that the mutual shift of the nodes exceeds the sum of the wave vectors k_L and k_R, thereby making impossible the overlap of their projections onto the interface plane.

This illustrative condition shows that both types of shifts, b_i and b_0, need to be finite and $\Delta b \neq 0$ in order to achieve chiral filtering for a range of injection energies. The relative shift Δb creates a window in energy where transmission between nodes of the same chirality vanishes. When b_0 is finite these windows are shifted relatively to each other allowing for the transmission of one chirality only for a range of injection energies (see Fig. 5.2 a), b), c). If $\Delta b = 0$, for any choice of $b_{0,L/R}$ and $\mu^{\tau}_{L/R}$ the contributions to transport from one of the node types will only disappear when choosing the injection energies $E = -\mu^{\pm}_{L/R}$, i.e. at the energy of the band crossings.

5.2.2 Conduction through bulk states

In this section, we compute the differential conductance through an interface between two distinct WSMs, in the geometry WSM$_1$/WSM$_2$. The interface is assumed to be sharp in x direction, and invariant by translations in the y and z directions. Only the 3D bulk states, written in the previous section, are considered.

We first treat the case of completely decoupled nodes ($m = 0$), demonstrate chirality filtering and show the corresponding experimental signature in differential conductance curves. We close this section by showing that chirality filtering is robust against a moderate internode coupling (finite m).

Differential conductance

Within the Landauer-Büttiker formalism the current between the leads forming the interface is

$$I = \frac{e}{h} \int_{-\infty}^{\infty} dE \sum_{mn} T_{m,n}(E) \left(f_L(E) - f_R(E) \right) , \tag{5.33}$$

where $T_{m,n}(E) = |t_{m,n}(E)|^2$ is the transmission between channels m in the left lead and n in the right lead. We assume elastic scattering, thus only modes with the same transverse momentum couple to each other. The summation over the different channel combinations reduces to a summation over all transverse modes. When the width of the sample is large against the Fermi wavelength and we assume that the quasiparticles get ideally reflected at the edges, we can perform a continuum limit of the summation over transverse modes. We label the channels in terms of the injection angles in the left WSM. Applying a bias eV_S in the left for $T = 0$, the differential conductance becomes

$$\frac{\partial I}{\partial V_S} = \sum_{\tau=\pm} \int d\varphi^{\tau}_L \int d\vartheta^{\tau}_L \cos\varphi^{\tau}_L \sin^2\vartheta^{\tau}_L G^{\tau}_0 T^{\tau}(eV_S) \, , \tag{5.34}$$

where $G^{\tau}_0 = \frac{e^2 N^{\tau}(eV_S)}{h}$, $N^{\tau}(E) = \frac{W^2(E+\mu^{\tau}_L)^2}{(2\pi\hbar v_F)^2}$ and we define $G_0 = G^{+}_0 + G^{-}_0$.

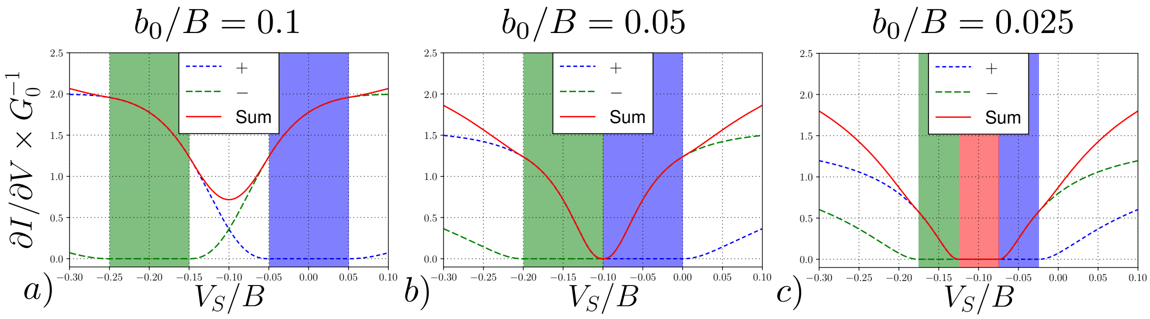

FIGURE 5.3: Differential conductance for parameter regimes where chiral filtering is visible. From a) to c) the shift in energy between Weyl nodes of opposite chirality is varied. Blue/green shaded regions determine the bias window in which transmission is blocked for the +/−-node respectively, The red shaded region corresponds to full blockage of the transmission. For all plots we set $\mu_L/B = \mu_R/B = 0.1$, $\Delta b/B = 0.1$, $m = 0$ and $T = 0$.

Chiral filtering for decoupled nodes

Let us start with the probably simplest case of equal and positive chemical potentials, the same shift in energy b_0 on both sides of the interface and a relative shift $\Delta b > 0$. Then according to Eq. (5.32) we get no transmission between nodes of chirality ± when

$$|E + \mu \mp b_0| < \Delta b/2. \tag{5.35}$$

The case of equally sized Fermi-spheres around nodes of same chirality is depicted schematically in Fig. 5.2 b) and c). In Fig. 5.2 b) nodes of both chiralities contribute to the transport. The projections of the Fermi spheres with same chirality onto the interface are marked by the grey shaded regions and have a finite overlap in the k_x-k_y plane in momentum space. In Fig. 5.2 c) the shift in momentum space between the nodes in the right WSM is increased and only quasiparticles with positive chirality are transmitted.

The evolution of the differential conductance when changing the Weyl node separation in energy relative to each other on both sides of the interface is shown in Fig. 5.3. When all parameters are chosen positive, spin filtering appears in bias ranges Δb centered around the points $-\mu \pm b_0$. If $b_0 > \frac{\Delta b}{2}$ the bias intervals for which only charge carries of one certain chirality get transmitted are well separated by an interval in which both chiralities are transmitted as shown in Fig. 5.3 a). When decreasing the shift of the nodes in energy b_0 relative to the shift in momentum Δb this intermediate interval disappears when $b_0 = \frac{\Delta b}{2}$ (Fig. 5.3 b). Finally if $b_0 < \frac{\Delta b}{2}$, the two chiral filtering regions are separated by an interval in which no transmission is possible (Fig. 5.3 c).

Weakly coupled nodes

To investigate the influence of a small internode coupling, we can derive effective Hamiltonians around the Weyl points. We start by expanding the Hamiltonian around the +-node, thus $\mathbf{k} = \mathbf{b} + \mathbf{q}$ and in a first attempt assume $m, |\mathbf{q}|, b_0 \ll |b_y|$. Then

$$\mathcal{H}^+(\mathbf{q}) = \begin{pmatrix} b_0 + \boldsymbol{\sigma}\mathbf{q} & m \\ m & -b_0 - \boldsymbol{\sigma}(\mathbf{q} + 2\mathbf{b}) \end{pmatrix} = \begin{pmatrix} H_{11} & H_{12} \\ H_{21} & H_{22} \end{pmatrix}. \tag{5.36}$$

The block H_{22} with the dominant parameter $\mathbf{b}$ is mainly contributing to the high-energy bands where the block H_{11} is related to the low energy bands. The Green's function determined by $\mathcal{H}^+(\mathbf{q})$ is defined by

$$G = \begin{pmatrix} G_{11} & G_{12} \\ G_{21} & G_{22} \end{pmatrix} = \begin{pmatrix} G_{11}^{(0)^{-1}} & H_{12} \\ H_{21} & G_{22}^{(0)^{-1}} \end{pmatrix}^{-1}, \tag{5.37}$$

with $G_{ii}^{(0)} = (H_{ii} - \varepsilon)^{-1}$. From this follows

$${G_{11}}^{-1} = G_{11}^{(0)^{-1}} - H_{12} G_{22}^{(0)} H_{21}, \tag{5.38}$$

so using $G_{11}^{(0)^{-1}} = H_{11} - \varepsilon$ one finds the projected operator

$${G_{11}}^{-1} + \varepsilon = H_{11} - H_{12} G_{22}^{(0)} H_{21}, \tag{5.39}$$

that is defined in the low energy subspace of the original Hamiltonian. To find an approximate operator for the low energy physics in this subspace, we make a expansion in $|\mathbf{b}|^{-1}$ for $G_{22}^{(0)}$. Up to terms of order $|\mathbf{b}|^{-2}$ we get

$$G_{22}^{(0)} \approx \frac{b_0 + \varepsilon}{4b_y^2}\sigma_0 - \frac{q_x}{4b_y^2} + \frac{q_y - 2b_y}{4b_y^2}\sigma_y - \frac{q_z}{4b_y^2}\sigma_z, \tag{5.40}$$

Repeating the procedure for the Weyl node of opposite chirality, we find that the low energy dynamics of the Weyl fermion in presence of a small internode coupling m is described by the following effective Hamiltonians:

$$\begin{aligned} \mathcal{H}_{\text{eff}}^{+} &= \quad (\beta b_0 - \mu)\,\sigma_0 + \gamma\,(k_x\sigma_x + k_z\sigma_z) + (\beta k_y - \delta b_y)\,\sigma_y, \\ \mathcal{H}_{\text{eff}}^{-} &= -\,(\beta b_0 + \mu)\,\sigma_0 - \gamma\,(k_x\sigma_x + k_z\sigma_z) - (\beta k_y + \delta b_y)\,\sigma_y, \end{aligned} \tag{5.41}$$

where $\beta = \left(1 - \frac{m^2}{4b_y^2}\right)$, $\gamma = \left(1 + \frac{m^2}{4b_y^2}\right)$ and $\delta = \left(1 - \frac{3m^2}{4b_y^2}\right)$. Thus, the mass introduces a anisotropy in the group velocity and rescales the shift parameters b_ν. The Fermi spheres for a given energy are ellipsoids where increasing m squeezes the surface in k_x, k_z and stretches it in k_y shifting the origin of the ellipsoid towards the origin. We can again use spherical coordinates to express the now distorted Fermi spheres individually. Then the expression for T^τ in Eq. (5.27) remains valid. What changes is the condition for the momentum conservation parallel to the interface, so for a given energy E and injection

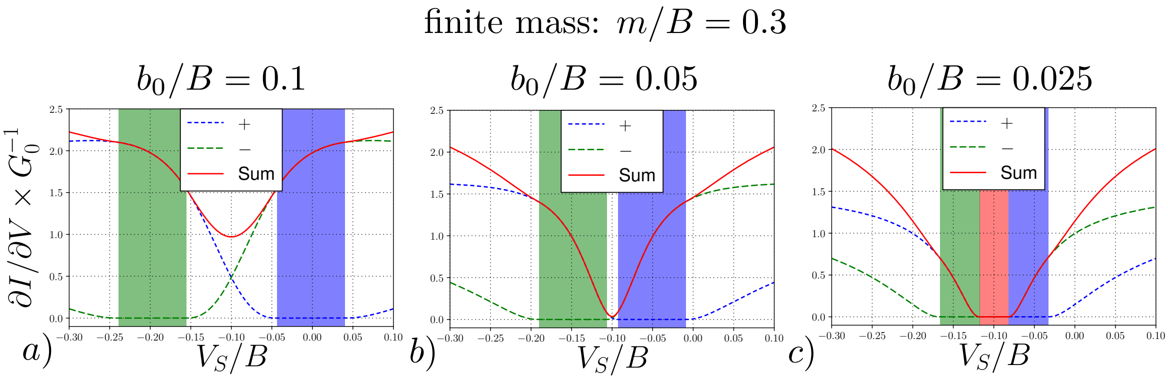

FIGURE 5.4: Differential conductance for parameter regimes where chiral filtering is visible for finite mass $m/B = 0.3$. From a) to c) the shift in energy between Weyl nodes of opposite chirality is varied. Blue/green shaded regions determine the bias window in which transmission is blocked for the +/−-node respectively. For all plots we set $\mu_L/B = \mu_R/B = 0.1$, $\Delta b/B = 0.1$, $m/B = 0.3$ and $T = 0$.

angles φ_L^τ, ϑ_L^τ

$$\varphi_R^\tau = \arcsin\left(\frac{\beta_R \sin\varphi_L^\tau \sin\vartheta_L^\tau k_R^\tau + \tau\left(\beta_R\delta_L b_{y,L} - \beta_L\delta_R b_{y,R}\right)}{\beta_L\sqrt{\left(k_R^\tau\right)^2 - \left(\gamma_R/\gamma_L\right)^2\cos^2\vartheta_L\left(k_L^\tau\right)^2}}\right), \tag{5.42}$$

$$\vartheta_R^\tau = \arccos\left(\frac{\gamma_R k_L^\tau \cos\vartheta_L^\tau}{\gamma_L k_R^\tau}\right), \tag{5.43}$$

with $k_{L/R}^\tau = |E + \mu_{L/R} - \tau\beta_{L/R}b_{0,L/R}|$ must be fulfilled, T is now fully determined by the external parameters. Let us turn to the condition for blocking and transmitting for a certain chirality. As before transmission is possible if the projection of the Fermi-surfaces on both sides of the junction onto the interface overlap . This time we deal with the overlap of ellipses that are shifted and stretched along the k_y-axis relatively to each other. Transmission, blocking between nodes of same chirality $\tau = \pm$ is possible if

$$\left|\frac{\mu_L + E}{\beta_L} - \tau b_{0,L}\right| + \left|\frac{\mu_R + E}{\beta_R} - \tau b_{0,R}\right| \gtrless \left|\frac{b_{y,L}\delta_L}{\beta_L} - \frac{b_{y,R}\delta_R}{\beta_R}\right|, \tag{5.44}$$

respectively. To get a feeling of this rather complicated expression for the blocking Eq. (5.44), let us examine the limit $\mu_L = \mu_R = \mu$, $m_L = m_R = m$, $b_{0,L} = b_{0,R} = b_0$, $b_{y,L/R}/B \approx 1$. Then the above condition for blocking simplifies to

$$|\mu + E \mp b_0| < \delta\left|\frac{\Delta b}{2}\right|. \tag{5.45}$$

Within this crude approximation the finite mass reduces the energy window in which chiral filtering appears due to the reduction of the relative shift of the nodes of same chirality in momentum space. The exact evaluation of the blocking condition (5.44) and the calculated differential conductivity for the same range of parameters as for the massless case are shown in Fig. 5.4 and indeed the windows of filtering, marked by shaded green and blue regions, are reduced compared to $m = 0$. As can be deduced from

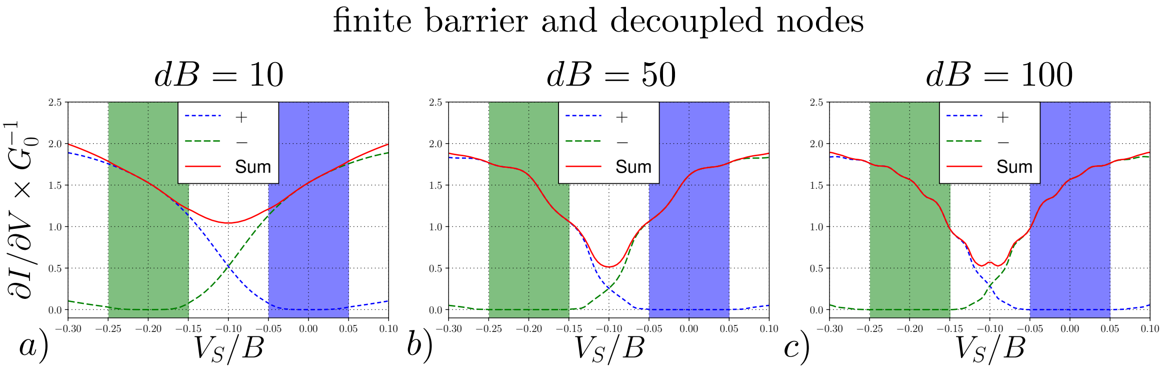

FIGURE 5.5: Differential conductance for parameter regimes where chiral filtering is visible for the case of the WSM$_1$/WSM$_2$/WSM$_1$ geometry. From a) to c) the length of the WSM$_2$ region is increased. Blue/green shaded regions determine the bias window in which transmission is blocked for the $+/-$-node respectively. For all plots we set $\hat{b}_0/B = 0.1$, $\mu_L/B = \mu_R/B = 0.1$, $\Delta b/B = 0.1$, $m/B = 0.0$ and $T = 0$.

the blocking conditions this is due to an interplay of stretching the Fermi surfaces for a given energy in k_y and shifting the nodes closer to the origin in momentum space and simultaneously closer in energy when m is increased.

Finite barrier

Here we consider the geometry of a WSM slab contacted between two distinct WSMs, in the geometry WSM$_1$/WSM$_2$/WSM$_1$. It consists of two interfaces (like the one considered in the previous section) separated by a finite length d. In that case, even if we are in a parameter regime, where transmission of only one chiral species of electrons is possible electrons of the blocked species can penetrate the barrier due to tunneling. These tunneling currents will be exponentially suppressed with increasing barrier thickness. Let us consider a WSM slab of width d centered (C) between two WSMs of the same kind ($L = R$). In the spirit of Eq. (5.24) the Ansatz for the wave function across the interface, if only conduction band like electrons propagate reads

$$\Psi_L^+(x) = \frac{e^{i\mathbf{k}_\parallel \mathbf{r}_\parallel}}{\sqrt{\alpha^+ \cos\varphi^+}} \begin{bmatrix} e^{iq_x^+ x} + re^{-iq_x^+ x} \\ \alpha^+ \left(e^{iq_x^+ x + i\varphi^+} - re^{-iq_x^+ x - i\varphi^+} \right) \end{bmatrix}, \tag{5.46}$$

$$\Psi_C^+(x) = e^{i\mathbf{k}_\parallel \mathbf{r}_\parallel} \begin{bmatrix} c_1 e^{iq_{x,C}^+ x} + c_2 e^{-iq_{x,C}^+ x} \\ \alpha_C^+ \left(c_1 e^{iq_{x,C}^+ x} e^{i\varphi_C^+} - c_2 e^{-iq_{x,C}^+ x} e^{-i\varphi_C^+} \right) \end{bmatrix} \tag{5.47}$$

$$\Psi_R^+(x) = \frac{e^{i\mathbf{k}_\parallel \mathbf{r}_\parallel r}}{\sqrt{\alpha^+ \cos\varphi^+}} t \begin{bmatrix} 1 \\ \alpha^+ e^{i\varphi^+} \end{bmatrix} e^{iq_x^+ x}. \tag{5.48}$$

The Ansatz is easily modified to the case when dealing with quasiparticles in other bands in any region of the junction or when we have decaying solutions in the center region. In the case of propagating solutions we obtain the transmission

$$T^{\tau} = \frac{4\left(\alpha^{\tau}\right)^{2}\left(\alpha_{C}^{\tau}\right)^{2}\cos^{2}\left(\varphi^{\tau}\right)\cos^{2}\left(\varphi_{C}^{\tau}\right)}{A_{1}\cos^{2}\left(dk_{C}^{\tau}\right)+A_{2}\sin^{2}\left(dk_{C}^{\tau}\right)} \tag{5.49}$$

where

$$A_{1} = 4\left(\alpha^{\tau}\right)^{2}\left(\alpha_{C}^{\tau}\right)^{2}\cos^{2}\left(\varphi^{\tau}\right)\cos^{2}\left(\varphi_{C}^{\tau}\right), \tag{5.50}$$

$$A_{2} = \left(\left(\alpha^{\tau}\right)^{2}+\left(\alpha_{C}^{\tau}\right)^{2}-2s^{\tau}s_{C}^{\tau}\alpha^{\tau}\alpha_{C}^{\tau}\sin\left(\varphi^{\tau}\right)\sin\left(\varphi_{C}^{\tau}\right)\right)^{2}. \tag{5.51}$$

Results for the differential conductance for the finite barrier are shown in Fig. 5.5. The decaying states contribute significantly to the transport in the filtering regime when the barrier is not long enough (Fig. 5.5 a) and thus the bias window where filtering appears is reduced. Increasing the width leads to interference in the barrier that we see as oscillations of the differential conductance (Fig. 5.5 b, c) and which leads to a lowered differential conductance when compared to the interface case. For very long barriers the filter quality is restored as the tunneling contribution is exponentially suppressed when the barrier length increases (Fig. 5.5 c).

5.3 Conclusion and perspectives

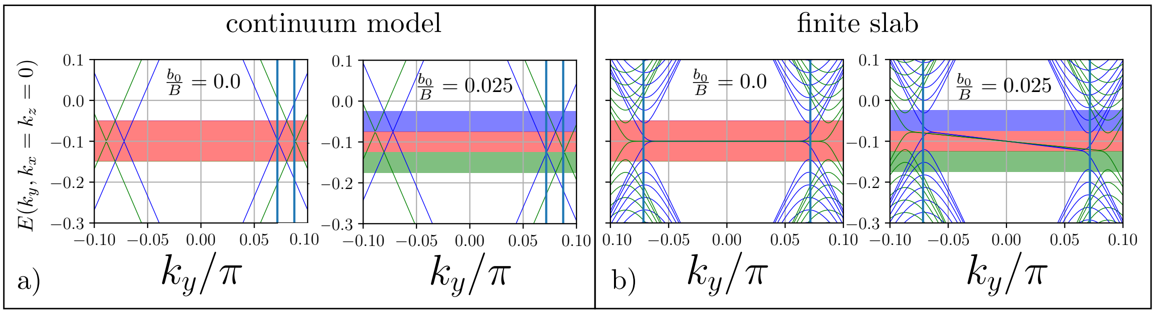

FIGURE 5.6: Projection of the band structures around the Weyl nodes of the leads for a WSM$_1$/WSM$_2$ interface in the blocking regime for a) the continuum model and b) a lattice model for a finite slab of $N = 200$ sites in the z-direction. Blue bands correspond to the left lead and green bands to the right lead. In both systems the interface is in the y-z plane, x is the transport direction, the Weyl node separation in y-direction is $\Delta b = 0.1B$ and $\mu_L = \mu_R = 0.1B$. In both systems we marked the blocking regime and the chiral filtering regimes as predicted by the continuum model. The blocking regime corresponds to the red shaded region while blue and green shaded regions correspond to the filtering regimes. In the blocking regime for the finite slab geometry only the surface states are present and would contribute to the charge transport.

We introduced the model for an interface WSM$_1$/WSM$_2$ between two distinct WSMs, and we derive the general criteria to obtain chirality filtering, or even a complete conduction blockade over all chirality channels. We calculated the differential conductance across the interface which can be measured in experiments. A regime of complete blocking of the bulk conduction has been identified and the effect of a moderate internode coupling has been investigated. We then extended the differential conductance calculations to the barrier geometry WSM$_1$/WSM$_2$/WSM$_1$.

In this chapter we investigated the transport properties of the bulk materials forming the interface. In a realistic finite system, additional transport channel can open due to the formation of Fermi arcs at the surfaces of the material. If the system dimensions are large against the Fermi wavelength, the number of open transport channels in the bulk will generally be much higher then the number of channels due to the edge states. Thus, if both contribute to the transport, the contribution from the edge states will be masked by the bulk conductivity. Clearly, in the blocking regime, there is no charge transport due to bulk states. This bulk blocking regime would provide an ideal set-up to measure the conduction carried solely by Fermi arcs (see Fig. 5.6). We are currently working on a proposal for realistic material interfaces which may be suitable to implement the chirality filter and the transport by Fermi arcs only.

Summary and Conclusion

This thesis studied the interplay between superconducting correlations and spin-active fields for a variety of hybrid systems. The biggest part of the thesis was dedicated to the Josephson effect under the influence of magnetic and spin-orbit coupling (SOC) fields. In chapter 2 we investigated the Andreev bound state formation and the current phase relationship, in a ballistic Josephson junction between spin-split superconductors. Collinear but asymmetric exchange fields led to a spin dependent asymmetry of the superconducting gap on both sides of the junction. This resulted in a reduction of the maximal Andreev bound state energy and the appearance of intervals of the phase difference between the superconductors, with no formation of Andreev bound states in the short junction limit. In these intervals, the Josephson current is carried purely by states of the continuous part of the spectrum. Outside this interval the spectral origin of the current can be tuned between the states of the continuum and the Andreev bound states by changing the transmissivity of the junction. The predicted spectral and transport properties due to spin-dependent gap asymmetry are qualitatively similar to those of a previously studied system which considered asymmetric gap sizes in the superconducting leads. However in the magnetic case the exchange field magnitude, and thus the gap asymmetry, is limited by the Clogston-Chandrasekar limit above which the paramagnetic pair breaking effect would cause a break down of superconductivity.

In chapter 3 we reviewed how to circumvent the paramagnetic pair breaking effect in diffusive S/F heterostructures and demonstrated how SOC can lead to a rotation of triplet superconducting correlations. Components that are perpendicular to the orientation of the exchange field are long ranged and decay on a length scale comparable to a non magnetic system. We proposed two realistic Josephson junctions to detect the long range triplet correlations (LRTCs) that are generated by SOC. We determined the signature of these correlations, a long-ranged Josephson current. We found that the Josephson current was composed of two distinct contributions, originating in spin precession and anisotropic spin relaxation effects. These strongly depend on the orientation of the exchange field and the strength of the SOC. Competition between the two contributions leads to a variety of current reversal scenarios which represent an unequivocal LRTC signature. Furthermore, the possible manipulation of the Josephson current through external fields demonstrates the applicability of the proposed junctions as current valves and switches.

Following these studies of the Josephson effect, in chapter 4 we turned to another equilibrium phenomenon, the equilibrium spin currents (ESC). We showed that in a nanowire with SOC breaking the time-reversal symmetry by a Zeeman field leads to a bulk equilibrium spin current that results in a edge spin accumulation transverse to the Zeeman field and the SOC field. This transverse edge spin accumulation appears in the normal state, but also when the nanowire is superconducting itself due to, for example, the proximity to a superconductor. The described correspondence between ESC and the edge spin accumulation is of particular relevance to the detection of possible Majorana zero modes in such systems. Several works proposed a transverse edge spin polarization at the critical value of the exchange field, where the wire enters the topological phase ($h = \sqrt{\mu^2 + \Delta^2}$), as a signature of Majorana zero modes. We show that the ESC, and therefore the transverse edge spin polarization, is finite for all values of the exchange field. Besides the previously predicted signature a cusp at the topological transition, we identify another maximum of the polarization in the quasi-classical parameter regime when $h \approx \Delta$. It is robust against disorder and can exceed the maximum at the topological transition by orders of magnitudes, especially for small SOC. Therefore a transverse edge polarization is not exclusively related to the appearance of Majorana zero modes but more importantly is a signature of ESC. Finally we determined the spatial distribution of the magnetization of a superconducting SOC wire in the quasi-classical regime and thus directly demonstrated the appearance of a transverse edge polarization in a finite system. In this work we showed that the theoretical concept of equilibrium spin currents is directly connected to a physical observable that can be detected using the methods of modern nanotechnology to measure spin-densities as scanning tunneling microscopy or nuclear magnetic resonance spectroscopy.

In the last part of the thesis we investigated the bulk transport properties of interfaces between Weyl semimetals (WSM). We proposed a simple realization of a three-dimensional chirality filter based on interfacing two distinct chiral WSMs, where the Weyl nodes of opposite chirality on each side of the interface are separated in energy and momentum space. We calculated the differential conductance across the interface and identified the regimes where it is possible to achieve transmission of one, none, or both chiralities. A moderate internode coupling and a finite length barrier geometry WSM$_1$/WSM$_2$/WSM$_1$ have also been investigated. We found that both cases restrict the parameter regime where the filtering effect takes place when compared to the interface in the massless case. Initially the project was aiming to study the influence of superconducting correlations on the transport properties across WSM interfaces however this has been left for future work.

We are currently investigating realistic materials that exhibit Weyl nodes at similar points in the Brillouin zone and would act as chirality filter when interfaced. We are also working on a full description of the conductivity of such interfaces including the contributions from edge transport channels that appear in finite slab systems. The blocking regime, where there is no transmission of either chirality through the bulk, is of particular interest as it opens the path to investigate the edge transport individually.

Acknowledgements

I would like to express my special appreciation and thanks to my supervisors Dr. Jérôme Cayssol, Dr. Dario Bercioux and Dr. Sebastián Bergeret. Each of my supervisors guided me in his unique style and helped me to grow professionally as well as personally. Without their support, advice and commitment none of the presented work would have been possible. I am especially grateful to Sebastián Bergeret who gave me the chance to be part of the Mesoscopic physics group and was the main motor behind most of the work presented in this thesis.

I would like to thank my collaborators and the ones who always had an open ear to discuss physics, Robert Biele, Adolfo Grushin, Ilya Tokatly, Vitaly Golovach, Carsten Timm, Phillip Brydon, Julie Baumard, Geza Giedke, Jérémy Sourd and Juan Borge.

Special thanks goes to all the people from inside an outside the physics community who accompanied me during my work on this thesis. Thank you Clemens Löbner, Matthäus Mittasch, Robert Biele and Franziska Hentsch for proofreading my thesis and for the general advice on writing. I want to thank the above and following people for making me feel home no matter where I was: Florian, Jakub and Maria, Özge, Ainara, Paul Doazan and the whole Doazan family, Kristina, Torsten and Akiko, Christian, Aron and Alexander.

Appendix A

Appendix

A.1 Spin generalized BdG equation

We start from a more general version of the BCS mean field Hamiltonian that allows arbitrary spin-pairing states between the electrons,

$$\hat{\mathcal{H}}^{\text{mf}}_{\text{BCS}} = \sum_{\mathbf{k}\sigma} \xi_{\mathbf{k}} c^{\dagger}_{\mathbf{k}\sigma} c_{\mathbf{k}\sigma} + \frac{1}{2} \sum_{\mathbf{k}} \sum_{\alpha\beta} [\Delta_{\mathbf{k},\alpha,\beta} c^{\dagger}_{\mathbf{k},\alpha} c^{\dagger}_{-\mathbf{k},\beta} + \Delta^{*}_{\mathbf{k},\alpha,\beta} c_{-\mathbf{k},\beta} c_{\mathbf{k},\alpha}]. \tag{A.1}$$

Here we defined the pair potential,

$$\Delta_{\mathbf{k},\alpha,\beta} = \sum_{\mathbf{k}'} \sum_{\gamma,\delta} \langle c_{-\mathbf{k}',\delta} c_{\mathbf{k}',\gamma} \rangle V(\mathbf{k},\mathbf{k}')_{\alpha,\beta,\gamma,\delta}. \tag{A.2}$$

where

$$V(\mathbf{k},\mathbf{k}')_{\alpha,\beta,\gamma,\delta} = \langle \mathbf{k},\alpha; -\mathbf{k},\beta | \hat{V} | \mathbf{k}',\gamma; -\mathbf{k}',\delta \rangle. \tag{A.3}$$

is the matrix element is given by of an general attractive two-particle interaction. We neglected mean field terms which only lead to a constant shift of the ground-state energy. Applying the Bogoliubov transformation,

$$c_{\mathbf{k},\sigma} = \sum_{\sigma'} (u_{\mathbf{k},\sigma,\sigma'} \gamma_{\mathbf{k},\sigma'} + v^{*}_{-\mathbf{k},\sigma,\sigma'} \gamma^{\dagger}_{-\mathbf{k},\sigma'}). \tag{A.4}$$

leads to a Hamiltonian diagonal in the new operators,

$$\mathcal{H} = \sum_{\mathbf{k}\sigma} E_{\mathbf{k}\sigma} \gamma^{\dagger}_{\mathbf{k}\sigma} \gamma_{\mathbf{k}\sigma}, \tag{A.5}$$

where we have again omitted constant terms. The new operators obey the fermionic anti-commutation relations and create the excitations of the system, the so-called Bogolons with dispersion $E_{\mathbf{k}\sigma}$. What we are interested in is how an eigenvector of $\mathcal{H}^{\text{mf}}_{\text{BCS}}$ can be expressed in the electron-hole basis. Therefore we calculate the equation of motion for the annihilation operator. In order to describe ferromagnetism we include a Zeeman term 1.81, so we need to compute

$$i\partial_t c_{\mathbf{k},\sigma} = [c_{\mathbf{k},\sigma}, \mathcal{H}^{\text{mf}}_{\text{BCS}} + \mathcal{H}_{\text{ex}}]. \tag{A.6}$$

This leads to

$$i\partial_t c_{\mathbf{k},\sigma} = \xi_{\mathbf{k}} c_{\mathbf{k},\sigma} - \sum_{\beta} (\boldsymbol{\sigma}\cdot\mathbf{h})_{\sigma,\beta} c_{\mathbf{k},\beta} + \frac{1}{2}\sum_{\beta} (\Delta_{\mathbf{k},\sigma\beta} - \Delta_{-\mathbf{k},\beta\sigma}) c^{\dagger}_{-\mathbf{k},\beta}. \tag{A.7}$$

$\Delta_{\mathbf{k},\alpha,\beta}$ has the same symmetry as a two-fermion wavefunction. Antisymmetry regarding particle exchange implies $\Delta_{\mathbf{k},\alpha,\beta} = -\Delta_{-\mathbf{k},\beta,\alpha}$. We insert the Bogoliubov-transformed operators (A.4) into the equation of motion (A.7). Calculating the time derivative of the quasiparticle operators on the left side ($i\partial_t \gamma_{k,\sigma} = E_{k,\sigma}\gamma_{k,\sigma}$) and gathering the terms with $\gamma_{k,\sigma}, \gamma^{\dagger}_{k,\sigma}$ respectively we obtain

$$E_{k,\sigma'} u_{k,\sigma,\sigma'} = \xi_{\mathbf{k}} u_{k,\sigma,\sigma'} - \sum_{\beta} u_{k,\beta,\sigma'} (\boldsymbol{\sigma}\cdot\mathbf{h})_{\sigma,\beta} + \sum_{\beta} \Delta_{k,\sigma,\beta} v_{k,\beta,\sigma'}, \tag{A.8}$$

$$E_{k,\sigma'} v_{k,\sigma,\sigma'} = -\xi_{-\mathbf{k}} v_{k,\sigma,\sigma'} + \sum_{\beta} v_{k,\beta,\sigma'} (\boldsymbol{\sigma}\cdot\mathbf{h})^{*}_{\sigma,\beta} - \sum_{\beta} \Delta^{*}_{-k,\sigma,\beta} u_{k,\beta,\sigma'}. \tag{A.9}$$

Rewriting the equations in a matrix form with respect to σ and σ' we obtain the BdG equation:

$$\begin{pmatrix} \xi_{\mathbf{k}} - h_z & -h_x + ih_y & \Delta_{\uparrow\uparrow}(\mathbf{k}) & \Delta_{\uparrow\downarrow}(\mathbf{k}) \\ -h_x - ih_y & \xi_{\mathbf{k}} + h_z & \Delta_{\downarrow\uparrow}(\mathbf{k}) & \Delta_{\downarrow\downarrow}(\mathbf{k}) \\ -\Delta^{*}_{\uparrow\uparrow}(-\mathbf{k}) & -\Delta^{*}_{\uparrow\downarrow}(-\mathbf{k}) & -\xi_{-\mathbf{k}} + h_z & h_x + ih_y \\ -\Delta^{*}_{\downarrow\uparrow}(-\mathbf{k}) & -\Delta^{*}_{\downarrow\downarrow}(-\mathbf{k}) & h_x - ih_y & -\xi_{-\mathbf{k}} - h_z \end{pmatrix} \begin{pmatrix} u_{\uparrow\sigma\mathbf{k}} \\ u_{\downarrow\sigma\mathbf{k}} \\ v_{\uparrow\sigma\mathbf{k}} \\ v_{\downarrow\sigma\mathbf{k}} \end{pmatrix} = E_{\sigma}(\mathbf{k}) \begin{pmatrix} u_{\uparrow\sigma\mathbf{k}} \\ u_{\downarrow\sigma\mathbf{k}} \\ v_{\uparrow\sigma\mathbf{k}} \\ v_{\downarrow\sigma\mathbf{k}} \end{pmatrix}$$

A more compact formulation is

$$\begin{pmatrix} \underline{\underline{\xi}}(\mathbf{k}) & \underline{\underline{\Delta}}(\mathbf{k}) \\ -\underline{\underline{\Delta}}^{*}(-\mathbf{k}) & -\underline{\underline{\xi}}^{*}(\mathbf{k}) \end{pmatrix} \begin{pmatrix} \underline{u}_{\sigma\mathbf{k}} \\ \underline{v}_{\sigma\mathbf{k}} \end{pmatrix} = E_{\sigma}(\mathbf{k}) \begin{pmatrix} \underline{u}_{\sigma\mathbf{k}} \\ \underline{v}_{\sigma\mathbf{k}} \end{pmatrix}, \tag{A.10}$$

where underlined and double-underlined characters indicate 2 component vectors and 2 × 2 matrices, respectively. Using the definition of the Bogoliubov transformation (A.4) one sees that the coefficients $u_{\sigma\mathbf{k}}$ correspond to the probability amplitude for having a electron-like excitation whereas $v_{\sigma\mathbf{k}}$ corresponds to a hole-like excitation. The submatrix $\underline{\underline{\Delta}}(\mathbf{k})$ describes a potential that couples electron-like and hole-like states. If the pairing potential is zero one again obtains the normal single-particle Hamiltonian to describe the F region. Setting the magnetization to zero we can describe the superconductor. The BdG equation allows us to calculate the four-component quasiparticle wavefunction for a given excitation energy. For this case is is not necessary to label the solutions by the second spin index σ thus we drop it in further calculations.

As already stated, the pairing potential has the same symmetry as the a two-fermion wavefunction, which implies

$$\underline{\underline{\Delta}}(\mathbf{k}) = -\underline{\underline{\Delta}}^T(-\mathbf{k}). \tag{A.11}$$

In the case of singlet pairing the orbital part of the wave function is even, so the pairing matrix has to be antisymmetric, and multiplied by an even function $\Delta(\mathbf{k})$,

$$\underline{\underline{\Delta}}(\mathbf{k}) = \begin{pmatrix} 0 & \Delta(\mathbf{k}) \\ -\Delta(\mathbf{k}) & 0 \end{pmatrix} = i\sigma_y \Delta(\mathbf{k}). \tag{A.12}$$

Transforming back into real space assuming a $\mathbf{k}$ independent paring matrix leads us to the BdG Eq.(1.83) used in Sec.(1.3) and chapter 2.

A.2 Linearized Eilenberger equation

Assume that the order parameter Δ is small compared to the typical excitation energy, in consequence

$$\check{g} \approx \text{sign}(\omega_n)\tau_3 + \begin{pmatrix} 0 & f \\ -\bar{f} & 0 \end{pmatrix} = \text{sign}(\omega_n)\tau_3 + \check{f}. \tag{A.13}$$

Inserting this approximation in Eq.(1.142), in equilibrium

$$v_{\text{F}} \left(n_i \tilde{\nabla}_i\right) \check{f} + \left[\tau_3(\omega_n - i\mathcal{A}_0) - i\check{\Delta}, \check{g}\right] - \frac{1}{2m} \left\{ n_i \mathcal{F}_{ij}, \frac{\partial \check{f}}{\partial n_j} \right\} = \frac{1}{2\tau} \left[\check{g}, \langle \check{g} \rangle\right]. \tag{A.14}$$

and we need to evaluate:

$$\begin{aligned} &\left[\tau_3(\omega_n - i\mathcal{A}_0) - i\check{\Delta}, \text{sign}(\omega_n)\tau_3 + \check{f}\right] = \left[\tau_3\left(\omega_n - i\mathcal{A}_0\right), \check{f}\right] - i\,\text{sign}(\omega_n)\left[\check{\Delta}, \tau_3\right] - i\left[\check{\Delta}, \check{f}\right] \\ &\left[\tau_3\left(\omega_n - i\mathcal{A}_0\right), \check{f}\right] = 2\omega_n\tau_3\check{f} - i\tau_3\left\{\mathcal{A}_0, \check{f}\right\} - i\left[\check{\Delta}, \check{g}\right] = i\,\text{sign}(\omega_n)\tau_3\check{\Delta} \quad \left(\left[\check{\Delta}, \check{f}\right] = 0\right). \end{aligned}$$

The right hand side becomes

$$\left[\check{g}, \langle \check{g} \rangle\right] = \left[\tau_3\,\text{sign}(\omega_n), \langle \check{f} \rangle\right] + \left[\check{f}, \tau_3\,\text{sign}(\omega_n)\right] = 2\,\text{sign}(\omega_n)\tau_3\left(\langle \check{f} \rangle - \check{f}\right).$$

We obtain the linearized Eilenberger equation which only depends on $\check{f}$

$$v_{\text{F}} \left(n_i \tilde{\nabla}_i\right) \check{f} + 2\omega_n\tau_3\check{f} - i\tau_3\left\{\mathcal{A}_0, \check{f}\right\} + 2i\,\text{sign}(\omega_n)\tau_3\check{\Delta} - \left\{ \frac{n_i \mathcal{F}_{ij}}{2m}, \frac{\partial \check{f}}{\partial n_j} \right\} = -\frac{\text{sign}(\omega_n)}{\tau}\tau_3\left(\check{f} - \langle \check{f} \rangle\right).$$

Since f and $\bar{f}$ are related by time reversal symmetry it is sufficient to extract the equation for f only

$$v_{\text{F}} \left(n_i \tilde{\nabla}_i\right) f + 2\omega_n f - i\left\{\mathcal{A}_0, f\right\} + 2i\Delta\,\text{sign}(\omega_n) - \frac{1}{2m} \left\{ n_i \mathcal{F}_{ij}, \frac{\partial f}{\partial n_j} \right\} \qquad = -\frac{\text{sign}(\omega_n)}{\tau}\left(f - \langle f \rangle\right). \tag{A.15}$$

A.3 Linearized Usadel equation

We expand f in spherical harmonics $f \approx f_0 + n_k f_k + \ldots$ and average the linearized Eilenberger equation over the momentum direction. We will obtain a set of coupled equations to determine the coefficients f_0, f_k. Performing the momentum average

$$\left\langle v_{\mathrm{F}} \left(n_i \tilde{\nabla}_i \right) f + 2\omega_n f - i \left\{ \mathcal{A}_0, f \right\} + 2i\Delta \ \mathrm{sign}(\omega_n) - \frac{1}{2m} \left\{ n_i \mathcal{F}_{ij}, \frac{\partial f}{\partial n_j} \right\} \right\rangle = 0,$$

and is easy to see that

$$\begin{aligned} \langle 2\omega_n f \rangle &= 2\omega_n f_0 = \{\omega_n, f_0\} \\ \langle 2i\Delta \mathrm{sign}(\omega_n) \rangle &= 2i\Delta \mathrm{sign}(\omega_n) \\ -i \left\langle \{\mathcal{A}_0, f\} \right\rangle &= -i \left\{ \mathcal{A}_0, f_0 \right\} \end{aligned}$$

and the last term on the right is

$$-\frac{1}{2m} \left\langle \left\{ n_i \mathcal{F}_{ij}, \frac{\partial f}{\partial n_j} \right\} \right\rangle = -\frac{1}{2m} \left\langle \left\{ n_i \mathcal{F}_{ij}, \frac{\partial (f_k n_k)}{\partial n_j} \right\} \right\rangle = -\frac{1}{2m} \left\langle \{ n_i, \mathcal{F}_{ij} f_j \} \right\rangle = 0.$$

The first term needs a closer look, we have

$$\left\langle v_{\mathrm{F}} \left(n_i \tilde{\nabla}_i \right) f \right\rangle = \underbrace{\left\langle v_{\mathrm{F}} \left(n_i \tilde{\nabla}_i f_0 \right) \right\rangle}_{=0} + \left\langle v_{\mathrm{F}} \left(n_i \tilde{\nabla}_i \right) n_k f_k \right\rangle = \frac{1}{\mathrm{dim}} v_F \tilde{\nabla}_k f_k. \tag{A.16}$$

with dim $= 1, 2, 3$ the dimension of the system. To determine the coefficients f_0, f_k we multiply Eq.(A.15) by n_k and again average over the momentum direction. We need to calculate

$$\begin{aligned} &\left\langle n_{k'} \left(v_{\mathrm{F}} \left(n_i \tilde{\nabla}_i \right) f + 2\omega_n f - i \left\{ \mathcal{A}_0, f \right\} + 2i\Delta \ \mathrm{sign}(\omega_n) - \frac{1}{2m} \left\{ n_i \mathcal{F}_{ij}, \frac{\partial f}{\partial n_j} \right\} \right) \right\rangle \\ &= \left\langle -\frac{\mathrm{sign}(\omega_n)}{\tau} n_{k'} \left(f - \langle f \rangle \right) \right\rangle. \end{aligned} \tag{A.17}$$

The right hand side is ($f \approx f_0 + n_k f_k$)

$$-\frac{\mathrm{sign}(\omega_n)}{\tau} \left\langle n_{k'} \left(f - \langle f \rangle \right) \right\rangle = -\frac{\mathrm{sign}(\omega_n)}{\tau} \left\langle n_{k'} n_k f_k \right\rangle = -\frac{\mathrm{sgn}(\omega_n)}{\tau} f_k \tag{A.18}$$

and the other terms are

$$\begin{aligned}
&\left\langle n_k v_{\mathrm{F}} \left(n_i \tilde{\nabla}_i\right) f\right\rangle = \left\langle n_k v_{\mathrm{F}} \left(n_i \tilde{\nabla}_i\right) f_0\right\rangle + \underbrace{\left\langle n_k v_{\mathrm{F}} \left(n_i \tilde{\nabla}_i\right) f_{k'} n_{k'}\right\rangle}_{=0} = v_{\mathrm{F}} \tilde{\nabla}_k f_0 \\
&\langle n_k \{\omega_n - i\mathcal{A}_0, f\}\rangle = \underbrace{\langle n_k \{\omega_n - i\mathcal{A}_0, f_0\}\rangle}_{=0} + \langle n_k \{\omega_n - i\mathcal{A}_0, n_{k'} f_{k'}\}\rangle = \{\omega_n - i\mathcal{A}_0, f_k\} \\
&\langle n_k 2i\Delta \ \mathrm{sign}(\omega_n)\rangle = 0 \\
&\left\langle n_k \left\{n_i \mathcal{F}_{ij}, \frac{\partial f}{\partial n_j}\right\}\right\rangle = \langle n_k \{n_i \mathcal{F}_{ij}, f_j\}\rangle = \{F_{kj}, f_j\}\,. \qquad \text{(A.19)}
\end{aligned}$$

We obtain the set of coupled equations

$$\frac{v_{\mathrm{F}}}{\mathrm{dim}} \tilde{\nabla}_k f_k + \{\omega_n - i\mathcal{A}_0, f_0\} + 2i\Delta \ \mathrm{sign}(\omega_n) = 0 \qquad \text{(A.20)}$$

$$v_{\mathrm{F}} \tilde{\nabla}_k f_0 + \{\omega_n - i\mathcal{A}_0, f_k\} - \frac{1}{2m}\{F_{kj}, f_j\} = -\frac{\mathrm{sgn}(\omega_n)}{\tau} f_k. \qquad \text{(A.21)}$$

The second equation allows to write f_k in terms of f_0 in orders of τ. Up to second order in τ (inserting the equation into it self):

$$\begin{aligned}
f_k \approx & -\tau \mathrm{sgn}(\omega_n)\left(v_{\mathrm{F}} \tilde{\nabla}_k f_0 + \left\{\omega_n - i\mathcal{A}_0, -\tau \mathrm{sgn}(\omega_n) v_{\mathrm{F}} \tilde{\nabla}_k f_0\right\}\right) \\
& - \tau^2 \frac{v_{\mathrm{F}}}{2m}\left\{\mathcal{F}_{kj}, \tilde{\nabla}_j f_0\right\} + \mathcal{O}(\tau^3) \\
= & -\tau \mathrm{sgn}(\omega_n) v_{\mathrm{F}} \tilde{\nabla}_k f_0 + \tau^2 v_{\mathrm{F}}\left\{\omega_n - i\mathcal{A}_0, \tilde{\nabla}_k f_0\right\} \\
& - \tau^2 \frac{v_{\mathrm{F}}}{2m}\left\{\mathcal{F}_{kj}, \tilde{\nabla}_j f_0\right\} + \mathcal{O}(\tau^3). \qquad \text{(A.22)}
\end{aligned}$$

The term $\left\{\omega_n - i\mathcal{A}_0, \tilde{\nabla}_k f_0\right\}$ can be written as

$$\left\{\omega_n - i\mathcal{A}_0, \tilde{\nabla}_k f_0\right\} = \tilde{\nabla}_k \{\omega_n - i\mathcal{A}_0, f_0\} + i\left\{\tilde{\nabla}_k \mathcal{A}_0, f_0\right\} \qquad \text{(A.23)}$$

where the first term on the right hand side is proportional to τ^3 [103], and the last term renormalizes the paramagnetic effects, i.e. it appears in the equation like $\mathcal{A}_0$. So we can neglect the first term and will neglect the second. Inserting this approximation into the first equation of our set, we obtain the Usadel equation for f_0

$$-\mathrm{sgn}(\omega_n) D \tilde{\nabla}^2 f_0 - \frac{\tau D}{2m} \tilde{\nabla}_i \left\{\mathcal{F}_{ij}, \tilde{\nabla}_j f_0\right\} + \{\omega_n - i\mathcal{A}_0, f_0\} + 2i\Delta \mathrm{sgn}(\omega_n) = 0$$

where $D = v_{\mathrm{F}}^2 \tau/\mathrm{dim}$ is the diffusion constant. The equation can be further simplified because

$$\tilde{\nabla}_i \left\{\mathcal{F}_{ij}, \tilde{\nabla}_j f_0\right\} = \left\{\tilde{\nabla}_i \mathcal{F}_{ij}, \tilde{\nabla}_j f_0\right\} + \underbrace{\left\{\mathcal{F}_{ij}, \tilde{\nabla}_i \tilde{\nabla}_j f_0\right\}}_{=0\ (\mathcal{F}_{ij} = -\mathcal{F}_{ji})}$$

and so the Usadel equation finally becomes

$$-\mathrm{sgn}(\omega_n)D\tilde{\nabla}^2 f_0 - \frac{\tau D}{2m}\left\{\tilde{\nabla}_i\mathcal{F}_{ij}, \tilde{\nabla}_j f_0\right\} + \{\omega_n - i\mathcal{A}_0, f_0\} + 2i\Delta\mathrm{sgn}(\omega_n) = 0. \tag{A.24}$$

A.4 Domain wall - perturbative solution

The solution of the linear domain wall problem up to first order in Q is obtained by solving Eqs.(3.14)-(3.17). In the domain wall the general solution is

$$\tilde{f}_t^y(x) = C_1 e^{\kappa_\omega x} + C_2 e^{-\kappa_\omega x} + Y_1 e^{\lambda^+ x} + Y_2 e^{\lambda^- x} \tag{A.25}$$

with $Y_{1/2} = -\frac{Q}{\lambda^\pm}\frac{\gamma f_{BCS}}{\lambda^{\pm 2} - \kappa_\omega^2}$ and C_i to be determined by the boundary conditions. At the S/F interface, using the condition (3.15) and assuming $h \gg T$ gives

$$C_1 - C_2 = iQ\mathrm{sign}(\omega_n)\xi_h\xi_\omega\gamma f_{BCS} \tag{A.26}$$

Rotating back the solution in the domain wall into the original frame gives

$$\hat{f}(x) = \tilde{f}_s(x)\hat{\sigma}^0 + \tilde{f}_t^y(x)\left(\hat{\sigma}^z\cos(Qx) + \sin(Qx)\hat{\sigma}^y\right) + \tilde{f}_t^z(x)\left(-\hat{\sigma}^z\sin(Qx) + \cos(Qx)\hat{\sigma}^y\right). \tag{A.27}$$

If we assume that $w \gg \xi_h$ and that the rotation of the field is only small $Qw \ll 1$, then $\tilde{f}_s(w), \tilde{f}_t^z(w)$ are very small. Also the part of $\tilde{f}_t^y(x) \propto Y_1, Y_2$ is decayed as well. We can approximately match the rotated homogeneous solution in the domain wall with the rotated homogeneous solution for $x > w$:

$$\hat{f}_t^y \approx \begin{cases} (C_1 e^{\kappa_\omega x} + C_2 e^{-\kappa_\omega x})\left(-\hat{\sigma}^z\cos(Qx) + \sin(Qx)\hat{\sigma}^y\right); & x < w \\ (C_3 e^{-\kappa_\omega x})\left(-\hat{\sigma}^z\cos(Qx) + \sin(Qx)\hat{\sigma}^y\right); & x > w. \end{cases} \tag{A.28}$$

Using that $Qw \ll 1$ as well as the continuity and continuity of the derivative at $x = w$, together with Eq.(A.26) leads to the folowing result in the homegenous part of the F region:

$$f_t^y(x) = i\mathrm{sign}(\omega_n)Q\xi_h\xi_\omega\gamma f_{BCS}e^{-\kappa_\omega x}. \tag{A.29}$$

A.5 Perturbative solution for the triplet junction

Basic equations

After performing the z-integration, the resulting system of differential equations for the transformed anomalous Green's function $\hat{\tilde{f}} = \mathcal{U}\hat{f}\mathcal{U}^\dagger$ for $|x| > L/2$ is:

$$\begin{aligned}
&D\left[\partial_x^2\tilde{f}_s\right] - 2|\omega_n|\tilde{f}_s - 2i\text{sign}(\omega_n)\bar{h}\tilde{f}_t^x = \\
&-D\bar{\gamma}f_{\text{BCS}}e^{-i\text{sign}(x)\frac{\varphi}{2}} && \text{(A.30)}\\
&D\left[\partial_x^2\tilde{f}_t^x + 2\bar{\mathcal{C}}_x^{xb}\left(\partial_x\tilde{f}_t^b\right)\right] - 2|\omega_n|\tilde{f}_t^x - D\bar{\Gamma}^{xb}\tilde{f}_t^b = \\
&2i\text{sign}(\omega_n)\tilde{f}_s\bar{h} && \text{(A.31)}\\
&D\left[\partial_x^2\tilde{f}_t^y + 2\bar{\mathcal{C}}_x^{yb}\left(\partial_x\tilde{f}_t^b\right)\right] - 2|\omega_n|\tilde{f}_t^y - D\bar{\Gamma}^{yb}\tilde{f}_t^b = 0 && \text{(A.32)}\\
&D\left[\partial_x^2\tilde{f}_t^z + 2\bar{\mathcal{C}}_x^{zb}\left(\partial_x\tilde{f}_t^b\right)\right] - 2|\omega_n|\tilde{f}_t^z - D\bar{\Gamma}^{zb}\tilde{f}_t^b = 0. && \text{(A.33)}
\end{aligned}$$

In the barrier region $|x| < L/2$ we get

$$\begin{aligned}
&D\partial_x^2\tilde{f}_s - 2|\omega_n|\tilde{f}_s - 2i\text{sign}(\omega_n)\bar{h}\tilde{f}_t^x = 0 && \text{(A.34)}\\
&D\partial_x^2\tilde{f}_t^x - 2|\omega_n|\tilde{f}_t^x - 2i\text{sign}(\omega_n)\bar{h}\tilde{f}_s = 0 && \text{(A.35)}\\
&D\partial_x^2\tilde{f}_t^y - 2|\omega_n|\tilde{f}_t^y = 0 && \text{(A.36)}\\
&D\partial_x^2\tilde{f}_t^z - 2|\omega_n|\tilde{f}_t^z = 0. && \text{(A.37)}
\end{aligned}$$

The z-integration causes a averaging of the couplings as described in the main text. The solution of this system of equations are continous and fullfill

$$\begin{aligned}
&\partial_x\tilde{f}_s\big|_{x=\pm\frac{L}{2}+0^-} = \partial_x\tilde{f}_s\big|_{x=\pm\frac{L}{2}+0^+} && \text{(A.38)}\\
&\partial_x\tilde{f}_t^a\big|_{x=\pm\frac{L}{2}+0^\mp} = \left[\partial_x\tilde{f}_t^a + \bar{\mathcal{C}}_x^{ab}\tilde{f}_t^b\right]_{x=\pm\frac{L}{2}+0^\pm}, && \text{(A.39)}
\end{aligned}$$

at the boundaries between the different regions. The spin precesion tensor components $\mathcal{C}_k^{ab}$ and DP tensor components Γ^{ab} in the rotated system are determined from the transformed fields

$$\begin{aligned}
\hat{\tilde{\mathcal{A}}}_x &= \frac{\hat{\sigma}^x}{2}\zeta(\vartheta) - \eta(\vartheta)\frac{\hat{\sigma}^y}{2}, && \text{(A.40)}\\
\hat{\tilde{\mathcal{A}}}_y &= \frac{\hat{\sigma}^x}{2}\eta(-\vartheta) - \zeta(-\vartheta)\frac{\hat{\sigma}^y}{2}, && \text{(A.41)}
\end{aligned}$$

with $\eta(\vartheta) = \bar{\alpha}\cos(\vartheta) + \bar{\beta}\sin(\vartheta)$ and $\zeta(\vartheta) = -\bar{\alpha}\sin(\vartheta) + \bar{\beta}\cos(\vartheta)$. The equations (A.30)-(A.39) fully determine the junction system within the limits of the approximations mentioned in the main text.

Zeroth order correction

As in the main text we consider the junction type 1 assuming semi-infinite leads. Solving the above system of equations for vanishing SOC gives the following zeroth order solution for the function $\tilde{f}_t^x$,

$$\tilde{f}_{t,0}^x = \begin{cases} \frac{A_1^L}{\lambda^+}e^{\lambda^+ x} + \frac{A_2^L}{\lambda^-}e^{\lambda^- x} + f_x^b e^{-i\frac{\varphi}{2}}, x < -\frac{L}{2} \\ \frac{B_1}{\lambda^+}e^{\lambda^+ x} - \frac{B_2}{\lambda^+}e^{-\lambda^+ x} + \frac{B_3}{\lambda^-}e^{\lambda^- x} - \frac{B_4}{\lambda^-}e^{-\lambda^- x} \\ -\frac{A_1^R}{\lambda^+}e^{-\lambda^+ x} - \frac{A_2^R}{\lambda^-}e^{-\lambda^- x} + f_x^b e^{i\frac{\varphi}{2}}, x > \frac{L}{2}. \end{cases} \tag{A.42}$$

where $\lambda^{\pm} = \sqrt{\frac{2|\omega_n|}{D} \pm i\frac{2\text{sgn}(\omega_n)\bar{h}}{D}}$,

$$A_{1/2}^L = \mp\lambda^{\pm}\frac{f_s^b \pm f_x^b}{2}\sinh\left(\frac{L\lambda^{\pm} - i\varphi}{2}\right) \tag{A.43}$$

$$B_{1/2} = \pm\frac{\lambda^+}{4}\left(f_s^b + f_x^b\right)\exp\left(\frac{-L\lambda^+ \pm i\varphi}{2}\right) \tag{A.44}$$

$$B_{3/4} = \mp\frac{\lambda^-}{4}\left(f_s^b - f_x^b\right)\exp\left(\frac{-L\lambda^- \pm i\varphi}{2}\right) \tag{A.45}$$

$$A_{1/2}^R = \pm\lambda^{\pm}\frac{f_s^b \pm f_x^b}{2}\sinh\left(\frac{L\lambda^{\pm} + i\varphi}{2}\right) \tag{A.46}$$

and the bulk solutions for the singlet and triplet x component

$$f_s^b = D\gamma\frac{f_{\text{BCS}}}{2}\frac{|\omega_n|}{|\omega_n|^2 + h^2} \approx \frac{\gamma|\omega_n|\xi_{\bar{h}}^2}{2\bar{h}}f_{\text{BCS}} \tag{A.47}$$

$$f_x^b = -iD\gamma\frac{f_{\text{BCS}}}{2}\frac{\text{sign}(\omega_n)\bar{h}}{|\omega_n|^2 + \bar{h}^2} \approx -i\frac{\gamma\text{sign}(\omega_n)\xi_{\bar{h}}^2}{2}f_{\text{BCS}}. \tag{A.48}$$

with $\xi_{\bar{h}} = \sqrt{D/\bar{h}}$.

First order correction

The Ansatz for the solution of Eq.(3.68) reads

$$\tilde{f}_{t,1}^z(x) = \begin{cases} K_1 e^{\kappa_\omega x} + Z_1^L e^{\lambda^+ x} + Z_2^L e^{\lambda^- x}, & x < -\frac{L}{2} \\ K_2 e^{\kappa_\omega x} + K_3 e^{-\kappa_\omega x}, & |x| < \frac{L}{2} \\ K_4 e^{-\kappa_\omega x} + Z_1^R e^{-\lambda^+ x} + Z_2^R e^{-\lambda^- x}, & x > \frac{L}{2} \end{cases} \tag{A.49}$$

where

$$Z_1^L = -\frac{\eta(\vartheta)A_1^L}{(\lambda^{+2}-\kappa_\omega^2)}, \quad Z_2^L = -\frac{\eta(\vartheta)A_2^L}{(\lambda^{-2}-\kappa_\omega^2)}, \tag{A.50}$$

$$Z_1^R = -\frac{\eta(\vartheta)A_1^R}{(\lambda^{+2}-\kappa_\omega^2)}, \quad Z_2^R = -\frac{\eta(\vartheta)A_2^R}{(\lambda^{-2}-\kappa_\omega^2)}, \tag{A.51}$$

Keeping only leading order terms when $\bar{h} \gg T, \max\left\{\bar{\Gamma}^{ab}\right\}$ and assuming $L \gg \xi_{\bar{h}}$ we find

$$\begin{pmatrix} K_1 \\ K_2 \\ K_3 \\ K_4 \end{pmatrix} \approx \frac{f_x^b}{\kappa_\omega}\frac{\eta(\vartheta)}{2} \begin{pmatrix} \sinh(\frac{L\kappa_\omega - i\varphi}{2}) \\ -\frac{1}{2}e^{-\frac{L\kappa_\omega}{2}}e^{\frac{i\varphi}{2}} \\ \frac{1}{2}e^{-\frac{L\kappa_\omega}{2}}e^{-\frac{i\varphi}{2}} \\ -\sinh(\frac{L\kappa_\omega + i\varphi}{2}) \end{pmatrix} \tag{A.52}$$

Second order correction

The Ansatz for the solution of Eq.(3.69) reads

$$\tilde{f}^y_{t,2}(x) = \begin{cases} (L_1 + xY_1^L)e^{\kappa_\omega x} + Y_2^L e^{\lambda^+ x} + Y_3^L e^{\lambda^- x} + Y_4^L, \; x < -\frac{L}{2} \\ L_2 e^{\kappa_\omega x} + L_3 e^{-\kappa_\omega x}, \; |x| < \frac{L}{2} \\ (L_4 + xY_1^R)e^{-\kappa_\omega x} + Y_2^R e^{-\lambda^+ x} + Y_3^R e^{-\lambda^- x} + Y_4^R, \; x > \frac{L}{2} \end{cases} \tag{A.53}$$

with

$$Y_1^{L/R} = \zeta(\vartheta)K_{1/4}, \tag{A.54}$$

$$Y_2^{L/R} = \pm\frac{2\lambda^{+2}\zeta(\vartheta)Z_1^L + \bar{\Gamma}_{yx}A_1^{L/R}}{\lambda^+(\lambda^{+2}-\kappa_\omega^2)}, \tag{A.55}$$

$$Y_3^{L/R} = \pm\frac{2\lambda^{-2}\zeta(\vartheta)Z_2^L + \bar{\Gamma}_{yx}A_2^{L/R}}{\lambda^-(\lambda^{-2}-\kappa_\omega^2)}, \tag{A.56}$$

$$Y_4^{L/R} = -\bar{\Gamma}_{yx}\frac{f_x^b e^{\mp i\frac{\varphi}{2}}}{\kappa_\omega^2}. \tag{A.57}$$

Considering only leading order terms when $\bar{h} \gg T, \max\left\{\bar{\Gamma}^{ab}\right\}$ consistent with the first order correction and assuming that $L \gg \xi_{\bar{h}}$ gives for the relevant coefficients inside the bride

$$\begin{pmatrix} L_2 \\ L_3 \end{pmatrix} = -\frac{1}{2}e^{-\frac{L\kappa}{2}}\begin{pmatrix} Y_4^R \\ Y_4^L \end{pmatrix}. \tag{A.58}$$

A.6 Solution of the Eilenberger equation for a semi-infinite wire

The Eilenberger equation in 1D for the Zeeman field and Rashba SOC oriented as in the main work is

$$\pm v_F \partial_x \check{g}_\pm = i \left[\pm \alpha k_F \hat{\sigma}^y + \tau_3 \left(i\omega_n + h\hat{\sigma}^z \right) + i\tau_2 \Delta, \check{g}_\pm \right] \; . \tag{A.59}$$

Here $\check{g}_\pm$ denotes the the Green's functions for both propagation directions $\pm v_F$. We assume that the wire extends over the region $x > 0$. This equation has to solved toghether with the boundary contitions

1. Total reflection at $x = 0$, $\check{g}_+(0) = \check{g}_-(0)$
2. Boundness at $x = +\infty$

We seek for a perturbative solution of Eq.(A.59) up to first order in h. We make the Ansatz

$$\check{g}_\pm(x) = \check{g}^{(0)} + \check{g}_\pm^{(1)}(x) \tag{A.60}$$

where $\check{g}^{(0)} = g_0\tau_3 + f_0\tau_2$ is the BCS Green's function in Matsubara frequency space, with $g_0 = \omega_n/E$, $f_0 = \Delta/E$ and $E = \sqrt{\omega_n^2 + \Delta^2}$. $\check{g}^{(1)}(x)$ is the first order correction in the Zeeman field h. The first order for correction is obtained from the Eilenberger equation

$$\partial_x g_\pm^{(1)} + \left[\pm E\check{g}^{(0)} - i\tilde{\alpha}\hat{\sigma}^y, \check{g}_\pm^{(1)} \right] = \pm 2\tau_1 \hat{\sigma}^z h f_0 \tag{A.61}$$

where we set $v_F = 1$ and $\tilde{\alpha} = \alpha m$. We search for the solution of the form

$$g_\pm^{(1)}(x) = U_\pm(x) \tilde{g}_\pm(x) U_\pm^{-1}(x) \tag{A.62}$$

with $U_\pm = \exp\left(\mp \check{g}^{(0)} E x + i\tilde{\alpha}\hat{\sigma}^y\right)$. Inserting this Ansatz into Eq.(A.59) gives

$$\partial_x \tilde{g}^\pm = \pm 2 h f_0 U_\pm^{-1} \tau_1 \hat{\sigma}^z U_\pm = \pm 2 h f_0 \tau_1 \hat{\sigma}^z U_\pm^2 . \tag{A.63}$$

Integrating the equation leads to

$$\begin{aligned} \tilde{g}_\pm(x) &= \tilde{g}_\pm(0) \pm 2hf_0\tau_1\hat{\sigma}^z \int_0^x dx' e^{\mp 2\check{g}^{(0)}Ex'} e^{2i\tilde{\alpha}\hat{\sigma}^y x\text{'}} \\ &= \tilde{g}_\pm(0) \pm \frac{2hf_0}{2(E^2+\tilde{\alpha}^2)} \tau_1 \hat{\sigma}^z \left(i\tilde{\alpha}\sigma_y \pm E\check{g}^{(0)} \right) \left(1 - U_\pm^2(x) \right) . \end{aligned} \tag{A.64}$$

With this the solution can be written as

$$\check{g}_\pm^{(1)}(x) = \tilde{g}_\pm(0) U_\pm^{-2} \pm \frac{hf_0}{E^2 + \tilde{\alpha}^2} \tau_1 \sigma_z \left(i\tilde{\alpha}\sigma_y \pm E\check{g}^{(0)} \right) \left(U_\pm^{-2} - 1 \right) \tag{A.65}$$

where we used that $e^{\check{g}^{(0)}Ex}\tilde{g}(0) = \tilde{g}(0)e^{-\check{g}^{(0)}Ex}$ due to the normalization condition of the Green's function. We need to impose boundedness of the solution. So $\tilde{g}(0)$ has to cancel exponentially growing terms in the second term of Eq.(A.6). Keeping only exponentially large terms, at $x \to \infty$,

$$U_{\pm}^{-2} = \frac{1}{2} e^{2Ex} (1 \pm \breve{g}^{(0)}) e^{-2i\tilde{\alpha}\hat{\sigma}^y x}, \tag{A.66}$$

and

$$\breve{g}_{\pm}^{(1)}(x_{\infty}) = \tilde{g}(0) U_{\pm}^{-2} \pm \frac{hf_0}{E^2 + \tilde{\alpha}^2} \tau_1 \hat{\sigma}^z \left(i\tilde{\alpha}\hat{\sigma}^y \pm E\breve{g}^{(0)} \right) U_{\pm}^{-2}. \tag{A.67}$$

We make the Ansatz $\tilde{g}(0) = -\frac{hf_0}{E^2+\tilde{\alpha}^2} \tau_1 (E\breve{g}^{(0)}\hat{\sigma}^z + \tilde{\alpha} b \hat{\sigma}^x)$, where b has to be determined from the boundary condition at infinity. From Eq.(A.67) we obtain

$$(-b \pm 1)(1 \pm \breve{g}^{(0)}) \frac{1}{2} e^{2Ex} e^{-2i\tilde{\alpha}\hat{\sigma}^y x} = 0 \tag{A.68}$$

which is solved by $b = \breve{g}^{(0)}$. Now we construct the full $\breve{g}^{(1)}(x)$ from Eq.(A.6). Writing $U_{\pm}^{-1} = u_{\pm}^{-1} A^{-1}$, with $A^{-1} = e^{-i\tilde{\alpha}\hat{\sigma}^y x}$ and $u_{\pm}^{-1} = e^{\pm \breve{g}^{(0)} Ex}$ we get

$$\breve{g}_{\pm}^{(1)}(x) = \frac{hf_0}{E^2 + \tilde{\alpha}^2} \left\{ \tilde{\alpha}\hat{\sigma}^x A^{-2} \tau_1 \left[-\breve{g}^{(0)} \pm 1 \right] u_{\pm}^{-2} + \left[\mp\tilde{\alpha}\hat{\sigma}^x + E\breve{g}^{(0)}\hat{\sigma}^z \right] \tau_1 \right\}. \tag{A.69}$$

The exponentially growing part gets canceled by construction, se we can keep only the decaying part of $u_{\pm}^{-2}$ which is $u_{\pm}^{-2} = \frac{1}{2} e^{-2Ex}(1 \mp \breve{g}^{(0)})$. Inserting this in the above equation finally leads to

$$\breve{g}_{\pm}^{(1)}(x) = \frac{hf_0}{E^2 + \tilde{\alpha}^2} \left[\mp\tilde{\alpha}\hat{\sigma}^x + E\breve{g}^{(0)}\hat{\sigma}^z \right] \tau_1 + \frac{hf_0}{E^2 + \tilde{\alpha}^2} \alpha e^{-2Ex} \hat{\sigma}^x e^{-2i\hat{\sigma}^y x} \left[\breve{g}^{(0)} \pm 1 \right] \tau_1 \tag{A.70}$$

The symmetric part of the above Green's function is

$$\delta\breve{g}_s^{(1)}(x) = \breve{g}_{+}^{(1)}(x) + \breve{g}_{-}^{(1)}(x) = 2 \frac{hf_0}{E^2 + \tilde{\alpha}^2} \breve{g}^{(0)} \tau_1 \left[E\hat{\sigma}^z + \tilde{\alpha}\hat{\sigma}^x e^{-2Ex} e^{-i2\tilde{\alpha}x\breve{\sigma}^y} \right] \tag{A.71}$$

The corresponding correction to the magnetization is obtained from

$$\delta h_j = \pi i T \mu_B N_0 \frac{1}{8} \sum_{\omega_n} \mathrm{Tr} \tau_3 \hat{\sigma}^j g_s^{(1)}. \tag{A.72}$$

Bibliography

[1] H. Onnes, KNAW, Proceedings , 1274 (1911).

[2] F. London and H. London, Proceedings of the Royal Society of London. Series A - Mathematical and Physical Sciences **149**, 71 (1935).

[3] V. L. Ginzburg and L. D. Landau, Zh. Eksp. Teor. Fiz. **20**, 1064 (1950).

[4] J. Bardeen, L. Cooper, and J. Schrieffer, Phys. Rev. **108**, 1175 (1957).

[5] M. Ribault, J. P. Pouget, D. Jerome, and K. Bechgaard, J. Physique Lettres **41**, 95 (1980).

[6] F. Steglich, J. Aarts, C. D. Bredl, W. Lieke, D. Meschede, W. Franz, and H. Schäfer, Phys. Rev. Lett. **43**, 1892 (1979).

[7] J. Bednorz and K. Müller, Z. Physik B - Condensed Matter **64**, 189 (1986).

[8] J. Nagamatsu, N. Nakagawa, T. Muranaka, Y. Zenitani, and J. Akimitsu, Nature **410**, 63 (2001).

[9] J. R. Ashburn, M. K. Wu, and C. J. Torng, Phys. Rev. Lett. **58**, 908 (1987).

[10] A. P. Drozdov, M. I. Eremets, I. A. Troyan, V. Ksenofontov, and S. I. Shylin, Nature **525**, 73 (2015).

[11] G. S. Paraoanu, Journal of Low Temperature Physics **175**, 633 (2014).

[12] J. Q. You and F. Nori, Nature **474**, 589 (2011).

[13] G. Wendin, Rep. Prog. Phys. **80** (2017).

[14] R. C. Jaklevic, J. Lambe, A. H. Silver, and E. Mercereau, Phys. Rev. Lett. **12**, 159 (1964).

[15] V. Bouchiat, D. Vion, P. Joyez, D. Esteve, and M. H. Devoret, Phys. Scr. **T76**, 165 (2003).

[16] J. Koch, T. M. Yu, J. Gambetta, A. A. Houck, D. I. Schuster, J. Majer, A. Blais, M. H. Devoret, S. M. Girvin, and R. J. Schoelkopf, Phys. Rev. A **76**, 042319 (2007).

[17] V. E. Manucharyan, J. Koch, L. I. Glazman, and M. H. Devoret, Science **326**, 113 (2009).

[18] B. D. Josephson, Phys. Lett. **99**, 144524 (1962).

[19] M. Rowell and P. Anderson, Phys. Rev. Lett. **10**, 230 (1963).

[20] S. Shapiro, Phys. Rev. Lett. **11**, 88 (1963).

[21] M. de Jong and C. Beenakker, Phys. Rev. Lett. **74**, 1657 (1995).

[22] L. Bulaevskii, V. Kuzii, and A. Sobyanin, JETP Lett. **25**, 290 (1977).

[23] S. V. Panyukov, L. N. Bulaevskil, and A. I. Buzdin, Sov. Phys. JETP **35**, 178 (1982).

[24] F. S. Bergeret, A. F. Volkov, and K. B. Efetov, Phys. Rev. B **64**, 134506 (2001).

[25] V. V. Ryazanov, V. A. Oboznov, A. Y. Rusanov, A. V. Veretennikov, A. A. Golubov, and J. Aarts, Phys. Rev. Lett. **86**, 2427 (2001).

[26] T. Kontos, M. Aprili, J. Lesueur, F. Genêt, B. Stephanidis, and R. Boursier, Phys. Rev. Lett. **89**, 137007 (2002).

[27] F. S. Bergeret, A. F. Volkov, and K. B. Efetov, Phys. Rev. Lett. **86**, 4096 (2001).

[28] F. S. Bergeret, A. F. Volkov, and K. B. Efetov, Rev. Mod. Phys. **77**, 1321 (2005).

[29] J. Linder and J. W. Robinson, Nat. Phys. **11**, 307 (2015).

[30] M. Eschrig, Phys. Today **64**, 43 (2011).

[31] F. S. Bergeret and I. V. Tokatly, Phys. Rev. Lett. **110**, 117003 (2013).

[32] F. S. Bergeret and I. V. Tokatly, Phys. Rev. B **89**, 134517 (2014).

[33] E. I. Rashba, Sov. Phys. Solid State **2**, 1109 (1960).

[34] G. Dresselhaus, Phys. Rev. **100**, 580 (1955).

[35] D. Bercioux and P. Lucignano, Rep. Prog. Phys. **78**, 106001 (2015).

[36] J. Nitta, T. Akazaki, H. Takayanagi, and T. Enoki, Phys. Rev. Lett. **78**, 1335 (1997).

[37] F. Dettwiler, J. Fu, S. Mack, P. J. Weigele, J. C. Egues, D. D. Awschalom, and D. M. Zumbühl, Phys. Rev. X **7**, 031010 (2017).

[38] E. Majorana and L. Maiani, Il Nuovo Cimento **14**, 171 (1937).

[39] A. Y. Kitaev, Physi.-Usp. **44**, 131 (2001).

[40] J. Leinaas and J. Myrheim, Nuovo Cimento Soc. Ital. Fis B **37B**, 1 (1977).

[41] C. Nayak, S. H. Simon, A. Stern, M. Freedman, and S. Das Sarma, Rev. Mod. Phys. **80**, 1083 (2008).

[42] J. Nilsson, A. R. Akhmerov, and C. W. J. Beenakker, Phys. Rev. Lett. **101**, 120403 (2008).

[43] J. D. Sau, R. M. Lutchyn, S. Tewari, and S. Das Sarma, Phys. Rev. Lett. **104**, 040502 (2010).

[44] M. A. Silaev and G. E. Volovik, J. Low Temp. Phys. **161**, 460 (2010).

[45] Y. Oreg, G. Refael, and F. Von Oppen, Phys. Rev. Lett. **105**, 177002 (2010).

[46] A. Das, Y. Ronen, Y. Most, Y. Oreg, M. Heiblum, and H. Shtrikman, Nat. Phys. **8**, 887 (2012).

[47] V. Mourik, K. Zuo, S. M. Frolov, S. R. Plissard, E. P. A. M. Bakkers, and L. P. Kouwenhoven, Science **336**, 1003 (2012).

[48] T. D. Stanescu, S. Tewari, J. D. Sau, and S. Das Sarma, Phys. Rev. Lett. **109**, 1 (2012).

[49] C. H. Lin, J. D. Sau, and S. Das Sarma, Phys. Rev. B **86**, 1 (2012).

[50] J. Liu, A. C. Potter, K. T. Law, and P. A. Lee, Phys. Rev. Lett. **109**, 1 (2012).

[51] D. Sticlet, C. Bena, and P. Simon, Phys. Rev. Lett. **108**, 096802 (2012).

[52] T. Ojanen, Phys. Rev. Lett. **109**, 226804 (2012).

[53] I. V. Tokatly, B. Bujnowski, and F. S. Bergeret, arxiv (2019), arXiv:1901.07890 .

[54] N. P. Armitage, E. J. Mele, and A. Vishwanath, Rev. Mod. Phys. **90**, 15001 (2018).

[55] H. Weng, C. Fang, Z. Fang, B. Andrei Bernevig, and X. Dai, Phys. Rev. X **5**, 1 (2015).

[56] S. M. Huang, S. Y. Xu, I. Belopolski, C. C. Lee, G. Chang, B. Wang, N. Alidoust, G. Bian, M. Neupane, C. Zhang, S. Jia, A. Bansil, H. Lin, and M. Z. Hasan, Nat. Commun. **6**, 1 (2015).

[57] B. Q. Lv, H. M. Weng, B. B. Fu, X. P. Wang, H. Miao, J. Ma, P. Richard, X. C. Huang, L. X. Zhao, G. F. Chen, Z. Fang, X. Dai, T. Qian, and H. Ding, Phys. Rev. X **5**, 1 (2015).

[58] N. Bovenzi, M. Breitkreiz, P. Baireuther, T. E. O'Brien, J. Tworzydło, I. Adagideli, and C. W. Beenakker, Phys. Rev. B **96**, 1 (2017).

[59] R. D. Hills, A. Kusmartseva, and F. V. Kusmartsev, Phys. Rev. B **95**, 1 (2017).

[60] V. H. Nguyen and J. C. Charlier, Phys. Rev. B **97**, 1 (2018).

[61] Q. D. Jiang, H. Jiang, H. Liu, Q. F. Sun, and X. C. Xie, Phys. Rev. Lett. **115**, 1 (2015).

[62] S. A. Yang, H. Pan, and F. Zhang, Phys. Rev. Lett. **115**, 1 (2015).

[63] Z. Zhu, A. Collaudin, B. Fauqué, W. Kang, and K. Behnia, Nat. Phys. **8**, 89 (2012).

[64] C. Yesilyurt, S. G. Tan, G. Liang, and M. B. Jalil, Sci. Rep. **6**, 1 (2016).

[65] A. Zagoskin, *Quantum Theory of Many-Body Systems* (Springer, 1998).

[66] H. Bruus and K. Flensberg, *Many-body quantum theory in condensed matter physics - An introduction* (Oxford University Press, 2004).

[67] N. N. Bogoliubov, Sov. Phys. JETP **7**, 41 (1958).

[68] A. A. Abrikosov and L. P. Gor'kov, *Methods of quantum field theory in statistical physics* (Prentice Hall, 1963).

[69] L. P. Gor’kov and T. Melik-Barkhudarov, Sov. Phys. JETP **18**, 1493 (1963).

[70] G. E. Blonder, M. Tinkham, and T. M. Klapwijk, Phys. Rev. B **25**, 4515 (1982).

[71] A. F. Andreev, Sov. Phys. JETP. **20**, 1490 (1964).

[72] C. W. J. Beenakker, in *Transport Phenomena in Mesoscopic Systems*, edited by H. Fukuyama and T. Ando (Springer, 1992).

[73] C. W. J. Beenakker and H. van Houten, Phys. Rev. Lett. **66**, 3056 (1991).

[74] W. L. McMillan, Phys. Rev. **175**, 559 (1968).

[75] C. Ishii, Prog. Theor. Phys. **44**, 1525 (1970).

[76] A. Furusaki and M. Tsukada, Solid State Commun. **78**, 299 (1991).

[77] S. Kashiwaya and Y. Tanaka, Rep. Prog. Phys. **63**, 1641 (2000).

[78] A. Furusaki, H. Takayanagi, and M. Tsukada, Phys. Rev. B **45**, 10563 (1992).

[79] I. Kulik and A. Omel’yanchuk, Sov. J. Low. Temp. Phys. **3**, 459 (1977).

[80] V. Ambegaokar, Phys. Rev. Lett. **10** (1965).

[81] I. Kulik and A. Omel’yanchuk, JETP Lett. **21**, 96 (1975).

[82] C. Muller, J. van Ruitenbeek, and L. de Jongh, Phys. Rev. Lett. **69**, 140 (1992).

[83] C. J. Muller, M. C. Koops, B. J. Vleeming, R. de Bruyn Ouboter, and A. N. Omelyanchouk, Physica C: Superconductivity and its applications **220**, 258 (1994).

[84] S. Datta, *Electronic Transport in Mesoscopic Systems* (Cambridge University Press, 1995).

[85] Dorokhov, Solid State Commun. **51**, 382 (1984).

[86] W. Meissner and R. Ochsenfeld, Naturwissenschaften **21**, 787 (1933).

[87] A. M. Clogston, Phys. Rev. Lett. **9**, 266 (1962).

[88] B. S. Chandrasekhar, Appl. Phys. Lett. **1**, 7 (1962).

[89] A. P. Mackenzie and Y. Maeno, Rev. Mod. Phys. **75**, 657 (2003).

[90] P. Fulde and R. Ferrell, Phys. Rev. **135**, 550 (1964).

[91] A. I. Larkin and Y. N. Ovchinnikov, Zh. Eksp. Teor. Fiz. **47**, 1136 (1964).

[92] G. Zwicknagl and J. Wosnitza, Int. J. Mod. Phys. B **24**, 337 (2010).

[93] R. Beyer, B. Bergk, S. Yasin, J. A. Schlueter, and J. Wosnitza, Phys. Rev. Lett. **109**, 1 (2012).

[94] Y. Takane and H. Ebisawa, JPSJ **61**, 1685 (1992).

[95] E. Wigner, Phys. Rev. **40**, 749 (1932).

[96] A. Polkovnikov, Annals of Physics **325**, 1790 (2010).

[97] J. E. Moyal and M. S. Bartlett, Math. Proc. Camb. Philos. Soc. **45**, 99 (1947).

[98] I. V. Tokatly, Phys. Rev. Lett. **101**, 106601 (2008).

[99] C. Gorini, P. Schwab, R. Raimondi, and A. L. Shelankov, Phys. Rev. B **82**, 1 (2010).

[100] F. Konschelle, EPJ B **87** (2014).

[101] H.-T. Elze, M. Gyulassy, and D. Vasak, Phys. Lett. B **177**, 402 (1986).

[102] H.-T. Elze and U. Heinz, Phys. Rep. **183**, 81 (1989).

[103] F. Konschelle, I. V. Tokatly, and F. S. Bergeret, Phys. Rev. B **92**, 125443 (2015).

[104] F. S. Bergeret and I. V. Tokatly, Epl **110** (2015).

[105] I. V. Tokatly, Phys. Rev. B **96**, 060502 (2017).

[106] K. Usadel, Phys. Rev. Lett. **25**, 507 (1970).

[107] M. Y. Kupriyanov and V. F. Lukichev, Sov. Phys. JETP **67**, 1163 (1988).

[108] P. M. Tedrow and R. Meservey, Phys. Rev. Lett. **26**, 192 (1971).

[109] R. Meservey and P. M. Tedrow, Phys. Rep. **238**, 173 (1994).

[110] P. M. Tedrow, J. E. Tkaczyk, and A. Kumar, Phys. Rev. Lett. **56**, 1746 (1986).

[111] X. Hao, J. S. Moodera, and R. Meservey, Phys. Rev. B **42** (1990).

[112] T. Tokuyasu, J. A. Sauls, and D. Rainer, Phys. Rev. B **38**, 8823 (1988).

[113] D. Huertas-Hernando, Y. V. Nazarov, and W. Belzig, Phys. Rev. Lett. **88**, 4 (2002).

[114] F. Giazotto and F. S. Bergeret, Appl. Phys. Lett. **102** (2013).

[115] P. Machon, M. Eschrig, and W. Belzig, Phys. Rev. Lett. **110**, 047002 (2013).

[116] A. Ozaeta, P. Virtanen, F. S. Bergeret, and T. T. Heikkilä, Phys. Rev. Lett. **112**, 057001 (2014).

[117] F. Giazotto, J. W. Robinson, J. S. Moodera, and F. S. Bergeret, Appl. Phys. Lett. **105** (2014).

[118] S. M. Albrecht, A. P. Higginbotham, M. Madsen, F. Kuemmeth, T. S. Jespersen, J. Nygård, P. Krogstrup, and C. M. Marcus, Nature **531**, 206 (2016).

[119] C. Klose, T. S. Khaire, Y. Wang, W. P. Pratt, N. O. Birge, B. J. McMorran, T. P. Ginley, J. A. Borchers, B. J. Kirby, B. B. Maranville, and J. Unguris, Phys. Rev. Lett. **108**, 127002 (2012).

[120] T. S. Khaire, M. A. Khasawneh, W. P. Pratt, and N. O. Birge, Phys. Rev. Lett. **104**, 137002 (2010).

[121] W. M. Martinez, W. P. Pratt, and N. O. Birge, Phys. Rev. Lett. **116**, 077001 (2016).

[122] F. S. Bergeret, A. F. Volkov, and K. B. Efetov, Phys. Rev. Lett. **86**, 3140 (2001).

[123] N. M. Chtchelkatchev, W. Belzig, and C. Bruder, JETP Lett. **75**, 646 (2002).

[124] Y. M. Blanter and F. W. Hekking, Phys. Rev. B **69**, 024525 (2004).

[125] J. W. A. Robinson, G. B. Halász, A. I. Buzdin, and M. G. Blamire, Phys. Rev. Lett. **104**, 207001 (2010).

[126] C. Holmqvist, W. Belzig, and M. Fogelström, Phys. Rev. B **86**, 054519 (2012).

[127] P. Stadler, C. Holmqvist, and W. Belzig, Phys. Rev. B **88**, 104512 (2013).

[128] C. W.J. Beenakker, Phys. Rev. Lett. **67**, 3836 (1991).

[129] L.-F. Chang and P. F. Bagwell, Phys. Rev. B **49**, 15853 (1994).

[130] F. Konschelle, F. S. Bergeret, and I. V. Tokatly, Phys. Rev. Lett. **116**, 1 (2016).

[131] P. W. Brouwer and C. W. Beenakker, Chaos, Solitons and Fractals **8**, 1249 (1997).

[132] Y. Tanaka and S. Kashiwaya, Phys. Rev. B **53**, 9371 (1996).

[133] V. M. Edelstein, Phys. Rev. B **67**, 020505 (2003).

[134] M. Duckheim and P. W. Brouwer, Phys. Rev. B **83**, 054513 (2011).

[135] J. Robinson, J. Witt, and M. Blamire, Science **329**, 59 (2010).

[136] M. S. Anwar, F. Czeschka, M. Hesselberth, M. Porcu, and J. Aarts, Phys. Rev. B **82**, 100501(R) (2010).

[137] X. L. Wang, A. Di Bernardo, N. Banerjee, A. Wells, F. S. Bergeret, M. G. Blamire, and J. W. A. Robinson, Phys. Rev. B **89**, 140508(R) (2014).

[138] E. C. Gingrich, P. Quarterman, Y. Wang, R. Loloee, W. P. Pratt, and N. O. Birge, Phys. Rev. B **86**, 224506 (2012).

[139] J. W. A. Robinson, F. Chiodi, M. Egilmez, G. B. Halász, and M. G. Blamire, Sci. Rep. **2**, 699 (2012).

[140] F. Chiodi, J. D. S. Witt, R. G. J. Smits, L. Qu, G. B. Halász, C.-T. Wu, O. T. Valls, K. Halterman, J. W. A. Robinson, and M. G. Blamire, EPL **101**, 37002 (2013).

[141] A. Pal, Z. Barber, J. Robinson, and M. Blamire, Nat. Commun. **5**, 3340 (2014).

[142] J. W. A. Robinson, N. Banerjee, and M. G. Blamire, Phys. Rev. B **89**, 104505 (2014).

[143] Y. Kalcheim, O. Millo, M. Egilmez, J. W. A. Robinson, and M. G. Blamire, Physical Review B **85**, 104504 (2012).

[144] N. Banerjee, C. B. Smiet, R. G. J. Smits, A. Ozaeta, F. S. Bergeret, M. G. Blamire, and J. W. A. Robinson, Nat. Commun. **5**, 3048 (2014).

[145] N. Satchell and N. O. Birge, Phys. Rev. B **97**, 214509 (2018).

[146] N. Banerjee, J. A. Ouassou, Y. Zhu, N. A. Stelmashenko, J. Linder, and M. G. Blamire, Phys. Rev. B **97**, 184521 (2018).

[147] N. Satchell, R. Loloee, and N. O. Birge, Phys. Rev. B **99**, 174519 (2019).

[148] X. Liu, J. K. Jain, and C.-X. Liu, Phys. Rev. Lett. **113**, 227002 (2014).

[149] J. Arjoranta and T. T. Heikkilä, Phys. Rev. B **93**, 024522 (2016).

[150] J. R. Eskilt, M. Amundsen, N. Banerjee, and J. Linder, arxiv (2019), arXiv:1906.07725 .

[151] I. Žutić, J. Fabian, and S. Das Sarma, Rev. Mod. Phys. **76**, 323 (2004).

[152] H.-A. Engel, E. I. Rashba, and B. I. Halperin, in *Handbook of Magnetism and Advanced Magnetic Materials Vol. 5*, edited by H. Kronmüller and S. Parkin (Wiley, New York, 2007).

[153] S. Maekawa, S. O. Valenzuela, E. Saitoh, and T. Kimura, eds., *Spin Current* (Oxford University Press, 2012).

[154] E. I. Rashba, Phys. Rev. B **68**, 241315 (2003).

[155] E. I. Rashba, in *Future Trends in Microelectronics. Up the Nano Creek*, edited by S. Luryi, J. M. Xu, and A. Zaslavsky (Wiley, Hoboken, 2007).

[156] J. Shi, P. Zhang, D. Xiao, and Q. Niu, Phys. Rev. Lett. **96**, 076604 (2005).

[157] E. B. Sonin, Phys. Rev. B **76**, 033306 (2007).

[158] E. B. Sonin, Phys. Rev. Lett. **99**, 266602 (2007).

[159] J. Wang and K. S. Chan, Phys. Rev. B **74**, 1 (2006).

[160] I. Tokatly and E. Sherman, Annals of Physics **325**, 1104 (2010).

[161] F. Dolcini and F. Rossi, Phys. Rev. B **98**, 045436 (2018).

[162] A. A. Abrikosov and L. P. Gor'kov, Sov. Phys. JETP. **15**, 752 (1962).

[163] A. A. Abrikosov, *Fundamentals of the Theory of Metals* (North Holland, 1988).

[164] L. P. Gor'kov and E. I. Rashba, Phys. Rev. Lett. **87**, 037004 (2001).

[165] M. T. Deng, C. L. Yu, G. Y. Huang, M. Larsson, P. Caroff, and H. Q. Xu, Nano Lett. **12**, 6414 (2012).

[166] J. Paajaste, M. Amado, S. Roddaro, F. S. Bergeret, D. Ercolani, L. Sorba, and F. Giazotto, Nano Lett. **15**, 1803 (2015).

[167] W. Chang, S. M. Albrecht, T. S. Jespersen, F. Kuemmeth, P. Krogstrup, J. Nygård, and C. M. Marcus, Nat. Nanotechnol. **10**, 232 (2015).

[168] M. T. Deng, S. Vaitiekenas, E. B. Hansen, J. Danon, M. Leijnse, K. Flensberg, J. Nyg{\r a}rd, P. Krogstrup, and C. M. Marcus, Science **354**, 1557 (2016).

[169] J. Tiira, E. Strambini, M. Amado, S. Roddaro, P. San-Jose, R. Aguado, F. S. Bergeret, D. Ercolani, L. Sorba, and F. Giazotto, Nat. Commun. **8**, 1 (2017).

[170] H. Zhang, Ö. Gül, S. Conesa-Boj, M. P. Nowak, M. Wimmer, K. Zuo, V. Mourik, F. K. De Vries, J. Van Veen, M. W. De Moor, J. D. Bommer, D. J. Van Woerkom, D. Car, S. R. Plissard, E. P. Bakkers, M. Quintero-Pérez, M. C. Cassidy, S. Koelling, S. Goswami, K. Watanabe, T. Taniguchi, and L. P. Kouwenhoven, Nat. Commun. **8** (2017).

[171] R. M. Lutchyn, E. P. Bakkers, L. P. Kouwenhoven, P. Krogstrup, C. M. Marcus, and Y. Oreg, Nat. Rev. Mater. **3**, 52 (2018).

[172] P. Szumniak, D. Chevallier, D. Loss, and J. Klinovaja, Phys. Rev. B **96**, 041401 (2017).

[173] K. Björnson, S. S. Pershoguba, A. V. Balatsky, and A. M. Black-Schaffer, Phys. Rev. B **92**, 214501 (2015).

[174] M. Serina, D. Loss, and J. Klinovaja, Phys. Rev. B **98**, 035419 (2018).

[175] G. Eilenberger, Zeitschrift für Physik **214**, 195 (1968).

[176] S. A. Wolf, D. D. Awschalom, R. A. Buhrman, J. M. Daughton, S. Von Molnár, M. L. Roukes, A. Y. Chtchelkanova, and D. M. Treger, Science **294**, 1488 (2001).

[177] V. Cerletti, W. A. Coish, O. Gywat, and D. Loss, Nanotechnology **16**, R27 (2005).

[178] L. Šmejkal, Y. Mokrousov, B. Yan, and A. H. MacDonald, Nat. Phys. **14**, 242 (2018).

[179] F. Bussolotti, H. Kawai, Z. E. Ooi, V. Chellappan, D. Thian, A. L. C. Pang, and K. E. J. Goh, Nano Futures **2** (2018).

[180] A. Rycerz, J. Tworzydło, and C. W. Beenakker, Nature Physics **3**, 172 (2007).

[181] A. Messiah, *Quantum Mechanics (Vol 2)* (North-Holland, 1962).

[182] H. Weyl, Zeitschrift für Physik **56**, 330 (1929).

[183] A. A. Burkov, M. D. Hook, and L. Balents, Phys. Rev. B **84**, 235126 (2011).

[184] R. Ilan, A. G. Grushin, and D. I. Pikulin, arxiv , 1 (2019), arXiv:1903.11088 .

[185] A. Westström and T. Ojanen, Phys. Rev. X **7**, 1 (2017).

[186] V. Peri, M. Serra-Garcia, R. Ilan, and S. D. Huber, Nat. Phys. **15**, 357 (2019).

[187] H. Jia, R. Zhang, W. Gao, Q. Guo, B. Yang, J. Hu, Y. Bi, Y. Xiang, C. Liu, and S. Zhang, Science **363**, 148 (2019).